OBSERVATIONS OF PARTICLE
MOTIONS IN OCEAN WAVES
by D. H. Shonting

July 67

NAVAL UNDERWATER WEAPONS
RESEARCH AND ENGINEERING STATION
NEWPORT, RHODE ISLAND

ed.

TM No. 377 (Vol. 1)

NAVAL UNDERWATER WEAPONS RESEARCH AND ENGINEERING STATION
NEWPORT, RHODE ISLAND

TECHNICAL MEMORANDUM

OBSERVATIONS OF PARTICLE MOTIONS
IN OCEAN WAVES

Prepared by: *D. H. Shonting*
————————————
D. H. Shonting

G. G. GOULD
Technical Director

July 1967

W. W. WITTER
Captain, USN
Commanding Officer

WEPTASK Assignment No.
RU22-20-000/219 1/R104-03-01

Distribution of this
document is unlimited.

FOREWORD

The time variable interactions of the wind together
with the heating and cooling at the sea-air interface
make the surface ocean layers a very complex medium to
understand. These dynamic and thermal perturbations at
the surface also make it very difficult to measure and
predict the acoustic properties of the upper ocean layers.
Navy ASW programs have spent millions of dollars on in-
strument development in an attempt to counteract the
disturbing effects of the ocean medium upon the trans-
mission of acoustical energy. Consequently, some effort
should be exerted to overcome our gross ignorance of the
physics of the ocean surface.

The momentum and energy supplied to the sea surface
by wind stress plays a critical role in determining the
turbulent and diffusion characteristics of the surface
layer; i.e., the parameters controlling the transfer of
heat and spatial and temporal acoustic variations.

This report describes some new experimental ap-
proaches for obtaining information about wind wave tur-
bulence and energy distributions in the surface layer.
It is hoped that these studies will help to stimulate
further direct measurements of ocean waves and turbu-
lence, and that the results reported can be helpful in
furthering the understanding of parameters which affect
ASW systems.

This work was performed under Naval Ordnance Sys-
tems Command Task Assignment RU22-2E-000/219 1/R004-03-01
for oceanographic studies, and under the Planetary Cir-
culations Project of the Department of Meterology at the
Massachusetts Institute of Technology. The report was
submitted by the author to the Department of Meterology
at MIT in partial fulfillment of the requirements for
the degree of Doctor of Science. The report is in two
volumes: volume one contains the complete basic text;
volume two contains the various appendices.

SUMMARY

Little is known of how wind stress is imparted to the sea surface and
how this stress generates both waves and ocean currents. Most wave studies
have concentrated upon measuring free surface fluctuations and have avoided
the examination of the dynamic regime beneath the free surface of the waves.
The work reported herein deals with making direct Eulerian measurements of
the complex motions within the wave regime.

A historical review and a discussion of the problems of measuring tur-
bulent and oscillatory motions are presented. The development of wave meter
instrumentation is discussed. The wave motion sensor consists of a cylindri-
cal housing containing an axially-mounted impeller. The instrument is sus-
pended beneath the free surface, and the component of flow parallel to the
cylinder axis imparts to the impeller an angular velocity proportional to
the flow speed. The impeller rotation is detected by the interaction of min-
iature magnets (mounted at the blade tips) with a small pickup coil on the
cylinder. The ducted meter systems consist of a pair of cylinders mounted:
(1) adjacent and orthogonal to detect the horizontal (u) and vertical (w)
flow components simultaneously at a single depth; or (2) spatially separated
on a vertical rod whereby both meters are aimed either horizontally or ver-
tically to detect simultaneous velocity pairs of u or w.

Various calibration techniques were used, including a wind tunnel, and
rotating boom and towing tank systems. Studies of both accelerative and
"off axis" response to flow were made, and an oscillation test simulated
wave motion effects upon the ducted meters. It was found that the ortho-
gonally mounted ducted meters registered steady flow in the plane defined
by the two orthogonal u and w meter axes. The flow components were found
to have a positive error, which was a function of the magnitude of the "off
angle" but independent of absolute flow speed. A means of correcting the
error in u and w is demonstrated.

The methods of data processing, using high speed digital computers,
are presented. Details of the analysis of time series data of wave motions,
using the Tukey spectrum techniques, are provided. Wave measurements were
made both in Narragansett Bay and on the Buzzards Bay Entrance Light Station.
A discussion is presented of the Light Station facilities and of environ-
mental measurements made of the current and tide conditions.

The wave measurements provided important information about the res-
ponse of the ducted meters to actual wave motions. In general, it was
found that the orthogonally mounted system displayed quite realistically
the u and w wave components, but that the u motion at times was somewhat
damped. Causes for this effect are associated with: (1) fundamental proper-
ties of trains of wind waves and swells moving in different directions; and
(2) the horizontal wave motions moving the suspended wave meter so as to
dampen its response to the u oscillations.

Several series of wave observations were made, which demonstrated the applicability of the wave meters to the following important studies.

1.   The determination of the auto-spectra of wave particle motions - Auto-spectra were obtained for various wave conditions and showed similarities to free surface motion auto-spectra observed, with energy peaks directly associated with the wave frequencies.

2.   The decrease of wave energy with depth - The variances of the wave motions showed an exponential decrease with depth and were compared to theoretical waves obtained from a classical wave model. Estimates of the total kinetic energy of the waves (obtained by vertical integration of the variances of the motions) showed a realistic amount of wave energy when compared to estimated wave potential energy.

3.   Short term variations of wave energy - Observations showed changes in both auto-spectra and variance distributions. These changes were associated with variations of the weather conditions over a twenty-four hour period.

4.   The "equilibrium range" of wave spectra - The slopes of the higher frequency range of the auto-spectra of the motions appeared to follow the "minus-fifth power" law attributed to free surface spectra.

5.   Reynolds stresses in waves - Covariances and cross-spectra are estimated for the u and w observations, giving values of the order of -25 cm^2 sec^{-2}. However, spurious values range from +28 to -162 cm^2 sec^{-2}. The larger covariances could be produced by instrument bias. Co-spectra indicate the covariance contributions are largely caused by correlations in the band of wind wave frequencies. Simple wave models are presented which contain the covariance and cross spectral properties observed in the real data. Discussion is also presented on ways which instrument bias could occur.

From observed mean shear of horizontal velocities, estimates are made of the dissipation of turbulent wave energy to mean flow.

This study provides evidence that the complex motions at the sea surface can and should be measured. With the relatively crude instrumentation, measurements were obtained which provided meaningful information on the momentum and energy transfer within the sea surface layer. Improvement of instruments and techniques can only result in a better understanding of the energetics of the ocean surface layer.

ACKNOWLEDGEMENTS

CONTENTS

CONTENTS (continued)

CONTENTS (continued)

CONTENTS (continued)

ILLUSTRATIONS

ILLUSTRATIONS (continued)

ILLUSTRATIONS (continued)

ILLUSTRATIONS (continued)

ILLUSTRATIONS (continued)

ILLUSTRATIONS (continued)

TABLES

SYMBOLS

A	Amplitude of wave
$A(K)$	Series approximation of auto-covariance function
A_n	Weighting constant
a_c	Centrifugal acceleration
C	Phase speed of waves
$C(L)$	Series approximation of cross-variance function (even or positive part)
$C_{uw}(f)$	Co-spectrum of the functions $u(t)$ and $w(t)$
D	Water depth
D	(subscript) Dissipation range
DF	Degrees of freedom
$D(L)$	Series approximation of cross-variance function (odd or negative part)
D_O	Orbital diameter
d	(subscript) Deep waves
E	(subscript) Equilibrium range
$E(K)$	Energy with a particular wave number range
E_{KW}	Turbulent kinetic energy per unit horizontal area
$E(L)$	In-phase correlation of $D(L)$ and $C(L)$
E_M	Peak or maximum value of $E(t)$
E_P	Potential wave energy per unit horizontal area
E_T	Total wave energy per unit horizontal area
$E(t)$	Voltage pulse generated by magnet
$F(L)$	Out-of-phase correlation of $D(L)$ and $C(L)$

f	Frequency function
f_K	Kth frequency in the spectrum
f_N	Nyquist frequency
f_V	Repetition rate or output frequency of voltage pulse
$f(\infty)$	Impeller frequency at equilibrium
g	Gravitational acceleration
H	Wave height
$\bar{H}$	Average wave height
I	Moment of inertia
I	Ordinate intercept (chapter 3)
i	$\sqrt{-1}$
i	(subscript) Intermediate waves
K or k	Wave number $(2\pi/L)$
K	Index number of a particular frequency (chapter 3)
K_A	Constant of proportionality relating resistance to drag force (in air)
K_f	Proportionality constant
K_l	Function of fluid viscosity and density
K_P	Proportionality constant
K_W	Constant of proportionality relating resistance to drag force (in sea water)
$|K_w$	Velocity vector in Z direction
L	Wave length
L	Lags (chapter 3)
$|L$	Time variable displacement vector
L_S	Linear distance (equal to shieve circumference)

ℓ	Line of axes separation
$\vec{1}u$	Velocity vector in X direction
M	Total number of units on frequency scale (maximum lag)
N	Number of turns in coil (chapter 2)
N	Number of interpolated data points
$P\eta$ or $P(\eta)$	Gaussian time probability distribution
Q	Dimensionless constant
$Q_{uw}(f)$	Qua-spectrum of the functions $u(t)$ and $w(t)$
R	Radius
R^2	Coherence (dimensionless quantity)
R_S	Ratio of flow velocity to towing speed
$R(\emptyset)$	Off-angle response in horizontal plane
$R(\theta)$	Off-angle response in vertical plane
R_θ	Ratio of virtual velocity to true velocity
r	Radius of the impeller (chapter 2)
r	Linear correlation coefficient
$r(h)$	Linear correlation coefficient between fluctuations at points separated by a distance h
T	Duration of record
T	Period of rotation (chapter 2)
$T_1, T_2 \cdots T_n$	Time intervals
T_A	Time constant in air
T_L	Period of swing (wave meter considered as a pendulum)
T_o	Period of forced oscillation
T_R or T_r	Response time

T_r	Time constant (appendix B)
T_S	Time interval or strip chart length - proportional to chart speed (chapter 2)
T_S	Period over which time average is made
T_S	Surface tension (chapter 5)
T_W	Time constant in sea water
t	Time
u	Horizontal velocity component $= u(t)$
$\bar{u}$	Mean value of $u(t)$
$\overline{u'^2}$	Variance of the record $u(t) = \sigma_u^2$
u_o	Amplitude (K_2/I)
$u(t)$	Time variable velocity in x direction $= u$
$u(\phi)$	Fluid velocity sensed by impeller
u_i'	Any time variable fluctuation (except u_w')
u_w'	Time variable oscillatory motion caused by waves
$\overline{u'w'}$	Covariance function between u' and w' at zero lag $= \phi_{uw}(0)$
$\mathbb{V}$	Vector velocity
$V_1, V_2 \cdots V_n$	Velocity-time data
V_B	Recorded wind speed
$V(K)$	Series approximation of auto-spectrum
V_N	Corrected wind speed
V_T	Towing speed
$V(t)$	Voltage fluctuation with time
$W(K)$	Out-of-phase energy spectrum or qua-spectrum
w	Vertical velocity component $= w(t)$

$\overline{w}$ — Mean value of $w(t)$

$\overline{w'^2}$ — Variance of the record $w(t) = \sigma_w^2$

$w(t)$ — Time variable velocity in Z direction (+ upward) = w

$w_T'(X_O,Z,t)$ — Deviation of the theoretical vertical velocity component about a zero mean

X_F^2 — Chi-square distribution

$Z(K)$ — In-phase energy spectrum or co-spectrum

GREEK SYMBOLS

ϵ — Turbulent energy transfer dissipation of small scale motions

ζ — Particle displacement in vertical direction (chapter 2)

ζ — Current speed (chapter 4)

η — Dynamic viscosity (chapter 2)

η — Time variable position of free surface on vertical wave staff

$\overline{\eta}$ — Mean free surface

η' — Instantaneous deviation from the mean $\widehat{\eta}$

η_A — Dynamic viscosity in air

η_W — Dynamic viscosity in sea water

⊕ — Phase difference between $u(t)$ and $w(t)$

⊕ (K) — Series approximation of the phase lead of u_n over w_n

θ — Inclined angle lying in the vertical XZ plane (chapter 2)

θ — Estimated direction of wind waves (sea) or swell

λ — Dimensionless scale factor

μ — Kinematic viscosity

$\mathcal{E}$ — Particle displacement (horizontal direction)

ρ	Fluid density
$\rho\,\overline{u'w'}$	Reynolds stress
σ	Standard deviation
σ^2	Variance
σ_u^2	Variance associated with horizontal velocity component $u(t)$
σ_w^2	Variance associated with vertical velocity component $w(t)$
τ	Time lag
ϕ	Azimuthal angle lying in the horizontal XY plane
ϕ_M	Number of lines of magnetic flux per unit area
$\Phi_u(f)$	Auto-spectrum function of u
$\phi_u(\tau)$	Auto-covariance function of $u(t)$
$\phi_{uw}(\tau)$	Cross-variance or covariance functions
$\Phi_w(f)$	Auto-spectrum function of w
$\phi_{wu}(\tau)$	Cross-variance or covariance functions
Φ_η	Spectrum function of free surface oscillation η
ω	Driving frequency
ω_B	Angular velocity
$\omega(t)$	Angular velocity of impeller

CHAPTER I

INTRODUCTION

Over the past two decades ocean wave research has made notable advances, particularly in the study of storm generation and prediction, and the recording of long surface gravity waves (e.g., Snodgrass, Munk, and Tucker, 1958). Most studies of wind driven waves have been involved with statistical analyses of the inferred or measured kinetic properties of the free surface oscillations. These properties are either determined by means of wave staff devices and bobbling floats, or inferred by use of slope detectors, optical glitter patterns, bottom-mounted pressure sensors, and other more esoteric devices. Much attention has been given to the theoretical derivations of classical relationships and to conjecturing empirical equations relating wave spectra to frequency, wave length and height, wind speed and duration, fetch and the like (see, for example, Ocean Wave Spectra, 1963, and Kinsman, 1965).

A perusal of the published literature on ocean wave research, of which indeed there is no dearth, reveals a conspicuous absence of recorded observations of actual particle motions associated with ocean waves. This situation can probably be attributed to two factors: (1) the lack of sensing equipment to record faithfully the quasi-oscillatory and relatively high frequency motions of waves, and (2) the difficulties involved in properly fixing the measuring instrument in the ocean without altering or interfering seriously with the wave motions.

Until the dynamic motions within the wind-generated waves can be accurately described and hence modeled, at least in a statistical sense, there is little hope of assessing the effects of wind stress in creating turbulent mixing of momentum and heat in the ocean surface layers and in helping to produce major ocean currents. In short, the motion beneath the sea surface holds the key to the time and space variable distribution of the wind-imparted energy and momentum flowing into and within the ocean.

Welander (1961) emphasizes the need for knowledge about the free surface and boundary processes and indicates that the basic laws of mechanics and thermo dynamics can be applied to an ocean of given dimensions and chemical composition. The distribution of temperature and salinity as well as the water motions in the entire ocean are determined by a knowledge of: (1) the pressure and shear stresses acting through the free surface; (2) the net heat flux through the surface layer; and (3) the net mass flux through the surface layer (due to evaporation, precipitation, freezing, melting, and estuary inflow). Further, the transport of heat and momentum through the surface layers can only be effected by the proper turbulent environment immediately beneath the ocean surface. This so-called "reactive layer" is completely respondent to the turbulence generated by the wind itself and by its dynamic counterpart, the driven surface waves. The flux of quantities such as momentum, kinetic energy, and heat must be extremely sensitive to the time variable climate of turbulence within the reactive surface layer. Hence, the need is great for at least establishing a method or parameter to describe the turbulent regime in the upper layer.

Henry Stommel in his book The Gulf Stream (1958) states: "In spite of the intensive effort that has been made to measure the stress of the wind on the sea, there is so much scatter in the various determinations that the stress is still not well known. It is hard to imagine an object of study more important to the physical oceanography of ocean currents."

Despite such statements, the understanding of the physical mechanism responsible for the generation, the wind stress and energy transfer, and the decay of wind waves seems to be at an impasse. A disproportionate emphasis has been placed upon empirical characterization of various spectral parameters, which can offer little understandindg of the physical mechanisms within the wave regime. Certainly a substantial effort should be made to directly measure the wave motions and to provide at least a statistical description thereof. The pursuit of this latter purpose may require certain bold, if not bizarre, innovations and improvements in both instrumentation and techniques.

Why have conventional current meters not been used to measure turbulent fluctuations associated with wind-driven waves? Examination of this question reveals a paradoxical situation. Most near-surface current measurements are made to observe mean flow or, at most, much lower frequency oscillations than those peculiar to the wind wave regime (e.g., tidal currents). In fact, estimates of flow fluctuations are usually avoided because this tends to complicate the otherwise smooth and well-behaved data. For this reason most modern current meters, such as the Savonius rotor (used in the Richardson type self-recording system), have built-in integrating systems that average the values of current speed and direction over periods of 10 minutes to several hours.

Moreover, most ocean current meters, when held on tethered moors, are adversely affected by oscillatory motions. This gives rise to potential biasing of low frequency or steady flow components. The Savonius rotor only senses speed of flow. Hence, any oscillatory flow about the rotor tends to bias its integrated output to give a magnified average value of flow; i.e., the rotor tends to half-wave rectify the oscillatory motions and add this to the lower frequency components. A similar effect occurs with a Roberts or Von Arx type meter. The oscillation of the meter in its pivoted bridle, in response to vertical oscillatory motions, causes spurious biasing of the quasi-continuous record.

As more is learned of the natural transfer processes in the ocean and the atmosphere, statistics on fluctuations of the motions are seen to be of equal or greater importance than those relating to the mean (or statistically smooth) motions. This is demonstrated both in the study of large scale transfer processes in the atmosphere (Starr, 1956) and in the study of the energy balance of the Gulf Stream (Webster, 1961).

It seems evident that the success of any study of the gross transfer of dynamic properties at the air-sea interface is dependent upon actual high resolution measurements of the fluctuating motions of the two fluids. This study of particle motions in ocean waves is therefore based upon in situ measurements.

Historical Background

Measurements of surface gravity waves have traditionally been made by recording either the time-variable height of the free surface, using various wave staff devices, or the dynamic pressure obtained from shallow bottom-mounted transducers. The latter method, in particular, is not well suited to studies of wind-driven waves of periods less than 4-5 seconds (greater than 0.25 cps) because the dynamic pressure induced by higher frequency surface waves attenuates with depth in a fashion similar to that of the velocity and acceleration of the orbital motions. Hence, pressure measurements reveal little of what is happening at the surface in the higher frequency bands.

Thus, a discussion of the background of work related to directly measuring the motions beneath the surface need not dwell on either of these methods of measurement, with one exception.

A series of wind wave measurements was conducted by Kinsman (1960) in which the actual observations were of the time variable fluctuations of the free surface. His report provides a concise statement of the problems involved with instrumentation, data processing, and analysis. This work involved a study of 24 point records of surface waves made in Chesapeake Bay at short fetches (2-5 km) and relatively low wind speeds (3.8 - 8.2 m sec^{-1}). In his results and analysis Kinsman deals with such problems as deviation of observations from Gaussian distribution, evidence of nonlinear interaction in the spectra, and examination of the so-called "equilibrium range" of the spectra. His work offered a means of comparison of the spectral characteristics of free surface fluctuations with the spectra of the oscillatory motions presented in this report. Kinsman's work will be discussed further in Chapter V.

There is no account in the published literature (known to the author) of a deliberate attempt to make insitu measurements of the particle motions in wind-driven waves in a Eulerian manner. Therefore, no source is available to obtain estimates of wave-induced turbulent fluctuations, variances, covariances, and the associated spectra. Measurements have been conducted in tidal estuaries in an effort to observe turbulent quantities present in tidal flows. Measurements have also been made in laboratory tanks to study orbital motions of artificially produced waves.

This historical review is concerned not only with the past measurements of wave motion per se, but also with the results of experiments made to measure turbulence on the surface layers of the ocean -- specifically, measurements of motions in which special care was taken to obtain a statistical estimate of the vector quantities and correlations. A general review of the measurements of oceanographic turbulence is given by Bowden (1962-A). Unfortunately, Bowden emphasizes in his introduction that "turbulent motions" are generally not considered in the same catagory as wave motions, which he states are of "more regular" fashion. It is this conception that should be avoided.

For all geophysical fluid motions are, after all, irrotational to varying
degrees. The quasi-oscillatory nature of some modes of motion should not
alter the fact that they have strong stochastic (random) attributes. Setting aside
all preconceptions of what types of motions are turbulent and what are not,
one should ask simply: what are the statistics and the defined turbulent
characteristics of a given set of motions represented by a series of care-
fully taken velocity data? The following is a brief resume of early and
recent experiments in which attempts were made to record turbulent or
oscillatory fluctuations, both in the ocean environment and in the laboratory.

In Situ Measurements - Thorade (1934) made measurements of velocity fluc-
tuations in the Kattegat using the Rauschelback current meter (Von Arx, 1962).
He derived records of speed and direction every 10 seconds and found fluctua-
tions having periods of several minutes.

Mossby (1947, 1949, and 1951) used arrays of revolving cups at various
heights above the bottom in the Alvoestrommen near Bergen, and in the open
ocean (at a depth of 100 meters) near the Viking bank about 100 km from the
coast.

Doodson (1940), who is widely known for his valuable contributions to
the measurement and analysis of tides, designed a current meter that re-
sponded to oscillations up to 1 cps. This meter was used by Bowden and
Proudman (1949) for near-bottom measurements in the river Mersey near Liver-
pool. The variances of the horizontal velocity along with the mean current
and the auto-covariance functions were determined for various depths.

Bowden and Fairbairn (1952) used a pair of Doodson meters mounted at
various vertical separations on a rigid staff to obtain the spatial vari-
ability (and, hence, the instantaneous shear flow) as a function of depth.

Probably the first attempt to measure simultaneously the horizontal and
vertical velocity components at a point in the water column was reported by
Francis, Stommel, Farmer, and Parson (1953). This work is of interest here
because it represents a direct, if not a daring, effort to measure turbulent
quantities in the ocean and to make some quantitative analysis regrading
these heretofore little known and little understood phenomena. Estimates
were made of turbulent fluctuations of momentum, heat, and salinity in the
vertical, while occupying anchor stations in the Kennebec Estuary, Maine.
It is worthwhile to describe these experiments in some detail.

A somewhat crude but novel type of instrumentation was developed to de-
tect both the horizontal and vertical velocity components simultaneously.
A propeller meter (Von Arx, 1950), which served to detect horizontal flow,
was used in conjunction with a pivoting vane device, which oscillated in the
vertical about a horizontal rod on its leading edge. The vane rod was coupled
to the shaft of a watertight potentiometer, which was wired in series to a
fixed voltage source aboard ship. The outputs of both systems were recorded
aboard ship on a strip chart recorder.

This system had obvious shortcomings in that it did not indicate the direction of horizontal flow and had relatively low time response (probably of the order of 1 or 2 seconds). Problems were encountered regarding the best method of suspending the system from the vessel; i.e., by a rigid vertical rod, a bottom mounting, or (as was finally decided) simply a counter-weighted cable suspension. Since the tidal current in the estuary attained 150 cm sec^{-1}, it is probable (and was indeed inferred in the report) that the dynamic interaction of the flow with the system may have biased the records.

Other measurements included mean current profiles, temperature, and salinity fluctuations. Computations were made of stability and of mixing attributes by using the methods of Jacobson (1918) and Pritchard (1952). Of particular interest are the estimated values of the Reynolds stress $-\rho\overline{u'w'}$ (see equation III-28). These were obtained from observations made on two cruises by abstracting the horizontal and vertical velocity values at 3-second intervals from the 2-minute records made at various stages of the tidal flow. All records were obtained at low sea states because gross wave motions would have disturbed the anchored vessel and, hence, perturbed the suspended meter system. Twenty-eight estimates of the Reynolds stress were reported at various depths from 0.2 meter down to 8.5 meters. Most of these estimates fell below the 0.1 probability that the results were simply a result of random correlation. The values of $-\rho\overline{u'w}$ ranged from -1.74 to +62.2 dynes cm^{-2}, with a mean of about +14 and +23 dynes cm^{-2} for the first and second cruises, respectively.

It is interesting, if not suggestive, that in both series of observations the largest estimated stresses often occurred near the surface, which was well above the strong mean shear zone at the point of the pycnocline caused by the salinity wedge present in the estuary.

A series of simultaneous measurements of the vertical and horizontal velocity components was obtained by Bowden and Fairbairn (1956) and Bowden (1962). These measurements were made utilizing a modification of an electro-magnetic flow meter designed by Guelke and Schoute-Vanneck (1947). The sensing head of this meter is about 10 cm in diameter and contains an external orthogonal array of electrodes and internal induction coils which generate a constant magnetic field. The sea water, being an electrolyte, produces an emf proportional to the flux of the ions through the magnetic field. This electric field is sensed by the two orthogonally mounted electrode pairs. Hence, from the voltage across the electrodes one can infer the instantaneous vertical and horizontal fluid velocities. The response time of this instrument is reported to be about 0.8 second. These measurements are significant in that they are the first recorded attempt to directly measure the Reynolds stress within the ocean. The authors report Reynolds stress values at distances from the bottom less than 2 meters, ranging from +1.4 to +4.1 dynes cm^{-2} and directed downward as indicated by a negative value of the co-variance. These stresses are

somewhat smaller than those estimated by Francis et al (1953). These studies, although somewhat inconclusive in their preliminary analysis, indicate that properly conducted Eulerian measurements of particle velocities in the water column can be used to estimate the statistical turbulent properties inherent in the motions of the water.

Stewart and Grant (1962) obtained near-surface measurements of high wave number, turbulent, velocity fluctuations (in one dimension) by towing a horizontal, hot film, anemometer-like device from a vessel while underway. The authors infer values of turbulent energy in its last stages of decay prior to frictional dissipation. The validity of the one dimensional measurement is based on the Kolmogoroff concept (Kolmogoroff, 1941) that fine structure turbulence tends to be isotropic. According to the authors, most of the energy acquired by the waves from the wind is quickly converted into isotropic turbulence within a depth commensurate with the wave height. If this is true, the value of the Reynolds stress should decrease sharply as one moves to a depth beyond one or two wave heights. These experiments, however, shed no light on the problem of what happens to the wind-imparted momentum from the time it is anisotropically transferred to the water surface until it is dissipated as fine structure isotropic turbulence.

One other system of interest is under development at the Chesapeake Bay Institute (of Johns Hopkins University). In this system the doppler shift of acoustic energy scattered from a small volume of water is used to infer the instantaneous particle velocities. The system, according to Pritchard (1964), is designed to supply a three-dimensional picture of the instantaneous motions in a volume of the order of a few cubic centimeters. Although certain technical problems will have to be overcome, this concept has promise because there is no apparent interference with the flow within the volume of water under examination.

Laboratory Experiments -- Three laboratory studies of particle motions are worthy of mention. Shuliykin (1959) reports on Lagrangian particle measurements in waves produced in a ring-shaped "storm basin" in the Marine Hydrophysical Institute, Moscow. Small, neutrally bouyant, spherical lamps were photographed as they oscillated beneath the surface of waves generated by an artificial wind in the basin.

The motion picture films display the orbital motions, with a quasi-circular component of the actual orbit superimposed upon a translational motion. The resulting Lagrangian orbit resembles a prolate cycloid, i.e., the locus of points generated at the end of a line segment extending from a radius of a circle which is rolling on a horizontal plane (see Larson, 1956). The slight elongation of the orbits is attributed to the shoal conditions in the tank. The relationship between these Lagrangian patterns and those which occur in natural waves is very tenuous, since no effort was made to assess the effects of the artificial generation and, even more important, the effects of the horizontal boundaries of the storm basin.

Kishi (1954) and Marlo (1957) also report on wave particle tracing techniques using high speed cinema cameras.

Mee (1963) reports on an investigation of wave surface particle velocities using a 3.2 cm wavelength doppler radar system. Observations of waves generated in a wave tank showed that the frequency spectra of microwave radiation backscattered from simple surface wave systems correlated with the orbital velocity spectra of surface water particles. An analytic description was developed for the observed trochoidal wave shapes and the non-circular orbital motions of the water particles. The stream-lines of the water particles were again found to have a geometry resembling a prolate cycloid, with an eccentricity increasing as a function of the wave steepness. The derived equations describe an orbital motion wherein the particles do not move with a constant angular velocity, but move faster on the wave crests than at the troughs. This effect was substantiated by actual estimates of particle velocities using the radar system. This noted effect of nonconstant angular velocity of wave particles is important because it provides a simple momentum transfer mechanism. Further discussion of this is found in chapter V.

This method could well be used in observations of wind waves from a fixed platform. Certainly this method lends itself to measuring waves in a standard fashion, whereby the doppler radar signatures of various sea states could be obtained with the standard system at a fixed angle of sight and at a fixed height above the water.

Eagleson, and Van de Watering (1963) report on experiments using a thermistor probe to measure particle orbital speeds in water waves. They describe development and testing of a thermistor probe and its associated electronic circuitry. The probe was used to make one-dimensional measurements of laboratory generated water waves.

This system utilizes the temperature measuring concept of a thermistor inversely; i.e., its function is similar to the hot wire anemometer in that the temperature variations in the fluid are neglected and the cooling effect of the thermistor bridge element is a known function of the fluid velocity. The system was towed in a tank at various speeds to provide a steady flow calibration. The response of the system was estimated up to 0.5 cps. The device was used to provide continuous values of velocity, and gave results comparing well with the theory of Stokes waves.

The preceding experiments are merely a sampling of laboratory work which could provide many innovations in the methods used to measure particle motions in ocean waves. Unfortunately, most of these techniques have never been applied in the real ocean. Certainly, here lies a storehouse of potential for making dynamic records of the complex motions of the wind wave regime.

In summary, there have been more than a few attempts to measure fluctuating motions both in the sea and in the laboratory. However,

with the exception of Francis et al (1953), Bowden and Fairbairn (1956), and Stewart and Grant (1962), there is little evidence that people have given much thought to the importance of measuring turbulence and to the potentialities of such data. In general, efforts have been directed toward the technical problems of instrumentation. Once these problems were more or less overcome, a few measurements were made and the project was dropped, probably because of an aversion to having to examine large volumes of complex and perhaps nebulous data that would certainly not hold the interest of an instrumentation engineer.

Studies of Atmospheric Turbulence -- No mention has been made thus far of atmospheric turbulence studies. Essentially, all of the near-surface wind measurements were made in order to understand wind turbulence and stress. Hence, instrumentation has been developed to measure shear and fluctuation properties of the moving air. Whereas oceanographers have, for the most part, confined their measurements to mean flows at a single depth, meteorologists have made very serious attempts to measure the energy and momentum transfer in the lower layers of the atmosphere by inferences from wind shear over land, Richardson number (stability), and even direct Reynolds stress determinations. See, for example, Cramer (1959) and Cramer, Record, and Tillman (1962). The results of these studies and the statistical methods developed to cope with the data have greatly added to the picture. For some reviews of the above studies, see Frenkiel (1962), Sutton (1953), and Priestly (1959).

Unfortunately, the meteorologist has confined his attention to the upper medium of the air-sea interface and has made few attempts to express the energy transfer through the interface. Estimates are available of the horizontal momentum and kinetic energy transfer through the lower air layers, but little information is available about the mode of transfer through or the interaction with the ocean surface layers. A general discussion of the thermodynamics of the upper ocean layers, in which the above problems are mentioned, is presented by Phillips (1963).

Measurements to determine the Reynolds stress in the atmosphere have been undertaken by many (e.g., Deacon, 1955). However, most of our knowledge of wind stress upon water is rather empirical and is based upon measurements of the following nature:

1. Determination of the vertical wind profile or shear above the water and conjecture about the stresses at the air-sea interface; e.g., Roll (1952), Helstrom (1953), Wust (1937), Montgomery (1936), Bruch (1940), and Thornthwaite and Halstead (1942).

2. Measurements of the wind pile-up (Windstau) of enclosed regions of water while strong steady winds are blowing across them, and estimates from this data of the mean stress values; e.g., Palmen (1932), Keuligen (1951), and Helstrom (1953).

3. Measurements of the geostrophic departure in the layer of frictional influence (Sheppard and Omar, 1952).

A review of the results of these studies is presented by Neuman (1956). In this paper Neuman emphasizes the inherent difficulties in marking and interpreting wind stress data. He also cites the various problems encountered in modeling natural wind stress phenomena in the laboratory.

Spectral Analysis -- One of the most significant, although perhaps unintentional, contributions made to the studies of waves -- and, in fact, to geophysics in general -- was the development of the modern techniques of spectral analysis, in which one can utilize the capabilities of the high speed electronic digital computer. These analysis techniques were developed by workers in the field of communications engineering and information theory, and then applied to general statistical problems.

The basic work is by Tukey (1949), Tukey and Hamming (1949), and Rice (1954). Spectral analysis is summarized by Blackman and Tukey (1958). The original work was developed to analyze noise in electrical circuits. Largely through the efforts of Pierson at New York University (see Pierson, 1952 and 1955), these statistical techniques became known to a few wave researchers and hence have become relatively familiar to oceanographers and geophysicists.

Over the past decade the application of the Tukey spectral estimates has become a commonplace tool in data analysis for a greatly diversified group of geophysical problems in which analysis is desired of complex interrelationships of two or more variables. These methods allow meaningful analysis of the spectra of time series observations of a particular variable, and also permit the assessment of the correlation or interaction of two or more variables. This latter analysis alludes to the estimate of the cross spectral properties associated with the two particular variables measured. Another facet of the technique is the development of criteria by which one may evaluate the reliability of the auto- and cross-spectral estimates through the use of coherence properties between auto- and cross-spectra. These spectral analysis techniques are the mainstay of this analysis of the wave observations. A general discussion of the techniques is given in chapter III.

Formulation of the Problem

With most scientific research the results are predicated more on the actual progressive pattern of work done (involving the usual numerous successes and failures) than upon the original portrayal of the problem to be solved. Such is the case with this investigation.

The original proposed problem was to determine a very specific parameter within the wind-driven ocean waves; i.e., the Reynolds stress. It was obvious at the outset that certain problems would arise as the study progressed -- problems involving instrumentation, methods of measurement, data processing,

and analysis. The type of velocity data obtained were unique, and there was no clearcut approach to the data analysis procedures. This preliminary statement of the problem must therefore be based on the experience gained in actually pursuing the studies without apologies for deviations from the original concept.

When the wind blows over the ocean, it imparts momentum and kinetic energy to the water surface by exerting a net stress in the direction of the wind. This stress results from the frictional drag produced by the wind on the water surface, and from wind pressure forces acting upon sloped regions of the free surface (i.e., the windward and leeward sides of the waves). The effects of this net stress are partitioned within the water column and are assumed to be directly or indirectly responsible for various observable phenomena; e.g., surface waves, wind currents, and turbulent mixing over a wide spectrum of wave numbers. It is obvious that the wind generation of surface waves and the turbulent or eddy mixing within the surface layers of the ocean are intrinsically related; for both phenomena are manifestations of the vertical transfer of wind-imparted momentum moving through the upper layers of the water. Thus, one should examine the effects of the more regular quasi-oscillatory particle motions of the waves, since the waves themselves are a manifestation of wind stress. For this reason, it was decided to apply the Reynolds stress concept to the analysis of the water particle motion within the dynamic wind wave regime and, specifically, to probe the following related questions: (1) is there a measurable Reynolds stress in ocean waves? (2) If it exists, is this stress essentially controlled by detectable interactions of the predominant motions of the time and length scales of the waves themselves? (3) How are the wave motions related to the more easily observable parameters such as wave height and wind speed?

Categories of Wave Motion -- In this formulation of the problem the sea surface, which is under the influence of the usual forces of wind stress, is portrayed as a strongly turbulent fluid regime in which the motions are, for the most part, rotational (i.e., possessing eddy viscosity), so that the totality of motions can be associated with a definite spectrum at a given instant. This leads to a consideration of three approximate frequency bands containing the characteristic motions of the sea surface.

The first band or category includes the mean or quasi-steady motions. It is usually assumed that the degree of isotropy of the broad distribution of turbulent motions increases directly with frequency and inversely with the eddy scale of motion. This certainly appears to be the case, since the greatest deviation from isotropic flow (i.e., rectilinear flow) is represented by the long period and gently meandering motions of the semi-diurnal tides and so-called drift currents. These flows are predominantly horizontal and can be relatively steady and unidirectional over periods of from 1 to 10 minutes. It is porbable that these quasi-rectilinear flows are strongly affected by both winds and bottom stress and by the gross topography.

The second category of motion includes the surface gravity waves, which are dominated by the relatively low frequency "swell", and the higher frequency wind-driven waves termed "sea". These motions are characterized by oscillatory flows, which are by no means irrotational. The flows do, however, tend to possess strongly two-dimensional geometry; i.e., they oscillate in complex orbits roughly approximating circles, ellipses, or cycloids that generally lie in the vertical plane, normal to the crestline of the waves. During periods of wind generation, many sets of waves of varying scales and varying directions are constantly being formed and propagated in the horizontal. All of these orbital motions peculiar to a particular wave frequency or scale interact (probably in a highly non-linear fashion) with every one of the other waves that happen to cross paths at a particular point. The results, of course, must be a highly stochastic or turbulent situation in which any physical processes taking place can be analyzed only in a statistical manner.

The third category of motion is that of the relatively small scale structure characterized by a dimension range from 0.1 to 20 cm. This sub-range includes small surface gravity and capillary waves, which tend to be quite regular in their structure; but, more important, these motions constitute the true turbulent regime or "fine structure" of the sea. This is seen as the swirling motions in breaking seas, both in the open ocean and along the ocean boundaries. These small scale motions inevitably play a large part in the final disposition of wind imparted momentum and energy because they possess the highest degree of quasi-random motion and so-called "eddy viscosity".

This study concentrates upon motions attributed to swell and to wind waves, for it is within this regime of motions that the sea is most responsive. The first observed response to the wind upon the ocean surface is the immediate generation of wind waves. Secondary effects, in terms of reaction time, are the evolution of breaking waves (wave turbulence) and, even later, the generation of gross "wind drift" currents.

The surface motions should not be divided into strict categories, for it is, after all, the interactions within the continuous spectrum of motions that produce the sum of the dynamic energy transfer within the sea and through its boundaries. Hence, the basic problem is that of measuring the previously defined ranges of motions so as to better understand their interactions and the energy transfer from one region of the spectrum to another.

Parameters To Be Measured -- This then is the general problem. Is it feasible to devise the instrumentation needed to make reasonably accurate measurements of particle motions in the dynamic regime of wind waves and swell? If so, can these measurements be used to provide a better understanding of the dynamics of wave generation, energy transfer, and dissipation? What specific parameters should be extracted from such velocity data so as to provide the most useful statistical information? In what ways can these statistics be compared to the available data on the free surface observed as a function of time?

The following parameters of the wave particle motions are pertinent and should be measured: variability, covariability, auto-spectra, cross-spectra, and velocity shear. (Complete definition and discussion of the statistical parameters are contained in chapter III.)

1. <u>Variability</u>. It is only natural to examine the variability or the variance of the velocity observations. Since the fluctuations of the wave motions must be due in large part to the gross movements of the dominant waves, the variance should serve as a scale by which to estimate the magnitude or energy of the waves. The change in variance of a velocity component can be evaluated as a function of depth (from the mean free surface), ambient wind speed, and the observable wave parameters such as estimated wave length, height and period.

2. <u>Covariability</u>. Interrelations of the velocity components can be obtained by estimating the covariance between two, simultaneously measured, orthogonal, velocity components, or between two, similar, velocity components that are spacially separated.

3. <u>Auto- and Cross-Spectra</u>. The auto-spectra obtained from the auto-covariance functions can be used to examine the contributions of the motions to the variance as a function of frequency. Examination of the auto-spectra associated with various depth and wind conditions can indicate: (1) the relative energy distribution with frequency as affected by the driving forces of the wind, and (2) the attenuation with depth.

The cross-spectra obtained from the covariance functions can indicate the degree to which the waves behave in a classical sense, and hence the degree of turbulence or quasi-randomness inherent in the motions. The cross-spectral functions can provide information regarding the magnitude of positive (or negative) correlation of two velocity components as a function of frequency.

4. <u>Velocity Shear</u>. The vertical shear of the horizontal velocity which is determined from measurements of the mean current at two depths simultaneously, is a measure of the mean vorticity and can be related to depth, variance, covariance, wind speed, and other parameters.

By identifiying and estimating the magnitude of the vertical distribution of those quantities associated with stress and dissipation, one may be able to offer a conceptual description of the mode of wind momentum transfer to and within the water column, and perhaps make some inferences as to the disposition of the wind-imparted kinetic energy. Of particular interest is the transfer of kinetic energy from the turbulent eddy motion to the mean motion. This is expressed by $-\rho\overline{uw}(\partial\overline{u}/\partial z)$, where the bar indicates a time average of the horizontal velocity u. This quantity is described by Webster (1961) in a study of the kinetic energy balance of the Gulf Stream.

In addition to the desired parameters to be extracted from the wave motion data, supplementary oceanographic measurements must be obtained. In the particular area chosen for wave measurements, one should have a knowledge of the tidal motions, non-tidal flows, bottom topography, fetches, and land boundary configurations. Likewise, it is important to obtain as much accurate meteorological and oceanographic data as possible at the location and over the period encompassing the wave measurements.

Aims of Wave Motion Study

In summary, this study of particle motions in ocean waves has the following aims:

1. To assess and analyze the problems involved in measuring Eulerian particle motions within the upper 20 meters of the sea surface layer.

2. To design, construct, calibrate, and use instrumentation to make actual field measurements.

3. To assess the overall usefulness of the instrumentation by evaluation of the calibration and field data.

4. Using modern statistical and spectral analysis in conjunction with high speed digital computer techniques, to provide an approximate description of the spectra of wave motions, and to relate this to the empirical and theoretical spectra of wind waves and currents.

5. To attempt to translate the particle velocity data into basic processes of energy and momentum transfer within the surface layers of the ocean.

Moreover, the substance of this study represents the first serious attempt to measure directly the complex motions within ocean waves. Despite inevitable shortcomings in the methods and instrumentation used, and hence in the results obtained, this work should serve several useful purposes. It should demonstrate that it is feasible and of value to make direct observations of wind wave motions, and that the instrumentation problems involved, though often unwieldy and difficult, are not insoluble. It should also present preliminary observations and analysis of characteristic motions within the wind wave regime. Finally it should provide some fundamental basis for defining the mechanism of wind-imparted energy and momentum flux within the ocean surface layers.

In short, it is hoped that this work will serve to encourage further concerted and bold efforts to experimentally come to grips with the turbulent processes occurring in the ocean.

13

CHAPTER II

DEVELOPMENT OF THE WAVE METER

Any measurement of the motions in ocean waves must take into account the fact that this dynamic environment contains a broad and time-variable spectrum of complex motions. This gives rise at once to the unavoidable problems of making fluid flow measurements in a turbulent or quasi-turbulent field of motion.

In this study "turbulence" is associated with particule motions in ocean waves. The term is defined at the outset because some oscillations of an approximate periodic character, such as those associated with surface gravity waves, are usually excluded from discussions of oceanic turbulence (see Bowden, 1962-A). This exclusion is justified by Bowden on the basis that wave motions are more predictable than the motions of a highly turbulent regime, such as that in the surf zone of a beach or at the base of a waterfall. This distinction, however, is quite arbitrary. Since the ocean is not inviscid and is acted upon by rotational stresses, its motions must contain major random and non-linear components. Thus, the particle motions in waves may have strong turbulent, but anisotropid, characteristics. These characteristics are the main point of interest.

The general principles of measuring turbulent flows are discussed by Hinze (1959). There are several general requirements that should be satisfied by any Eulerian flow-detecting apparatus before turbulent motions can be delineated with any degree of reliability.

1. The sensing elements introduced into the water flow field must cause a minimum of disturbance to the flow pattern.

2. The instantaneous velocity distribution must be uniform in the region occupied by the element. In other words, the sensor should be dimensionally much smaller than the scale of turbulence under examination.

3. The inertia of the sensor response (i.e., the response time) must be much smaller than the period of the turbulent fluctuations.

4. The sensor should respond to fluctuations that may be small compared to the mean motion.

5. The instrument must have a stable calibration for periods much longer than the sampling periods.

6. The device must be strong and rigid or otherwise able to absorb oscillations of a periodic motion impressed by the turbulent flow. This requirement may be particularly critical where the sensor support has a tendency to oscillate with the impressed drag of the fluid.

7. Most important of all is a clear understanding of the principle of measurement so that the limitations of the instrument system, which is necessarily imperfect, can be assessed.

Specifically, the device used must measure both horizontal and vertical velocity components, and thus must contain a coupled system of two speed sensors, one for each component. It is desirable to have a remote recording system that can register the two velocity components simultaneously and quasi-continuously. The frequencies of the recorded fluctuations are limited on the upper end by the frequency response of the instrument and on the lower end by the chosen duration of the record, which is governed by the time scale of the fluctuations to be measured. The instrument should have a frequency response that encompasses the highest frequency fluctuations that contribute significantly to the particular phenomena being studied.

What then are the probable magnitudes of the relevant parameters of the waves in which measurements are to be made? Approximations of the scale of motions can be made by use of classical theory.

Surface waves may be classified empirically into deep water (short) waves, intermediate waves, and shallow water (long) waves, depending upon the ratio of the depth of the water to the length of the wave.

Deep water waves occur if

$$\frac{D}{L} > 0.5 \; ; \tag{II-1}$$

where D is the water depth and L is the wavelength. Waves that can be described by the ratio

$$0.05 < \frac{D}{L} < 0.5 \tag{II-2}$$

are termed intermediate water waves. Shallow water waves are defined by the relation

$$\frac{D}{L} < 0.05 \; . \tag{II-3}$$

Wave measurements were made at the NUWS pier facilities in Narragansett Bay and at the Buzzards Bay Entrance Light Station. The depth of water at the NUWS pier facilities is about 7 meters. The wavelengths, which were measured under relatively high wind conditions, ranged from 3-10 meters. At Buzzards Bay Entrance Light Station the water depth is about 20 meters, and the locally generated wind waves have wavelengths from 10-50 meters. Thus, predominantly deep water waves exist at both locations. During storm and ground swell conditions at the light station, the larger wavelengths do exceed twice the water depth; thus, the wave parameters do tend on occasion to satisfy the conditions for intermediate water waves. However, this study is concerned with the properties of wind waves, which are classified, for the most part, as deep water waves.

The motion of water particles in a deep water wave approximates a circular orbit in which the period of orbital motion is equal to the period of the wave. The orbital diameter is given by

$$D_0 = H e^{\kappa z} \; ; \tag{II-4}$$

15

where H is the wave height or twice the wave amplitude, and K is the wave number $= 2\pi/L$. With the vertical z axis measured positively upward (at the surface, $z=0$), then $D_o=H$.

According to simple linear theory, as a wave crosses the transition point from deep to shallow water, the quasi-circular orbits of the wave particles "feel" the bottom boundary. The circular orbits are transformed into ellipses, and the eccentricity of the elliptical orbits increases with depth. Since at the bottom boundary the vertical component must vanish, the elliptical orbits degenerate at the bottom into horizontal rectilinear oscillations.

Two wave attributes are of importance to the design of the instrumentation and to the measuring procedures. For deep and intermediate waves having small amplitudes, the first order approximations for the horizontal and vertical components of particle velocity are given as a function of depth and time (see Coulson, 1958).

$$u_d = \frac{H}{2}\sigma e^{Kz}\cos\sigma t. \tag{II-5}$$

$$w_d = \frac{H}{2}\sigma e^{Kz}\sin\sigma t. \tag{II-6}$$

$$u_i = \frac{H}{2}\sigma \frac{\cosh K(z+D)}{\sinh KD}\cos\sigma t. \tag{II-7}$$

$$w_i = \frac{H}{2}\sigma \frac{\sinh K(z+D)}{\sinh KD}\sin\sigma t. \tag{II-8}$$

The subscripts d and i refer to deep and intermediate. These four equations apply for a water level profile that varies as $\cos\sigma t$. In the case of intermediate waves, at the bottom, where $z = -D$, w vanishes.

Particle displacement is defined as the total excursion taken by the particle along either the horizontal or vertical axis, and is obtained by integration (with respect to time) of the particle velocity components. The absolute values for particle displacements can be approximated by:

$$|\xi_d| = \frac{H}{2}e^{Kz}\cos\sigma t \tag{II-9}$$

$$|\zeta_d| = \frac{H}{2}e^{Kz}\sin\sigma t \tag{II-10}$$

$$|\xi_i| = \frac{H}{2}\frac{\cosh(z+D)}{\sinh KD}\cos\sigma t \tag{II-11}$$

16

$$\left| \zeta_i \right| = \frac{H}{2} \frac{\sinh k(z+D)}{\sinh kD} \sin \sigma_t \quad . \tag{II-12}$$

As with particle velocity, for intermediate waves the particle displacement 'in the vertical is zero at the bottom.

Any sensor will have certain limitations such as the threshold velocity, time, and scale response. It is reasonable to assume that the wave motion detector can measure current velocities down to 10 cm sec^{-1}, and that the dimensions of the detector will preclude the sensing of turbulent "eddies" less than 10 cm in length (or diameter).

An estimate of the wave magnitudes that might provide such threshold parameters and of the range of depths at which these threshold values occur can be made by using equations II-5, 7, 9, and 11. Neglecting the time variable terms, one can assess the maximum value of the amplitude of the oscillating functions at various depths. Table II-1 is a summary of observed and theoretical relationships for surface wind waves. Columns A through E were taken from a table presented by Stewart (1961), and the parameters listed therein are strictly estimates from large amounts of observed data. The wind speeds given in the table occurred for a long enough interval to produce waves in a steady or fully developed condition.

TABLE II-1

Summary of Observed and Theoretical Relationships for Surface Waves

A Wind Speed (m sec^{-1})	B Period Avg. (sec)	C Period of Max. Energy (sec)	D Wave-length Avg. (m)	E Wave Height Significant (m)	F 10 cm sec^{-1} Velocity (Depth m)	G 10 cm Orbital Diameter (Depth m)
1.1	0.5	0.7	0.25	0.02	0.17	-
2.6	1.4	2.0	2.06	0.08	0.19	-
4.4	2.4	3.4	6.10	0.30	1.34	1.08?
5.2	2.9	4.0	8.25	0.42	1.98	1.88
6.2	3.4	4.8	12.2	0.67	3.44	3.76
6.9	3.9	5.4	15.8	0.88	4.92	5.45
7.2	4.0	5.6	18.0	1.01	5.92	6.64
8.2	4.6	6.5	21.6	1.40	7.73	9.47
9.3	5.1	7.2	27.2	1.86	10.57	12.64
9.8	5.4	7.7	30.2	2.10	12.00	14.58
10.3	5.7	8.1	33.8	2.42	13.93	17.18
11.3	6.3	8.9	40.8	3.05	15.64[1]	15.69[1]
12.3	6.8	9.7	48.8	3.65	17.24[1]	17.09[1]
12.6	7.0	9.9	50.0	3.97	17.57[1]	17.31[1]

1 = from Intermediate Wave Theory (see equations II-7 and II-8)

Column F shows the depth at which a gravity wave with the attributes listed in B, C, D and E has particles oscillating at a velocity of at least 10 cm sec^{-1}. For the last three values in column F a water depth of 20 meters forced an intermediate wave calculation (using equation II-7); all other values are estimated using the deep water wave equations (e.g., II-5). Similarly, column G gives the water depths at which an orbital diameter of 10 cm exists. Deep water equations (e.g., II-9) are used except for the bottom three terms, which are estimated using equation II-11 for intermediate waves.

Winds observed in Narragansett Bay and Rhode Island Sound frequently occur in the range of speeds given in table II-1 (i.e., 2-15 m sec^{-1}). Hence, at the higher wind speeds, the surface waves can be expected to produce the minimum particle velocities and displacements at depths to 18 meters. Thus, it appears feasible to measure perturbations of surface waves (which fall within the somewhat conservative limits established for velocity and scale) at a variety of depths and under realistic wave conditions occurring in the area of measurement.

Since measurements are to be made of the dynamic perturbations associated with the motions of wind waves, the measuring instrument should respond to frequencies somewhat higher than the wave frequencies. Table II-2 is a sea state chart taken from Marks (1964). The wave characteristics have been converted from English to metric units. The table lists wave periods associated with various wind speeds, fetches, and durations. For wind speeds between 2 and 15 m sec $^{-1}$ the average periods of the waves run from 1.4 to about 8.5 seconds. It is obvious that the sensor selected must resolve oscillations of less than one second.

Kinsman (1960), in making free surface elevation measurements of relatively small (and thus, relatively high frequency) wind driven waves, sampled at 0.2 second intervals from the analog output of his wave staff. This study and other experiments discussed in Ocean Wave Spectra (1961) indicate that sampling intervals of 0.5 to 0.2 second are used to obtain data for statistical analysis of even the highest frequency ocean waves. Thus, the response time of the sensor must be equal to or less than 0.2 second.

Choice of an Instrument

The brief historical review in chapter I indicates that past experience offers no firm basis to assist in choosing a method of wave measurement. To embark on some instrumentation development, although tempting, would certainly result in extreme complexity (even if it were based upon conventional systems) and considerable expense. Moreover, the guarantee of success would be very tenuous.

The purpose here is to explore the conceptual approach to studying wave particle motions in the hope of providing the impetus for further concerted effort. The success of this preliminary study will determine the worth of an all-out assault on the problems associated with the measurement of wave motions and the development of properly sophisticated instrumentation. Thus,

TABLE II-2
SEA STATE CHART

WIND AND SEA SCALE FOR FULLY ARISEN SEA

Sea State[1]	Description[2]	Beaufort Wind Force	Wind Description	Range (m/sec)	Wind Velocity Average (m/sec)	Wave Ht Average (m)	Wave Ht Significant (m)	Wave Ht Average 1/10 Highest (m)	Significant Range of Periods (sec)	Period of Max Spectral Energy (sec)	Aver. Period (sec)	Average Wave Length (m)	Minimum Fetch (km)	Minimum Duration (hrs)
0	Sea like a mirror.	U	Calm	less than 0.5	0	0	0	0						
1	Ripples with the appearance of scales are formed, but without foam crests.	1	Light Air	.6-1.6	1.1	.02	.024	.03	up to 1.2 sec	0.7	0.5	2.5	9.25	18 min
	Small wavelets, still short but more pronounced, crests have a glassy appearance, but do not break.	2	Light Breeze	2-3.1	2.6	.05	.08	.11	0.4-2.8	2.0	1.4	2.06	14.7	39 min
	Large wavelets, crests begin to break. Foam of glassy appearance. scattered white horses.	3	Gentle Breeze	3.6-5.1	4.4	.18	.3	.37	0.8-5.0	3.4	2.4	6.1	18.1	1.7 hrs
					5.2	.27	.42	.55	1.0-6.0	4	2.9	8.25	18.5	2.4
2	Small waves, becoming larger, fairly frequent white horses	4	Moderate Breeze	5.6-8.2	6.2	.43	.67	.85	1.0-7.0	4.8	3.4	12.2	33.3	3.8
					6.9	.56	.88	1.1	1.4-7.6	5.4	3.9	15.8	44.5	4.8
3					7.2	.60	1.01	1.28	1.5-7.8	5.6	4.0	18.0	51.7	5.2
					8.2	.88	1.4	1.76	2.0-8.8	6.5	4.6	21.6	74.0	6.6
4	Moderate waves, taking a more pronounced long form, many white horses are formed. (Chance of some spray.)	5	Fresh Breeze	8.8-10.8	9.3	1.15	1.86	2.38	2.5-10.0	7.2	5.1	27.2	104.0	8.3
					9.8	1.30	2.1	2.65	2.8-10.6	7.7	5.4	30.2	111.0	9.2
					10.3	1.82	2.42	3.05	3.0-11.1	8.1	5.7	33.8	138.8	10
5	Large waves begin to form, the white foam crests are more extensive every where. (Probably some spray.)	6	Strong Breeze	11.4-13.9	11.3	1.95	3.05	3.96	3.4-12.2	8.9	6.3	40.8	185.0	12
					12.3	2.11	3.65	4.87	3.7-13.5	9.7	6.8	48.8	241.0	14
6					12.6	2.5	3.97	5.18	3.8-13.6	9.9	7.0	50.0	259.0	15
					13.8	2.9	4.57	6.10	4.0-14.5	10.5	7.4	57.2	333.0	17
	Sea heaps up and white foam from breaking waves begins to be blown in streaks along the direction of the wind. (Spin drift begins to be seen.)	7	Moderate Gale	14.2-17.0	14.4	3.36	5.5	7.0	4.5-15.5	11.3	7.9	64.5	426.0	20
					15.4	4.25	6.7	8.55	4.7-16.7	12.1	8.6	76.1	519.0	23
					15.6	4.25	7.0	8.85	4.8-17.0	12.4	8.7	78.6	537.0	24
7					16.4	4.9	7.9	10.8	5.0-17.5	12.9	9.1	86.9	630.0	27
	Moderately high waves of greater length, edges of crests break into spindrift. The foam is blown in well marked streaks along the direction of the wind. Spray affects visibility.	8	Fresh Gale	17.5-20.6	17.4	5.8	9.15	11.6	5.5-18.5	13.6	9.7	98.0	779.0	30
					18.6	6.4	10.6	13.4	5.8-19.7	14.5	10.3	111.8	925.0	34
					19.1	7.0	11.7	14.2	6-20.5	14.9	10.5	114.5	980.0	37
					19.6	7.6	12.2	15.2	6.2-20.8	15.4	10.7	119.5	1110.0	38
					20.6	8.5	13.7	17.7	6.5-21.7	16.1	11.4	135.1	1310.0	42
8	High waves. Dense streaks of foam along the direction of the wind. Sea begins to roll. Visibility affected.	9	Strong Gale	21.1-24.2	21.6	9.4	15.2	19.5	7-23	17.0	12.0	150.0	1534.0	47
					23.6	11.0	17.7	22.2	7-24.2	17.7	12.5	162.0	1774.0	52
					23.7	12.2	19.5	24.7	7-25	18.6	13.1	180.0	2053.0	57
	Very high waves with long overhanging crests. The resulting foam is in great patches and is blown in dense white streaks along the direction of the wind. On the whole the surface of the sea takes a white appearance. The rolling of the sea becomes heavy and shock-like. Visibility is affected.	10	Whole Gale*	24.7-28.3	24.7	13.4	21.6	27.5	7.5-26	19.4	13.8	197.0	2350.0	63
					25.7	14.9	24.1	30.2	7.5-27	20.2	14.3	213.0	2660.0	69
					26.5	15.8	25.3	32.4	8-28.2	20.8	14.7	224.1	2880.0	73
					26.8	16.5	26.5	33.6	8-28.5	21.0	14.8	248.1	2980.0	75
					27.8	18.0	29.0	37.0	8-29.5	21.8	15.4	246.5	3325.0	81
9	Exceptionally high waves (Small and medium-sized ships might for a long time be lost to view behind the waves.) The sea is completely covered with long white patches of foam lying along the direction of the wind. Everywhere the edges of the wave crests are blown into froth. Visibility affected.	11	Storm*	29.4-31.4	28.8	19.5	31.2	39.7	8.5-31	22.6	16.3	276.8	3880.0	88
					30.6	22.1	35.4	45.1	10-32	24	17.0	300.0	4620.0	101
	Air filled with foam and spray. Sea completely white with driving spray, visibility very seriously affected.	12	Hurricane*	33.0-36.5	>33.0	>24.2b)	>39.0b)	>50.1b)	10-(35)	(26)	(18)	~	~	~

*For hurricane winds (and often whole gale and storm winds) required durations and fetches are rarely attained. Seas are therefore not fully arisen.

a) A heavy box around this value means that the values tabulated are at the center of the Beaufort range.

b) For such high winds, the seas are confused. The wave crests blow off, and the water and the air mix.

1) Encyclopedia of Nautical Knowledge, W. A. McEwen and A. H. Lewis, Cornell Maritime Press, Cambridge, Maryland, 1953, p. 483.

2) Manual of Seamanship, Volume II, Admiralty, London, H. M. Stationery Office, 1952, pp. 717-718.

3) Practical Methods for observing and forecasting Ocean Waves, Pierson, Neumann, James, N. Y. Univ., College of Engin, 1953.
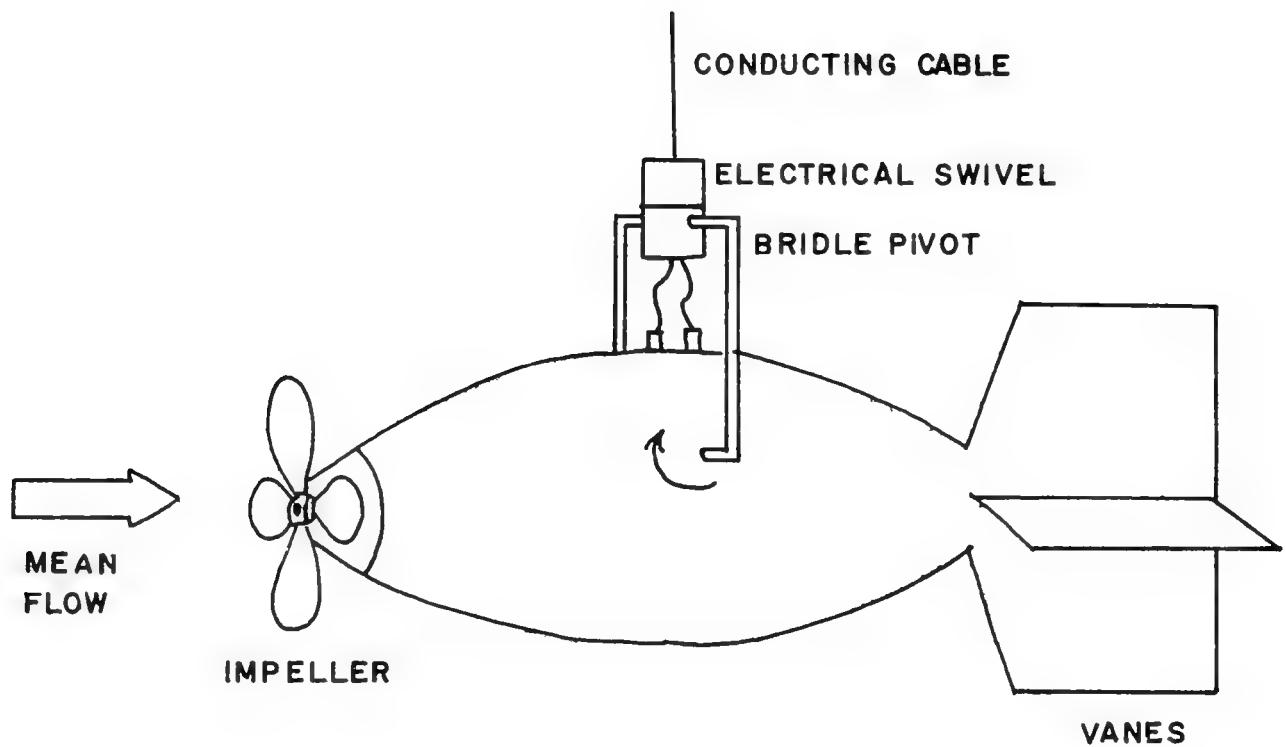
Typical Configuration of Electrical Impeller Type Current Meters.

Figure II-1

the initial goal is to make simple measurements with simple sensors without having to solve intricate problems of elaborate instrumentation development. This should come later.

There are four general categories of sensors from which to choose: sea water emf induction systems (Bowden and Fairbairn, 1956); acoustic flow meters (Chelupmik and Green, 1962, and Lester, 1961); force deflection or thrust systems (Flow Corp., 1965); and the common impeller devices.

Each of these instrument categories has definite drawbacks. Both the induction and acoustic systems are relatively untried. They have met with difficulties involving the stability of the electronics and are very expensive to fabricate. The force response meters (i.e., drag or thrust spheres and deflecting plate systems) are difficult to calibrate and expensive. Although they have been successfully developed for the atmosphere (see Doe, 1963), they have met with electronic difficulties when placed in the turbulent ocean medium (Zeigler, 1963). Use of these three types of systems in the measurement of oceanic turbulence is certainly not precluded, but a major development effort would be required.

The impeller devices offer the attributes of rapid and stable response combined with simple and inexpensive electronic packaging. A continuous recording of fluid flow can be made with the impeller flow meter by coupling the propeller magnetically to a magnetic-pickup amplifier circuit or to an induction coil. The pickup coil must be isolated electrically (but not magnetically) from the sea water.

The most common types of rotor or impeller devices are the Von Arx meter (Von Arx, 1950) and the Roberts-type current meters, all of which are really electronic variations of the mechanical Ekman meter (Ekman, 1926). These instruments utilize an impeller mounted on a horizontal axis. An electrical swivel and a tail-vane arrangement (figure II-1) permit the axis of the impeller to seek the current direction. The speed of flow is registered by the frequency of the impeller revolutions. The magnitude of the emf (or, in the case of the Roberts meter, the frequency of the inductive voltage pulses) provides an analogous relation for speed of the current. The relationship of the angular velocity of the impeller (and hence, the induced emf) to the flow speed is usually linear. In some meters the direction of flow is detected by an electrical analog comparison of the compass heading with the vane heading.

Analysis of a current vector in two dimensions (in the XY plane) requires a pivoting-vane type instrument that can rotate in response to the oscillatory motions of the waves. Since available pivoting impeller devices are 50-80 cm in length, the directional time response of the instrument would be strongly limited by the large moment of inertia. Moreover, there would be no response to oscillatory motions having a scale diameter less than the length of the instrument. It is quite obvious, therefore, that without extreme modifications and miniaturization, pivoting impeller-type meters would be undesirable for measuring wave motions.

PILLBOX
INDUCTION
COIL HOUSING

PIN CONNECTOR

STRUTS

CYLINDER
HOUSING

IMPELLER

IMPELLER SHAFT

Schematic Diagram of the Ducted Meter.

Figure II-2
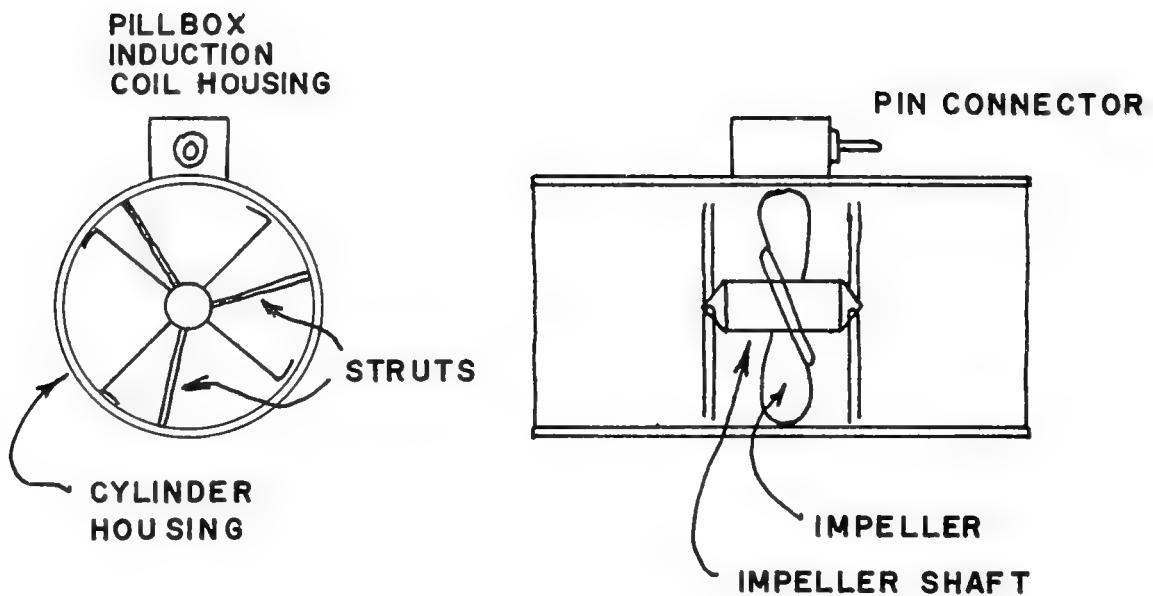
In 1961 Marine Advisors, Inc. of La Jolla, California, advertised a so-
called "ducted meter" for measuring current flow. This instrument consists
of a right circular cylinder within which is mounted an impeller having an
axis of rotation coincident with that of the cylinder. Fluid flow through
the cylinder causes spinning of the impeller. This spinning is detected as
an induced emf which is generated by iron slugs or magnets (fixed in the
impeller blades) as they pass an induction coil. Figure II-2 is a schematic
diagram of the ducted meter. A detailed discussion of the system is given
later in this chapter. However, there are some important and possibly unique
dynamic characteristics of this device that should be examined here.

The ducted meter is inherently much more responsive to current fluctuation
than the unshrouded or open impeller devices. Since the impeller intersects
with a straight line path through the cylinder, all flow through the cylinder
must produce an impeller rotation. The result, in effect, is that of an inverse
pump. Any pressure perturbation occurring at the entrance of the cylinder is
hydrostatically and almost instantaneously transmitted to the impeller blades.

In this discussion of instrumentation, the term "response time" is used
as a measure of the degree to which an impeller sensor can respond (i.e.,
commence to spin) to high frequency fluctuations of the fluid flow. Classi-
cally, response time is defined as that interval required for the impeller to
attain a rotation equivalent to a flow velocity which is $(1 - \frac{1}{e})$, or about
63 percent of an instantaneously applied constant velocity. The response
time T_R is derived from the equation of motion in appendix A. The time
response is given by

$$T_R = \frac{I}{K_1} \quad ; \tag{II-13}$$

where I = moment of inertia of the impeller $(gm\ cm^2)$, and K_1 $(gm\ cm^2\ sec^{-1})$ is
a function of the fluid viscosity and density. Obviously, there is a threshold
of dynamic pressure below which the combination of fluid pressure and shear on
the blades is too small to overcome the inertia and bearing friction of the
blade mounting. When this occurs the fluid would just flow around the blades
producing no spinning. However, this threshold of flow response can be mini-
mized: (1) by making the impeller as lightweight as possible; (2) by using
very low friction pivot bearings upon which the impeller would be axially
balanced; and (3) by minimizing the magnetic force coupling between the impeller
blade ferromagnets and the pickup coils.

This dynamic loading cannot occur with an impeller mounted semi-openly, as
with the Von Arx and Roberts type instruments, because the fluid pressing upon
the blades is completely free to diverge radially from the impeller. This
radial divergence reduces the efficiency of the impeller as a flow detector.
The inherent differences between a ducted and a semi-open or open system are
analagous to the efficiency gained by using a wind tunnel to provide a pre-
scribed air flow at a given point, as opposed to using the same fan in the
open air.
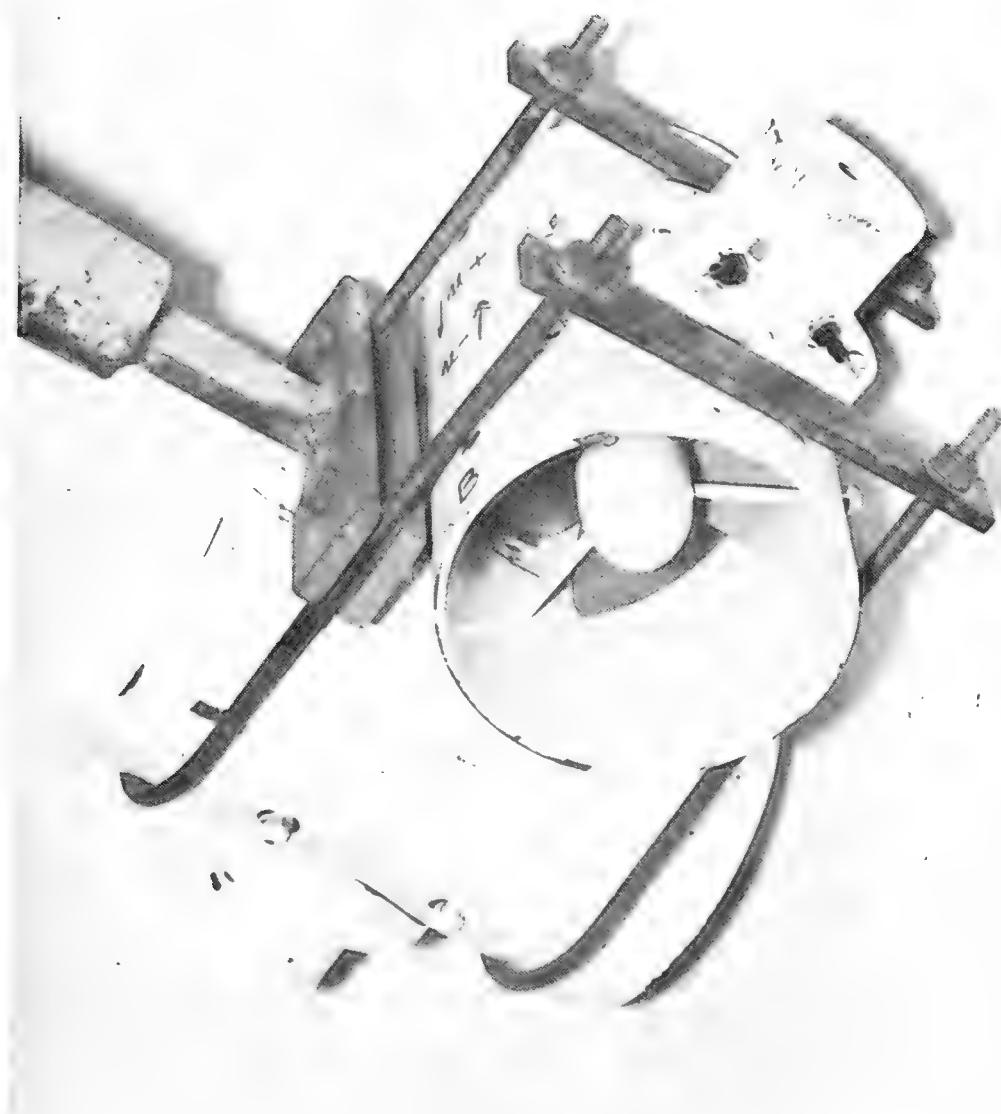
First Orthogonally Mounted Ducted Meter System

Figure II-3

Thus, the cylindrical shroud of the ducted meter greatly increases its response to axial directed pressure perturbations. But most important (if not imperative) for wave measurements, the cylindrical shroud makes the impeller response a predictable function of the angle formed by the instantaneous fluid flow and the cylinder axis. In other words, if the response of each ducted meter is known as a function of speed and off angle; then, by coupling two meters orthogonally, it should be possible to sense a two-dimensional field of motion in the plane of the orthogonal cylinder axes.

A discussion of the dynamic properties of such an instrument coupling would be premature at this point. The geometry of flow response was interpreted only after some calibration measurements were performed. These are discussed in later sections.

Another interesting feature of the impeller is that the angular velocity is essentially independent of the density of the fluid. Thus, steady calibration can be made with no required water density information. In fact, the wave meter can be calibrated in a wind tunnel. The response time, however, is dependent upon the viscosity and density of the fluid.

Another important aspect in the choice of an instrument is that of mounting or suspending the wave meter in the ocean. Any force detector or deflection device in which minute beam displacements are measured by means of strain gauges or linear differential transformer systems requires a completely rigid support system in the fluid medium. This is because the operation depends upon the flexure or strain (with respect to a rigid coordinate system) of a drag device in response to the pressures imparted by the fluid flow. These flexures are usually of the order of a few thousandths of a centimeter.

A deflection device must interfere with or inhibit the fluid flow in order to work properly. The impeller device, however, does not offer rigid resistance to flow, but responds or reacts rather completely to the flow. There is, of course, some interaction with the cylinder housing, which must be kept reasonably fixed in space.

The main point is that a force deflection device requires completely rigid mounting; whereas an impeller device can be suspended by means of wires and weights, since displacements of the order of a few millimeters would in no way affect its sensitivity. The ability to suspend the impeller system greatly favors the use of this device in preference to a force-deflection system.

Orthogonally Mounted Ducted Meter - OMDUM I

The OMDUM I system is the result of the first attempt made at NUWS to fabricate a particle velocity meter for sensing two-dimensional wave motions.

Design Characteristics -- OMDUM I consists of a coupling of two identical ducted flow meters manufactured by Marine Advisors of La Jolla, California (1961). The two meters are mounted together in an adjacent orthogonal position (figure II-3) and sense fluid flow components in the planes defined by
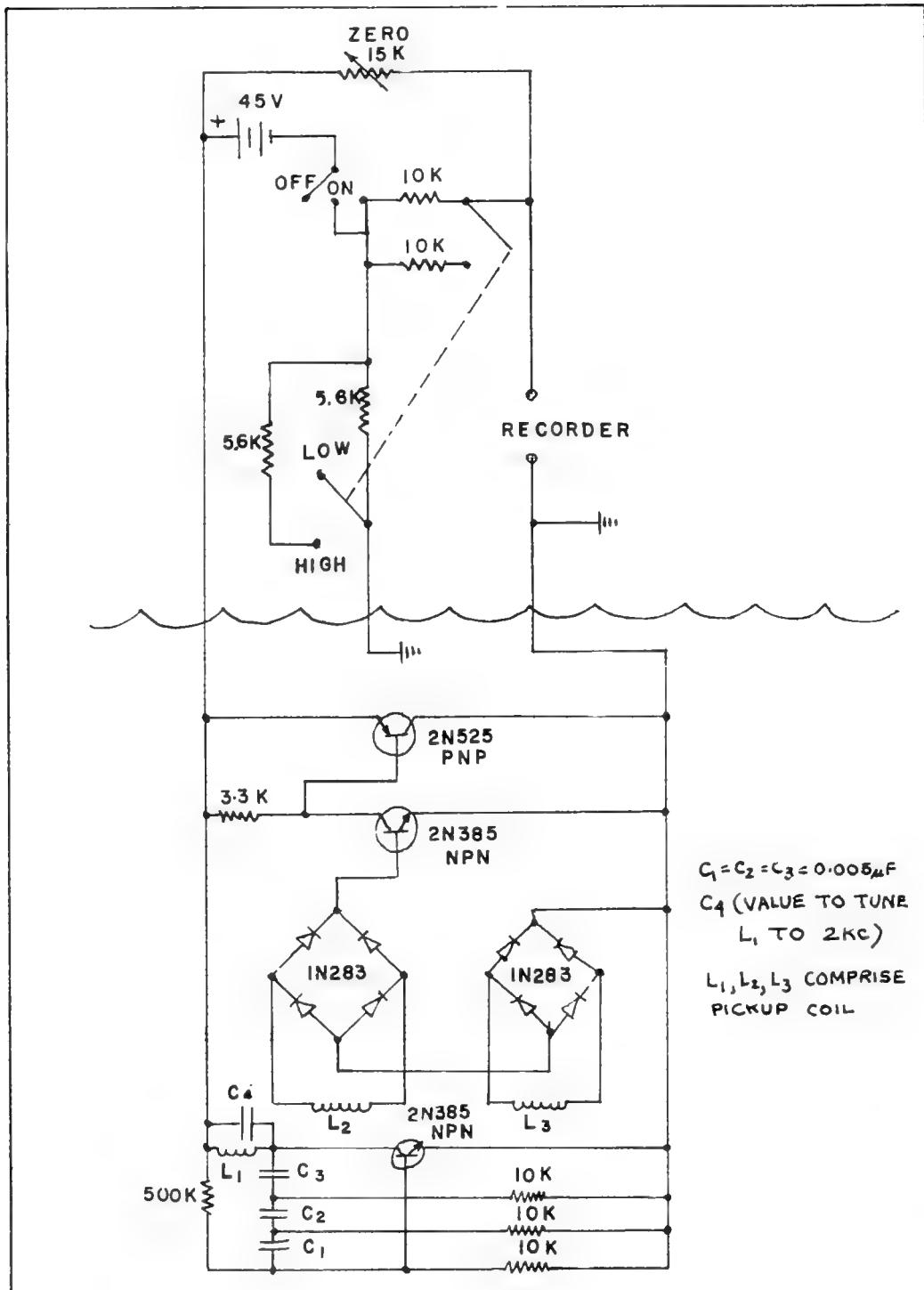
Wiring Diagram for Ducted Meter Magnetic Pickup, Amplifier, Oscillator Circuit, and Power Supply.

Figure II-4

the axes of two cylinders. If the cylinder axes are aligned coincident with the X and Z axes, the associated velocity components may be written simply as u and w, respectively.

Each flow meter consists of a brass right circular cylinder 21.5 cm long with a 13.3 cm inside diameter and a 0.3 cm wall thickness. The cylinders are held together by two supporting U-bolts which are made of 3/8-inch brass rod and clamped to a T-shaped piece welded to the support pipe. The flow sensor is a five bladed impeller mounted within the cylinder at its mid-point so that the axis of rotation is coincident with that of the cylinder. The impeller shaft consists of a Teflon cylinder with brass needle bearing inserts at each end. The fore and aft impeller bearing supports are suspended at each end by three thin struts. The needle bearings can be adjusted in or out to provide proper seating of the pins in the axis support housing held by the supporting struts.

The impeller blades are made of 1.5 mm thick micarta (phenol formaldehyde with a cellulose filler), which has a specific gravity of about 1.3. The blades are fixed to the Teflon shaft at an angle of about 45° with respect to their axis of rotation. At the outer tip of each impeller blade is mounted a small iron slug weighing about 1 gm and having dimensions of about 10 by 4 by 0.5 mm. The slugs are set into the blade tips with epoxy glue. The long axis is normal to the impeller axis and is positioned so that the end of the slug is flush with the outer tip of the blade.

The impeller responds to the component of flow parallel to the cylinder axis by spinning, thus allowing flow through the cylinder. The angular velocity of the impeller is a known function of the magnitude of the flow. The rotation of the impeller as a function of time is monitored by a magneto-inductive coupling between the iron slugs and an energized miniature induction coil. This coil and the associated circuitry are contained within the small brass pillbox braised to the side of the cylinder (see figure II-3).

Figure II-4 is an electrical schematic of the circuitry. The arm of the induction coil L_1 is excited by a 2 kc carrier oscillator circuit as shown. As the impeller spins, the iron slugs pass within 0.5 - 1.0 mm of the coil arms. This causes a change in the inductance and, hence, a perturbation of the 2 kc carrier frequency. This magnetic induction is also registered in coil windings L_2 and L_3 which are mounted on either side of the winding L_1. The sense of impeller rotation determines which winding (L_2 or L_3) is perturbed first. By means of the parallel diode circuits, the shape of the amplitude modulated voltage disturbance entering the transistor NPN 2N385 is uniquely defined by the sequence of coil excitation. This pulse is amplified through PNP 2N525 and led to the surface recorder. The entire circuitry, consisting of a miniature coil, oscillator, and modulator-amplifier, is potted within the pillbox. The surface electronics include the DC power supply, a high and low amplification circuit, and the zero balance. The input voltage from the DC power supply and the output signal are led to the pillbox by two watertight male connectors manufactured by

CALIBRATION CURVE

OMDUM I (5 BLADES)
MARINE ADVISERS DATA
(INDIVIDUAL TOWING)

$V_T = (K_f) f_V + 1.5 \text{ CM SEC}^{-1}$

$K_f = 4.25 \text{ CM}$

$K_f^{-1} = 0.233 \text{ CM}^{-1}$
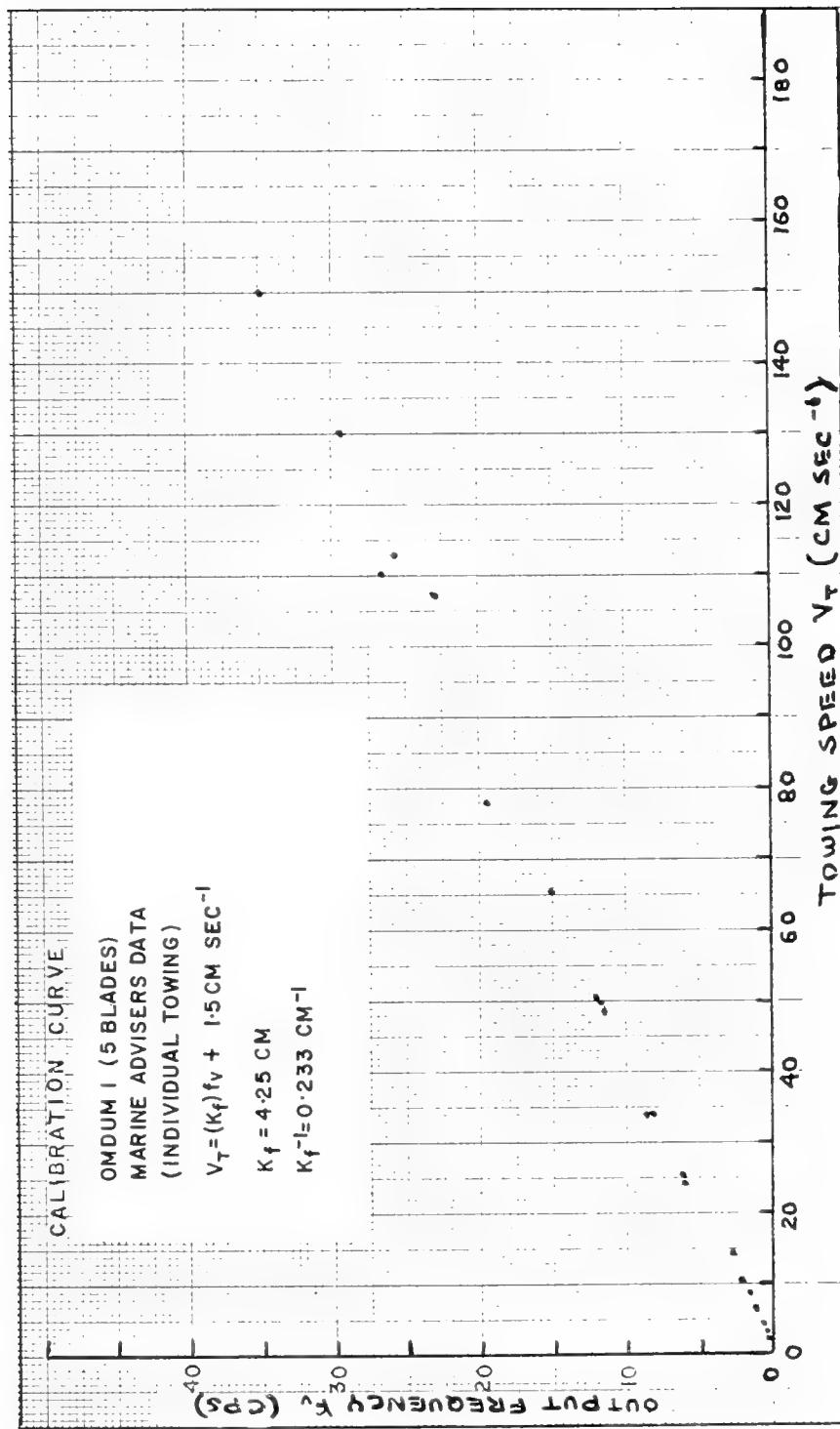
Calibration Curve Showing Impeller Response to Steady Rectilinear Towing.

Figure II-5

Mecca Cable and Service, Inc., Houston, Texas). The output from the modulator circuit is fed through a shielded sea water cable to a zero balance adjuster and, from this, is recorded on a two-channel 720 Sanborn recorder (Sanborn Co., Waltham, Mass.).

The repetition rate of the pulses of the modulated output voltage is inversely proportional to the angular velocity of the impeller. The shape or signature of the pulse provided by the emf-generating circuit indicates in which sense the impeller is spinning. The result is a kind of algebraic frequency analog of the angular velocity and sense of impeller rotation as a function of time.

The pulse trace was not completely satisfactory, since it was often difficult to distinguish positive from negative rotation signatures. Also, the Marine Advisors circuitry was too sophisticated for the job for which it was intended. Still, the elaborate amplifier and circuitry, involving transistors and diodes, allowed the small perturbations due to the iron slugs passing the coils to be well detected. This facilitated the use of very light iron slugs, which added little to the moment of inertia (hence, to the response time) of the impellers. However, since the entire circuitry of each ducted meter system was potted with an epoxy resin within the pillbox mounted on the cylinder, failure of any electrical components meant complete destruction and replacement of the entire circuitry. Within three months, after two complete circuit replacements, the system was discarded in favor of a simpler system consisting solely of a miniature pickup coil and small alnico magnets.

Dynamic Characteristics and Calibration -- The ducted meters were calibrated for steady and accelerated flow by the manufacturer, and calibration data in the form of a curve were supplied with the meters. These data were obtained by towing the ducted meters individually in a Lockheed Corporation test tank, but only in the direction parallel to the axis of the individual cylinder.

The calibration curve for steady flow provided by the Marine Advisors for the ducted meters is shown in figure II-5. The abscissa is towing speed V_T (cm sec^{-1}), and the ordinate is the repetition rate or output frequency of the voltage pulses f_V (cps). Since the impeller has five blades, f_V represents five times the impeller frequency. This curve was taken from data plotted on semi-logarithmic paper, and originally contained 38 points ranging from 2.1 to 361 cm sec^{-1}. The linearity of the calibration plot was preserved extremely well for even these extreme high speeds. The relation of f_V to the towing speed is linear with a proportionality constant K_f of 4.25 cm. It appears that the threshold of velocity measurable is near 2.0 - 3.0 cm sec^{-1}. The slope of the line K_f^{-1} is about 0.233 cm^{-1}.
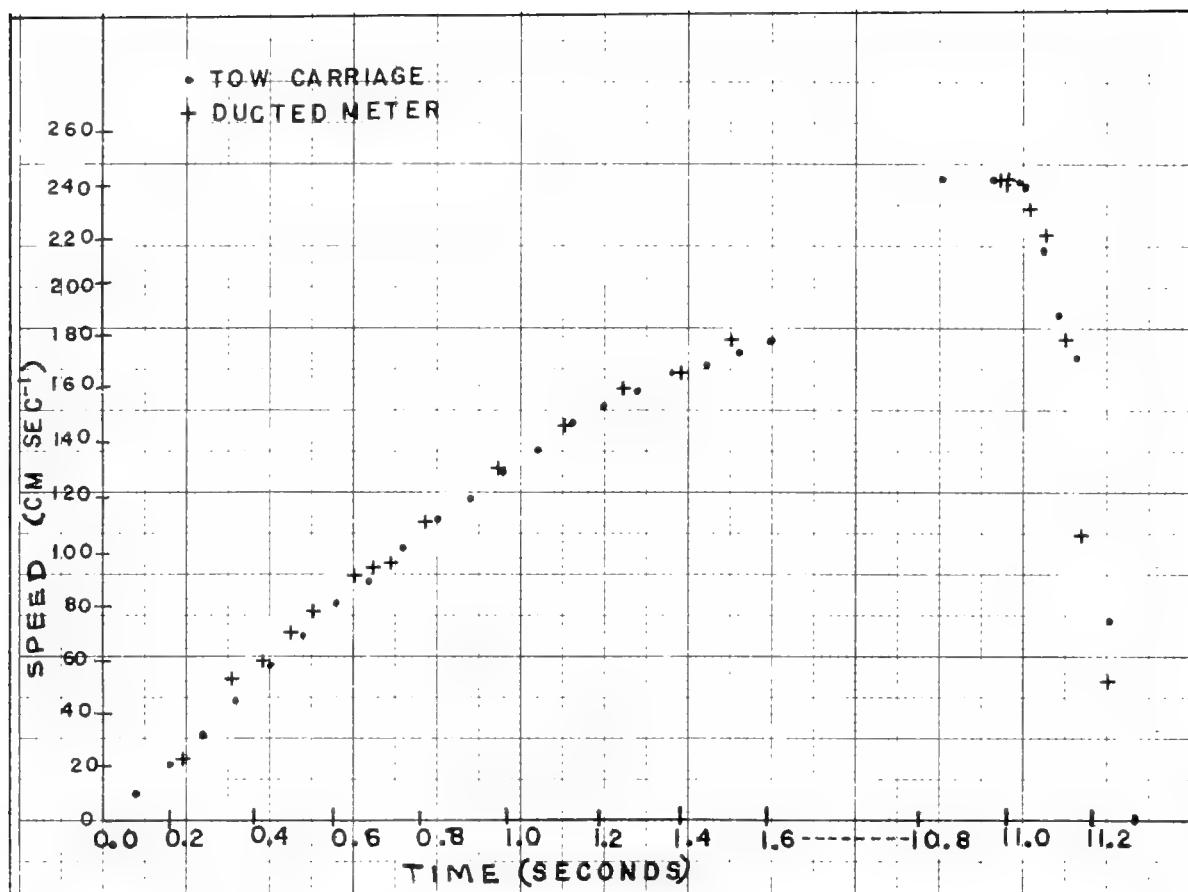
Impeller Response to Accelerated and Decelerated Towing.

Figure II-6

Since the impellers had to be disassembled several times for circuit maintenance, a later calibration check was performed in the NUWS hydrodynamics laboratory wind tunnel. The in-water calibration data were reproduced well within the limits of experimental error. It was found that as long as the needle bearing mounting was left with at least 1 mm of axial clearance, the calibration was essentially unaffected by disassembling the impellers.

The time response of the ducted meter was roughly evaluated by Marine Advisors by means of an acceleration towing test. The results of this test are shown in figure II-6. The speed of the tow carriage of the tank was monitored as the ducted meter was accelerated and decelerated. The pulse frequency output of the meter was converted to speed, and a comparison of the monitored carriage speed and the speed registered by the ducted meter is depicted in the figure. In general, the indicated speed of the carriage lags behind the response of the ducted meter, both during acceleration (from 0.0 to 1.6 seconds) and deceleration (from 11.0 to 11.2 seconds). It is inferred from these results that the response time is somewhat less than 0.1 second (frequency response is above 10 cps).

It is not possible to derive the exact response time from these data because the frequency response of the meter is apparently faster than the monitoring device. Hence, no time lag is obtained; i.e., the meter response is in equilibrium with the impressed variations in fluid flow.

A cursory examination was made of impeller response by simulating sudden impulses of flow while the meter was suspended from a wire off a pier. The almost instantaneous coupling with the water when the immersed device was rapidly raised and lowered indicated an extremely fast response time.

The impeller blades are designed to completely fill the cross-sectional area of the cylinders, thus providing a maximum torque-to-flow ratio. Also, loading on the needle bearings is minimized by buoyancy effects, since the overall density of the micarta impellers and the Teflon shaft is near that of sea water.

A single series of preliminary wave measurements was made in Narragansett Bay using the OMDUM I system. Upon completion of these measurements the electronics failed, and the system was modified (OMDUM II) before any further calibration was made. These preliminary measurements cast some doubt upon the usefulness of the OMDUM I system for measurement of particle velocity motions in the XZ plane, and on system response to the non-steady motions inherent in the wave regime, particularly when the flow is at off angles to the axis of the impellers. An estimate of system response (for OMDUM I and II) was obtained later and is presented under the next heading.

The experimentation with OMDUM I, however crude, served as a guide to the modifications that resulted in OMDUM II. OMDUM II was used to examine more thoroughly the laboratory calibration and the ability of the instrument to measure wave motions.
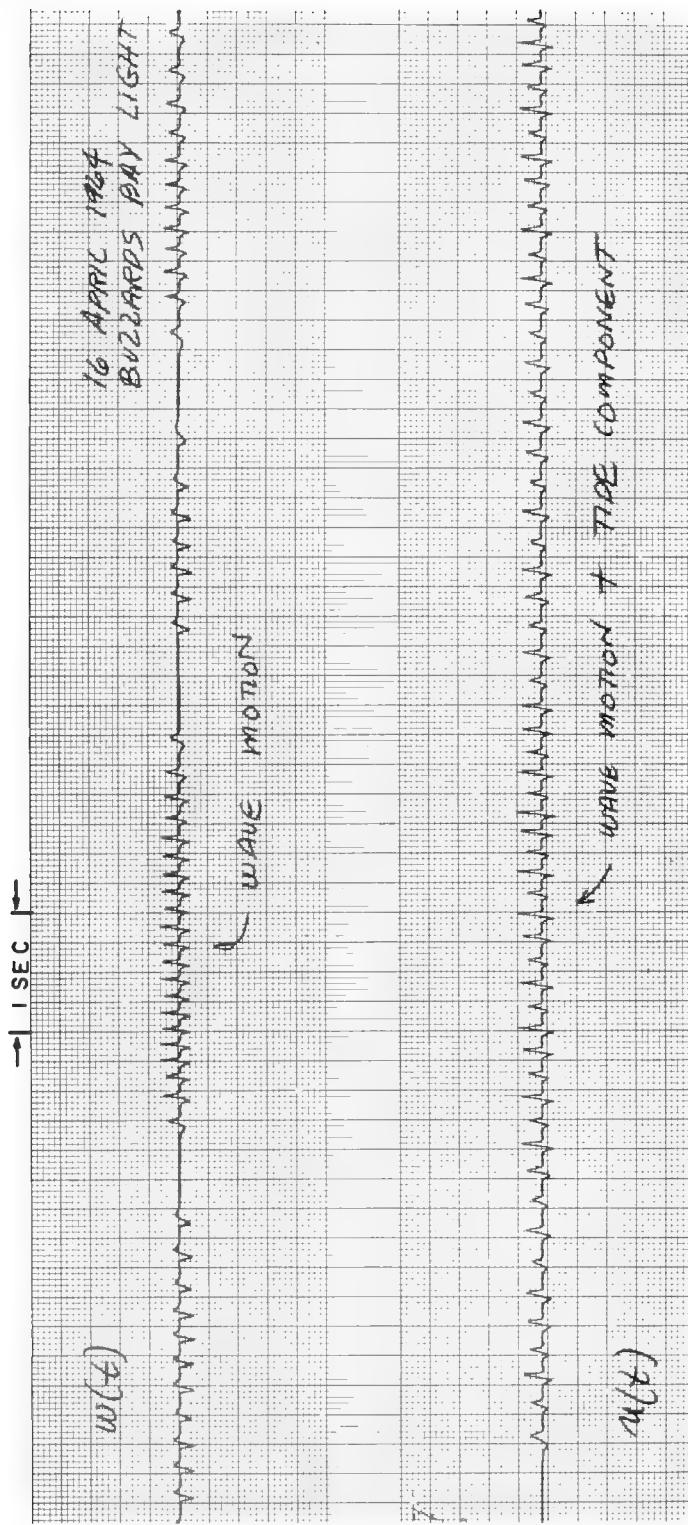
Typical Voltage Pulses Produced by the Magnet-Coil Detector

Figure II-7

Modified Orthogonally Mounted Ducted Meter (OMDUM II)

As stated previously, the electronics of OMDUM I were judged inadequate because of circuit failures and unclear trace generation. This detector was therefore replaced by simple electronic circuitry, consisting of a coil and magnets.

Design Characteristics -- In the resulting OMDUM II system, small alnico magnets (10 by 5 by 2 mm) weighing about 0.7 gm each are mounted in the impeller blades in place of the smaller and lighter iron slugs used in OMDUM I. These magnets were provided by the Magnetic Seal Corp., Barrington, R. I. A miniature induction coil (replacing the entire transistorized circuit in OMDUM I) is installed in the pillbox. The coil (manufactured by Precision Electronics Company, Marshfield, Mass.) is open-ended and wound with #36 insulated copper wire. Its U-shaped geometry is designed to provide maximum voltage pickup as the impeller magnet moves by the open side of the potted coil. The coil is positioned on its side so that one arm of the U lies parallel to the tangent of the circular trajectory inscribed by the outer magnet tip at the point opposite the coil housing. With this geometry, the sign of the induced voltage pulse indicates the sense of the angular velocity of the impeller. Figure II-7 shows the voltage spike patterns generated by each of the two outputs of the OMDUM II system. The upper trace is the output of the vertical flow sensor (w meter), and the lower trace that of the horizontal flow sensor (u meter). The dominant oscillatory motion of the w component is clearly evident. The motion of the u component is that of the wave motion superimposed on a tidal current of about 20 cm sec^{-1}. This record was obtained while the meter was at a depth of 5 meters below the mean wave trough level. At this depth much of the surface wind wave motion is filtered out. The gentle (7-8 second period) oscillations in velocity are mainly caused by swell, which was visually observed during the period of the measurements.

This system was a modified version of the original OMDUM I. An exterior modification was made by reducing the height of the side pillboxes from 4 cm to 2 cm in an effort to reduce drag. This was possible since the induction coil required much less space than the original electronics.

The original needle bearings had become oxidized and deteriorated during the preliminary tests. The Braincon Corp. of Marion, Mass., replaced them with bearings used in their Savonius rotor type current meters. This bearing consists of a hard chrome steel pin with a hemispherically polished end. The pins are mounted at each end of the Delrin (Teflon) impeller shaft. Each pin seats against a polished, machined flat, sapphire wafer and is supported by a cylindrical quartz collar with a sideways clearance of about 0.2 mm.

Calibration and Response Studies -- The use of relatively heavy magnets in lieu of the thin iron slugs was expected to increase the moment of inertia of the impeller, and hence to increase proportionally the response time (see equation (A-12) in appendix A). It was even more important to ascertain the effect of this modification upon the minimum or threshold velocity at which the impeller would commence to spin.

Worcester Polytechnical Institute Rotating Boom System at Holden, Mass.

Figure II-8

In the OMDUM I system the threshold velocity is about 2-3 cm sec^{-1} (figure II-5) and is determined primarily by the friction bearings. In OMDUM II the threshold velocity is more dependent upon the pole strength of the magnets in the impellers than on the bearing friction. The attraction between the magnets and the iron core of the induction coil is such that, when the impeller is spun, a magnet always comes to rest directly opposite the coil core. (This did not occur with the thin slugs in OMDUM I.) It is this force of attraction that must be overcome before the impeller can commence spinning.

The ability of the modified system (OMDUM II) to measure wave motions was assessed by evaluating three distinct dynamic characteristics of the system: (1) the calibration of the impeller response as a function of the speed of a steady rectilinear flow parallel to the cylinder axis (referred to as "end-on flow"); (2) impeller response to flow at a given angle to the cylinder axis (referred to as "off-angle flow"); and (3) the time frequency response of the impeller system to fluctuations of flow.

A calibration of the OMDUM II system to determine its response to steady flow in both the end-on and off-angle positions was performed during June, 1964, using a rotating boom towing system maintained by the Department of Civil Engineering of the Worcester Polytechnical Institute. The boom system, shown in the figure II-8, is located in a shallow pond (1.5-2.0 meters deep) at Holden, Mass., near the institute.

This relatively simple boom system provides an in-water towing facility without the great expense of an elaborate towing tank. Perhaps more significant is the ability of the system to tow at the desired speed for an unrestricted length of time or distance. The double-ended boom (24 meters long) rotates about a vertical axis shaft. The shaft is supported by bearings set in a concrete platform in the middle of the pond. The boom system is driven by a 117-volt DC motor with a variable speed control. The object to be towed is fixed to one end of the boom and rotated at the proper angular velocity Ω_B to give the desired towing (tangential) velocity V_T.

The boom structure has two collinear arms that are symmetrical about the vertical rotating axis. One arm is equipped with electrical leads and is used as the towing end whereas the other arm serves as a counterbalance to facilitate smooth rotation. The boom operator is stationed at the center of the boom at the speed controls. The rugged construction permits an additional man to position himself at the instrument (towing) end for observations during rotation. Power is provided to the drive motor and the recording equipment through a slip ring commutator mounted on the boom axis.

The OMDUM II system was attached rigidly by a vertical shaft which extended into the water at the towing end of the boom. For the various angular velocities of the boom the tangential velocity V_T (or quasi-rectilinear velocity) is calculated from the relation

$$V_T = R\,\Omega_B = \frac{2\pi R}{T}\ ;$$

<div align="right">(II-14)</div>
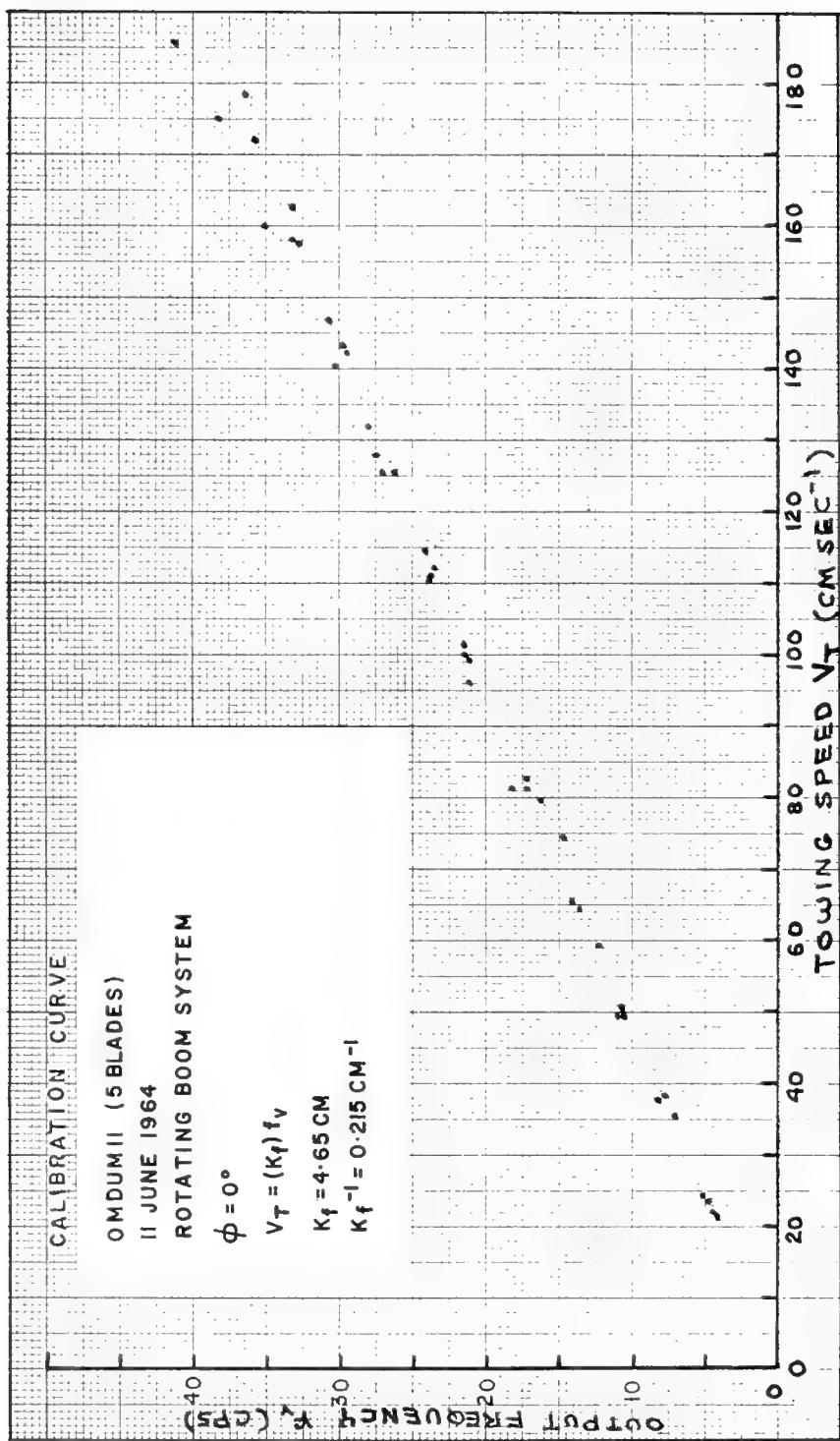
Calibration Curve of Impeller Response to Steady Boom Rotation.

CALIBRATION CURVE

OMDUMII (5 BLADES)
II JUNE 1964
ROTATING BOOM SYSTEM

$\phi = 0°$

$V_T = (K_f) f_v$

$K_f = 4.65$ CM

$K_f^{-1} = 0.215$ CM^{-1}

Figure II-9

where R is the radius measured from the boom axis to the position of the instrument mounting, and T is the period of rotation. The value of T is measured by the operator using a stop watch. His position near the center of the boom allows him to align a boom guy wire with a telephone pole near the edge of the pond. The rotation is timed only after the system attains constant speed. For slow rotations the time of one-half rotation was measured, and for fast rotations the time of a complete rotation was monitored.

How closely does this method of rotational towing approximate the characteristics of rectilinear towing in a tank? One effect of rotation would be to increase the load upon the pin bearings caused by the centrifugal acceleration. This is given by

$$a_c = \frac{V_T^2}{R} = \frac{4\pi^2 R}{T^2} \tag{II-15}$$

The fastest tangential velocity was about 180 cm sec^{-1}. Hence,

$$a_c \sim 2.7 \text{ cm sec}^{-2} \sim 0.0028g$$

where g = gravitational acceleration (980 cm sec^{-2}). The effect of this increase in bearing load may be disregarded, since the acceleration inherent in the towing is much less than the gravitational bearing load (weight) of the impellers and shaft in air.

Rotation also results in a gyroscopic effect produced by the difference in angular momentum between the inboard and outboard side of the impeller, whose axis of rotation lies in the plane tangent to the boom radius. (This is the case for both the u and w meters.) The torque thus produced across the impeller blades is imparted to the impeller axis so as to thrust the leading end of the axis outward. This torque is proportional to the difference in towing radius of the inboard and outboard impeller. The net moment is proportional to $(R + r)/(R - r)$, where r is the radius of the impeller. Since R $\sim$ 1200 cm and r is about 5 cm, the ratio is about 1.0084. Hence, this small effect can also be disregarded.

The first series of calibrations, conducted on 11 June 1964, involved end-on calibration. The range of towing speeds was from 21.9 to 186.5 cm sec^{-1}. A total of 45 calibration runs were made, using the u and w meters individually. Each meter was driven in the forward and backward positions to determine any variations in response.

A tabulation of the calibration data is given in appendix C. Figure II-9 shows the results in terms of the known speed of towing and the resultant frequency of consecutive voltage spikes produced by the impeller rotation. The calibration data for positive and negative directions were essentially indistinguishable; hence, no effort was made to identify the source of points in figure II-9. The output frequency f_v is clearly linear with V_t.
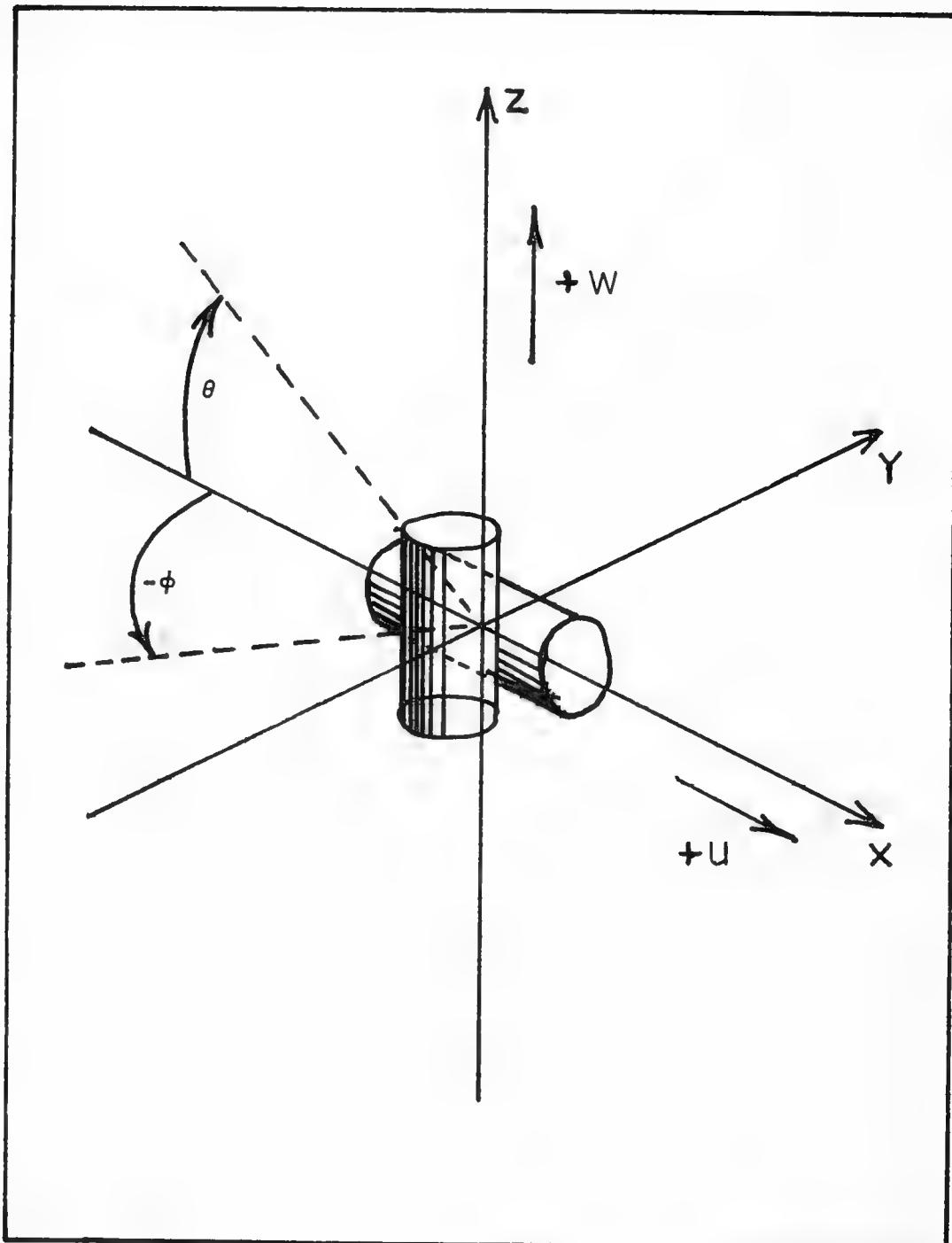
Orientation of Ducted Meters to Define the Angles ∅ and ϴ.

Figure II-10

Unfortunately, the lowest speed obtained for this end-on towing series was 21.9 cm sec^{-1}. When lower speeds were attempted,, an unevenness (jerking) occurred in the towing. It was later found that, with a different boom operator, lower speeds were obtainable, and these were used for the off-angle tests.

The slope K_f^{-1} is 0.215 cm^{-1} compared to a slope of 0.233 cm^{-1} for the OMDUM I system calibration (figure II-5). This change in slope could be caused by the increase in bearing load associated with the replacement of the iron slugs by the relatively heavy alnico magnets. The relationship of the slope constant to the physical dynamic characteristics of the impeller, however, is not obvious. The slope difference is more probably due to the differences in flow characteristics associated with the coupled versus the individual meter configuration. The extrapolation of the line delineated by the data points in figure II-9 to a zero value of f_v appears to intersect the origin.

There is indication of a higher scatter of points with the rotating boom calibration than with the Marine Advisors tests. The scatter seems to increase with towing speed. This is not surprising, since there were uncontrollable ambient motions in the pond caused by slight wind waves and wake generation.

The second calibration series was conducted on 15 June 1964, and involved the study of system response to off-angle flow. The geometry of the coupled meters and the orientation with respect to flow are shown in figure II-10. The angle θ lies in the vertical XZ plane, and the angle ϕ lies in the horizontal XY plane. Thus, ϕ represents an azimuthal angle, and θ represents an inclination to the horizontal.

This second series of calibration was made to study the variation of OMDUM II response as a function of the azimuthal angle θ. For these tests OMDUM II was suspended from the instrument boom as shown by the schematic plan view in figure II-11. For each test rotation OMDUM II was oriented so that the axis of the u meter made an angle $\pm\phi$ with the tangential velocity vector. For each angle ϕ OMDUM II was driven at various speeds.

Note that the negative values of ϕ are defined when the u meter is pivoted outward from the center of the boom rotation, and positive values are defined when it is pivoted inward. The instrument was towed at various steady speeds at ϕ values of $\pm20°$ $\pm40°$, $\pm60°$ and $\pm80°$. The results of the impeller response at the various towing speeds and for the various values of ϕ are listed in Appendix C.

Analysis of the results of these off-angle flow tests may be aided by first considering the following simple model, in which the results of the off-angle response are compared with a theoretical cosine law defined by:

$$u(\phi) = V_T \cos \phi \; ; \qquad\qquad (II\text{-}16)$$

where $u(\phi)$ is the velocity of the fluid sensed by the impeller. More specifically, $u(\phi)$ is the speed obtained from the calibration curve for the parti-
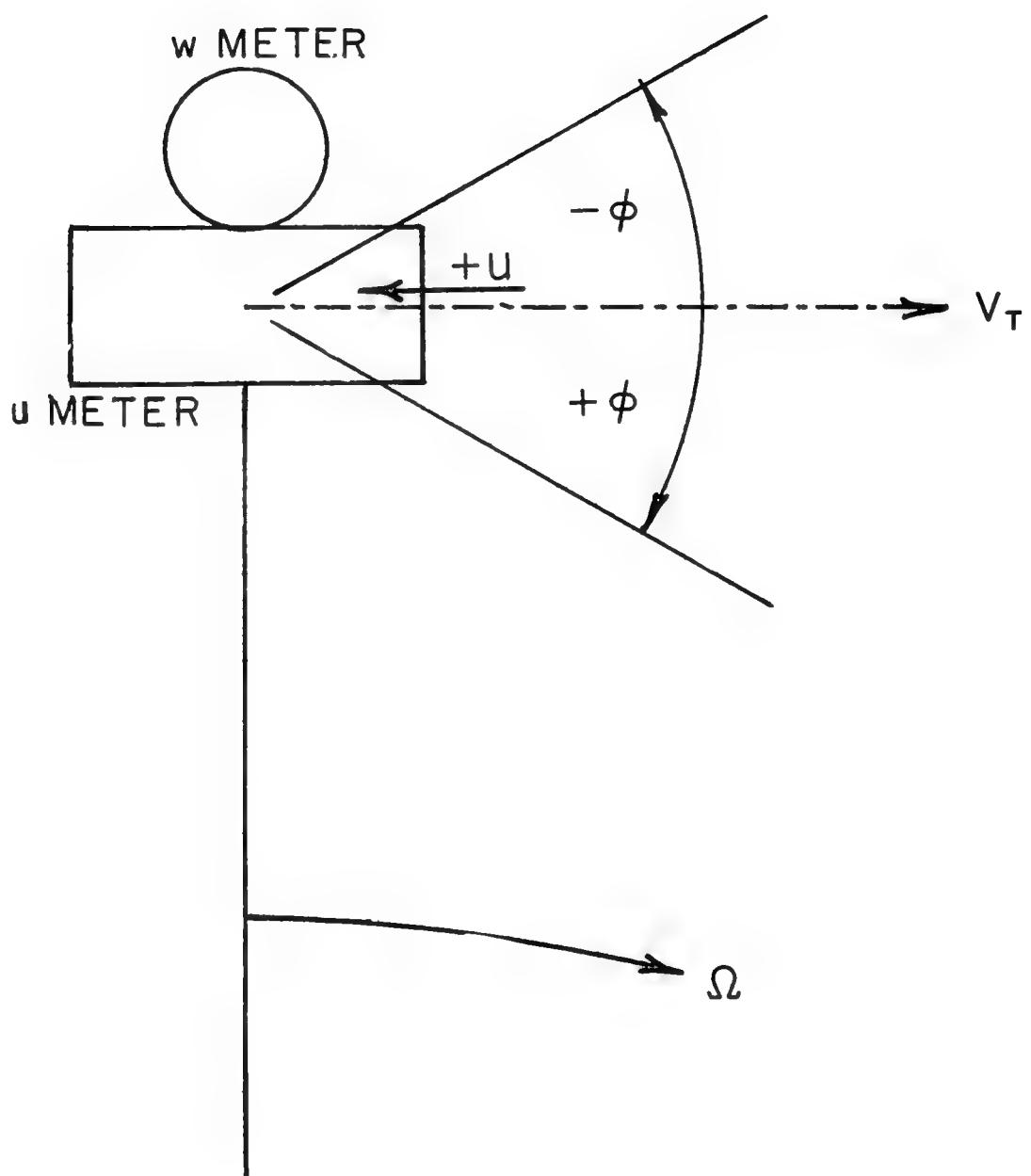
Orientation of OMDUM II System at End of Boom.

Figure II-11

cular f_V produced by the rectilinear flow at a velocity V_T making an angle ϕ with the u meter axis. The relationship in (II-16) can then be evaluated by defining the function given by:

$$R(\phi) = \frac{u(\phi)}{U_r \cos\phi} . \tag{II-17}$$

Thus, for an ideal response to the cosine law, $R(\phi) = $ constant $= 1.0$. This can be used to examine the calibration data given in appendix C. Values of $R(+\phi)$ and $R(-\phi)$ were calculated, and these values are plotted as a function of the towing speed V_t in figure II-12. Due to the closeness of the points in the lower plot, lines were not connected between data values.

There is a gross asymmetry of the response with respect to the sign of ϕ. For values below 40° both coefficients, $R(-\phi)$ and $R(\phi)$, are similar in their behavior. However, for values above 40° the $R(-\phi)$ deviates substantially from 1.0.

The flow at angles near 90° apparently tends to be unstable, resulting in a gross deviation from the cosine relation. At these high angles the tendency toward instability is understandably great because of the likelihood of vortex shedding at a leading edge of the cylinder. In general, the cosine relation seems to hold well for all values of ϕ except for large angles, as shown by the point at $+80^{\circ}$. Both sets of values show that $R(+\phi)$ and $R(-\phi)$ are essentially independent of the absolute towing velocity. There is a slight tendency to attain a maximum value of $R(\phi)$ between 40 and 60 cm sec^{-1}; otherwise, the values of $R(\phi)$ appear independent of V_t.

During all runs of the series, there was no visible response (i.e., no rotation) of the vertical w meter. Hence, any vortex shedding or other turbulent disturbance was not intense enough to affect the equilibrium of the perpendicular impeller.

The asymmetry of function $R(\phi)$ appears to be associated with the geometric asymmetry of the coupled cylinders, with respect to the rotation in the plane of ϕ. Fig. II-11 indicates that flow with a positive angle of attack $(+\phi)$ would encounter a somewhat different shade configuration than flow at a negative angle $(-\phi)$. This could give rise to the asymmetric calibration with respect to the $+\phi$ values. The exact interpretation of this dynamic asymmetry is obscure, and no effort was made to further examine this problem.

It was planned to calibrate the OMDUM II system in terms of its response to flow in the vertical or XZ plane. Unfortunately, this calibration could not be performed with the rotating boom system because of scheduling problems. Since work was proceeding on a new wave meter system (OMDUM III), no further calibrations were performed on OMDUM II.

The first series of wave measurements in the open ocean was made in May 1963 using OMDUM II suspended from the Buzzards Bay Entrance Light Station (BBELS). These preliminary observations (reported in detail as
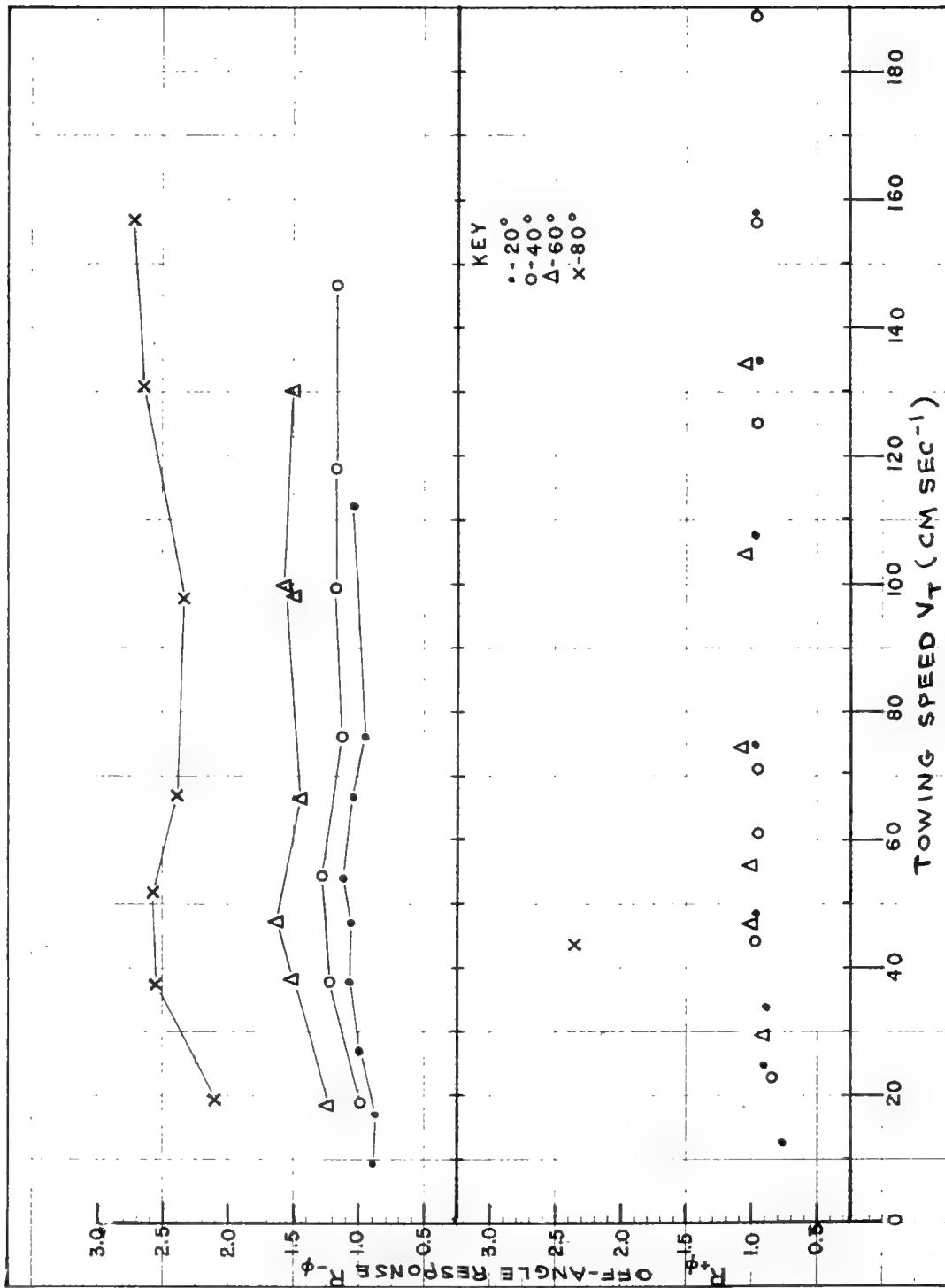
Values of R(+∅) and R(−∅) for Various Towing Speeds.

Figure II-12

BBELS 5 and 7, in chapter IV) were made using OMDUM II in the configuration shown in figure II-10. The purpose of the experiments was to evaluate the instrument response to motions occurring in the XZ plane or in the plane of the angle θ. Results were very encouraging, in that they seemed to produce a very realistic record of the wave oscillations.

However, the question of instrument response to variations of motion in the XZ plane had not been probed sufficiently. Data obtained from these preliminary experiments were therefore considered to be of questionable validity until further calibration experiments allowed proper interpretation.

What is the deviation from the cosine law for motion in XZ plane? Figure II-10 reveals a symmetry in the XZ plane; i.e., the vector rotating in the XZ plane experiences the same cross sectional area for a particular value of $+\theta$. Thus, $R(\theta)$ and $R(-\theta)$ should be identical and close enough to 1.0 so that the OMDUM II system can approximate the oscillatory motions of the waves.

The actual distortion of the wave motions in the XZ plane was further examined during the calibration of the OMDUM III system. Fortunately, the data obtained in BBELS 5 and 7 proved to be valuable for the overall studies.

The modification of the ducted meters, involving replacement of the iron slugs with heavier magnets, required that the response time of the new impeller configuration should be examined. Despite the modifications, it was still hoped that the response time of the impellers would be less than 0.1 second (or have an equivalent frequency response of more than 10 cps).

A simple experiment was performed by oscillating the OMDUM II system vertically in an acoustic test tank at NUWS. Specifically, the orthogonally coupled meter system was suspended with a heavy shock cord to a depth of about 30 cm in the center of the round acoustical test basin, which was about 4 meters deep. A waterproof accelerometer was fixed to the side of the vertical cylinder (w meter). The accelerometer (Model 4949 ASA a-20-2700, manufactured by Statham Laboratories, Los Angeles, California) was an internal strain gauge type, utilizing a balanced bridge system with a 34 volt DC input and a 0-3 volt DC output for moderate acceleration ranges.

The OMDUM II system (weighing about 3 kgm) was oscillated vertically, producing a quasi-simple harmonic motion. The amplitude and period of the oscillation were about 8 cm and 0.7 second, respectively.

The w channel output was recorded simultaneously with the accelerometer voltage. A sample of the two-channel record is shown in figure II-13. The accelerometer signal produced a well-defined sinusoidal trace. There was a slight DC drift and some evidence of 60-cycle pickup, but this did not affect the gross signal. The OMDUM II output voltage pulses (upper trace) oscillated at a frequency similar to that of the accelerometer.
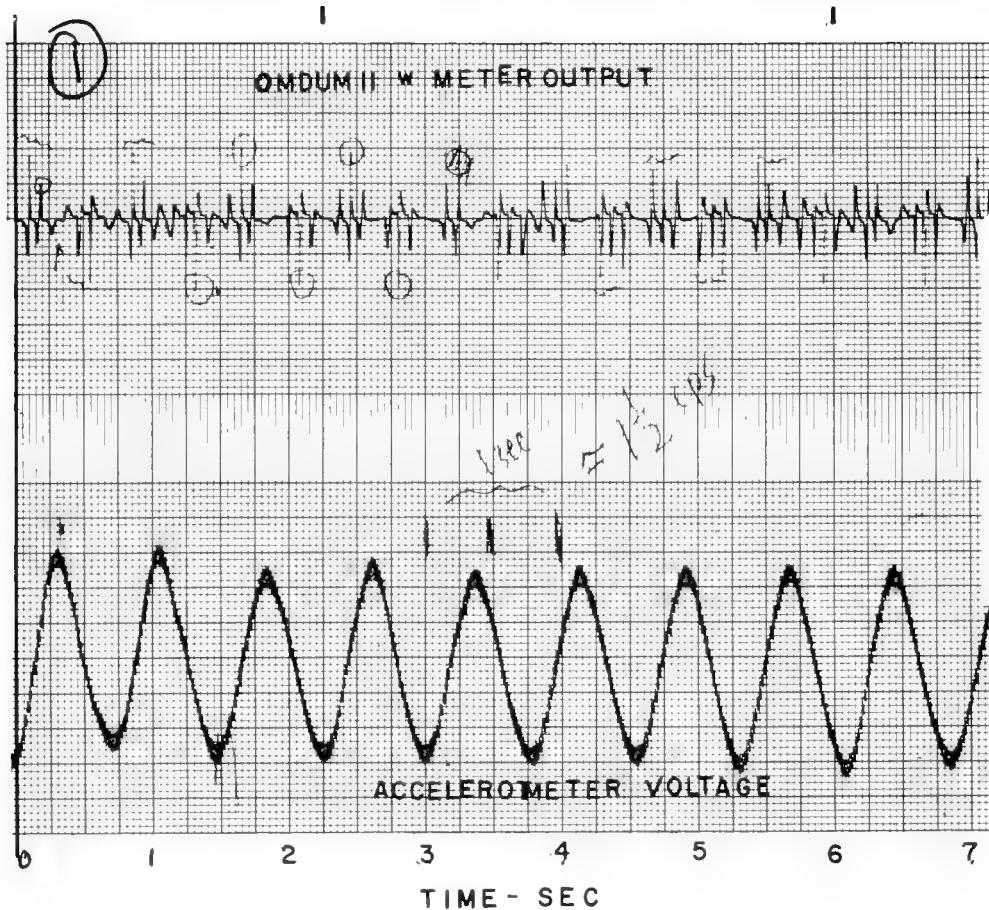
Strip Chart Record Showing Simultaneous Recording of
OMDUM II and Accelerometer Outputs

Figure II-13

By examining the wave meter output in terms of the indicated velocity with respect to the acceleration, one can determine any lag in the OMDUM II response, using the accelerometer trace as a comparison. This is valid because: (1) the time response of the accelerometer with its high impedence output is less than a millisecond and may thus be used as an absolute reference; and (2) the accelerometer trace, being the virtual derivative of the velocity function, can represent the relative velocity of the oscillated meter with a phase shift of 90°. Thus, the phase lag of the wave meter trace can be determined with respect to the absolute velocity of the system.

The voltage pulse data in the upper trace of figure II-13 was converted to velocity (the method used is described in detail in chapter III). For purposes of comparison, the data from both instruments were interpolated at 0.1-second intervals and plotted on the same time base. Figure II-14 is a segment of the processed record. Clearly, the accelerometer record (lower curve) appears to be approximately 90° out of phase with the OMDUM II velocity record (upper curve).

The interpolated time of zero crossings was used to indicate the mean phase difference of the two traces. From these two traces, the various statistical parameters listed in table II-3 were derived. The mean phase angle of the lag in the vertical velocity output with respect to the accelerometer trace is about 106° ± 12°.

TABLE II - 3. Results of OMDUM II Oscillation Test

	OMDUM II	Accelerometer
Number of consecutive oscillations	12	12
Time interval (sec)	9.40	9.40
Mean period (sec)	0.773	0.776
Standard deviation (sec)	0.029	0.017
Velocity amplitude (cm sec^{-1})	40	-

Mean phase angle $\Delta\phi$ between OMDUM II and accelerometer outputs determined from (a) zero crossings: $\Delta\phi = 106.8°$, with a standard deviation $\sigma_{\Delta\phi}$ of 12.1°; and (b) maximum and minimum values: $\Delta\phi = 106.2°$, with a standard deviation $\sigma_{\Delta\phi}$ of 11.6°.

A discussion of the theoretical phase angle relationship of a simple harmonic oscillator and its driving function is given in appendix A. If the OMDUM II wave meter is driven by an oscillatory wave motion u(t), then

$$u(t) = u_0 \cos \Omega t;$$

(II-18)
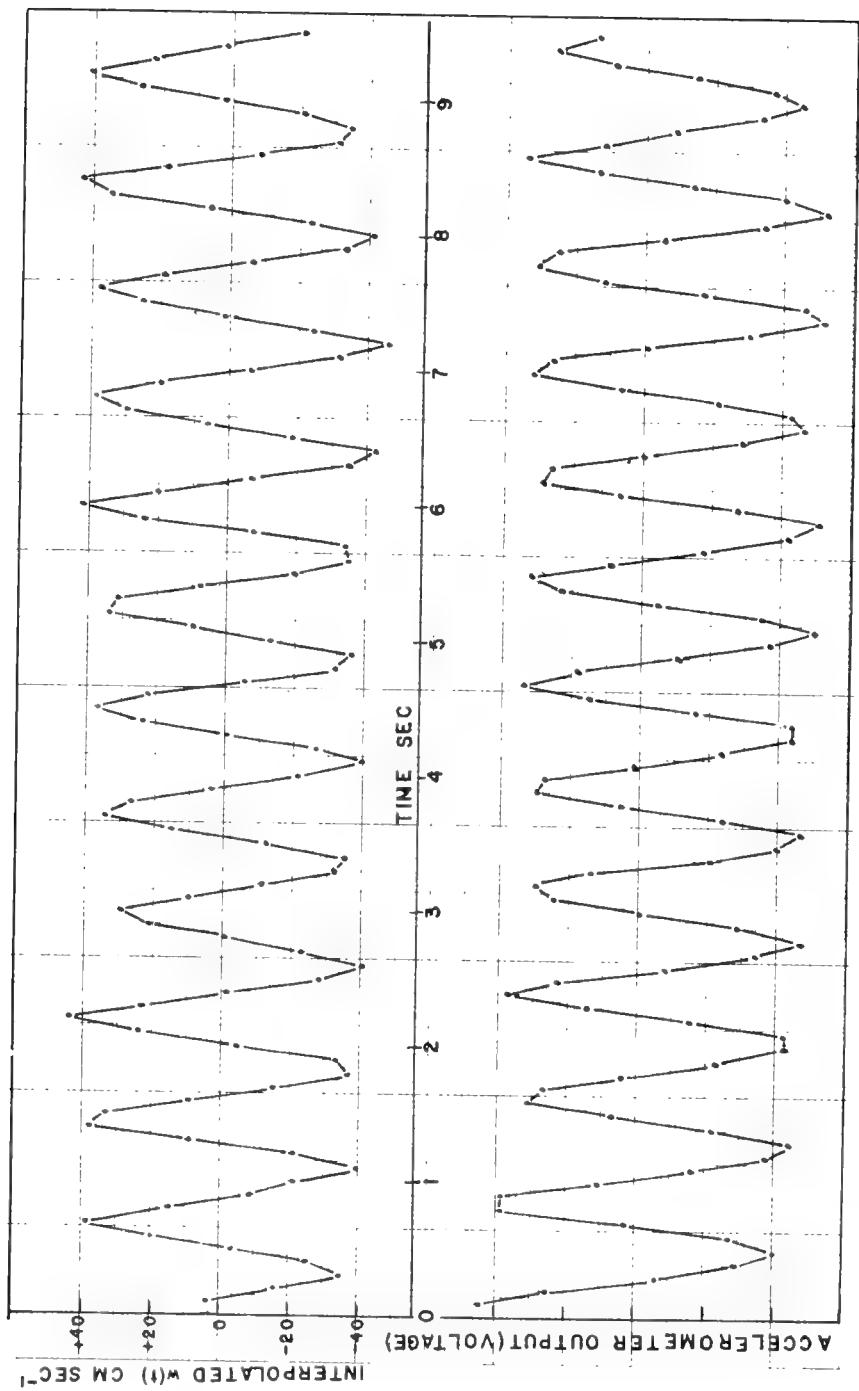
Interpolated Impeller Response Compared to Accelerometer Response

Figure II-14

where U_O is the amplitude K_2/I defined in appendix A, and Ω is the driving frequency. The phase lag of the detector is related to the driving frequency by the relation:

$$TAN \, \Delta\phi = \Omega \, T_R \, ;$$

where T_R is the response time of the instrument defined in appendix A.

Using the value for the phase lag given in table II-3, $\Delta\phi - 90^\circ = 16.2^\circ \pm (\sigma = 11.6^\circ)$. Solving for the response time using equation (A-20):

$$T_R = \frac{T_o \, TAN \, \Delta\phi}{2\pi} \, ; \qquad \text{(II-19)}$$

where T_0 is the period of the forced oscillation depicted in figure II-14. For the mean value of $\Delta\phi$ (16.2), T_R = 16 milliseconds. For the upper value of $\Delta\phi$ (27.8°), T_R = 65 milliseconds. For the lower value of $\Delta\phi$ (4.6°), T_R is about 9 milliseconds. Thus, the estimate for T_R is below 100 milliseconds, which is desirable for a wave meter designed to properly detect wind wave motion with a 3-5 second period.

This manual oscillation experiment was, at best, a very crude attempt to simulate oscillatory motion. Indeed, it is surprising how consistently the period of oscillation was reproduced. The large scatter in the standard deviation of the calculated phase angle lag is undoubtedly due to the interpolation error; i.e., the attempt to resolve small time lags with coursely interpolated data. However, this crude experiment did provide a good estimate of the response characteristics of the OMDUM II wave meter.

The most significant result of this oscillation experiment is that the instrument faithfully reproduced the quasi-simple harmonic motion with which it was driven. For all its axial asymmetries, the instrument produced no visible distortion of the motion while attaining a peak velocity of 40 cm sec^{-1}. Moreover, there was no evidence that the wave meter grossly interfered with its surrounding medium. As the instrument was oscillated in the tank, any turbulence or vortex shedding produced by the interaction of the meter with the fluid would most likely have intensified with time, since no advective processes existed in the tank to carry away the perturbations. However, no visible time variation in the velocity function was evident, and the motion appeared stationary. Any eddy disturbance caused by interaction of the oscillating wave meter with the fluid was of too high a frequency or wave number to interfere with the dominant motion sensed by the meter.

Small-Scale Ducted Meters (OMDUM III and LIMDUM I)

The cylindrical ducted meters used in the OMDUM I and II systems were used because of their availability. They proved useful as a prototype with which to evaluate this new concept of wave measurement. It was fairly evident that, although this system showed much potential, it could readily be improved upon. Hence, it was decided to design a new system containing the main characteristics of OMDUM I and II but with certain improvements.

Small Scale Orthogonally Mounted Ducted Meter System

Figure II-15

Design Characteristics -- The new system was designed to reduce the mean cross-sectional area and volume and to streamline the overall geometry. The aim was to decrease the form drag of the system and thereby reduce any tendency to interfere with the flow, both around and through the wave meter. Reduction in size would also enable the new wave meter to spatially resolve smaller scale orbital motions than those resolved with OMDUM I and II. Moreover, reduction in form drag would reduce the wave forces on the instrument when it was not rigidly suspended (as in measurements from Buzzards Bay Entrance Light Station), thus decreasing its tendency to swing.

An effort was made to further inhibit horizontal reaction to the wave motions by using a more efficient wire suspension system. The possibility of using the individual ducted cylinders to measure parallel velocity components in waves at two (or more) depths simultaneously was also examined. This would require a simple method of altering the geometric placement of the two meters with respect to one another.

Two new ducted meters were designed and fabricated to meet these goals. Figures II-15 and II-16 show the meters mounted in the orthogonal position (OMDUM III). The cylinders are constructed from bronze tubing 15.3 cm long, with an 8.8 cm outside diameter and a 0.2 cm wall thickness. Instead of the bulky pipe support and U-bolts used in the previous devices, the cylinders are held in the orthogonal configuration by a set of 1/2-inch bolts attached to a piece of flat brass stock 6 cm long, 10 cm wide, and about 0.4 cm thick. This flat plate is brazed tangent to each cylinder on the side opposite the pillboxes (see figure II-16). The bolts hold the two plates to a center plate which is, in turn, brazed at each end to a brass rod 2 cm in diameter. This rod is about 130 cm long and, as shown in figure II-15, has a large pad eye brazed onto each end.

The cylindrical housing, support braces, and shaft were fabricated at NUWS. The impellers and bearing mounts were built and installed by the Braincon Corp., Marion, Mass. The impellers are constructed of micarta, similar to the OMDUM I and II systems; however, they contain six blades. As in OMDUM II, small alnico magnets are potted into the blade tips. The pillboxes housing the induction coils are about 3.0 cm high and 3.5 cm in diameter. The miniature coils (similar to those used for OMDUM II) are oriented within the pillboxes so as to provide a signed voltage pulse unique to the sense of impeller rotation. The inductance of the coil is high enough to produce a pulse of about 45 millivolts when the impeller is spun at 10 cps (equivalent to 180 cm sec^{-1} for water flow).

Within the open-top pillboxes each output lead of the inductance coil is soldered to one end of a 30 cm long, single-pin, watertight connector (manufactured by Mecca Cable and Service, Inc., Houston, Texas). The solder joints are coiled in the pillbox, which is filled with expoxy resin (no. 5, manufactured by Minnesota Mining and Manufacturing Corp., Needham, Mass.). When potted, the resin forms a very strong and rigid watertight seal. The male ends of the connectors are led around the cylinder (figure II-16) and taped tightly to the support shaft.
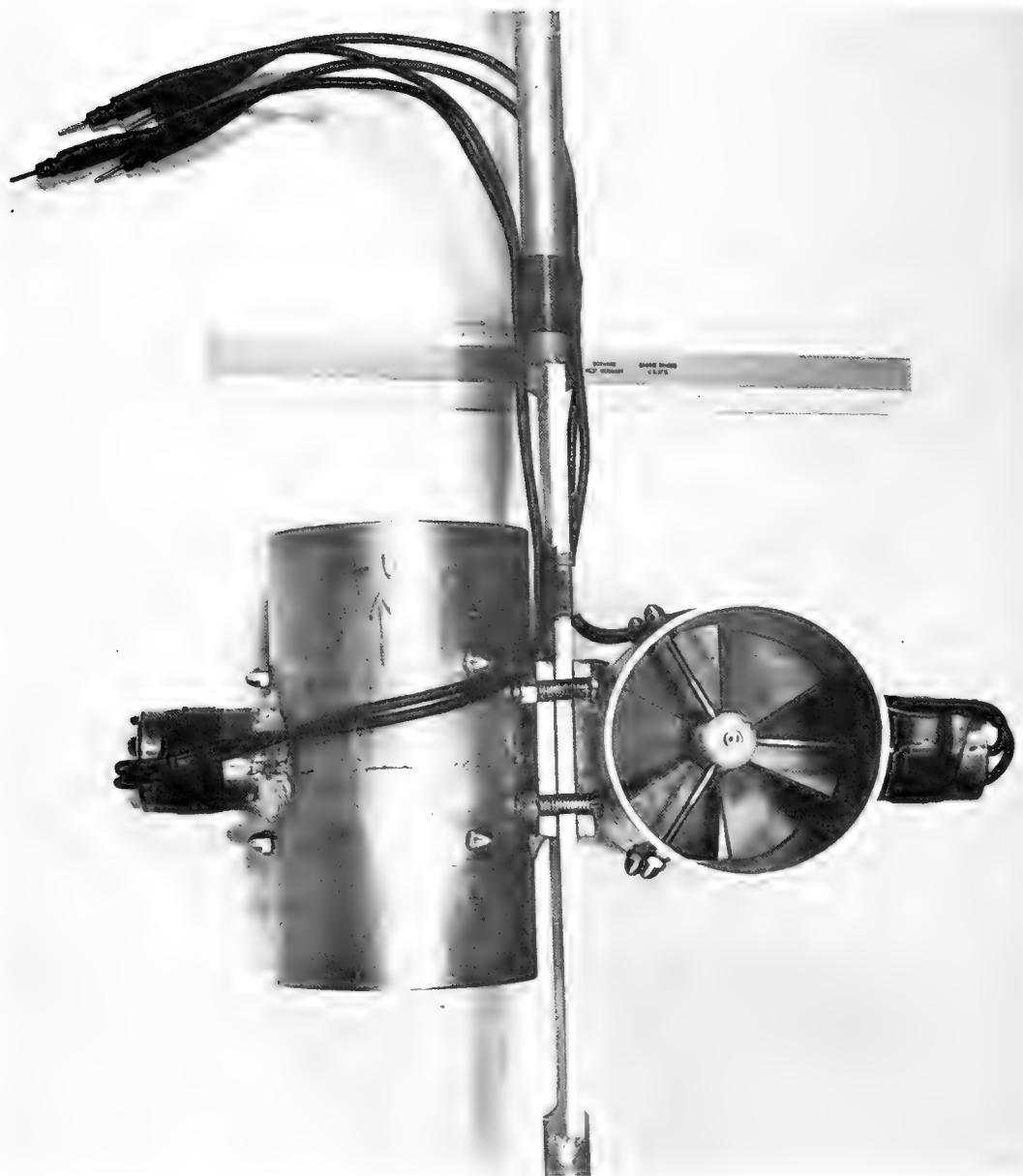
Closeup of Small Scale OMDUM System Showing Impeller Mounting

Figure II-16

Figure II-17 shows a second system configuration, in which the wave meters are spatially separated. The cylinders are mounted linearly so that their axes are either collinear in the vertical (as in figure II-17) or parallel in the horizontal. The spatial separation permits simultaneous measurement of the vertical or horizontal velocity component of flow at two different vertical levels. Mounted on a rigid brass rod 2 cm in diameter by means of stainless steel hose clamps, the cylinders can be separated up to 3 meters when the rod is suspended vertically. This configuration is termed the Linearly Mounted Ducted Meter System (LIMDUM I) because of the straight shaft suspension of the cylinders.

Since the modified smaller-scale ducted meters were, in a sense, an end product of the instrument development and of the knowledge gained in the study and use of the previous instruments, a very complete examination of the dynamic characteristics of the new meters is requisite.

Calibration -- The first calibration of the OMDUM II model was, at most, a rough estimation of the characteristic response. As noted earlier, the rotating arm system had certain limitations that prohibited precise determination of the reaction of the orthogonally mounted meters to the off-angle flow. The calibration data, however, did permit a fair interpretation of these preliminary measurements of wave motions (listed as BBELS 5 and 7 in appendix B).

For the OMDUM III system, which is a more precise instrument for measuring wave particle motions in the XZ plane, a more exacting calibration was required. System calibrations were made in the orthogonal configuration (OMDUM III) and also with the cylinders individually mounted in the ⋯ linear configuration (LIMDUM I).

Towing Tank and Associated Equipment. The new wave meters were calibrated in the Capt. Mary B. Converse Towing Tank in Marion, Mass. These experiments were made to determine system response to steady and accelerated rectilinear flow, both end-on and at various angles between the cylinder axis and the relative direction of towing.

The Converse Towing Tank is a privately owned installation. Calibration was therefore accomplished with the assistance of the Braincon Corporation of Marion, Mass. The tank is about 21 meters long, with a rectangular cross-section 71 cm wide and 66 cm deep. The towing carriage support for the individual and the coupled meters is shown in figures II-18 and II-19 respectively. The carriage is supported by a center beam upon which rubber caster wheels move. The carriage is towed by a 3/32-inch-diameter stainless steel aircraft cable, which is run through a shieve at each end of the tank. Thus, the carriage can be moved freely between the two shieves. The tight clearance of the wheel and shieve drive permits a minimum amount of free play in the track mount.

The power drive of the system is a 10 hp electro-hydraulic motor. A small pulley (10 cm diameter) on the motor shaft is connected by a rubber

33

Linearly Mounted Ducted Meter System
(Assembled for Measurement of Vertical Velocity Component)

Figure II-17
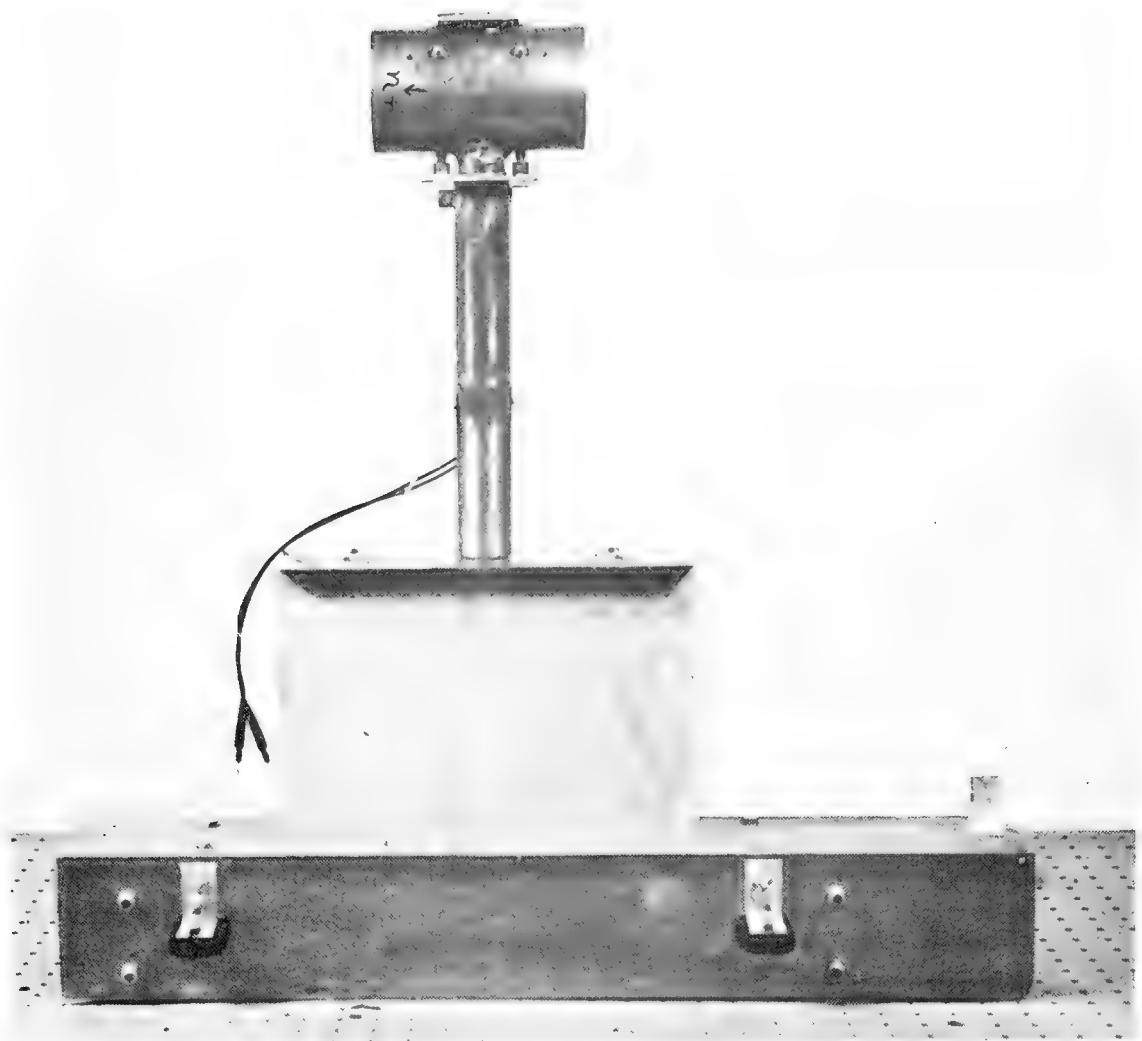
Towing Carriage (Inverted) Support for a Single   Ducted Meter

Figure II-18
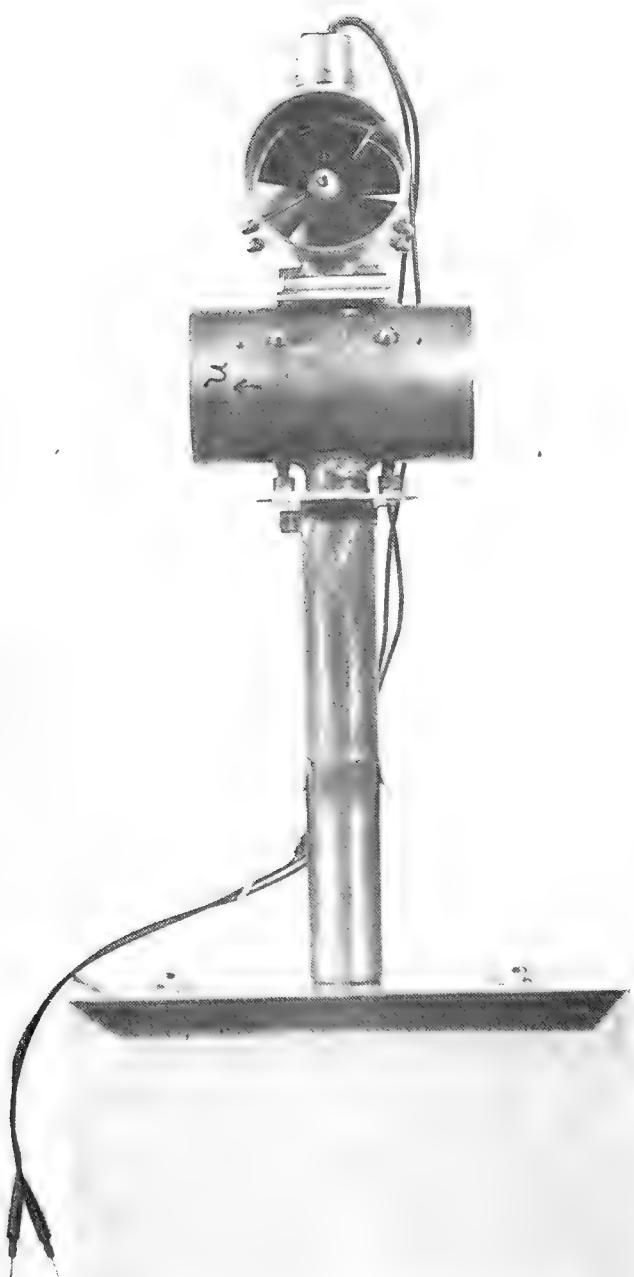
Support for Orthogonally Mounted Ducted Meters

Figure II-19

belt to the driving pulley on the north shieve axle. This driving system is so tight that there is no perceptable slippage or lag of the carriage and flow meter upon starting or stopping the carriage drive. Thus, with the greatly "over-powered" tow system, equilibrium speed was attained almost instantly, allowing for maximum time of steady flow calibration during a single trip. Also, the drive system could be run just as smoothly in the reverse direction. This permitted calibration runs to be made back and forth along the tank, simulating alternately positive and negative flow directions.

The most important aspect of the towing tank calibration was the requirement for precise monitoring of tow speeds. It was not possible to preset the tow speed closer than about 10 percent of the desired value because there was no precision setting or reference dial on the electro-hydraulic control valve. This had no effect, however, upon the constancy of the tow speed once the control valve had been set. Thus, although the preset tow speed for a particular run was only approximate, the resulting speed was monitored very accurately.

The tow rate was monitored by two independent methods. The first method involved sensing the rotation of the driving shieve mounted at the north end of the tank. A small alnico magnet was attached with epoxy cement to the outer rim of the driving shieve. As the shieve wheel rotated, the magnet repeatedly passed within 2 mm of a magnetic reed switch mounted adjacent to the shieve support. This closing switch was wired inseries with the remote marker input on a two-channel Sanborn strip chart recorder model 320 (figure II-20), which was also used for recording the output of the towed wave meters. The closing of the reed switch by the shieve magnet produced voltage spikes, which were recorded on the same strip chart as the wave meter system outputs. One revolution of the shieve represented a horizontal displacement L_s of the carriage of 44.60 cm. The space between two consecutive voltage peaks represented both a linear distance L_s (equal to the shieve circumference) and a known time interval T_s or strip chart length proportional to the chart speed used. Hence, the tow speed given by L_s/T_s was derived for incremental points during the individual run.

The second method of tow speed monitoring involved placement of a pair of micro-switches nearly equidistant from the center of the tank and separated by a measured distance of 629.9 cm. Connected to the tow carriage was a small plywood cam, which struck and closed upon each micro-switch button as the carriage rolled by. The first switch started a 1-second sweep electronic timer, and the closing of the second switch shut it off. The elapsed time for the carriage to travel the distance separating the two switches was read to the nearest 0.01 second. Thus, the average speed was obtained for the time of carriage travel between the two switch positions.

For the steady flow towing tests both methods of carriage speed monitoring were used. For acceleration tests the shieve rotation method was used because only an average value (which is meaningless for short accelerations) can be obtained by the consecutive micro-switching method.

Calibration Run at Converse Tow Tank Using Strip Chart Recorder

Figure II-20

During all of the towing experiments, the tank was filled with standard tap water at a temperature of about 16°C and having a density of 0.9989 gm cm⁻³.

Calibration of Individual Ducted Meters. The first towing tests were conducted to determine the response of the individual ducted meter to fluid flow simulated by various steady towing speeds. Of particular interest is the difference in impeller response for forward and backward motion through the cylinder, and also the differences in calibration between the two meters.

The individual ducted meter was mounted on the tow carriage as shown in figure II-18. The meter was mounted on a brass pipe (shown in the inverted position) upon which was fixed a circular disc inscribed with angular marks at 5-degree increments. The pillbox containing the potted induction coil was locked with screws into the center hole of the angle-measuring disc. The cylinder and disc could be rotated about 360° with respect to the towing direction marker fixed rigidly to the suspension column. This column was braced to a heavy plywood support, which in turn was bolted to the towing carriage. The two Mecca connector cables were led from the pillbox into the support column and out through a hole near the base. During the towing these signal leads were connected to a 20-meter length of "shielded pair" which led to the recorder. This long connecting lead was then strung the length of the tank so that it could easily follow as the carriage was driven back and forth.

The first series of tests involved the towing of each meter (mounted individually) at various steady speeds. The cylinder axis was parallel to the towing axis of the tank. Runs of the carriage were made in both directions along the tank, simulating positive and negative flows.

The results of the steady towing tests are depicted in figure II-21. The curve (dots) shows the frequency of voltage pulses f_v in cps versus the towing speed in cm sec⁻¹ for the individually mounted meters. The range of tow speeds was from 6.7 cm sec⁻¹ through 210.8 cm sec⁻¹ (not shown in figure II-21). A complete tabulation of the experimental data is given in appendix B.

In figure II-21 it is difficult, if not impossible, to distinguish between points derived from "down tank" runs and those derived from "up tank" runs. It is also difficult to distinguish between points from each of the two meters. The tightness and linearity of the curve establish the similarity in response of the two meters.

An attempt was made to determine the minimum tow speed at which the impeller responds. This threshold speed was found to be between 6.6 and 7.5 cm sec⁻¹ (in either direction) for both meters.

In the upper range of speeds, the impellers appeared to respond in the same linear fashion. There was no indication of an abrupt change in the shape of the curve (even for speeds as high as 140-160 cm sec⁻¹), indicating a marked stability over the range of speeds tested. At the extreme high speeds, the meter produced visible surface "bow" waves as it was towed
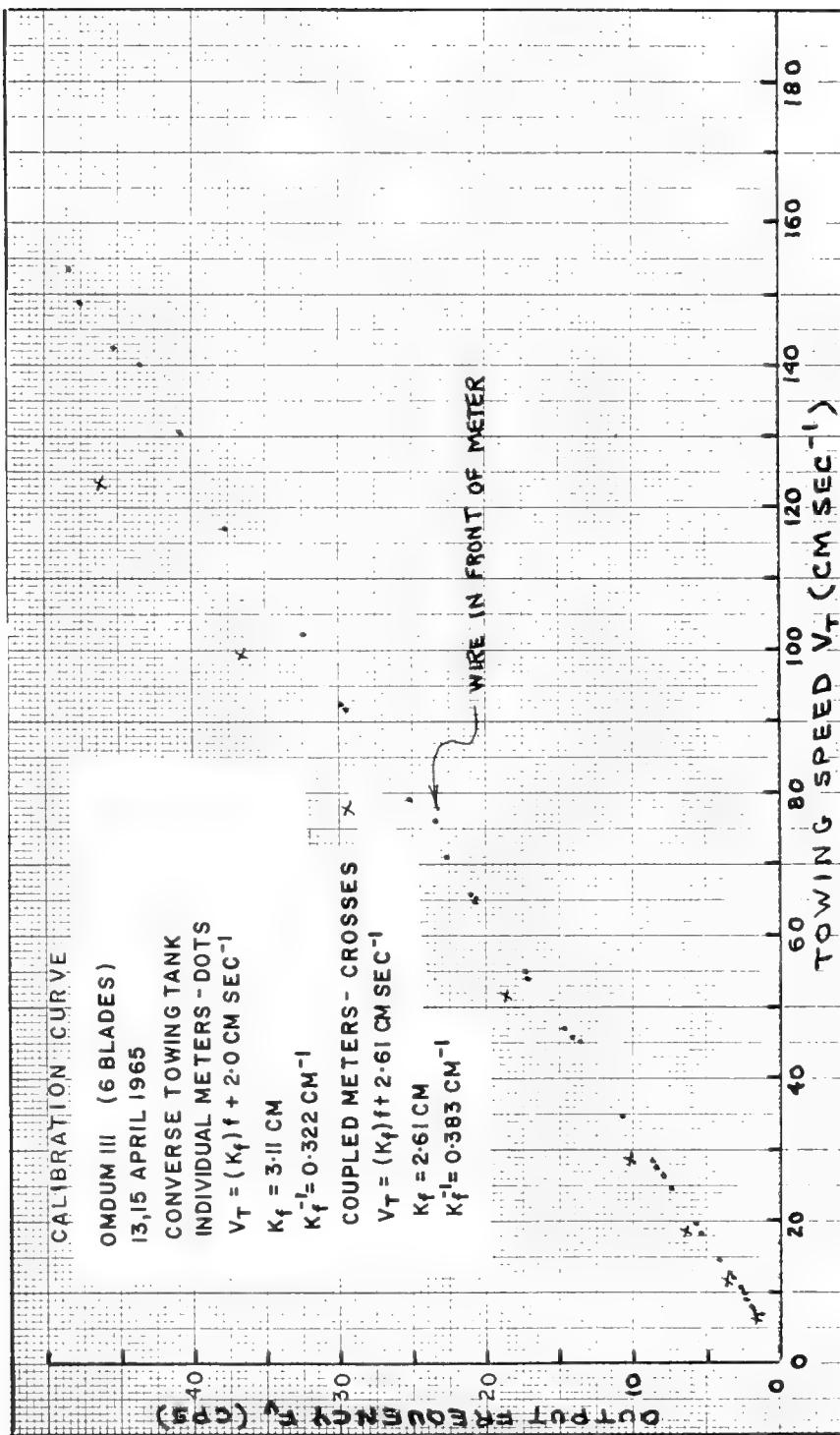
Calibration Results of End-On Towing Tests with Individual and Coupled Meters.

Figure II-21

through the water. The high speed runs had to be spaced at least a minute apart to allow the free surface to approach equilibrium.

Instrument Response to Off-Angle Flow. Ideally, the response of the ducted meter should follow the cosine law; i.e., it should be proportional to the cosine of the angle θ between the line of fluid flow and the axis of the meter. The rotating arm towing tests (OMDUM II) indicated that the cosine law was only approximated by the response of the ducted meter system. The deviation from the cosine law was assessed by towing each of the single meters at various speeds and at various angles of θ. The results of this test are depicted in the upper curve in figure II-22. This plot shows R_θ (defined as $R(\emptyset)$ in equation (II-17)) as the ratio of the detected velocity to the product of the tow velocity V_T and cos θ.

Recall that the detected velocity corresponds to the velocity-pulse period calibration for zero angle. The ratio R_θ would therefore be unity if the meter response obeyed the cosine law. The numbers next to the plotted points denote the number of data points obtained for each value of θ. The vertical bars represent the two sigma width (σ = standard deviation). The data points were obtained over a wide range of tow speeds and at a full range of values for θ. A complete listing of the experimental data is given in appendix B.

Values of R_θ for $\theta > 80°$ were not obtained because (as with the OMDUM II calibrations) the impeller response tended to become unstable as θ approached $90°$. The meter response at $90°$ for speeds below 175 cm sec^{-1} corresponded to zero flow, indicating a certain degree of stability in the flow around the cylinder. At speeds over 200 cm sec^{-1}, a slight oscillation in the impeller was noted. Part of this effect was probably caused by an inability to position the cylinder axis closer than 2 or 3° normal to the line of flow. Thus, the meter detected a slight net flow through the cylinder, which must have been accompanied by vortex shedding at this angle from the flow.

The deviation from the cosine law is indicated in figure II-22 by the increasing value of R_θ with increases in θ. The dynamics of the flow about the cylinder caused it to indicate a higher rate of flow than would be defined by the cosine law. Whether this was due to a higher relative volume of flow or to a greater impeller sensitivity at off-angle flow is not immediately obvious.

Figure II-22 shows that the R_θ can be used as a correction factor for determining the actual fluid flow at different angles of θ. As demonstrated later, the angle θ can be determined uniquely from the observed outputs of two orthogonally mounted meters. With a single cylinder suspended in the water, one cannot, of course, determine θ. However, if a single cylinder is immersed in a flow environment consisting of orbital oscillations (as beneath the ocean waves), then the average error of measurement of an oscillating velocity vector can be obtained by averaging the ratio R_θ over the total excursion of the motions (2π radians). This error value appears to be about 10-12 percent except for incidence angles near $90°$.
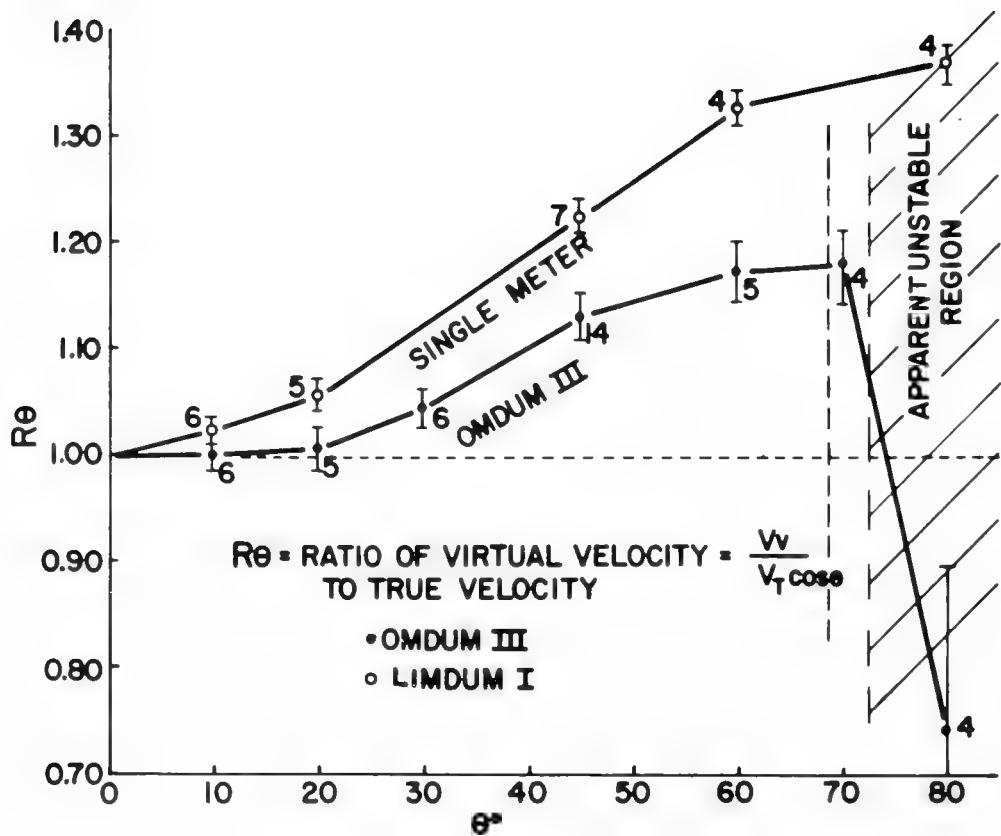
Variation of R_Θ as a Function of Θ for Single Meter and OMDUM III.

Figure II-22

Calibration of the OMDUM III System. The calibration procedures for the orthogonally mounted ducted meter system (OMDUM III) in the Converse Towing Tank were similar to those used for the individually mounted ducted meters. A series of tests was made to obtain the response of each cylinder in the coupled position at various speeds for end-on flow. Then the system was towed at various constant speeds and at various angles of θ as depicted in figure II-10. Finally, both procedures were repeated under acceleration and deceleration of the towing carriage.

Results of steady towing at various speeds with $\theta = 0$ are shown in figure II-21 (crosses). The slope of the curve for the orthogonally mounted system is distinctly greater than that obtained for the individually mounted meters. The slope of the upper plot (OMDUM III) is about 0.383 cm^{-1}, whereas the slope of the curve for the individual meters is 0.322 cm^{-1}. The geometric configuration of the orthogonally mounted meters affects the flow through the forward looking impeller so as to render the impeller more responsive or more efficient. This is due to a greater impeller angular velocity per unit flow speed than with the single ducted meter.

This modified wave meter was designed to obtain precise knowledge of system response characteristics as a function of off-angle flow, and to determine how off-angle response varies with the absolute speed of flow. This information is particularly critical for the orthogonal meters because covariance functions between the horizontal and vertical velocities within ocean waves must be estimated. Since the covariance function is derived by averaging the products of pairs of velocity values, it would be a severe handicap to have to contend with products of data values containing errors; e.g., a 10 percent error in the speed value of the velocity components could give a 20 percent error in the covariance functions.

The tests to determine the response to off-angle flow were similar to those made with the individually mounted cylinders. Runs were made at various steady speeds to measure the response of each meter as a function of θ. Again the results were evaluated on a basis of how closely the output of the OMDUM system compared to the actual tow speed. This is shown in figure II-23 where R_S is the ratio of the flow velocity detected by the wave meter to the actual tow speed. The numerator of R_S is the square root of the sum of the squares of the values of u and w obtained at various angles of θ with respect to the fluid flow. (Velocity outputs were transformed into speeds using the OMDUM III calibration curve in figure II-21.) The average value of R_S is 1.069 ($\pm$ $\sigma = 0.055$). It is clear that the error in the calculated flow velocity (i.e., the velocity appearing in the denominator of R_S) is essentially independent of the actual value of the speed.

The lower curve (OMDUM III) in figure II-22 shows that between 0° and 25° the OMDUM III system deviates only slightly from a value of unity, as contrasted with the single meter curve. This deviation increases gradually to a value of about 1.17 for $\theta = 70^o$. Between 70° and 90° there is a region of apparent instability where the value of R_θ becomes erratic. This same phenomenon of gross deviation from the cosine law was displayed in the rotating boom calibration of OMDUM II.

RATIO OF DETECTED VELOCITY (DERIVED FROM ZERO ANGLE CALIBRATION) TO ACTUAL TOWING SPEED

$$R_\sigma = \frac{[U_V^2 + W_V^2]^{1/2}}{V_T}$$

- $\theta_W = 10°$ △ $\theta_W = 45°$
○ $\theta_W = 20°$ □ $\theta_W = 60°$
◇ $\theta_W = 80°$

$\overline{R} = 1.069 \pm \sigma = 0.055$
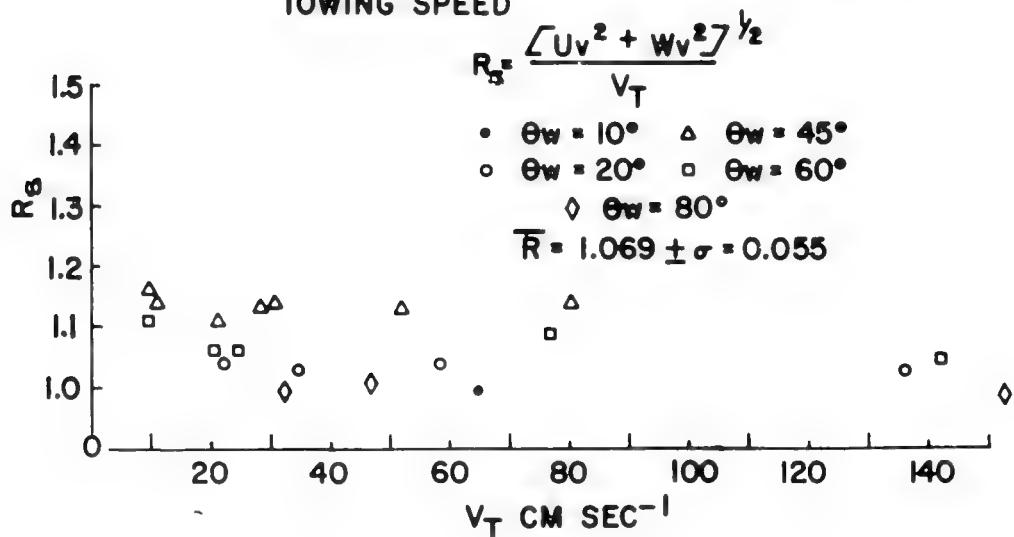
Ratio of Derived Velocities to True Towing Velocity

Figure II-23

The instability between 70° and 90° is probably caused by the gross drag--the boundary effect around the cylinder that is normal to the flow or towing direction. The horizontal projected area of the cylinder is about 180 cm^2. This drag inducing area is, of course, absent in the single meter system. As with the single meter, at $\theta = 90^\circ$ no output was sensed except for a slight wobble occurring at speeds greater than 180 cm sec^{-1}.

These calibration tests showed that the average error of measurement of a sinusoidally oscillating vector, using the OMDUM III device in a two-dimensional flow field (in the XZ plane), is of the order of 7-12 percent.

Error Correction for OMDUM III. Since the ducted meter system produces a bias in the measurement of current speeds at various angles with respect to the meter axes, an attempt was made to devise a method of correction. The approximate error in the velocity components was determined to be a function of the angle θ. Now, if θ is known, the value of R_θ can be applied as a correction coefficient to the velocity value obtained from the zero angle calibration curve. This is, of course, predicated on the assumption that, for a particular ratio of the outputs of the u and w meters, there is a unique value of θ; i.e., that the relative magnitudes of the two orthogonal velocity components determine a unique θ.

For example, examine the relationship of the ratio of the detected horizontal velocity to the detected vertical velocity as a function of the angle θ (defined as the angle made by the axis of the w meter with respect to the flow). The relationship is shown in figure II-24 (dashed curve). The numbers and the vertical bars adjacent to the points refer to the number of data points and to the two sigma spread, respectively. These data points are the result of tests at steady tow speeds and at various values of θw. The curve is very similar to the tangent θ curve (dotted line). The greatest deviation occurs beyond 80°, which is, of course, where the greatest error occurs in the determination of the w component. (This corresponds to the unstable region of the error curve shown in figure II-22). The similarity of the ratio curve to the tangent curve is easily explained if the two speed components are considered as approximately following the cosine law. In this case:

$$w = |\mathbf{V}| \cos \theta , \qquad\qquad\qquad (II-20)$$

and
$$u = |\mathbf{V}| \cos (90-\theta) = |\mathbf{V}| \sin \theta . \qquad\qquad (II-21)$$

Thus, $u/w = \tan \theta .$ $\qquad\qquad\qquad\qquad\qquad\qquad (II-22)$

The question arises about the possible dependence of the ratio u/w upon the flow speed; also about the possible effects of accelerative flow on this relation. Figure II-25 shows a plot of the ratio u/w as a function of the angle θ and of the tow speed. The abcissa is the tow speed in cm sec^{-1}, and the ordinate is the numerical value of the ratio u/w plotted on a logarithmic scale for convenience. The crosses along the ordinate axis indicate the ratios determined under steady towing conditions. These

RATIO U/W AS A FUNCTION
OF ΘW FOR STEADY
TOWING SPEEDS

- - - - ACTUAL U/W
.... TAN Θ
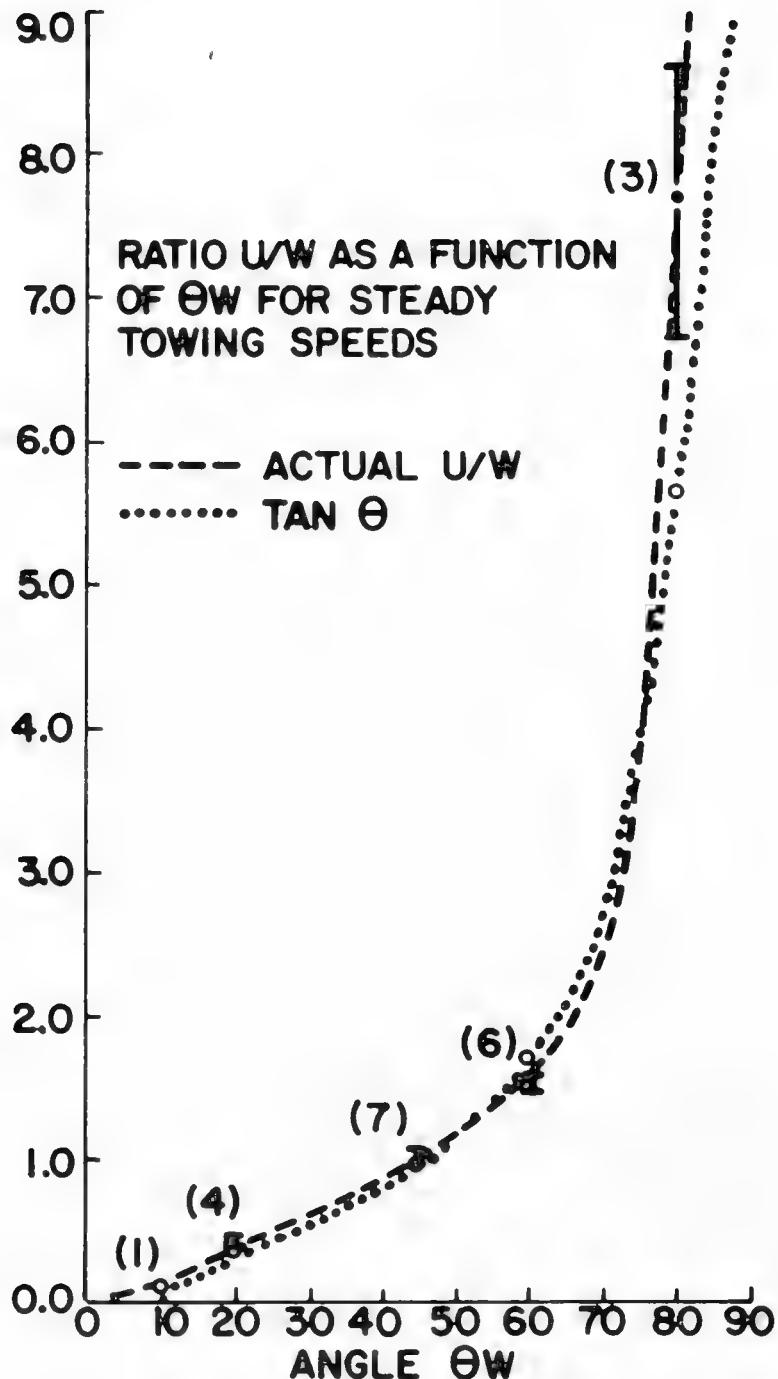
Ratio of Horizontal to Vertical Velocities (Uncorrected) as a Function of θ_w
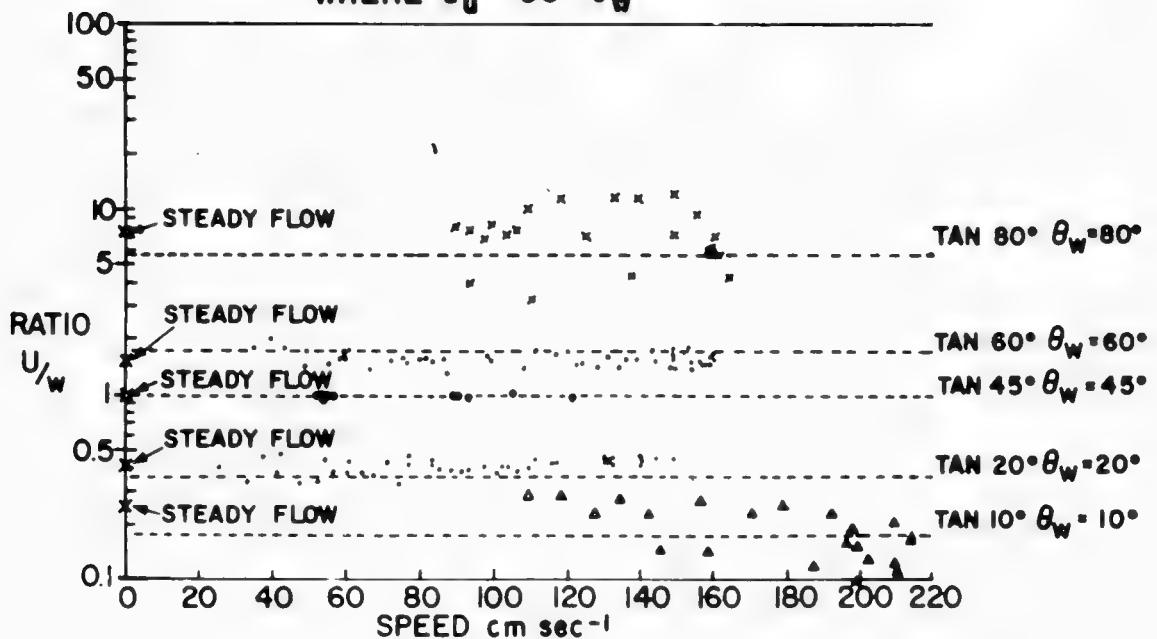
Figure II-24

Velocity Ratios at Various Tow Speeds and Angles of θ_w
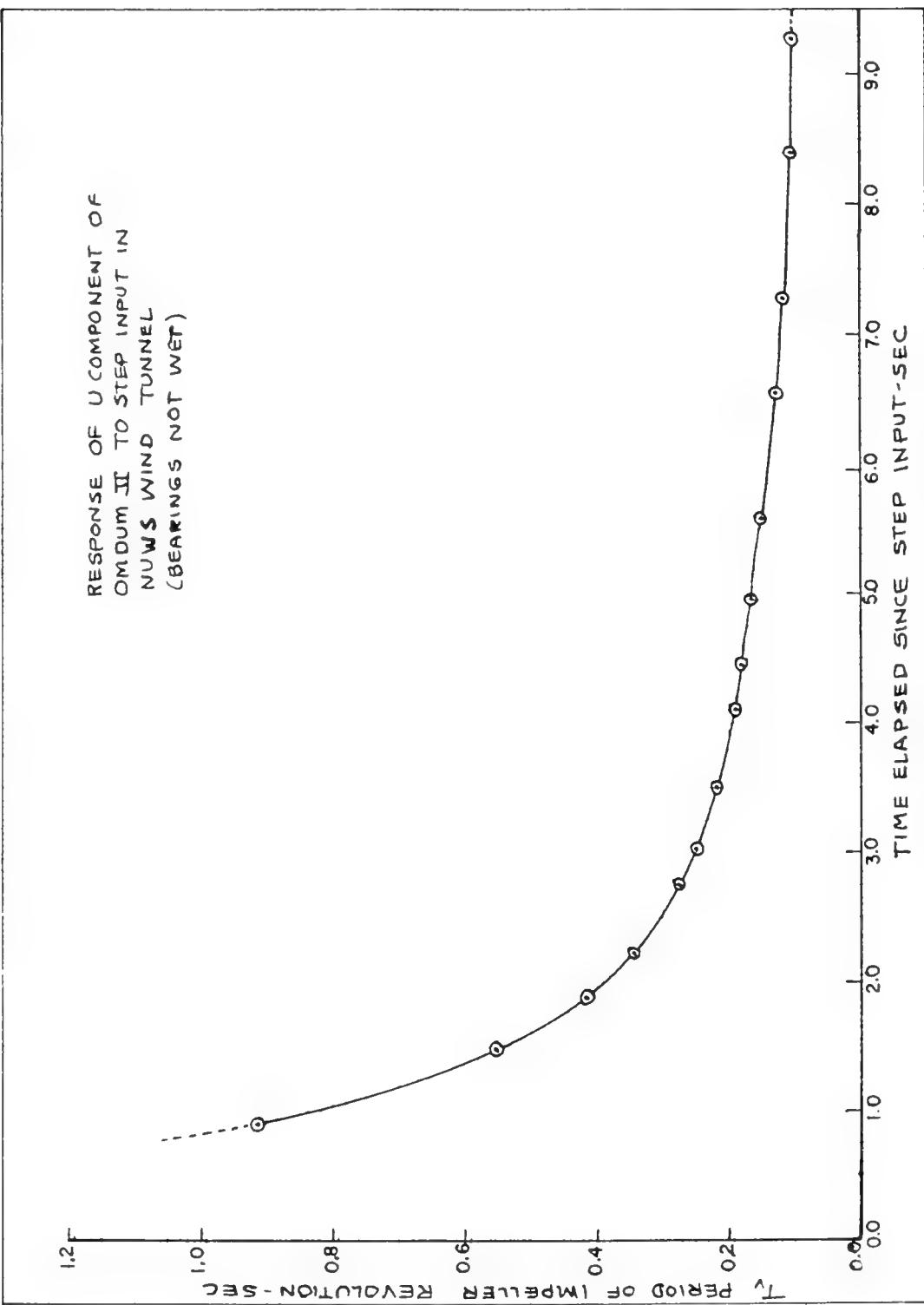
Figure II-25

Acceleration Response of Ducted Meter to a Stepped Velocity Input

Figure II-26

ratios are plotted in figure II-24. The horizontal dashed lines represent the tangents of the various angles shown on the right hand side of the figure; the values are read off the ordinate axis. The points clustered about each tangent line are actual data points taken from a series of acceleration tests. Since the ordinate is logarithmic, the spread of data points, with the exception of $\theta = 80^\circ$, is relatively small. Note, in particular, that there is no apparent variation of the ratio with tow speed.

Thus, the ratio u/w is essentially independent of the absolute speed of the velocity vector in the plane of the u and w meter. By determining the value of θ from the ratio and applying a correction to each of the velocity components, one can obtain an estimate of the error of u as a function of θ and of w as a function of $90^\circ - \theta$ (and vice-versa). The method of correction of the OMDUM III data output is discussed in the section on data processing in chapter III.

Estimation of Response Time. The response time of the OMDUM III system was estimated using the 1.5-meter-diameter wind tunnel in the NUWS hydro-dynamic laboratory. The system was mounted with the u meter axis centered in the tunnel and parallel to the air flow. The tunnel fan was driven to provide a steady flow at about 200 cm sec^{-1}. A square of cardboard was held flush to the upwind u meter cylinder, blocking out all air flow. The cardboard was removed smartly, and the impeller output registered on a strip chart recorder.

Figure II-26 is a plot of the time between every sixth voltage pulse (which is equivalent to the period of revolution for the six bladed impeller) as a function of time after the cardboard was removed. The period calculated occurs at the mid-point between each sixth pulse. For the first few pulses the curve is somewhat distorted because the period is changing exponentially with time. However, at the outer end of the curve, the rapidity of the points gives a more realistic value of the period of rotation as a function of time.

The curve in figure II-26 is easily shown to be exponential. It can be represented by the equation:

$$f(t) = \left[f(\infty) \right] \left[1 - e^{-\frac{\kappa}{I} t} \right] ; \tag{II-23}$$

where the frequency function is

$$f = T^{-1} \tag{II-24}$$

and $f(\infty)$ is the frequency attained by the impeller when it has come to equilibrium with the steady air flow.

Using the curve in figure II-26, $f(\infty) \sim 9.62$ cps, and the time consant in air T_A is about 3.5 seconds. This time constant can be measured directly

from the impeller frequency-time plot as the time required to reach about
63 percent of the final frequency value. Four estimates were made of the
time constant, involving both directions of the u and w meters. The results
were essentially identical.

The impeller bearings were dry during the wind tunnel test. This may
result in an added frictional drag, tending to lengthen the response time.
The impellers in water are constantly lubricated, which certainly contri-
butes to their overall sensitivity to oscillatory flow.

The dynamic response time of the impeller system in sea water (desig-
nated by T_W) can be estimated by utilizing a principle of dynamic simi-
larity. The time constant T_r is given in appendix B as:

$$T_r = \frac{I}{K_1} \; ; \tag{A-12}$$

where I is the moment of inertia, and K_1 is the constant of proportionality
relating resistance to the drag forces that oppose the driving force produced
by the fluid velocity u.

The law of dynamic similitude can be used to estimate the value of T_W.
Since the moment of inertia I of the impeller is independent of its sur-
rounding medium, equation (A-12) can be rewritten:

$$T_W \, K_W = T_A \, K_A \; ;$$
$$\text{or} \quad T_W = T_A \, K_A / K_W \; ; \tag{II-25}$$

where the subscripts W and A represent the water and air media. The next
problem is to determine the ratio of the constants K_A/K_W. Since the K's
are, in a sense, drag coefficients of the impeller, they are related to the
impeller interaction with the fluid medium. They should be a function,
therefore, of the fluid density ρ, the kinematic viscosity μ, and a
dimensional scale λ. Setting K_A equal to a function of density ρ, some
scale factor λ associated with the impeller dimensions, and the dynamic
viscosity $\eta (= \rho\mu)$, and using methods of dimensional analysis (see
Bridgeman, 1956):

$$K = Q \, \rho^A \eta^B \lambda^C \; ; \tag{II-26}$$

where Q is a dimensionless constant. Since the units of K are $M \, L^2 \, T^{-1}$
(where M = mass, L = length, and T = time), the exponents A, B, and C can
be evaluated:

$$K = Q \, \rho^0 \eta^1 \lambda^3 = Q \eta \lambda^3 \; . \tag{II-27}$$

The ratio of the values K for air and sea water (K_A/K_W), which is needed
to solve for T_W in equation II-25, is given by:

$$\frac{K_A}{K_W} = K_r = \frac{\eta_A}{\eta_W} \, . \tag{II-28}$$

The ratios of λ^3 divide out, since the same impeller is used in both air and water. Thus:

$$T_r(\omega) = K_r = \frac{\eta_A}{\eta_W} \, . \tag{II-29}$$

For air at 20° C, $\eta_A = 1.83 \times 10^{-4}$ poises. For sea water at 15° C, $\eta_W = 1.00 \times 10^{-2}$ poises. Thus, for a time constant of 3.5 seconds in air, equation II-29 becomes $T_r(W) \sim 64$ milliseconds. Five estimates were made of the impeller time constants, involving response of the u and w meters to flow in both directions. The results are tabulated in table II-4.

Table II-4.   OMDUM III Response Time, Evaluation From Wind Tunnel Tests

Meter and Direction	Air Speed (cm sec^{-1})	$T_r(A)$ (ms)	$T_r(W)$ (ms)
+ u	500	3500	64.0
+ u	500	4340	79.4
- u	500	3680	67.4
+ w	500	2860	52.2
- w	500	3800	69.5

Average value $T_r(W)$ = 66.5 ms.
Standard deviation $\sigma_{T_r} = \pm$ 8.9 ms.

These values seem reasonable in view of the previous estimates of T_W for OMDUM I and II, and are well within the desired range for measurements of ocean wave oscillations.

Amplitude of Induced Voltage as an Analog of Flow. Turning again to the principle of the voltage output of the wave meters, let ϕ_M be the number of lines of magnetic flux per unit area emanating from each magnet inbedded in the impeller blade of a wave meter. If the miniature coil of the meter contains N turns, then the voltage pulse generated by the magnet passing the potted coil is (according to Faraday's law):

$$E(t) = N \frac{d\phi_M}{dt} \tag{II-30}$$

In other words, the instantaneous voltage generated is proportional to the rate at which the magnet passes the coil. This rate, in turn, is proportional to the angular velocity of the impeller $\omega(t)$. Thus:

$$E(t) = K_P\, \omega(t) \; ; \qquad\qquad \text{(II-31)}$$

where K_P is a proportionality constant.

The individual voltage traces in figure II-7 show sinusoidal-like pulses and not really sharp spikes. This is due to the induction factor $d\phi_m/dt$ which varies with time as the magnet approaches, passes, and moves away from the fixed coil. In other words, the closer the magnet approaches, the more lines of magnetic flux cut per unit area per unit time. Thus, for each passage of a coil by the magnet, a voltage peak always occurs having a sign associated with the sense of w.

The peak or maximum value of $E(t)$ (designated by E_M) can therefore be used to estimate the instantaneous value of $\omega(t)$:

$$\omega(t) = K'\, E_M(t) \; ; \qquad\qquad \text{(II-32)}$$

where $K' = K^{-1}$.

The amplitude of the voltage (either positive or negative) can supply a velocity value for the time of occurrence of the peak (see figure II-7). This is, in fact, an amplitude modulated vector. Measuring the frequency and the amplitude of the voltage passes with time, thus provides two indicators of the direction and magnitude of flow through the impellers.

Further mention of the use of the voltage amplitude modulation to portray wave motions is made in chapter V.

Summary of Dynamic Characteristics of the Wave Meters

Various tests and calibrations were made, including steady state towing at various angles with respect to flow direction, and accelerative and oscillatory tests. The following summary of the characteristics of the wave meters is based on results of these tests and calibrations. (Table II-5 lists some of the more important system characteristics.)

1. The ducted meters have a linear response for impeller rotation frequency with speed of flow up to at least 200 cm sec^{-1}.

2. The impeller response time is about 65 milleseconds.

3. The impeller system is simple in geometry and easy to build. Hence, it can be fabricated to give essentially identical calibrations.

4. The electronics (consisting of magnets and a coil) are the antithesis of the very expensive and complex photographic or digitizing electronics used with Savonius rotor systems. The system is free flooding, requiring no pressure case or protected electronics. No power is needed and no pre-amplification is required prior to the strip chart recording of the signal.

TABLE II-5

SUMMARY OF WAVE METER CHARACTERISTICS

Wave Meter	Velocity Components Sensed	Threshold Velocity (cm sec^{-1})	Impeller Freq Response with Velocity	Upper Velocity Limit (cm sec^{-1})	Response Time (ms)	Variance Error in Angular Response
OMDUM I		4	Linear	300-400	16-30	
OMDUM II	Two orthogonal velocity components measured simultaneously at a single depth.	5	Linear	200	16-30	20%
OMDUM III		5-7	Linear	150	~65	(20% correctable to less than 5%)
LIMDUM I	Two similar velocity components measured simultaneously at two depths.	5-7	Linear	150	~65	10-12%

5. The off-angle calibrations indicate that two orthogonally mounted meters can detect flow (in the plane determined by the axes of the impellers) to within 10-12 percent of the true velocity. The error, which is positive, can be corrected by using an empirically determined relationship in which the error is a function of the angle subtended by the current vector and the cylinder axis. This error relationship is independent of the absolute speed of the current.

There are, however, complex interactions between wave meters and ocean wave motions which can be better judged on the basis of actual wave measurements. It was therefore necessary to obtain and examine actual field data in order to provide a real test of the instrument. The orthogonally mounted ducted meter systems (OMDUM II and III) and the collinearly mounted system (COMDUM I) were used extensively on the Buzzards Bay Entrance Light Station. They were suspended at various depths beneath the waves by a system of counterweights and guy wires. This provided a highly damped suspension, which showed little, if any, reaction to the horizontal drag inducted by the oscillatory action of the waves. Since the exact method of suspensions of the instruments varied with the particular series of measurements, a complete description of the mounting procedures for the various experiments is given in chapter IV in the discussion of the field measurements.

CHAPTER III

DATA PROCESSING AND ANALYSIS

Meaningful measurements of wave motions depend to a great extent upon the reliability of the sensing device. Instrumentation characteristics, such as response time, precision, and accuracy of measurement, must be known if the value and limitations of the data are to be fully realized. No less important, however, is the method used for data analysis. Without careful and critical evaluation of the data, valuable information may be lost; or, more importantly, biased or even wrong conclusions may be drawn.

The observational data on wave motions are derived from several different types of measurements made with various instruments. First and foremost are the measurements of surface wave motions using the wave meters discussed in chapter II. A single series of observations was made in Narragansett Bay; the bulk of the measurements were made in the open sea at the Buzzards Bay Entrance Light Station (BBELS) Since these primary observations were made to determine the character of the relatively high frequency motions of waves and, hopefully, to provide information regarding the energetics inherent in the surface layers, the analysis of these data is somewhat extensive.

The remaining observations were of a supplementary nature and provide background information to more fully analyze and better discuss the wave data. These measurements include: free surface electronic wave staff observations, conventional horizontal current measurements, wind speed and direction records, tidal amplitude, and numerous visual estimates of wave parameters and weather conditions.

Table III-1, which includes both primary and supplementary measurements, shows the various types of data acquired and the requirements for data analysis. The first three columns list the variables measured, the location and series identification number, and the instrument used. The time interval ΔT is the frequency of sampling of the data. The period T is the total span of time during which the data were obtained.

This chapter contains a discussion of the data processing procedures-- from raw data handling through to final analysis and presentation of spectra-- used to analyze the results of the various observations.

Processing of Wave Particle Velocity Observations

Raw Data Preparation -- The data output from the various wave meter systems (OMDUM I, II and III, and LIMDUM I) discussed in chapter II was essentially identical. The preparation of the raw data from these instruments can there- fore be discussed together. Figure III-1 is a diagram delineating the processing procedures. Also included in the diagram is a description of the manner of processing the free surface elevation data provided by the U. S. Army Corps of Engineers Wave Staff System, which is mounted on the Buzzards Bay Entrance Light Station.

Block Diagram for Raw Data Processing.
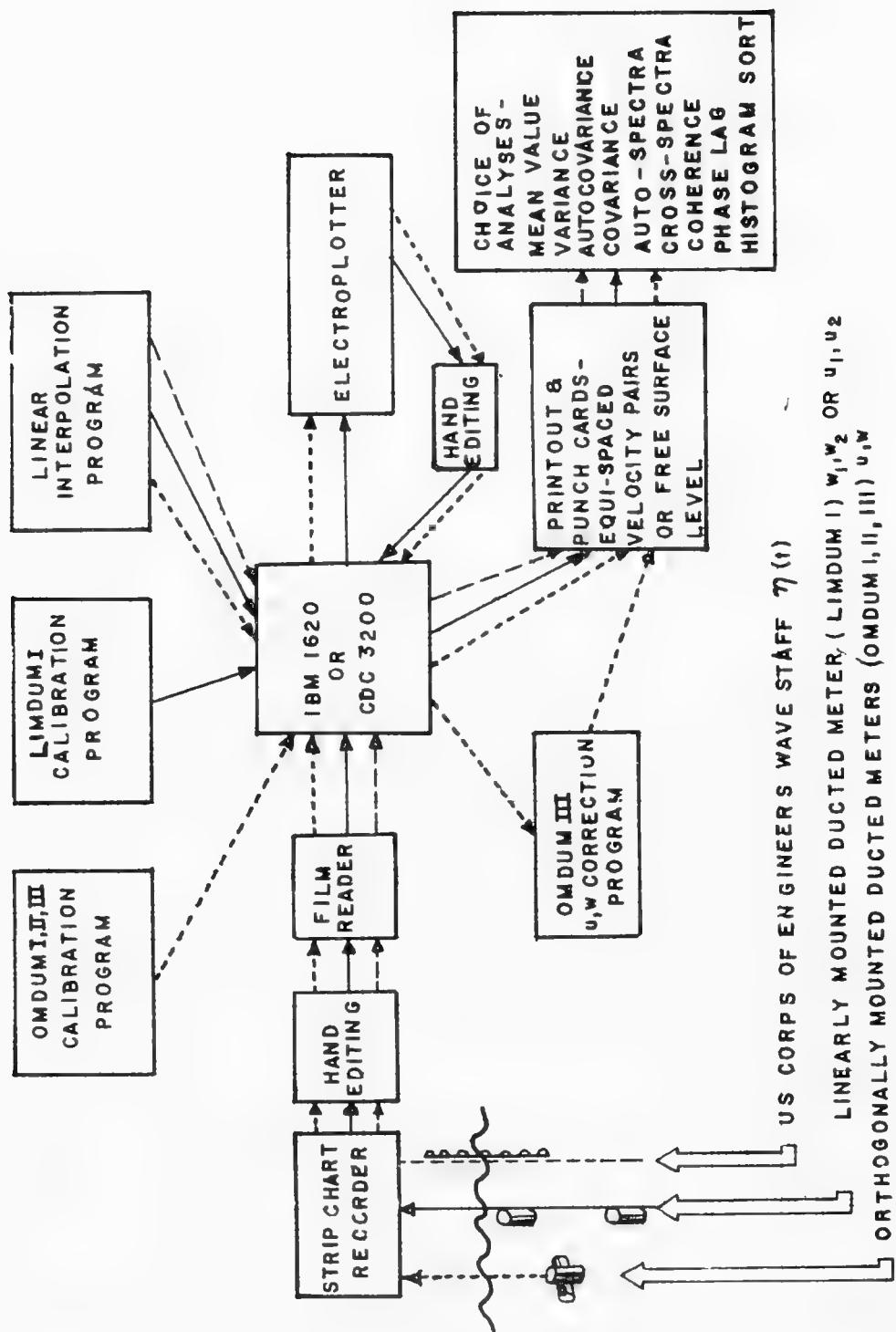
Figure III-1

Table III-1 Environmental and Wave Measurements

Variable(s) Measured	Location & Series	Instrument & Mounting	Sample Interval ΔT	Period T	Data Analysis
Simultaneous record of u(t) & W(t) in small wind waves (bay)	NUWS pier Narragansett Bay	OMDUM I wave meter (rigid pipe support off pier)	0.3 sec	300-400 sec	Mean & variance Auto-covariance Covariance Auto-spectra Cross-spectra
Simultaneous records of u(t) & w(t) in wind waves (open sea)	BBELS #3,5,7	OMDUM II wave meter (various guy wire & counterweight suspensions)	0.2, 0.3, 0.5, 1 sec	300-500 sec	Mean & variance Auto-covariance Covariance Auto-spectra Cross-spectra
Simultaneous records of u(t) & w(t) in wind waves (open sea)	BBELS #7,8,9, 10,13,14,16	OMDUM III wave meter (pyramid guy support & counterweight)	0.2 sec	300-600 sec	Means & variance Auto-covariance Covariance Auto-spectra Cross-spectra Histogram sorts
Simultaneous records of velocity pairs u(t) & u(t) or u(t) & w(t) at two depths	BBELS #11,12, 14,15,16	LIMDUM I wave meter (pyramid guy support & counterweight)	0.2 sec	300-600 sec	Means & variance Covariance Auto-covariance Auto-spectra Cross-spectra Histogram sorts
Record of free surface elevation	BBELS (during #14)	CERC electronic wave staff (mounted outboard on SE leg of BBELS)	0.2 sec	600 sec	Variance Auto-covariance Auto-spectra

Table III-1   Supplementary Environmental Measurements

Variable(s) Measured	Location & Series	Instrument & Mounting	Sample Interval ΔT	Period T	Data Analysis
Horizontal current speed & direction	BBELS	Braincon histo-gram current meter #316	20 min	9 days	Mean & variance of speed & direction Auto-covariance Auto-spectra Lagrangian Hodograph plots
Horizontal current speed & direction	BBELS	Braincon histo-gram current meter #316	5 min	14 days	Mean & variance of speed & direction Auto-covariance & Auto-spectra of speed Lagrangian hodograph plots
Elevation of free surface due to tide	BBELS data recorded during most wave obs	C&GS tide gauge (back pressure type)	Continuous for reference		Hand tabulation
Records of wind speed & direction	BBELS	USWB system (Electric Speed Indicator Corp. Belford wind in-dicator)	Continuous for reference		Hand tabulation and plots
Miscellaneous observations of wave parameters and weather	BBELS	Eye			Hand tabulation

The strip chart record (figure II-7) for either the OMDUM or LIMDUM wave meters was edited and labeled as to location, date, time sequence, depth, and recorder chart speed. The strip chart tapes were then taken to the NUWS computer laboratory, where the tapes were read on a Telerecordex film reader (manufactured by Data Instruments, Division of Telecomputer Corp., North Hollywood, Calif.). This device allows scanning of the strip chart data. The conversion step is shown in schematic form in figure III-2. The strip chart contains the train of voltage pulses. The frequency of a pulse is directly proportional to the current speed, and the sense (plus or minus) designates the direction of flow. When the vertical hairline of the film reader is adjusted in line with the peak of the pulse and a foot pedal is pressed, the pulse time is automatically placed upon punch cards. At a point in the sequence when a reversal in the sign of the pulse indicates a zero crossing or null (see figure III-2), a "zero crossing card" is introduced by pushing the appropriate button on the film reader. This card has no time associated with it. Its function is to indicate to the computer that the time points occurring before and after the zero crossing should not be used as a pair to compute a velocity, since the computation would have no meaning.

The result thus far is a deck of punch cards listing the time of occurrence of each voltage pulse, which delineates the time intervals $\Delta T_1, \Delta T_2, \Delta T_3, \ldots \Delta T_n$ (figure III-2) indexed by the proper sign. The output of the reader constitutes a proper card format for further conversion into velocity data.

Analog Velocity Conversion Program -- The cards produced from the film reader were placed as input data in an IBM 1620 or a CDC 3200 digital computer, whereupon the velocity data were generated. The calibration programs (figure III-1) discussed in chapter II were programmed into the memory cells of the computer so that the appropriate program could be selected. The computer scanned the sequence of time values of the pulses and allocated a velocity value to each time difference between successive cards (except those separated by a zero crossing card). Thus, for each pair of cards representing a time interval in milliseconds, a unique value of velocity was produced. This value was indicated as occurring at an instant of time halfway between the time interval defined by two consecutive cards (see figure III-2). Note the need to "interpolate" a speed value. This value is, in a sense, the average velocity unique to the indicated instantaneous rate of impeller rotation; i.e., the rate of passage of two consecutive impeller magnets. For nominal flow speeds encountered in wind waves of 15 cm sec^{-1} and 60 cm sec^{-1}, this interval of time was of the order of 240 milliseconds and 50 milliseconds, respectively. The faster the flow speed, the more data points produced per unit of time. Hence, the faster the flow speed, the less the error in the estimate of the moving average of the velocity. The velocity conversion program for the OMDUM III meter data output is given in appendix E.

Linear Interpolation Program -- At this point in the data processing, the velocity-time data (i.e., V_n' at time T_n' in figure III-2) have been printed out and usually plotted, or at least visually edited. A close scrutiny has been made for bad points, which occurred (as was pointed out in chapter II) mostly at the peak velocity regions. The graphing of the data points, when
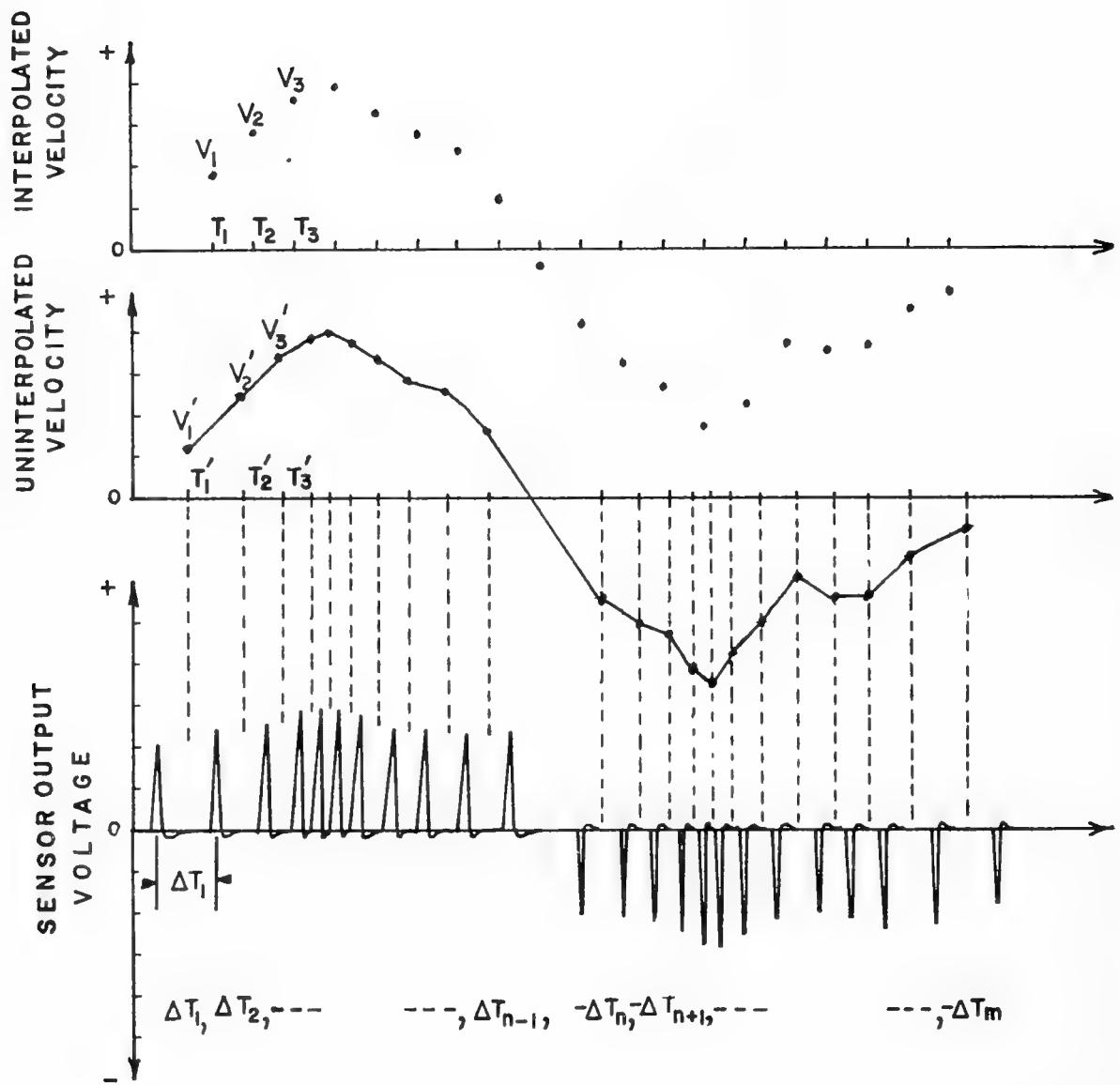
Schematic Illustration of Wave Velocity Data Processing.

Figure III-2

desired, was done with a Benson-Lehner model J electro-plotter (manufactured by Data Instruments, Division of Telecomputer Corp., North Hollywood, Calif.). Upon removal of any bad point cards, the data are ready for linear interpolation. This produces the velocity data as an equi-spaced time series, which is necessary for subsequent spectral analysis.

The linear interpolation is graphically portrayed at the top of figure III-2. Straight lines are drawn connecting the uninterpolated velocities $V_1', V_2', V_3', \ldots V_n' \ldots$ located on the time axis at $T_1', T_2', T_3', \ldots T_n' \ldots$ These velocities, in general, are unequally spaced. A sequence of new velocity values is then obtained at equi-spaced time intervals ΔT. Thus, a new velocity distribution is formed of $V_1, V_2, V_3, \ldots V_n' \ldots$ (The Fortran program for linear interpolation is listed in the appendix E.) The time series of interpolated pairs (u_n, w_n) or of similar velocity components $(u_m, u_n \text{ or } w_m, w_n)$ is now in a form for statistical analysis, including estimation of mean values, variance, and calculation of the various spectral parameters shown in figure III-1. A discussion of possible errors due to interpolation and a graphic comparison with uninterpolated data are presented later in this chapter.

Correction Program for the OMDUM III Data -- In chapter II a method was suggested for making corrections to the vertical and horizontal velocity data pairs obtained from the OMDUM III system. This correction was found to be possible, since the bias, which produces a possible 10-12 percent error in the values, can be determined fairly accurately as a function of the ratio of the magnitudes of the uncorrected velocity pairs (u, w).

To apply these correction procedures, one must use the linearly interpolated data pairs because the ratio computation requires simultaneous velocity components. The first velocities obtained from the raw data (V_n') are not equi-spaced in time, and would not be simultaneously in the u and w records. The punch cards listing the interpolated velocity data along with the curve fitting data allowed evaluation of the correction factor for each velocity component. This factor is a known function of the magnitude of their ratio (i.e., u/w). The ratio actually determines an angle θ for the u component, applying the appropriate correction; and, since the detectors are orthogonally mounted, the appropriate correction for $90^\circ - \theta$ is applied to the w component. The values of the corrected velocity components are then suitable for final analysis. The Fortran computer program and a description of the orthogonal velocity corrections is presented in appendix E.

Data from the Free Surface Elevation Wave Staff System

Two records of free surface fluctuation data, which were obtained from the wave staff system (discussed in chapter IV) installed by the U. S. Army Corps of Engineers on the southeast leg of the BBELS tower, were processed in order to compare some free surface wave spectra with those of wave particle velocity motions. The output of the recording system provides both a magnetic tape and a pen and ink analog record of the time variable position of the free surface η on the vertical wave staff. Copies of pen and ink records

were provided by the U. S. Army Corps of Engineers, Coastal Engineering
Research Center, Washington, D. C. The procedure used for the raw data
processing in included in figure III-1.

For a spectral analysis, it was desired to digitize the analog tape
data on punch cards representing equal time spacing at the desired interval
of 0.2 second (i.e., the same ΔT as the wave motion data). However, the
high scanning sensitivity of the Telerecordex film reader (about 16 counts
per mm of horizontal slide distance) rendered a precise setting on the
required 0.2 second sampling intervals too difficult. Instead, the trace
was read at approximately 0.1 - 0.2 second intervals, and punch cards were
produced containing unequally spaced values of ΔT. As indicated in figure
III-1, the cards were then processed like the velocity data to produce in-
terpolated data at the desired 0.2 second intervals.

Data from Horizontal Current Observations

Two series of supplementary current data were taken at BBELS. The first,
a 9-day record of the horizontal surface current at 20-minute sampling inter-
vals, was made to ascertain the gross properties and variability of the tidal
or drift currents peculiar to the tower location. The second series was made
over a 14-day period, at 5-minute sampling intervals, to observe relatively
high frequency horizontal current variations.

The instrument used for both sets of observations was the Braincon type
316 histogram current meter, which utilizes a Savonius rotor as a speed
sensor.

The Braincon meter provides a photographically displayed sensor output
as a concentric circular analog format. The sensor outputs are recorded
simultaneously on film during the preset sampling interval for each frame.
The recorded data include total Savonius rotor revolutions, current direction
relative to magnetic north, instrument tilt angle from the vertical, and
instrumental vane direction relative to magnetic north.

Upon retrieval of the instrument from BBELS, the filmed data were delivered
to Braincon Corp., Marion, Mass., for film development and processing. Data
retrieval involves a film reading device, which converts the angular analogs
into binary punch-paper tape. The paper tape data were taken to the NUWS
computer laboratory and converted into magnetic tape storage for use in the
computation of the statistical parameters and related spectra.

Statistical Analysis of Processed Data

The records of the wave particle motions can be treated as time series
data. Precise, but somewhat sophisticated, techniques for studying time
series data have been developed from communications theory. This theory,
in turn, originally stemmed from the work of Wiener (1933), and was abstracted
and applied to the harmonic analysis of time series and to noise analysis (see
Blackman and Tukey, 1958). Many geophysical, meteorological, and oceanographic

phenomena are amenable to time studies (whether the sampling interval be one millisecond or a million years), and workers in these fields now frequently utilize such methods in many applications. (See, for instance, Platzman and Rao, 1964, and Hamon and Hannan, 1963.)

For examination of the time series data, the methods of power density spectral analysis were used. There are many reasons for applying these methods in lieu of the classical Fourier techniques for evaluating sinusoidal amplitude coefficients. Barber (1961) presents a lucid discussion of these advantages when dealing with random functions. His discussion, as it might apply to ocean waves, is briefly summarized below.

If a sample of the wave velocity component described as the random oscillation u(t) is measured over the period I, it can be represented (see James and James, 1949) by a Fourier series of even-cosine and odd-sine functions as:

$$u(t) = \sum_{-\infty}^{\infty} A_n \, e^{2\pi i n \frac{t}{T}} \; , \tag{III-1}$$

where A_n is the appropriate weighting constant for each term. It can be shown that no correlation must be expected between successive amplitudes A_n and A_{n+1}. The amplitudes are complex numbers whose phases and arguments occur in a random fashion.

If different samples ($T_1, T_2, T_3, \cdots T_n, \cdots$) are taken off the infinite spanning function u(t), no correlation is necessarily expected between the different values of any one harmonic. Hence, the values of A_n can be considered as random choices of a family of complex Fourier coefficients. The variance of a sequence of values $\overline{\sigma_u}^2$ may be large, but any individual A calculated for a particular Fourier component of u(t) may or may not be indicative of the total energy associated with a finite band of energy centered around A_n.

In the analysis of a quasi-random function such as u(t), the significant quantity is a statistical parameter. This parameter should be associated with the variance of the family from which the amplitudes of A_n are derived. If the sample is of sufficient time length and has a large number of values (i.e., a large number of n's in equation (III-1)), then a large number of different Fourier components are produced. It therefore follows that a large number of adjacent harmonic amplitudes $(A_n, A_{n+1}, \cdots)$ are associated with a spectral band of similar variance or energy content. One may, in effect, estimate the variance or energy content as a function of frequency by calculating the mean squares of a number of neighboring harmonic amplitudes. The concept of the auto covariance function can therefore be used, and the function can then be formulated into a power density spectrum. In other words, a time series can have associated with it a spectral function, or simply a spectrum that displays in a histogram-like form the variability of the function (i.e., the contribution to the variance associated with a

range of frequency). Spectral analysis is associated directly with the auto-covariance and the covariance functions, which themselves provide much information about the original time series (see Lee, 1960). Another important factor is that confidence measure estimates or error can be determined for the computed spectra by use of standard statistical parameters.

It may be helpful to review briefly the basic assumptions and definitions needed to understand the application of the pertinent statistical parameters to time series data. There are several extensive reviews of the methods used in the so-called Tukey spectral estimates, including Blackman and Tukey (1958), and Ellis and Collins (1964).

Basic Assumptions for Time Series Analysis -- The time series data under analysis were assumed to be representative of a random or mixed process. A random (or stochastic) process is an ensemble of time functions given by $X_n(t)$, where $n = 1, 2, 3, \ldots$ and $-\infty < t < \infty$; so that the ensemble can be characterized through its statistical properties. A mixed process is a random process containing time-periodic constituents. The mixed process is probably quite well suited to describing the motions of wind waves and, in fact, many scales of oceanic flow. A word of explanation may be required here regarding the use of the term "ensemble". According to Kinsman (1965), this term can denote an infinite or a finite collection of records of variables (associated with the same property) that are governed by identical phenomena and evaluated for all time. In this sense, for simplicity, the ensemble is the collection of time series measurements of waves made at different spatial positions in the ocean.

The classical theory for the analysis of time series data is based upon three assumptions; that the process is stationary, ergodic, and of infinite extent. This latter requisite is, of course, experimentally inconceivable; however, it is important from a heuristic point of view to approximate this assumption.

"Stationary" may be defined as the property of a time series in which the probability of any particular event occurring during the series record is constant. To illustrate, let X_p be a sample in a particular time interval P. If the statistical properties of X_p are the same as those of X_{p+q}, where q is any other sampled interval, then the record is stationary. Ideally, a system should be stationary during the time interval of the sampling. The only factual justification for assuming stationarity, other than by an intuitive inference from visual observations, is by an assessment of the variation of statistical properties at discreet intervals in the records. For instance, the first and last 10 percent of a particular wave record could be analyzed for its auto-spectra. Similarities in the two spectra would thus be indicative of the degree of stationarity.

The ergodic hypothesis is also a very important assumption related to the study of time series. This theorem states that the ensemble average (i.e., the average of the process over both a time and space domain from $-\infty$ to $+\infty$) may be replaced with unit probability by the time average of a single series

(i.e., a finite length sample) in the ensemble. (See Lee, 1960.) For example, let an experiment last T seconds and be repeated N times. Let X_{ij} be a sample from the i^{TH} experiment at time j. If the statistical properties of X_{ij}, for fixed j and i from 0 to N, are the same as those for fixed i and j from 0 to T (as both N and T tend to infinity) the process is ergodic. Thus, in a sense, the ergodic hypothesis is an extension of the concept of stationarity applied to both time and space for the complete data ensemble.

Note that for the definition the spatial distribution concept has been applied to ensemble. What has been described is sometimes referred to as a homogeneous statistical environment; i.e., a system which contains both time and spatial stationarity. The physical implications of this concept should be emphasized. One can learn about a fundamental ergodic process occurring over a large physical region by sampling only a relatively small volume (or, in fact, a single point) within the region as a function of time. Conversely, one can theoretically learn as much about this process by an instantaneous sampling over the whole region. From an experimental point of view, the first method of making observations is obviously more applicable to ocean wave study. However, both types of measurements have been applied to free surface wave studies. The first method is exemplified by wave staff observations at a point in the ocean as a function of time. The second method is demonstrated by observations (stereo photographs) of waves on a large area of ocean at a given instant of time (see Chase, et al, 1957).

The existing mathematical models for time series analysis incorporate both stationarity and ergodicity concepts. It is obvious, however, that no geophysical process can be stationary in the mathematical sense. The geophysicist must be satisfied with the statistics of the process under study if he can state that they change very little in the duration of the sampling. If this condition holds, then the mathematical abstraction will assist his analysis; albeit, somewhat imperfectly.

Planning Data Sampling for Spectral Measurements -- The plans for the spectrum analysis were guided by discussions with Professors V. P. Starr and E. N. Lorenz of the Department of Meteorology at M.I.T., and with personnel in the NUWS computer laboratory. Also consulted were the references of Blackman and Tukey (1958), Miller and Kahn (1962), Kinsman (1960), and Munk and MacDonald (1960).

The value of a spectral measurement program is heavily dependent upon the following: (1) the quality and quantity of data; and (2) the desired precision, resolution, and cutoff frequency. Each estimate of the energy (or contribution to the total variance) obtained from a finite data record for a particular frequency is actually an approximation of the average value contained within a bank centered at the nominal frequency. The spectral values are evenly spaced on a frequency interval from zero to the so-called "Nyquist" frequency. This is defined by:

$$f_N = \frac{1}{2\Delta T} \quad ; \tag{III-2}$$

where ΔT is the sampling interval of the time series. This interval may be the preset real time sampling interval of the instrument sensor. It can, moreover, be the selected time interval over which a continuous analog record was sampled, or the interval at which data were interpolated from an unequally spaced digital record. This was the case for the wave meter records processed, as discussed in the previous sections. The use of digital data (rather than continuous records) can introduce into the spectrum the phenomenon known as "aliasing". For example, the harmonic oscillations of the frequencies

$$f, (\Delta T)^{-1} - f, (\Delta T)^{-1} + f, 2(\Delta T)^{-1} - f, \ldots \qquad (III-3)$$

can appear, under certain conditions, as a single frequency contribution to the spectra. If the frequency f is slightly lower than the sampling frequency $(\Delta T)^{-1}$, then it cannot be distinguished from the low frequency $(\Delta T)^{-1} - f$. Thus, the high frequency f appears under the alias of the low frequency $(\Delta T)^{-1} - f$. To minimize the aliasing effect and to obtain the best possible spectrum, the sampling interval ΔT should be small enough to include all frequencies containing quantities of energy that contribute significantly to the variance of the motions studied. Note that the response time of the instrument sensor defines the lower limit of ΔT; or, in effect, the highest Nyquist frequency one can choose. Assuring that the sensor response time (as defined in appendix A) is well below the chosen ΔT, one can incorporate an appropriate low-pass filter, either in the output of the sensor or into the data record prior to analysis, and use a sampling rate at which the Nyquist frequency coincides with the filter cutoff frequency. Filtering direct output data is not good practice, in general, because one is irreversibly excluding information (at higher frequencies) which later may be desired.

Another method of assimilating the spectral information at a desired frequency band is to assess the sensor response, and choose what might be the natural cutoff frequency based on physical grounds. This choice can be governed by a trial spectrum, using the highest frequency resolution attainable (governed by the sensor) and examining the energy at the upper limit of the frequency range. This should guide one in the optimum choice of the Nyquist frequency.

The next consideration is that of the resolution desired in the spectral estimates. The frequency resolution may be defined as:

$$\Delta f = \frac{1}{2M\Delta T} = \frac{f_N}{M} \quad ; \qquad (III-4)$$

where M is the total number of units on the frequency scale. M is actually the maximum lag at which the auto-covariance function is computed if the

spectrum is substantially flat. The larger the value of M, the greater is the resolution over the chosen frequency band given by:

$$0 \le f_K \le f_N .$$ (III-5)

Thus, since the quantity ΔT is the time interval between successive observations (or interpolation points), the spectral estimates are centered at frequencies:

$$f_K = \frac{K}{2M\Delta T} .$$ (III-6)

The Nyquist frequency position is that at which:

$$f_K = f_M = \frac{1}{2\Delta T} = f_N .$$ (III-7)

According to Blackman and Tukey (1958), it is not desirable to use lags longer than a moderate fraction (perhaps 5 or 10 percent) of the length of the record. Thus, the magnitude of M should be adjusted so as to give

$$2M\Delta T \le 10\% T ;$$

where T is the length of the record. Thus, the value of ΔT determines the highest frequency f_K to be studied, and the value of T determines the lowest.

In making a statistical analysis of wave data, one must be aware that a certain indeterminacy or variability of precision is inherently associated with the estimates. This degree of uncertainty is directly related to the statistical methods of analysis, and is over and above those uncertainties in the data caused by such instrumental deficiencies as limitations in frequency response, or biasing of the sensor or the recording systems.

It may be helpful to consider briefly the fundamental method of estimating the precision of spectral estimates, as presented by Blackman and Tukey (1958) and elaborated upon by Kinsman (1965). Given a series of random variables

$$X_1, X_2, X_3, \cdots X_\eta, \cdots X_F ,$$ (III-8)

each of which can be represented by a standard normal or Gaussian distribution with a mean equal to zero and a variance of unity (hence, having a standard
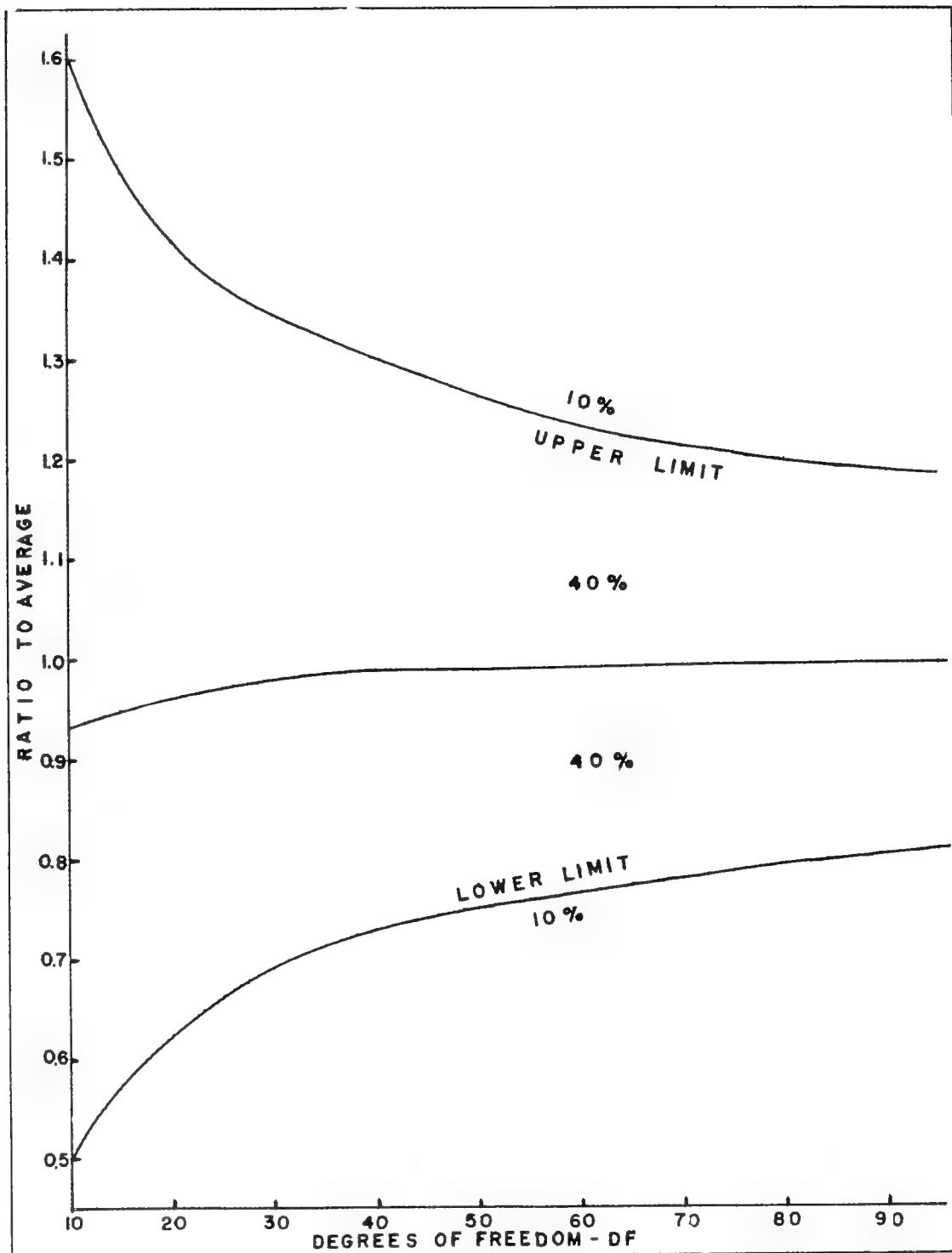
Behavior of Chi-Square for Increasing Degrees of Freedom.

Figure III-3

deviation also equal to unity); the sum of these Gaussian distributed variables can be represented as:

$$\chi_F^2 = x_1^2 + x_2^2 + x_3^2 + \cdots x_n^2 + \cdots x_F^2 \ . \ \text{(III-9)}$$

This sum (always a positive quantity) is defined as a chi-square distribution with F degrees of freedom, and is designated by DF. Defining the variability of χ_F^2 by the ratio of the standard deviation to the mean value, (both as function of k) this parameter is equivalent to $(2/k)^{1/2}$. Thus, as k increases, the variability of χ_F^2 becomes less. This applies also to any multiples of χ_F^2. The variable DF can therefore be used to describe the statility of a given statistical estimate; assuming, of course, that the distribution is approximately Gaussian. The stability or reliability of the statistical estimate may then be obtained as a function of the number of points in the particular sample.

Tukey (1949) has shown that, with certain assumptions, the samples provide values of the spectra function (designated as $\Phi_x(f)$) which can be represented as a chi-square distribution for each value of DF. The desirable length of the record may be determined by calculating the DF for each spectral estimate (for DF = 1,2,3, $\cdots$ M-1) from the following relations:

$$DF = 2 \ \frac{n}{M} - \frac{1}{4} \qquad \text{for } n = 1,2,3, \cdots \text{ M-1.}$$
$$DF = \frac{n}{M} - \frac{1}{4} \qquad \qquad \text{for } m = o, \text{ M.} \qquad \qquad \text{(III-10)}$$

n is the number of data points in the record, and M is as previously defined. The larger the value of n, the larger is the value of DF; hence, the precision of the spectral estimate. With a chi-square distribution the gain in the precision of the estimate is great up to values of DF around 40 to 50. Beyond 50 the precision gains become rapidly less.

An unequivical interpretation of the results requires that the process measured by quasi-stationary, as previously discussed. However, in measuring ocean waves, which are an uncontrolled phenomenon in the field, the apparent gain in precision (resulting from making very long records or, equivalently, from obtaining a very large value for N in equation (III-10)) is often offset in a complex manner by the changes in the nature of the process being measured. In other words, the longer the sampling continues, the smaller the probability that the record will be stationary.

Figure III-3 shows the behavior of the chi-square distribution as a function of DF. Within the upper and lower boundary curves, the probability is 80% that the ratio of an obtained estimate to its mean value will fall within the limits defined by the intersection of the line of constant value of DF with the upper and lower limit curves. Likewise, there is a 40% probability for a given DF that the ratios will fall between the middle and upper, or

middle and lower limiting curves. By using these probability curves, one can estimate the confidence limits of a given spectral curve. In subsequent discussions of particular wave velocity spectra, the 80 percent confidence limits are indicated on certain spectra plots.

Classical Equations and Definitions -- The classical descriptions of the auto-covariance, covariance, and associated spectral functions are given here for both single and paired time series analysis. For a very complete discussion of these parameters see Lee (1960). The approximations of these functions suitable for computational procedures are given in the following section.

1. Single Time Series Analysis. Assume that the process under study is both stationary and ergodic, and that it can be represented by a variable determined as a single time series $u(t)$. It is assumed also that $u(t)$ is bounded in amplitude but unbounded in time duration. The mean or d-c component of the time series is given by the time average:

$$\bar{u} = \lim_{T \to \infty} \frac{1}{T} \int_{-T/2}^{T/2} u(t)\, dt \ . \tag{III-11}$$

The time variable fluctuating quantity is given by:

$$u'(t) = u(t) - \bar{u} \ . \tag{III-12}$$

The mean square or the variance is given by the usual formulation of the time average:

$$\sigma_u^2 = \overline{[u'(t)]^2} = \overline{[u'(t) - \bar{u}]^2} = \lim_{T \to \infty} \frac{1}{T} \int_{-T/2}^{T/2} [u(t) - \bar{u}]^2\, dt \ . \tag{III-13}$$

It will be seen later that when $u(t)$ is given as a particle velocity component, the variance $\sigma_u^2 = \overline{u'^2}$ is proportional to the turbulent kinetic energy associated with the u velocity component.

The auto-covariance function of the process $u(t)$ is given by:

$$\phi_u(\tau) = \lim_{T \to \infty} \frac{1}{T} \int_{-T/2}^{T/2} u'(t)\, u'(t+\tau)\, dt \ , \tag{III-14}$$

sometimes written as

$$\langle u(t)\, u(t+\tau) \rangle \ ;$$

54

where τ is the time lag at which the point-for-point self-multiplication of the time series values is carried out. From equation (III-14), for zero lag ($\tau = 0$):

$$\phi_u(0) = \sigma_u^2 = \overline{[u'(t)]^2} ,$$

(III-15)

or, stated simply, the auto-covariance function at zero lag is the variance of the function. The auto-covariance function, when normalized by dividing it by $\phi_u(0)$, is often called the auto-correlation function (see Kinsman, 1965). Note that:

$$\phi_u(\tau) = \phi_u(-\tau) ,$$

(III-16)

or the auto-covariance is an even function of the lag τ.

Taking the Fourier transform of the auto-covariance produces the spectral function given by:

$$\Phi_u(f) = \frac{1}{2\pi} \int_{-\infty}^{\infty} \phi_u(\tau) e^{-2\pi i f \tau} d\tau .$$

(III-17)

The spectrum may actually be defined as:

$$\Phi_u(f) = \frac{1}{2\pi} \int_{-T/2}^{T/2} \phi_u(\tau) e^{-2\pi i f \tau} d\tau .$$

(III-18)

This is because the basic function u(t) is defined by:

$$u'(t) = \begin{cases} u'(t) & |t| \leq T/2 \\ 0 & |t| > T/2 \end{cases} .$$

(III-19)

This provides information only over the period $-T/2$ to $+T/2$. However, in view of the assumptions regarding stationariness, one may interchange the limits, as with equations (III-17) and (III-18), and not change the meaning of the spectral function. The function in equation (III-18) is called the "power spectra" by engineers, because the variance is often referred to voltage squared per unit resistance, which is proportional to power dissipated. Since this study is generally concerned with the variances of velocity components that are proportional to kinetic energy, the "energy spectra" will be used throughout the discussion of the statistics of wave or current motions.

Since the function $\phi_u(\tau)$ is an even function of τ, equation (III-17) can be written as:

$$\Phi_u(f) = \frac{1}{\pi} \int_0^\infty \phi_u(\tau) \cos 2\pi f \tau \, d\tau . \qquad \text{(III-20)}$$

The inverse transform relationship is given by:

$$\phi_u(\tau) = 2 \int_0^\infty \Phi_u(f) \cos 2\pi f \tau \, df . \qquad \text{(III-21)}$$

For $\tau = 0$ the relation in equation (III-21) becomes:

$$\phi_u(0) = 2 \overline{\sigma_u^2} = 2 \int \Phi_u(f) df . \qquad \text{(III-22)}$$

Thus, the integral of the energy spectrum over all frequencies is equivalent to the total variance of the velocity function. The wave or current motions under examination usually occur within a defined range of frequencies; hence, instead of infinity for the upper frequency limit, an appropriate $\Delta\tau$ can be chosen which will define a reasonable Nyquist or cutoff frequency. Equation (III-22) is more realistically represented by:

$$\phi_u(0) \cong 2 \int_0^{f_N} \Phi_u(f) df . \qquad \text{(III-23)}$$

Equation (III-21) represents the total energy of the record. $\Phi_u(f) df$ is the contribution to this total energy from a frequency band of $f - \frac{1}{2} df$ to $f + \frac{1}{2} df$. The function $\Phi_u(f)$ is the energy density or spectral density, and is in units of the square of the quantity $u(t)$ per unit frequency. If $\Phi_u(f)$ is constant over some range of frequencies,

$$\Phi_u(f) = \Phi = \text{CONSTANT FOR } f_1 < f < f_2 . \qquad \text{(III-24)}$$

Then all frequencies contribute equally to the energy and the spectrum is termed "white" over this range.

2. Paired Time Series Analysis. In this situation two variables, $u(t)$ and $w(t)$, were simultaneously recorded. Aside from the individual auto-spectra, the common statistical properties of the two time series must be studied. By computation of the covariance, the linear correlation coefficient, and the cross-spectra, one may determine a statistical relationship of one time series to another or, in effect, see if definite common periodic fluctuations exist. The phase relationships of any periodic relationships may also be estimated.

The analysis of the time series pair involves the usual auto-covariance and energy spectrum estimates delineated in the previous section on single time series analysis. The cross-covariance functions or simply the covariances are defined as:

$$\phi_{uw}(\tau) = \lim_{T \to \infty} \frac{1}{T} \int_{-T/2}^{T/2} u'(\tau) w'(t+\tau) dt \qquad (III\text{-}25)$$

and

$$\phi_{wu}(\tau) = \lim_{T \to \infty} \frac{1}{T} \int_{-T/2}^{T/2} w'(t) u'(t+\tau) dt \; ; \qquad (III\text{-}26)$$

where $-\infty < \tau < \infty$. The covariance functions are even (symmetric in τ); thus, changing the order of $u(t)$ and $w(t)$ changes the value. However, $\phi_{uw}(\tau)$ and $\phi_{wu}(\tau)$ can be related by:

$$\phi_{uw}(\tau) = \phi_{wu}(-\tau) . \qquad (III\text{-}27)$$

The term $\phi_{uw}(o)$ has special significance when the functions in the covariance represent orthogonal velocity components (u and w) measured at a point in the plane:

$$\phi_{uw}(o) = \lim_{T \to \infty} \frac{1}{T} \int_{-T/2}^{T/2} u'(t) w'(t) dt = \overline{u'w'} . \qquad (III\text{-}28)$$

Here the covariance at zero lag is proportional to the well-known Reynolds stress. Further discussion of the physical meaning of this term is presented later.

The ordinary linear correlation coefficient between two functions u(t) and w(t) is expressed as:

$$r = \frac{\overline{u'w'}}{\left[\sigma_u^2 \; \sigma_w^2 \right]^{1/2}} \qquad (III\text{-}29)$$

As before, the covariance function is expressible as a Fourier integral:

$$\phi_{uw}(\tau) = \int_{-\infty}^{\infty} \left[\frac{1}{2\pi} \int_{-\infty}^{\infty} \phi_{uw}(\tau) e^{-2\pi i f \tau} d\tau \right] e^{2\pi i f t} df . \qquad (III\text{-}30)$$

Defining a function $\Phi_{uw}(f)$ so that

$$\Phi_{uw}(f) = \frac{1}{2\pi} \int_{-\infty}^{\infty} \phi_{uw}(\tau) e^{2\pi i f \tau} d\tau , \qquad (III\text{-}31)$$

equation (III-31) may be written as

$$\phi_{uw}(\tau) = \int_{-\infty}^{\infty} \Phi_{uw}(f) \, e^{2\pi i f \tau} df \; . \tag{III-32}$$

$\Phi_{uw}(f)$ is the cross-spectrum of the functions $u(t)$ and $w(t)$.

The complex covariance function may be described in terms of the Fourier transform of its even function (real part) and odd function (imaginary part) as:

$$\Phi_{uw}(f) = \left[C_{uw}(f) - i \, Q_{uw}(f) \right] \; . \tag{III-33}$$

The in-phase spectral energy characteristics are given by the value of the function $C_{uw}(f)$, termed the co-spectra; whereas the out-of-phase energy distribution is given by the function $Q_{uw}(f)$, termed the quadrature or qua-spectra.

The dimensionless quantity R^2, given by

$$R^2 = \frac{\left[C_{uw}(f) \right]^2 + \left[Q_{uw}(f) \right]^2}{\Phi_u(f) \, \Phi_w(f)} \tag{III-34}$$

is termed the coherence. This function of frequency is a measure of the phase relation between the two records. The phase difference between the two records $u(t)$ and $w(t)$ is given by:

$$\Theta = \text{ARCTAN} \; \frac{Q_{uw}(f)}{C_{uw}(f)} \; . \tag{III-35}$$

At regions of the spectrum where strong correlation exists, $R^2 \to 1$. Where Θ is randomly distributed, $R^2 \to c$. Clearly, the reliability of the computed Θ depends upon the coherence between the spectra of the time series. The resemblance between the coherence function and the linear correlation coefficient is noteworthy in that it is a type of correlation coefficient of the spectra of u and w.

Computation Formulas for Computer Processing -- The relations in the preceding section are idealized classical descriptions of the various statistical parameters to be derived from the wave data. In the various integrals occurring in equations (III-11) through (III-34), $u(t)$ and $w(t)$ are continuous functions. To utilize numerical methods of analysis, one must first digitize the data over equally spaced time intervals (as already described). In the same manner, the mathematical formulation must be made amenable to digital computation by conversion to the appropriate formulas. These formulas, which are described by Tukey (1949), eliminate the difficulties that would occur if an attempt were made to

analyze using Fourier series approximations. Certain statistical pitfalls associated with truncated series expansions and peculiarities in the spectrum estimates have been avoided in the empirical formulations, making life relatively easy for the geophysist.

The following is a resume of the methods and formulation of the statistical analysis used with the M.I.T. IBM-7090 and the NUWS IBM-1620 and CDC-3200 digital computers. The Fortran program suitable for these and similar computers is listed in appendix D.

The experimental data were presented at equally spaced time intervals ΔT, yielding a discreet time series,

$$u_1, u_2, u_3, \cdots u_N , \tag{III-36}$$

which had been previously edited and properly scaled. Other than the editing for spurious points, no smoothing was done. It was hoped thus to preserve the high frequency characteristics of the data.

According to NUWS procedures, the arithmetic mean must be removed from the data, as indicated by equation (III-12). The mean value is given by:

$$\bar{u} = \frac{1}{N} \sum_{n=1}^{N} u_n(t) ; \tag{III-37}$$

where N is the total number of samples. Subtracting the mean $\bar{u}$ from each data point $u_n(t)$, results in a new time series:

$$u_n'(t) = u_n(t) - \bar{u} ; \tag{III-38}$$

and, by definition,

$$\sum_{n=1}^{N} u_n(t) \equiv 0 .$$

Note that the total time over which the data are sampled is given by:

$$T = T_N = N \Delta T . \tag{III-39}$$

The auto-covariance function $\phi_{u}(\tau)$ (see equation (III-14)) is approximated by:

$$A(L) = \frac{1}{n-L} \sum_{i=L+1}^{N} u_{i-L} - u_i - \frac{1}{(N-L)^2} \sum_{i=L+1}^{N} n_{i-L} \sum_{i=L+1}^{N} n_i ; \tag{III-40}$$

where L = 0,1,2,$\cdots$m, and m is the number of lags used.

The energy estimate of the spectrum function (equation (III-18)) is approximated by:

$$V(K) = \frac{\delta_K}{M}\left[\sum_{L=1}^{M}\left(1 + \cos\frac{L\pi}{M}\right)\cos\frac{KL\pi}{M}A(L) + A(0)\right] ; \quad \text{(III-41)}$$

where

$$\delta_K = \begin{cases} \frac{1}{2} & , K = 0, M \\ 1 & 0 < K < M \end{cases} \quad \text{(III-42)}$$

and

$$K = 0, 1, 2, --- M .$$

Here K represents the index number of a particular frequency (analogous to the L for lags). It is used to index both the lag number for the auto-covariance and covariance functions, and also to index the frequency scale; i.e., the K frequency is defined from equation (III-6) as:

$$f_K = \frac{K}{2M\Delta T} = \frac{K f_N}{M} . \quad \text{(III-43)}$$

The value of V(0) is the variance of u(t); hence, because of equation (III-21), $\delta_0 = 1/2$ in equation (III-41). The term $(1 + \cos\frac{L\pi}{M})$ in equation (III-41) is a type of filter or lag window, which slowly varies from 2 at L = 0 to 1 at L = m. This filter provides an inherent correction for gross truncation errors in the series records $u_1, u_2, u_3 --- u_n$ AND $w_1, w_2, w_3 --- w_n$. The cross-covariance functions are indicated as:

$$C(L) = \left[\frac{1}{n-L}\sum_{i=L+1}^{N} u_{i-L}\, w_i\right] - \left[\frac{1}{(n-L)^2}\sum_{i=L+1}^{N} u_{i-L}\sum_{i=L+1}^{N} w_i\right] \quad \text{(III-44)}$$

for the even or positive part of the covariance, and

$$D(L) = \left[\frac{1}{n-L}\sum_{i=L+1}^{N} w_{i-L}\, u_i\right] - \left[\frac{1}{(n-L)^2}\sum_{i=L+1}^{N} w_{i-L}\sum_{i=L+1}^{N} u_i\right] \quad \text{(III-45)}$$

for the odd or negative part of the covariance.

The in-phase correlation of the two records is given by:

$$E(L) = \frac{1}{2}\left[D(L) + C(L)\right] . \qquad \text{(III-46)}$$

The out-of-phase correlation of the two records is given by:

$$F(L) = \frac{1}{2}\left[D(L) - C(L)\right] . \qquad \text{(III-47)}$$

The in-phase energy spectrum or co-spectrum is approximated by:

$$Z(K) = \frac{\delta_K}{M}\left[\sum_{r=1}^{M}\left(1+\cos\frac{L\pi}{M}\right)\cos\frac{KL\pi}{M}E(L)+E(0)\right] . \qquad \text{(III-48)}$$

The out-of-phase or qua-spectrum is given by:

$$W(K) = \frac{\delta_K}{M}\left[\sum_{r=1}^{M}\left(1+\cos\frac{L\pi}{M}\right)\sin\frac{KL\pi}{M}F(L)\right] . \qquad \text{(III-49)}$$

The estimate of the coherence (see equation (III-34)) is given by:

$$R^2(K) = \frac{\left[Z(K)\right]^2 + \left[W(K)\right]^2}{V_u(K)\ V_w(K)} ; \qquad \text{(III-50)}$$

where $V_u(K)$ and $V_w(K)$ are the auto-spectra of the u_n and w_n series in the form of equation (III-41).

The phase lead of the function u_n over w_n is given by:

$$\Theta(K) = ARCTAN\ \frac{W(K)}{Z(K)} . \qquad \text{(III-51)}$$

Finally, the linear correlation coefficient, formed from equation (III-29), is of the form:

$$r_{uw}(K) = \frac{E(0)}{A_u(0)\ A_w(0)} ; \qquad \text{(III-52)}$$

where $A_u(0)$ and $A_w(0)$ are the auto-covariance functions of u_n and w_n at zero lag (given by equation (III-46)).
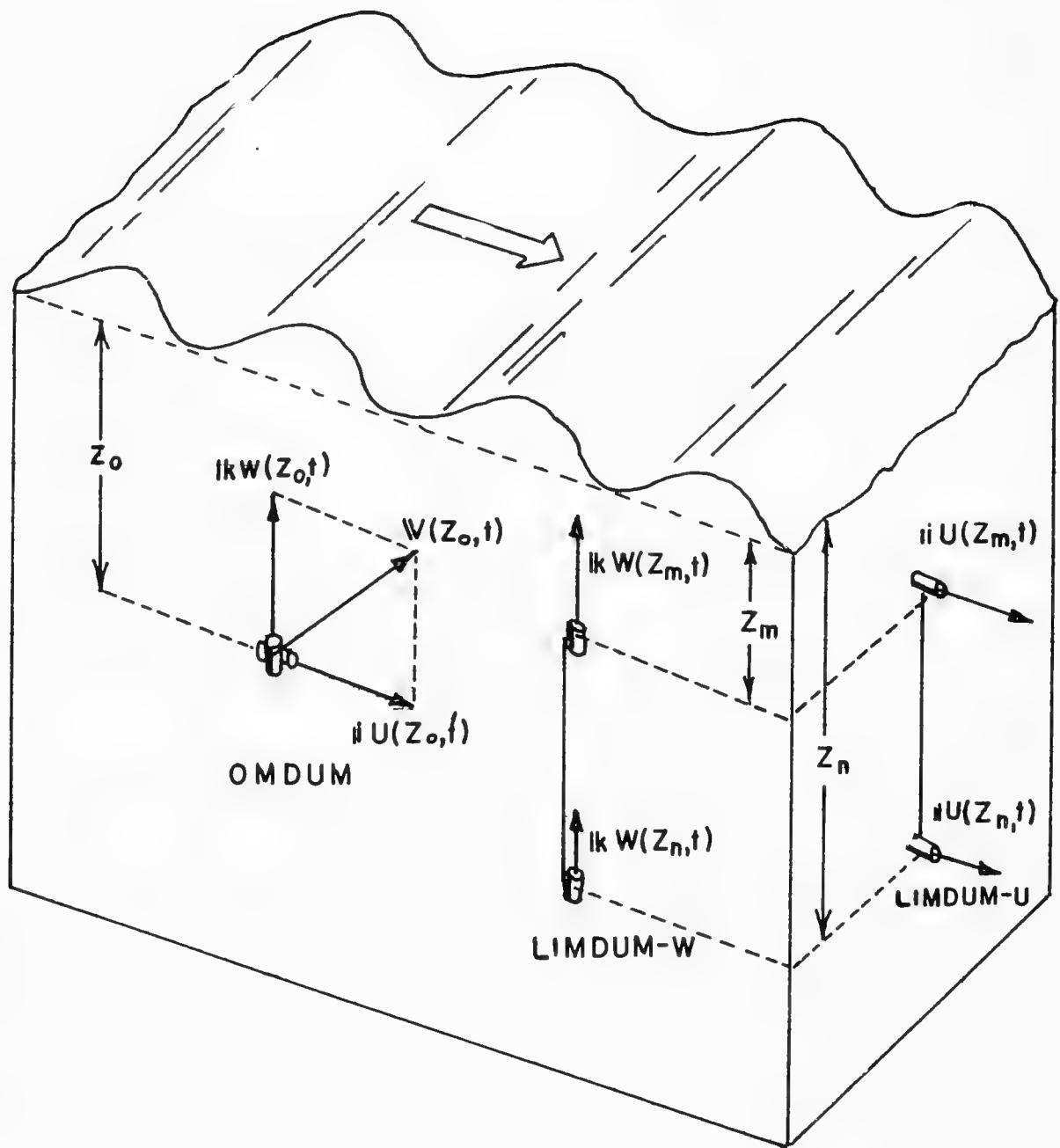
Various Modes of Wave Motion Observable with the Different Wave Meters.

Figure III-4

Procurement of Statistical and Physical Parameters -- In the previous
sections the various definitions of the statistical parameters were pre-
sented. This section considers them as they apply to the data obtained
from the wave measurements and serve as a basis for the auto-spectra and
cross-spectra calculations. The two configurations of wave meters -- the
orthogonally mounted (OMDUM) and linearly mounted (LIMDUM) systems -- pre-
sent specific types of data. It is therefore proper to clearly define the
modes of measurement of the two systems.

1. Vector Representation. Picture an ocean whose surface contains wind
waves moving in the +X direction. The problem is to measure the motion in the
XZ plane, normal to the horizontal wave crests (see figure III-4). The
Eulerian vector representation of the two-dimensional, time-variable, particle
velocity at a geographical position and as a function of depth is:

$$\mathbf{V}(z,t)_{X_0 Y_0} = \mathbf{I}\, u(z,t)_{X_0 Y_0} + \mathbf{K}\, w(z,t)_{X_0 Y_0} \cdot \quad \text{(III-53)}$$

X_0 and Y_0 are the fixed coordinates and, for brevity, will be neglected in
further formulation. The XY plane defines the mean free surface of the ocean,
and Z is measured positive upward. Using the orthogonal or the linear wave
meters, there are several ways to measure the wave motions. These are shown
schematically in figure III-4.

With the OMDUM system, the horizontal and vertical velocities (u and w)
are measured simultaneously at n meters below the wave troughs. These
components are written as:

$$\mathbf{V}(z_n,t) = \mathbf{I}\, u(z_n,t) + \mathbf{I}\mathbf{K}\, w(z_n,t) \cdot \quad \text{(III-54)}$$

Note the inference, from the initial statement that the waves are moving
in the +X direction, that the u and w velocities are associated with a single
wave train. This is not actually the case; and, as shown in chapter V, deter-
mining the origin of the motions detected with the wave meters can be difficult.
Spectrum estimates of the record, however, render much assistance in the analysis.

With the LIMDUM system a pair of horizontal or vertical velocities are
measured simultaneously at two depths on the Z axis (figure III-4). The nota-
tion for the pair of horizontal components is:

$$u(z_n,t) \quad \text{AND} \quad u(z_m,t) \cdot \quad \text{(III-55)}$$

For the vertical components the rotation is:

$$w(z_n,t) \quad \text{AND} \quad w(z_m,t) \cdot \quad \text{(III-56)}$$

The vertical spacing of the cylinders is $Z_m - Z_n$ meters. With this system one can measure instantaneous vertical shear of horizontal velocities given as:

$$\frac{\partial u}{\partial z} \sim \frac{u(z_n,t) - u(z_m,t)}{z_m - z_n} \; . \qquad (III-57)$$

2. Variance. The variances of the orthogonal pairs, using equation (III-15), can be represented as:

$$\sigma_u^2 = \overline{\left[u'(z_n,t)\right]^2} \text{ AND } \sigma_w^2 = \overline{\left[w'(z_n,t)\right]^2} \; . \quad (III-58)$$

Using equation (III-38):

$$u(z_n,t) = \bar{u}(z_n) + u'(z_n,t) \; . \qquad (III-59)$$

The $\bar{u}(z_n)$ is the mean value of $u(z_n,t)$ averaged over the sampling period T.

The variances of the spatially separated data pairs, from equation (III-55), are therefore:

$$\overline{\left[u'(z_m,t)\right]^2} \quad \text{AND} \quad \overline{\left[u'(z_n,t)\right]^2} \; , \qquad (III-60)$$

and similarly for the vertical velocity components.

The variances of the velocity components are proportional to dyanmic pressures (see appendix A) and also to the turbulent kinetic energy associated with motion in a particular component direction. Hence, the variances allow estimation of the spatial distribution of kinetic energy. Application of this concept is discussed in chapter V.

3. Linear Correlation Coefficient. The linear correlation coefficient, defined by equation (III-29), is given for the orthogonal components $u(z_n,t)$ and $w(z_n,t)$ as:

$$r_{uw} = \frac{u'(z_n,t)\, w'(z_n,t)}{\left\{\left[u'(z_n,t)\right]^2 \left[w'(z_n,t)\right]^2\right\}^{1/2}} \; . \qquad (III-61)$$

The term in the numerator is the covariance function at zero lag given by equation (III-28). This parameter denotes the amount of correlation between the orthogonal velocity components.

63

A corresponding coefficient (γ_{uu} or γ_{ww}) can be defined for the pairs u_m, u_n AND w_m, w_n and the obvious substitution can be made in equation (III-61). This function can now be interpreted as a spatial correlation indicator. In other words, the "spatial coherence" of the motions at points at various separations within the waves is indicated by the magnitude of the coefficient.

Miscellaneous Data Analysis -- Aside from the spectrum analysis programs, two other simple and useful computer programs were used to provide information about the time series data by rendering it more suitable for visual inspection of some of its more obvious statistical attributes. These programs involved histogram construction and progressive vector diagram calculation.

1. Histogram Construction. This simple digital computer program makes a frequency or population sort of N data points (sampled at equally spaced time intervals ΔT) from a time series record. The data points are sorted and placed into compartments associated with their individual magnitudes (in equal increments) and, in the case of velocity values, with their signs. From this sort of the tabulation and plotting of the equi-time-spaced interpolated data, the shape of the skewness of the distribution can be assessed to indicate how much the wave data deviate from the Gaussian. A few histograms were prepared on samples of the wave data, and a brief discussion is given in chapter IV. A listing of the histogram Fortran computer program is given in appendix E.

2. Progressive Vector Diagram Calculation. This program converts a time-pair sequence of two orthogonal vector components into a new series of data points. These points, if represented in the two dimensional plane, delineate the consecutive "head-to-tail" positions of the sequence of vectors represented by the time series. This program produces the vector plotting data on punch-cards, which can then be used in conjunction with an automatic plotting machine to produce a diagram for visual study. The plots portray roughly either the possible Lagrangian paths of the water particles, if the vector representation is in the horizontal plane XY; or the possible orbital trajectories, if the vectors are representative of motion occurring in a vertical plane XZ. Moreover, the plots show clearly the amount of mean flow present, and any gross variation from the mean (i.e., any trend) occurring during the sampling period. This technique was applied to data obtained from measurements of the horizontal current at the Buzzards Bay Entrance Light Station over periods of several days. Further discussion of this analysis is included in chapter IV. The computer program of this plotting data generation is given in appendix E.

Sources of Error Introduction

In the preceding summary of the data reduction procedures, some of the steps involved are quite critical to the quality of the processed data. This section discusses the errors which may be introduced into the data processing from the time the data are abstracted from the strip chart
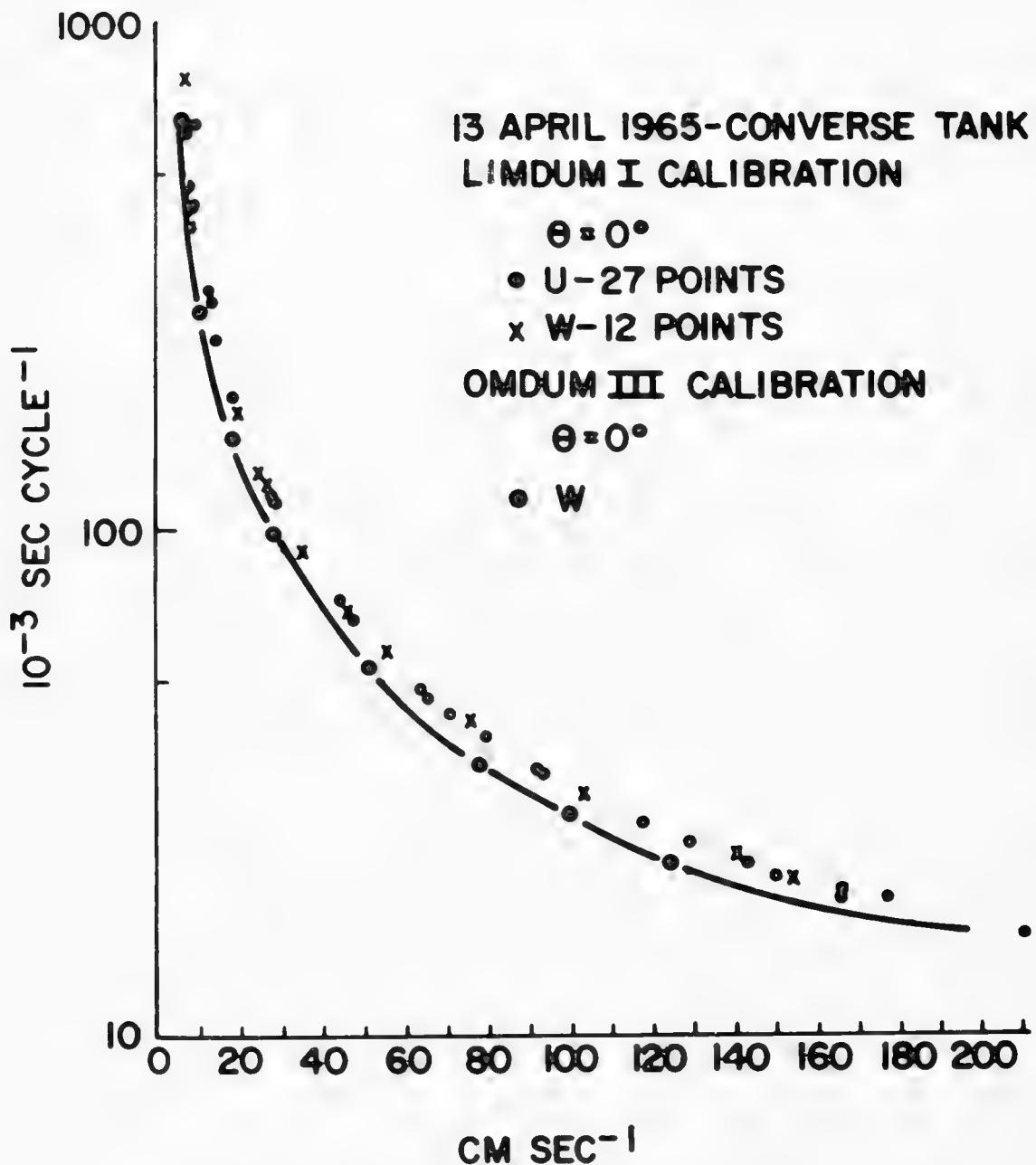
Calibration Curve Showing Inverse Relationship Between Flow Speed and Time
Spacing of Voltage Pulses.

Figure III-5

recorder to the final presentation. These include errors in editing, data tape reading, and possible biasing associated with interpolation and final computations. Errors in velocity measurement incurred by the wave meters or induced by the strip chart recorder are more fittingly considered in chapter V after we have seen some of the field results.

Data Editing -- The hand editing of the primary raw data tapes (see figure II-7) was a straightforward procedure. This step was critical, however, in that it provided information needed by the person reading the tapes on the film reader. Explicit directions were written on the tapes concerning the sense of the voltage pulses in relation to the sign of the associated velocity values and the tape speeds.

The most serious error that can be introduced into the wave data is associated with the reading of the raw data tapes using the Telerecordex film reader. The crux of the problem lies in the fact that the linear spacing of the voltage spikes on the data tape varies inversely with the fluid flow driving the impeller. This is shown from a calibration curve (figure III-5) where voltage pulse separation is plotted against flow speed. This inverse or hyperbolic relationship occurs because the frequency of the impeller varies directly with fluid velocity (as shown by the calibration curves in figure (II-21). Hence, the period of impeller rotation (or the time spacing between consecutive voltage pulses) is inversely related to the fluid flow. At increasingly higher flow speeds, the difficulty in resolving and measuring the spacing of the pulses rapidly increases. The strip chart recorder speed (1, 5, 20 or 100 mm sec^{-1}) was adjusted to give the pulse resolution, while at the same time not wasting chart paper.

Lack of concentration and precision on the part of the person running the hairline marker over the tape reader can result in serious timing errors; hence, corresponding serious velocity errors. The problem is compounded by the fact that, in the range where high repetition rate of pulses renders the reading most difficult, the velocity values are the largest. Also, since the high velocity values give rise to the high frequency voltage spikes, and since the paper feed is run at maximum speed in this range, the result is a lowering in the optical density of the trace due to the high pen speed across the tape. This makes resolution of the voltage spikes even more difficult.

This increase of errors with higher velocities occurred in the early data series of BBELS-5 and BBELS-7 (see chapter IV). In the tabulations of velocity data, a small percentage of points displayed a disturbingly large scatter at peak velocity values above 60-80 cm sec^{-1}. These peak values occur on wave records obtained both during high wind speeds and with the wave meter positioned near the surface. The scatter was predominantly at the peaks of the wavelike oscillatory motions. The few spurious values were as much as 10-15 percent above or below the normal fluctuation of the velocities. The punch-cards containing these spurious values were removed from the card deck of the uninterpolated data.
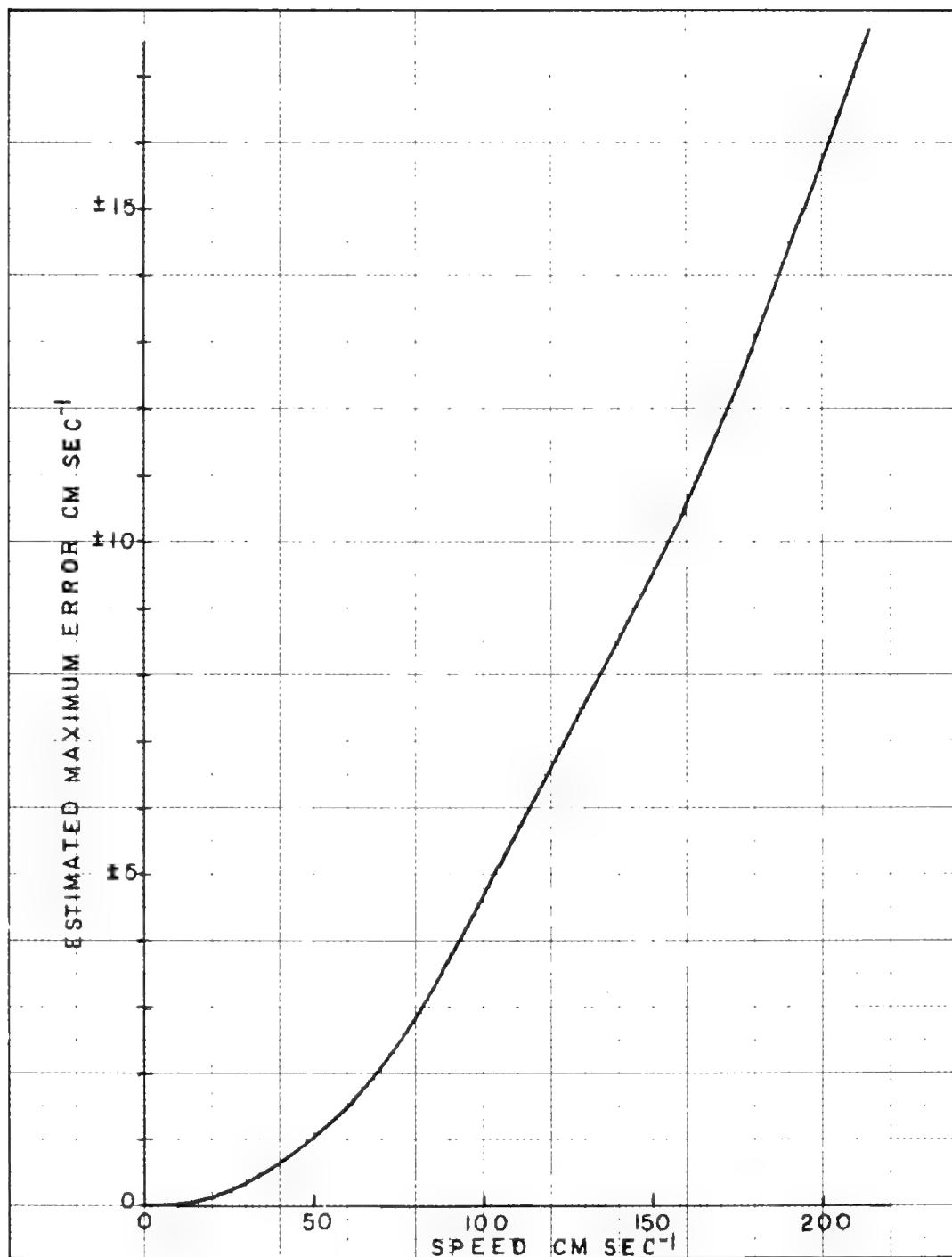
Estimated Error in the Determined Velocity as a Function of Velocity.

Figure III-6

An experiment was run during calibration tests in the Converse tank
(see chapter II) to further examine this source of error. In an acceler-
ation test the OMDUM III meter was towed parallel to the u meter axis.
Over a period of about 14 seconds, the meter was accelerated from rest to
about 300 cm sec^{-1} and then decelerated to rest again. At velocities
above 150-180 cm sec^{-1}, the recorder (running at the maximum tape speed
of 100 mm sec^{-1} and full pen darkness) displayed a blurred trace, making
visual resolution difficult. An attempt was made to read the tapes. The
results of the data record in the range from 200-300 cm sec^{-1} were disas-
trous. At about 150 cm sec^{-1}, the range of scatter of the points was
almost 10 percent of the mean value. Above 200 cm sec^{-1} the scatter at-
tained about 30 percent of the mean magnitude of the velocity. Below
150 cm sec^{-1} the data seemed increasingly well-behaved, with few or no
spurious points appearing in velocity ranges below 110-120 cm sec^{-1}.

In the estimate of both the variance and the auto-spectra, the over-
all contribution of errors by a small number of spurious points is mini-
mized because of the averaging processes involved. Since the errors are
caused by human reading of the data record, they tend to be random, except
that they do occur mostly at the positive and negative peaks of the wave
motions. These errors would most likely contribute a relatively small
amount of energy to the higher frequency bands of the spectra. This is
because the spurious rises and falls of the points occur abruptly during
the period of sampling (i.e., generally at 0.2-second time intervals).
The covariance and cross-spectra, however, are liable to be more sensitive
to spurious fluctuations, in a manner discussed later in this section.

Data Tape Reading -- The resolution of the tape reading device (Tele-
reader) is 403 counts per inch, or about 15.87 counts per mm. According
to the manufacturer (Telecomputer, Inc.), and also in the opinion of
personnel reading charts, the random error in reading the horizontal
position of the vertical pulses is well within 5 counts or ± 0.158 mm.
(It was indicated by the service representative that, with practice,
one could read within 3 counts; but, for purposes of discussion, assume
the former value). This means that for a chart speed of 100 mm sec^{-1}
(which gives the greatest pulse spacing) the time of the pulse interval
may be accurately determined to within ± 1.58 milliseconds. Since the
voltage pulse spacing is a hyperbolic function of time, the error or
uncertainty in the velocity estimate grows larger with increased velo-
city. Figure III-6 shows the error in the estimated velocity based on
a constant tape reading error of ± 0.158 mm (at 100 mm sec^{-1} tape speed),
equivalent to a time error of ± 1.58 milliseconds. Since the general
shapes of all wave meter calibration curves are similar, (e.g., figure III-5),
this graph (figure III-6) provides a suitable error estimate for all wave
meters.

The slope of the curve in figure III-6 is monatonically increasing (in
fact, as the square of the current speed); thus, at the higher velocities
(upwards of 150-200 cm sec^{-1}), errors could account for sizable percentages
of the total value. This study is concerned, of course, with the velocity

Figure III-7B   BBELS-9 (023)
Vertical Velocity w   0.5 m

Original $\phi_w(f)$ ———

Reread $\phi_w(f)$ — — —

$N = 1341$
$\Delta T = 0.2$
$m = 50$

Original $\sigma_w^2 = 739.1$

Reread $\sigma_w^2 = 734.7$

Figure III-7A   BBELS-9 (023)
Horizontal Velocity u   0.5 m

Original $\phi_u(f)$ ———

Reread $\phi_u(f)$ — — —

$N = 1341$
$\Delta T = 0.2$
$m = 50$

Original $\sigma_u^2 = 555.1$

Reread $\sigma_u^2 = 583.4$
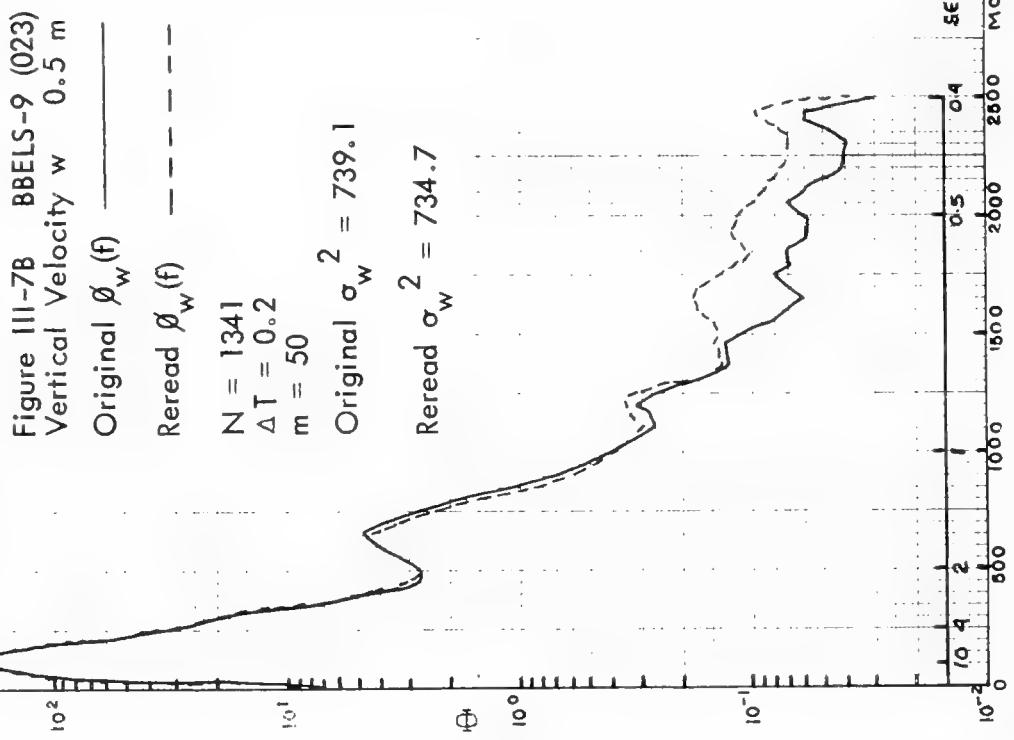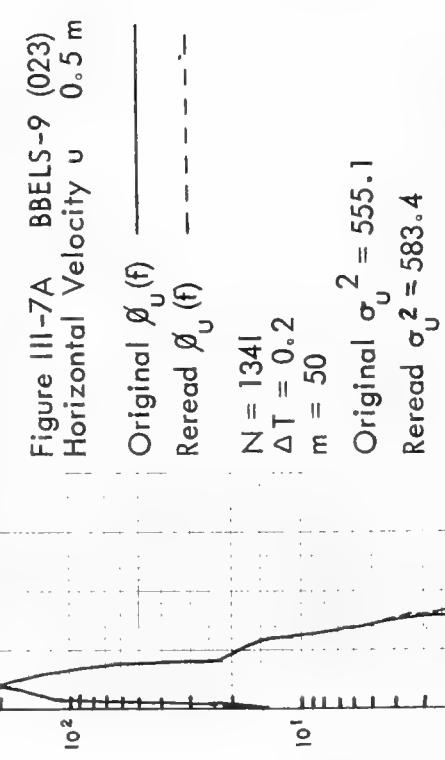
Auto-spectra of Original and Re-read Velocity Data.

Figure III-7

range from 0 to about 125 cm sec^{-1}. The relative error for the upper value is about ± 6 percent and drops off rapidly with decreasing speed; e.g., at 50 cm sec^{-1} the error is about ± 2 percent.

Thus there is a certain amount of subjectivity involved in abstracting the velocities from the raw data tapes. For better or worse, much of the responsibility for successful data abstraction rests with the man operating the film reader. It proved beneficial to attempt to convey to him the nature of the measurements and the data. With this background he was able to anticipate the critical areas (such as keeping the data pairs exactly on the same time base).

The repeatability of the data-reading step was checked by re-reading a raw data tape. To ensure an unbiased experiment, the person re-reading the tape was unaware of the purpose of the experiment. The re-evaluation was made on the 1,341 data pairs from (023) 3BE1S-9 (0.5 m I). (The Roman numeral after the depth refers to the number of the observation at that depth.) This sample was obtained near the surface; hence, it displayed a maximum number of high frequency surface fluctuations. It also contained a generous number of data points. The aim was to compare the gross velocity values; but, even more important, to compare the variances, covariances, and spectra.

The results of the data-reading check were, in general, very encouraging. Table III-2 lists the pertinent parameters and compares the read and re-read velocity series. The variances, covariances (at zero lag), and correlation coefficients are all within a few percent of each other. Likewise, the peak auto-spectra and cross-spectra values occur at about the same frequencies. A direct comparison of the two pairs of auto-spectra, Φ_u and Φ_ω, is shown in figures III-7A and III-7B. The ordinate is the spectral density (cm^2 sec^{-1}); the abscissa is given in millicycles per second (mcps) for frequency and in seconds for period.

Examine first the Φ_u curves (figure 7A). The low frequency regions (below 1500 mcps) are almost identical, whereas in the higher ranges the curves are somewhat divergent. The major peak at 100 mcps and a lesser peak occuring at 650 mcps are clearly delineated by both curves. The Φ_ω spectrum displays remarkable similarity over the whole frequency range, displaying the identical peaks at 100, 650, and 1200 mcps, and similar profiles through 2500 mcps. Thus, with conscientious use of the Telereader, the recorded data can be quite faithfully reproduced from the original tapes.

The velocity data, after being preliminarily processed (including interpolation and corrections), are examined in terms of their auto-covariance and covariance functions. From these functions the corresponding auto-spectra and cross-spectra are estimated. It should be emphasized that computations dealing with the estimates of the covariance function and the covariance spectra between two simultaneously recorded variables demand a maximum amount of accuracy in the determination of the two functions relative to the same time base. Errors such as spurious single values, which may be few in number compared to the total sample, can be easily tolerated in the estimates of the auto-covariance function and the auto-covariance spectra. However, in the estimates

Table III-2.   Comparison of Statistical Parameters Obtained from Velocity
            Data Read and Re-read on Telecordex Film Reader

Sample: BBELS - 9, 26 January 1965
Depth : 0.5 m
Time : 1145-1150

	Read	Re-read
Variance (cm^2 sec^{-2})	555.1	583.4
	739.1	734.7
Covariance (cm^2 sec^{-2})	-333.5	-340.1
Peak Auto- Spectra (cm^2 sec^{-1})	217 (@ 100 mcps)	226 (@ 50 mcps)
	258 (@ 100 mcps)	251 (@ 100 mcps)
Peak Co- Spectra (cm^2 sec^{-1})	-162 (@ 100 mcps)	-165 (@ 100 mcps)
Correlation Coefficient	-0.521	-0.519

of the covariance function and the covariance spectra, the higher order
errors can become of lower order, depending upon their degree of non-random-
ness. This is caused by the phenomenon of correlation, in which relatively
small deviations of the data pairs (which tend to be in or out of phase) are
highly magnified in the process of taking the products of time sequence pairs.
Thus, errors in the individual factors can greatly bias the covariance function.
Because of this great sensitivity of the covariance function and the covariance
spectra, great care must be taken to insure simultaneity of the two variable
records. This requires keeping the data pairs on the same time base after they
are abstracted from the two-channel tape record.

As will be demonstrated in chapter V, any artificial phase lead or lag
introduced into one time series with respect to the other can cause large
changes in the covariance. An inaccurate covariance estimate can, in turn,
cause misinterpretation of the fundamental processes.

Biasing Errors -- Another processing stage that is critical to the final
data output is the linear interpolation. The question naturally arises: how
much is the original data distorted by linear interpolation? The justification
of linear interpolation is based on the assumption that one has sampled a vari-
able closely enough so that linear interpolation does not distort the pattern
protrayed by the original raw data points.

Figure III-8 shows plots of both the uninterpolated w velocity points
(lower curve) and the interpolated data points (upper curve). This velocity
record is taken from (057A) BEELS-11 at a depth of 0.5 meter. The interpola-
tion time interval is 0.2 second. The calibration curves of all the wave meters
indicate that, for flow speeds greater than about 25 cm sec^{-1}, the period
between voltage pulses is less than the interpolated sampling interval. Thus,
for the upper range of speeds nominally peaking at 60-80 cm sec^{-1} (occurring in
moderately sized waves and with the sensor close to the surface), no resolution
is lost by interpolation. Examination of the points in figure III-8 indicates
little distortion in the interpolated velocity pattern. On this basis it was
assumed that a linear interpolation having a 0.2 second time interval gives a
reasonable portrayal of the velocity pattern.

The linear interpolation for most of the wave meter data was made at 0.2
second intervals. In general, the value of 0.2 second was well chosen, since
the wave motions within the upper 3-5 meters of depth supplied data points of
the order of time spacing of 0.2 second or less. Note from figure III-5 that
the repetition rate of the impeller at speeds of about 0.2 second is equivalent
to a velocity of about 25 cm sec^{-1}. For records of velocity with relatively
low variances (e.g., records below 4-5 meters depth, with average surface wave
conditions), the spacing of the data points becomes, on the average, greater
than 0.2 second. In view of this, a few early wave records were interpolated
at 0.3, 0.5, and 1.0 second intervals in an attempt to be more consistent with
the data point density. The longer time spacing, however, made negligible
difference in the calculation of the variance and spectra when compared with
statistics produced from the same records using a 0.2 second interpolation time
spacing. The lengthening of the sampling time produces a shortening of the
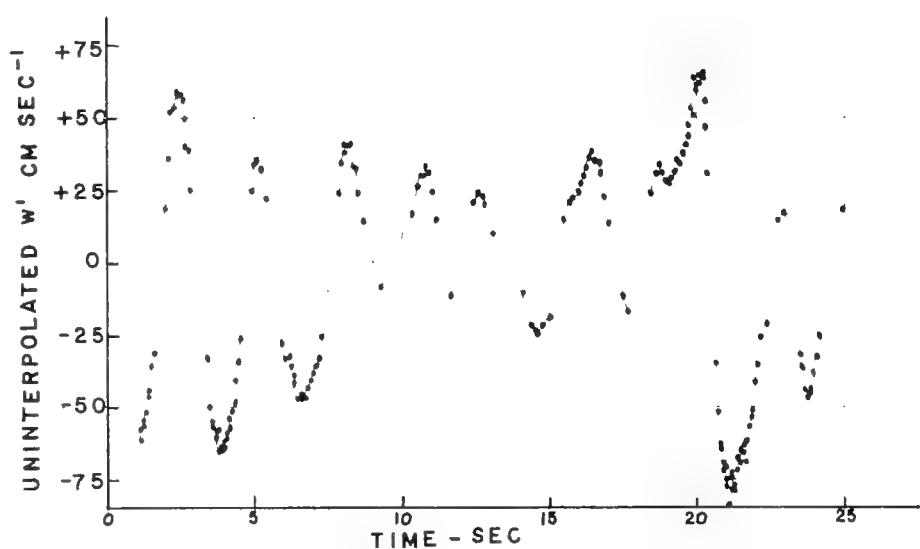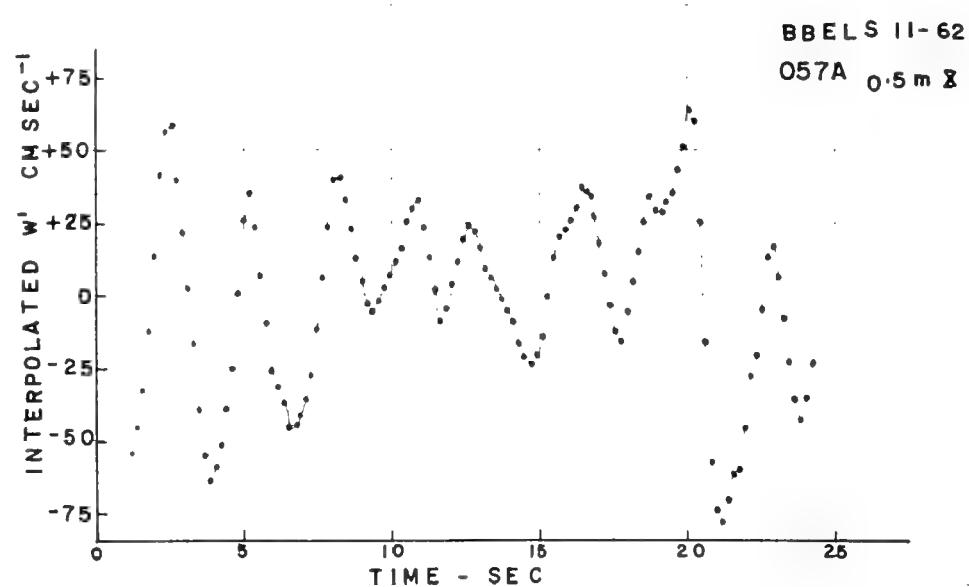
Plot of Uninterpolated and Interpolated Velocity Data (BBELS-II, Serial 057A, 0.5 m)

Figure III-8

frequency scale, as shown by equation (III-2). But at the deeper depths, where the low particle velocities supply a low density of data points, the rapid fluctuations are filtered out anyhow, leaving the effects of the low frequency swells to dominate the variance contribution. Thus, the relatively high sampling rate may still be used to portray the ambient oscillations at this depth without biasing the spectral character of the swell or longer wind wave motions.

There is, however, a subtle form of potential biasing inherent in the linear interpolation which is associated with low variance velocity records. This is illustrated in figure III-9, which represents a 25 second segment of the vertical velocity record of (040) BBELS-11 (3.5 m I). The lower graph is a plot of the uninterpolated velocity values obtained by conversion from the raw data tapes. The upper curve represents the linearly interpolated, equally time spaced, data points obtained from the bottom curve. The upper curve displays the same slight smoothing effect as in figure III-8. However, note that the amplitudes of the velocity function are relatively small; i.e., the peaks occur at less than 30 cm sec^{-1}. As was discussed in chapter II, the threshold velocity of OMDUM III and LIMDUM I is between 5 and 7 cm sec^{-1}. Hence, when the instrument is recording oscillatory motions with relatively small variance (as displayed in figure III-8), there is a certain fraction of time when the instrument produces no output. This fraction increases as the oscillatory motions grow weaker.

The linear interpolation method introduces an obvious error into the final record (upper curve) as demonstrated for the time interval AB. Although only one point occurs between A and B (in the lower curve), the interpolation places 13 points of approximately equal velocity value. It is obvious that, with a threshold of sensitivity of 5-7 cm sec^{-1}, the 13 points are not very representative of the actual flow. In fact, it is probable that the velocity value became negative between A and B. If a zero crossing is indicated by a sign reversal of consecutive velocity values, the interpolation error is much less, since a more probable portrayal of the velocity function would be obtained.

The biasing effect between points A and B only occurs when the data points are of low density. It would not occur with high velocity fluctuations (i.e., when there is a large variance), since the ducted meters produce a higher data point density (average number of points per unit time) the higher the variance of the sample. This is readily seen by comparing the uninterpolated traces of figures III-8 and III-9. This biasing would probably affect the mean values of the records, since the mean is calculated from the equally spaced interpolated data. This error in the mean should be small, however, since it should average out algebraically over the record. Also not that these biased values are always of the order of 5-7 cm sec^{-1} or less.
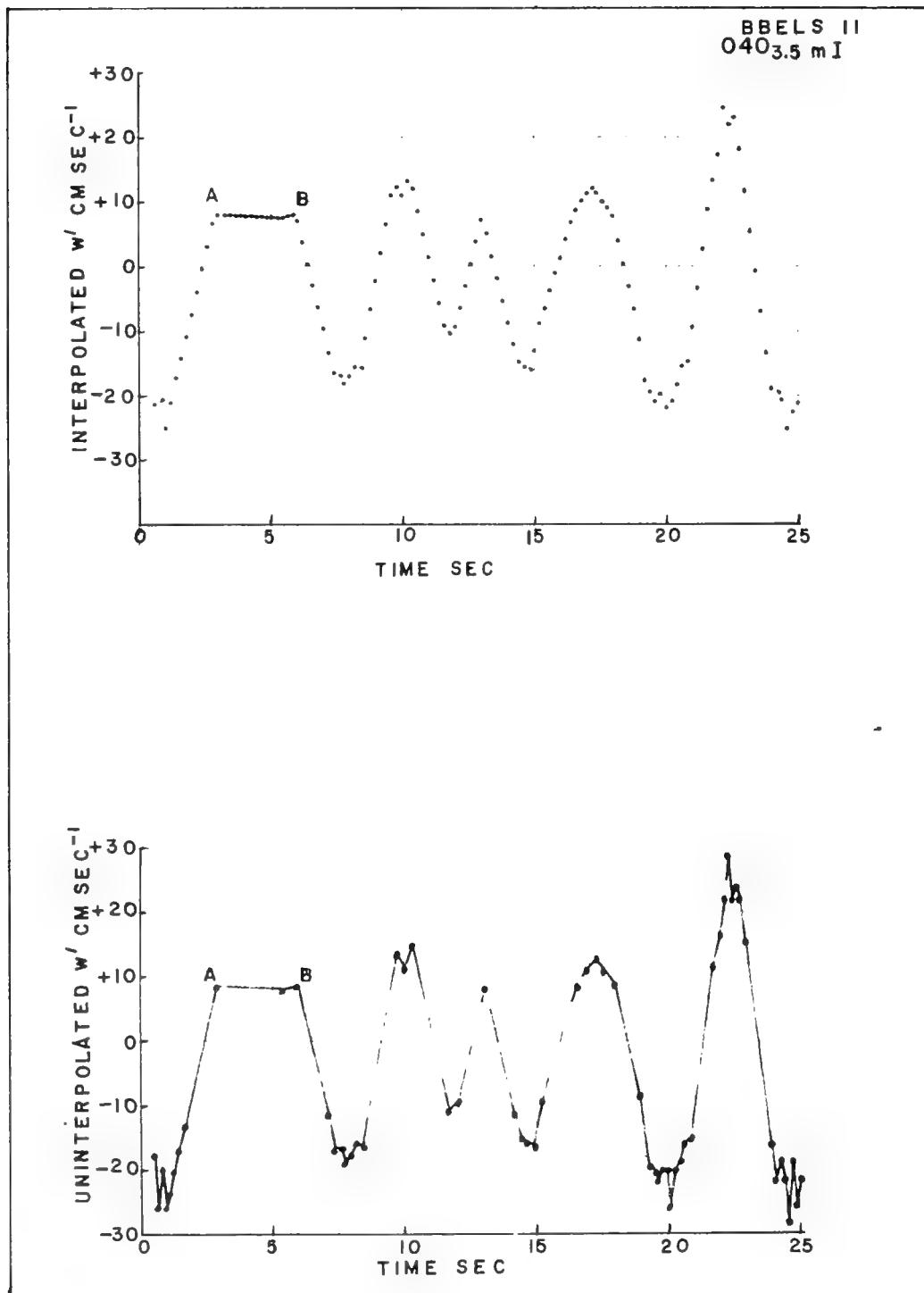
Plot of Uninterpolated and Interpolated Velocity Data (BBELS-II, Serial 040, 3.5 m).

Figure III-9

This bias is probably felt most in the covariance function. Even if the biased regions are randomly dispersed throughout a record pair, the spurious d-c effects (because of correlation) would not necessarily tend to average out. Further discussion of the biasing problem is best deferred until the examination of some actual field data.

Errors in Bookkeeping -- Other sources of minor errors included improper tape labeling, accidental switching of title format cards, etc. -- errors of bookkeeping for the great number of data samples, card decks, and the like. Minimizing these errors requires careful and systematic procedures, backed up by the drudgery of checking and double-checking all data at each step of the reduction and processing.

CHAPTER IV

FIELD OBSERVATIONS

This chapter presents a discussion of the various wave observations, emphasizing the equipment and techniques utilized. Preliminary wave measurements made from a Navy pier in Narragansett Bay are briefly summarized. The remainder of the chapter is devoted to the various observations made from the Buzzards Bay Entrance Light Station.

In reporting these experiments, an effort is made to describe precisely the method of using the wave meters, paying careful attention to the manner of instrument suspension in the ocean. A knowledge of the methods used to make the observations is important, since the assessment of the instrument response to wave motions presents obvious difficulties. The calibration procedures described in chapter II involved no measurements of real ocean waves along with simultaneous observations employing an independent method. Hence, it was necessary to depend, to a certain extent, upon the results of the field measurements to evaluate the wave meters.

The field observations made from the Buzzards Bay Entrance Light Station (for brevity called BBELS) may be divided into three catagories. First are the primary wave measurements using the various wave meter systems (OMDUM II and III, and LIMDUM I) discussed in chapter II. The second type are those observations that provide direct supplementary information regarding the meteorological and oceanographical conditions (wind velocity and estimates of sea and swell) at the time of the wave measurements. The third catagory is associated with relatively long term complementary observations of the oceanographic "climate" around the BBELS.

Since it is one aim of this report to explore and, if possible, to demonstrate both the feasibility and value of making oceanographic observations from ocean tower facilities such as BBELS, the pertinent features of the BBELS facility are described. Information is also presented regarding the general characteristics of the wind and wave conditions and of the regional geography. A discussion of the current and free surface tide level variations is based on actual observations made. In making tidal current measurements, information was also obtained regarding short term horizontal current fluctuations. This information was important in assessing the observed wave motions.

The presentation of the wave data posed some difficulty because of its quantity. The voluminous results were therefore condensed and summarized (see table IV-3 at the end of this chapter). Computer listings of the statistical data and plots of the auto-spectra are presented in appendix B. The data are discussed in chapter V.

71

Preliminary Wave Measurements in Narragansett Bay

Two series of preliminary wave measurements were made with the OMDUM I wave meter from a Navy pier in Narragansett Bay during May and August of 1963. These measurements were conducted primarily to determine the feasibility of using the orthogonally mounted ducted meter (OMDUM) design to study surface waves.

The experiments were conducted from the seaward (southwest) end of the pier at the NUWS still basin, which is located at Coddington Cove in the east passage of Narragansett Bay (see figure IV-1). Wave records could only be made when the wind was from the SSW to SWW directions. Otherwise, the wind-driven waves would have been grossly affected by refraction and defraction caused by the breakwater to the west of the still basin and the Navy piers to the south (figure IV-1).

The first experiment was conducted on 20 May 1963. The OMDUM I wave meter (shown in figure II-3) was supported by a vertical pipe 8 cm in diameter. This pipe was securely fastened to the cap log of the pier, which was about 2 meters above the mean free water surface. Since the supporting pipe was fastened at only one point, it displayed a slight horizontal oscillation (about 1-2 cm) in response to the waves moving past the meter. At the time of the wave measurements, estimates of the wind speed and direction, wave length, height, and direction were obtained. Since it was desired to measure wave particle motions in the vertical plane normal to the wave crests, care was taken to aim the horiztonal flow sensing component (the u meter) directly into the oncoming waves radiating from the southwest, and to place the vertical motion sensor (the w meter) in the exact vertical position.

The power supplies required for the electronics of OMDUM I and the two-channel Sanborn recorder were housed in the oceanography laboratory located about 100 meters from the end of the pier. The power and signal were relayed between the pier and the laboratory via a shielded, multi-conductor, weather-proof power cable.

This first experiment ended in failure. Shortly after recording commenced, the signal leads of the two meters shorted. The resulting electrical leakage caused cross-talk from one channel to the other, giving a garbled record on both the u and w channels. The brief two-channel record made prior to the failure clearly displayed wavelike oscillations associated with the components (similar to the upper trace of figure II-7). When the electrical short was repaired, the voltage supply was mistakenly plugged to the amplifier-oscillator circuit (see figure II-4), and the transistorized amplifier circuit was damaged beyond repair.

After electrical repairs were made to the OMDUM I system, wave measurements were resumed on 14 August 1963 at the still basin. The second experiment yielded results which were encouraging, and a brief resume of the preliminary results was published (Shonting, 1964 and 1965).

DEPTHS IN FEET
(F = 0.305 M)

SCALE OF KILOMETERS

STILL BASIN PIER
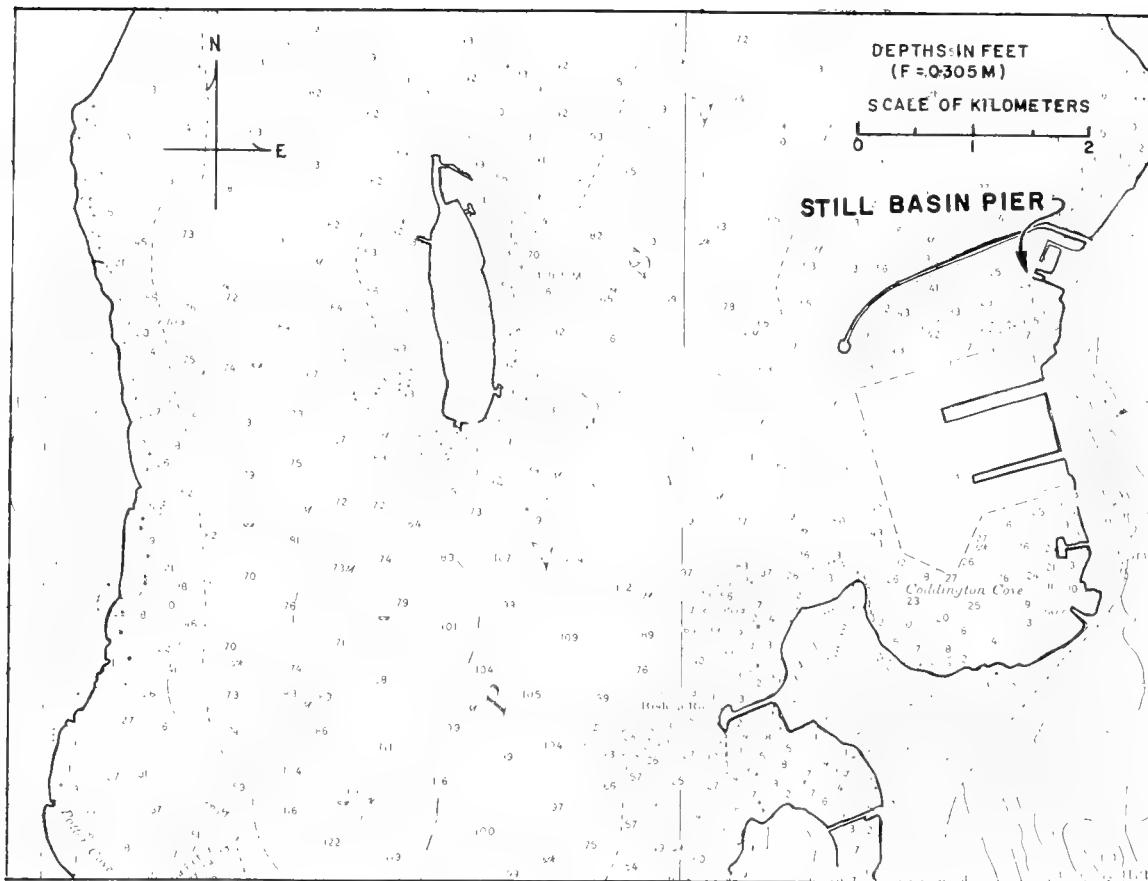
Location of NUWS Pier in East Passage of Narragansett Bay

Figure IV-1

This experiment was conducted with the OMDUM I system held by a vertical T-beam supported at two points on the pier. This support held the wave meter rigidly in place beneath the surface waves. As in the first experiment, the u meter was positioned normal to the crests of the waves. The meters were immersed to a depth of about 75 cm below the average trough level of the waves. The measured waves were well-developed; i.e., they exhibited clearly defined crests with a visually estimated period averaging about 1.5 seconds. The sky was clear, and the wind speed was about 9 m sec^{-1} from the southwest, allowing the waves to build up over a fetch of about 6 km. The wave height was estimated to be about 50-75 cm, with a wave length of roughly 5-7 meters. Since the water depth at the position of measurement was about 8 meters, the waves measured were considered essentially "short" or "deep water" waves (as defined in chapter II).

The voltage pulse record of the OMDUM I wave meter was processed; i.e., the consecutive voltage pulse distribution was measured and converted to u and w velocity components, using the procedures discussed in chapter III. A Tukey spectral analysis of the data was made. The period of sampling was 356.4 seconds. Use of an interpolated sampling interval of 0.3 second gave 1188 data pairs (of u and w) for analysis.

The variances of each velocity component σ_u^2 and σ_w^2 were 22.3 cm^2 sec^{-2} and 62.9 cm^2 sec^{-2}, respectively. Note that there is a relatively large difference in the magnitude of the variances of the orthogonal velocity components u and w. The covariance function at zero lag $\overline{u'w'}$ between the 1188 pairs of vertical and horizontal velocity components was calculated as -7.8 cm^2 sec^{-2}, providing an estimate of the magnitude and sign of the observed Reynolds stress. The linear correlation coefficient r between u and w was -0.21.

The auto-covariance and covariance spectra are shown in figure IV-2. The auto-spectra of both velocity components (Φ_u and Φ_w) show peaks at the frequency of the observed waves. The co-spectrum is shown by the negative curve. The area between the horizontal axis and the solid curve is the (negative) covariance.

The covariance function and the co-spectrum could have been caused by some spurious effect in the meter system. As a check to examine the extent to which the correlation function and the individual time series were stationary (see chapter II), the spectral analysis was re-run using varying percentages of the data. The values of the covariance function at zero lag were as follows:

Number of Data Points	Percent of Total Data Pieces	Covariance($\overline{u'w'}$) cm^2 sec^{-2}
1188	100	-7.8
1176	99	-7.9
792	66	-8.3
540	45	-9.3
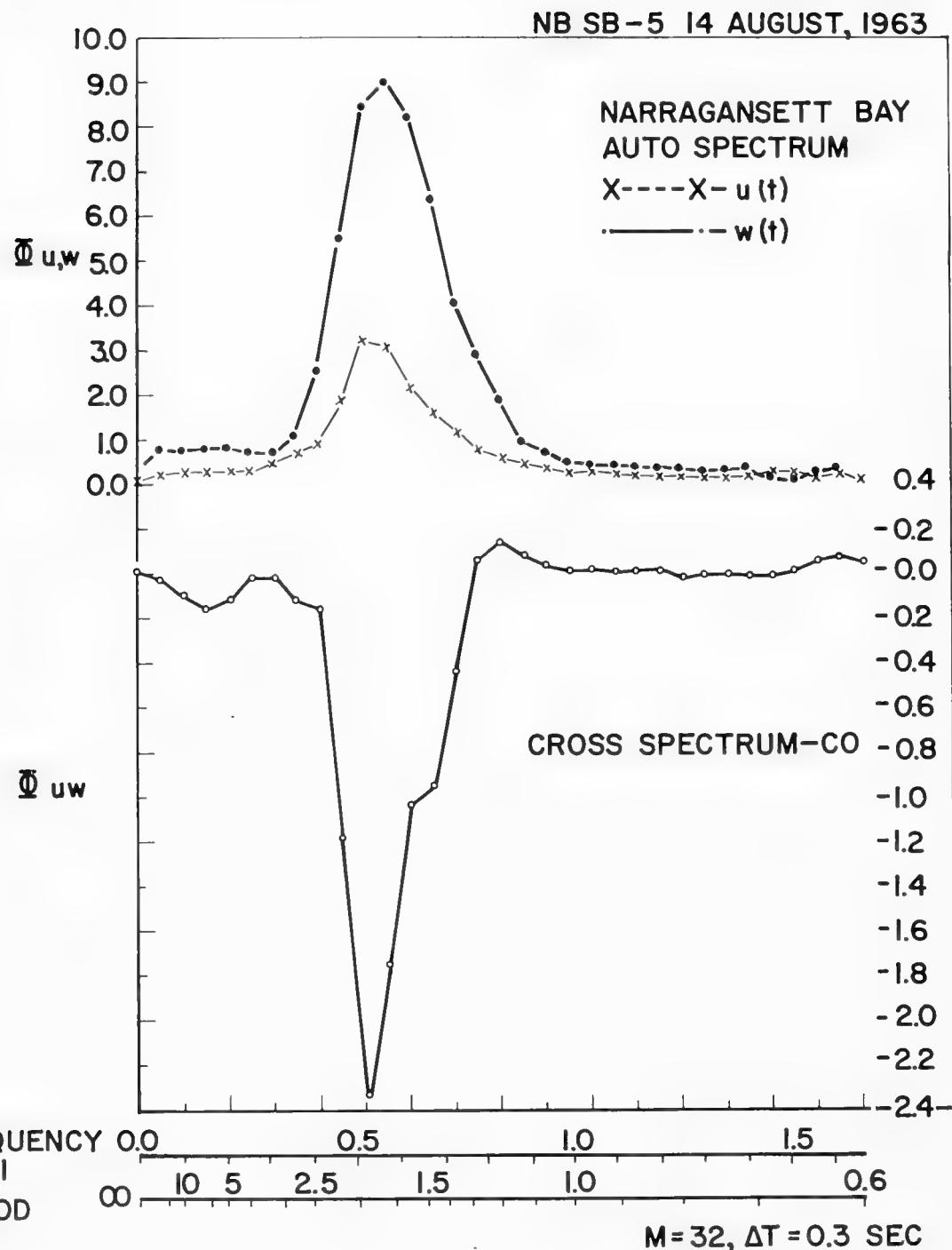
Auto-Spectra and Co-Spectra of u and w Particle Velocity Data
Obtained with OMDUM I

Figure IV-2

There does seem to be a small decrease in the covariance with time. However, no shifts in the peak positions of the spectra were obtained. Further discussion of the results of the spectral analysis are presented in chapter V.

These preliminary results showed that this type of instrument, however crude, can definitely sense and discriminate periodic oscillations associated with relatively small amplitude and high frequency (i.e., low energy) wind waves. Thus, the auto-spectra and cross-spectra of wave motions can be examined for their relationship to the physical processes occurring within the waves.

Further measurements of waves to substantiate these preliminary results could not be made from the Navy pier. Reconstruction made the pier facilities unavailable shortly after the above experiments were completed. Work was then concentrated on calibration (discussed in chapter II) and on possible wave meter modifications. It was also decided to explore the possibilities of making wave measurements under open sea conditions.

BBELS as a Platform for Open Ocean Measurements

The preliminary wave measurements in Narragansett Bay were far from perfect. The location of the pier, near a breakwater and large Navy docks, provided a rather unique environment in which the waves generated were likely to be quite different from those in the open ocean. It was therefore judged worthwhile to make measurements using the wave meters where local boundary effects would be minimized.

A suitable platform was the first requirement. The use of a ship as a platform presents numerous problems. The greatest is the distortion of the measured wave motions caused by ship response to the wave. Another involves the effect of vessel dimensions upon the field of motion around the vessel. This is a particularly complex problem if one is trying to measure a scale of fluctuating motion of smaller dimensions than those of the vessel (which is certainly the case for moderate sized wind waves). Tucker (1956) makes use of ship motions to record larger ocean waves by judicious use of vertical accelerometers, hull-mounted pressure gauges, and a shipborne computer. But this method is rather ineffective for measuring smaller wind waves.

The ideal platform from which to make measurements of motions associated with surface waves should: (1) provide minimum interference with the waves; (2) be fixed relative to the ocean bottom; and (3) be located far enough from the coastline to provide an approximate open sea environment. (See chapter II.) If there is an interaction of the platform with the environment, it should be quantititively assessed so that the effects can be neglected or subtracted out of the data. Also, since the majority of locally generated wind waves have wavelengths that are smaller in magnitude than the water depth, measurements should be made in a depth of water commensurate with the existance of relatively large deep water waves. Finally, at any site chosen to measure waves, one should have a general knowledge of the gross climatic and oceanographic environment.
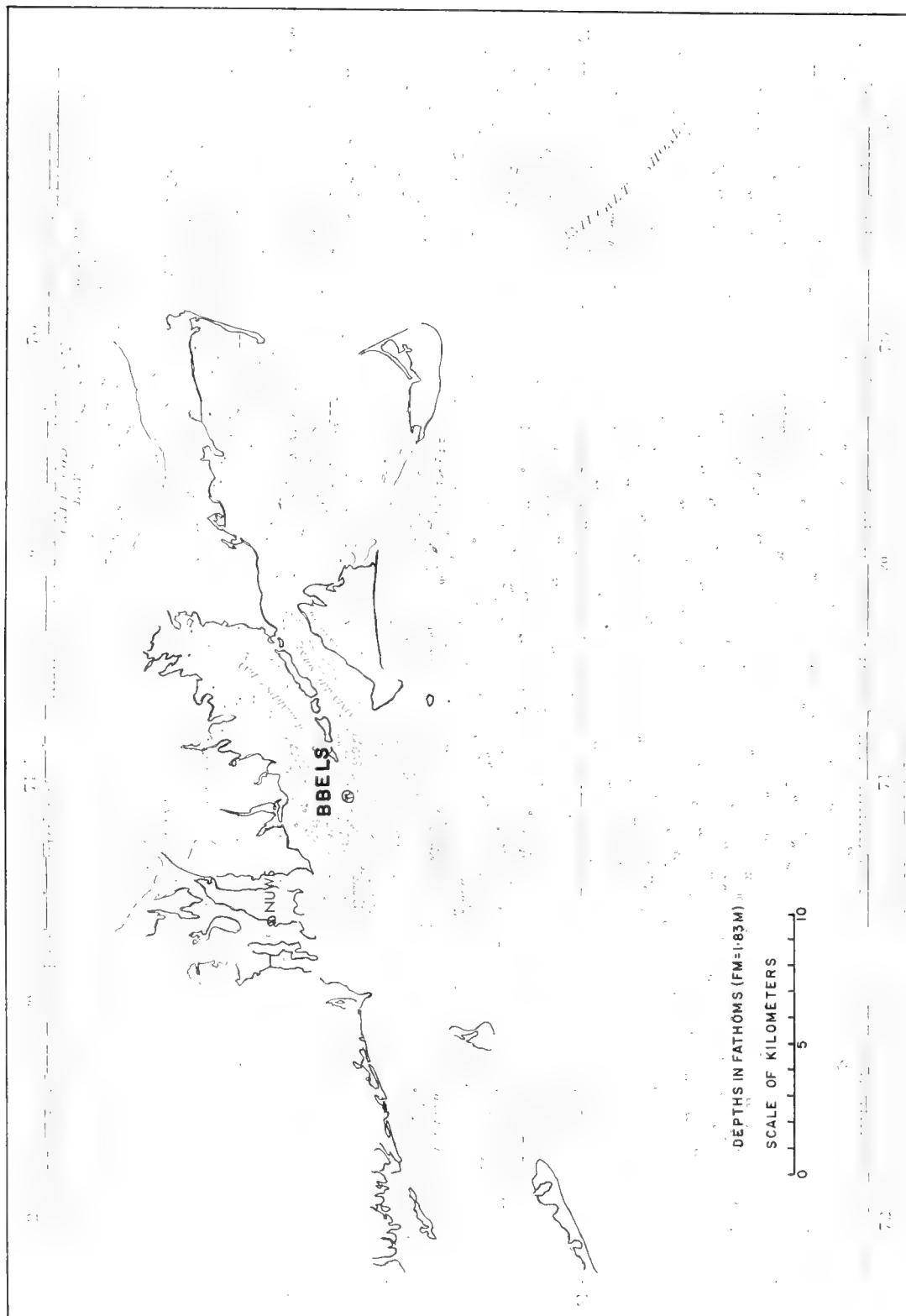
Location of Buzzards Bay Entrance Light Station (BBELS)

Figure IV-3

The Buzzards Bay Entrance Light Station (BBELS) was chosen as a platform from which to make the open ocean wave measurements. This structure, a manned light station maintained by the Coast Guard, is located at 41° 23.8' N and 71° 02.1' W -- about 7 km WSW of Cuttyhunk Island and about 12 km south of the Massachusetts coast. (See the reproduction of the Coast and Geodetic Survey Chart No. 70 in figure IV-3.) The depth of water at BBELS is about 20 meters. The light station, shown in figure IV-4, is a rigid steel platform supported about 24 meters above the water by four steel legs which are driven some 63 meters into the sandy bottom. The top deck (the roof of the house), serves as a helicopter landing pad. Because of the problems of transfer in the prevailing swell conditions, personnel are usually transported to and from the tower by helicopter in lieu of surface craft.

The light station is located 28 km, or about a 15-minute helicopter flight, from the Naval Underwater Weapons Research and Engineering Station at Newport, Rhode Island (see figure IV-3). Fortunately, a Naval Air Torpedo Unit was stationed at the Quonset Point Naval Air Station (located on the west side of Narragansett Bay) and could provide helicopter service to and from the tower for personnel and equipment.

As is shown in figure IV-4, the four main support legs (85 cm outside diameter) are interconnected with smaller piping both above and below the water line. The tower is thus a rigid structure, but at the same time offers little gross drag resistance to currents. More important, it is quite transparent to the trains of surface waves passing through the legs, particularly when the wavelengths far surpass the diameter of the cylindrical legs, which is most often the case. The station housing contains the aid-to-navigation equipment, power generators, and living quarters for the men. With its inherent stability, ample a-c power, winch equipment, and protected laboratory facilities, the light station provides an ideal platform for making a variety of oceanographical and meteorological measurements. During certain periods from 1962 to the present, both the Navy Oceanographic Office and the Coastal Engineering Research Center (formerly the Beach Erosion Board) have maintained various wave sensing probes for making observations throughout the year. Also, station personnel make daily samplings of the surface water temperature and salinity for the Woods Hole Oceanographic Institution.

Permanently installed in the tower laboratory is a bubble-type pressure recording tide gauge maintained by the Coast and Geodetic Survey (C&GS). Since the Coast Guard personnel aboard the BBELS keep a weather log much the same as on a vessel, a large backlog of information is available regarding the general meteorological environment. Wind, sea, and swell data are logged on a four hour basis. The wind data are obtained with an anemometer system (maintained by the Weather Bureau) mounted on the northeast corner of the main platform.

The gross bottom topography and land boundary configurations in the vicinity of the BBELS are delineated in figure IV-3. Depths are given in fathoms (about 1.83 m). The 10, 20, 30 and 40 fathom contours are depicted as broken lines. As shown in the figure, there is an unobstructed or "infinite" wind fetch of open ocean in the sector bounded by the azimuths 160° and 250° T. To the north and northwest, the fetch from the coast varies from 8-10 km.
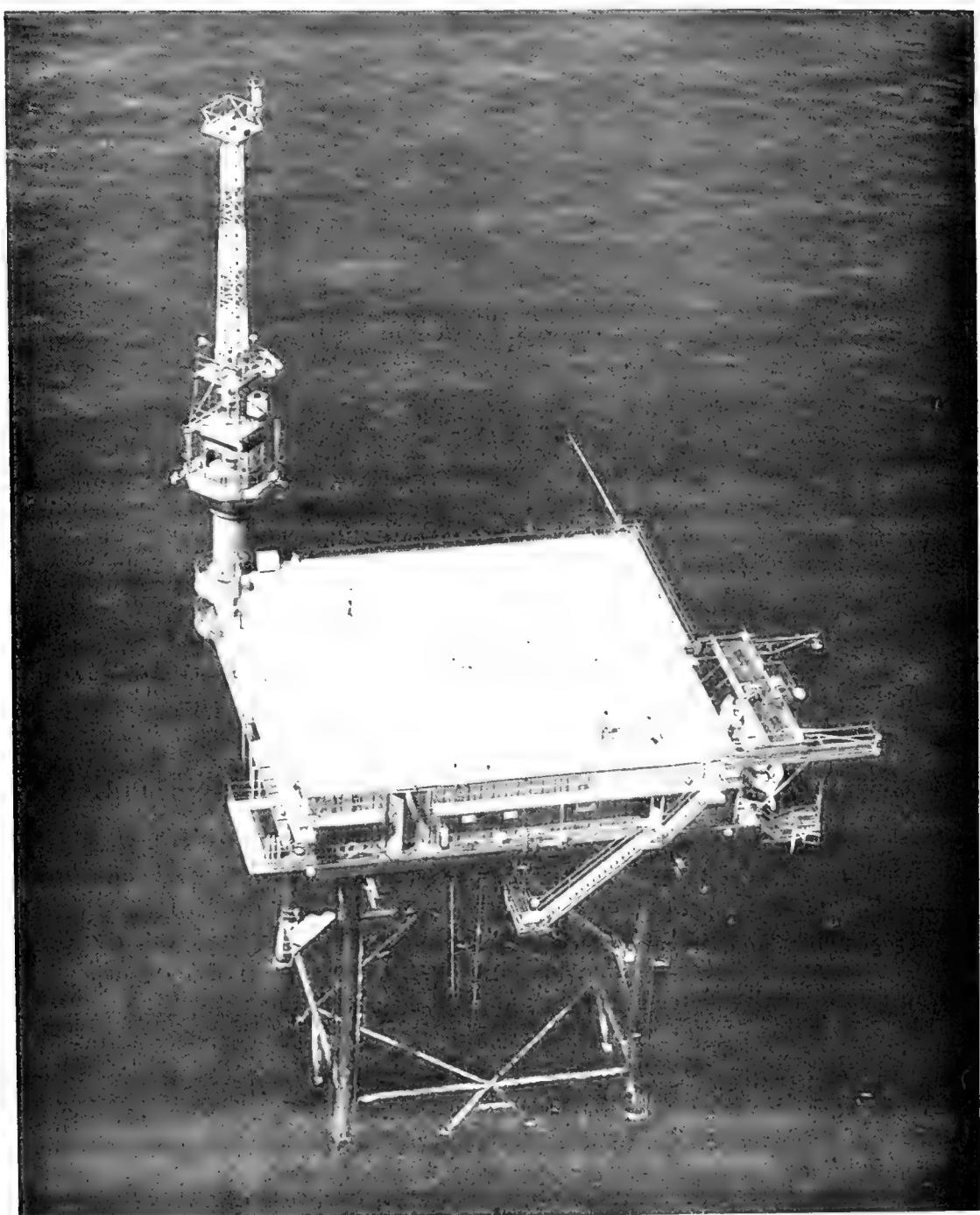
East Side View of BBELS Platform

Figure IV-4

The mean winds at the BBELS are typical of the east coast in the north temperate zone. In the warmer months, during periods of fair weather, prevailing winds are from the west to southwest. East and northeast winds, and generally foul weather, occur during passage of low pressure cyclones moving to the northeast off the New England coast. In the winter months, the semi-permanent Canadian polar high tends to impress a strong north-westerly wind component in this area. During the periods of wave measurements, the spring and summer of 1964 and 1965, the prevailing winds were generally from the west and west-southwest.

Starting in April and continuing through the summer months (in fair weather periods), a sea breeze effect occurs at about 1200-1300 hours, intensifying the southwesterly component of the wind vector. By mid-afternoon, there is a very predictable southwest wind from 6-9 m sec⁻¹. This wind dies down by sunset, and on occasion gives way to a slight land breeze effect.

Waves passing the station are usually a combination of ground swells, which almost always travel from the south or south-southeast, and of ambient local wind waves, which generally move in the same direction as the local wind field.

Gross Environmental Studies Made at BBELS

In measuring any time variable oceanographical or meteorological phenomenon, one must have at least a cursory knowledge of ambient con-ditions, of the so-called background environment. The purpose of the present experiment was to study the motions of surface waves having a frequency range from 50 to 2500 mc sec⁻¹ and a wave number ($2\pi L^{-1}$) range from 0.6 to 20 m⁻¹. It is clear that the open ocean environment has components of motion other than those associated with surface gravity waves. Thus, in measurements of two-dimensional wave motions in a vertical plane, the observed horizontal velocity record will certainly have components associated with tidal currents and other phenomena, which may or may not appear as a mean current over the period of wave measurement. Specifically, the wave record may have a component of horizontal flow which occurs as a monatonic variation (a trend) in the horizontal u record. Or horizontal eddying motions could produce several fluctuations during the wave record. This low frequency motion can be described by a modification of equation (III-12):

$$u(t) = \overline{u} + u'_w + u'_c \qquad \text{(IV-1)}$$

where $u' = u'_w + u'_c$. The u'_w is the time variable oscillatory motion caused by the waves; and u'_c is any other time variable fluctuation in the horizontal motion, which would be of somewhat lower frequency than u'_w. The u'_c component might be caused by a horizontal meandering motion such as that observed on or near the continental shelf, where the interaction of local

CAMERA

VANE

SAVONIUS
ROTOR

Histogram Current Meter

Figure IV-5

topography and wind conditions, together with tidal action, bring about complex motions (see Shonting and Cook, 1966). Whatever the source of the low frequency motion, its effect could be injurious to the assumptions of stationariness discussed in chapter III. These quasi-random horizontal motions may be of an appropriate frequency to contribute unwanted spectral energy to the wave motions during a 5- to 15-minute period of observation. Although it is not obvious how these motions (u_c') interact with actual wave motions (w_w'), an attempt should be made to establish the existence or non-existence of these low frequency components.

The following sections present results of two series of long term observations of the gross current structure at the BBELS, along with the simultaneous tide gauge records. This discussion of the gross environment of BBELS is rounded out by a brief consideration of the seasonal sea temperatures and meteorological measurements which supplemented the actual wave measurements.

Tidal and Non-Tidal Current Observations -- The most obvious motions observed at the BBELS, aside from the waves, are currents generally associated with the semi-diurnal tides. During relatively calm seas, surface flow is observed from the platform in the form of wakes, extending down-current from the platform legs, and in the motion of seaweed and flotsam. Also, during periods of maximum current, deflection can be observed in the vertical cables supporting submerged anti-corrosion electrodes, which are suspended from the catwalk underneath the platform. No quantitative data are available regarding the tidal currents at the BBELS. The tidal amplitude is recorded continuously on the Coast and Geodetic Survey tide gauge system permanently installed in the BBELS laboratory.

It was decided to make some long-term current records at the tower; but to use a relatively short sampling interval. This was done to provide information on current fluctuations having a tidal origin as well as those having periods approaching the sampling intervals of the wave measurements. The specific aim was to determine: (1) the consistency of the pattern of current speed and direction throughout the tidal cycle; (2) the relationship of current speed and direction to the free surface tide record; and (3) the energy contained in motions having periods smaller than the semi-diurnal tide, expecially those approaching the sampling periods of the wave observations (i.e., 5-10 minutes).

Two long-term current observations were made at the BBELS and provided much information on these subjects. The sensor system used for both series of measurements was a type-316, self-recording, histogram current meter (shown in figure IV-5) manufactured by the Braincon Corp. of Marion, Mass. The cylindrical housing is about 120 cm long and 18 cm in diameter. The meter utilizes a Savonius rotor speed sensor enclosed in a bail at the end of the cylinder housing.

The instrument detects and records the following data as a photographic analog on 16 mm film: (1) total number of rotations of the Savonius rotor;

(2) current direction relative to magnetic north; (3) instrument tilt angle; and (4) tilt direction. Each of these data is photometrically averaged over a preset time interval. This photometric averaging process is accomplished in the following manner. The Savonius rotor (speed sensor) located at the base of the meter is magnetically coupled to a gear train within the cylinder housing. During the sampling interval, this gear train, which has a reduction ratio of 7200 to 1, rotates a radioactive, phosphorescent light source through an angle proportional to the number of revolutions. This light source is photographed with the 16 mm camera as it traverses an arc. The estimate of speed is obtained from the film as an arc of varying intensity, with the highest exposure density at the slowest speeds.

Current direction is obtained by referencing the direction of the current meter cylinder housing with respect to a precision fluid-damped compass mounted in the meter. The cylinder housing is connected to a fiberglass vane about 1 square meter in area (see figure IV-5). The cylinder case and vane systems tend to align themselves with the direction of mean flow by pivoting about the support shaft. The vane direction is recorded on film by use of two phosphorescent light sources, one of which remains at magnetic north while the other rotates with the instrument. As with the speed record, the position on the arc of the highest optical density indicates the most prominent direction of flow, whereas the extremes of the arc delineate the azimuthal excursion over the sampling interval.

The instrument incorporates a tilt sensor in the form of a viscous-damped plumb bob containing at its lower extremity a phosphorescent light source. A disk indicator, which is mounted between the plumb bob light source and the film, permits simultaneous recording of the tilt angle and direction, referenced again to the compass. The tilt record allows one to compare the tilt angle and azimuth with the velocity vector, and also to correct the speed record for extreme tilt. For both records the tilt was not over $5°$ so that no correction was needed.

A cam system driven by an electric clock controls the periodic advance of the film record (i.e., the sampling interval). The period of sampling can be adjusted to the desired interval (from 5 minutes to many hours) by varying the cam geometry. The photographic film data from the current meter system were processed and decoded by the Braincon Corp. The punch-paper tape listings were then taken to the NUWS computer laboratory and placed on digital magnetic tape, giving mean current speed and direction at equal time intervals. Wind speed and direction were recorded at four-hour intervals during the periods of current observation and are lssted in appendix C.

Throughout both series of current measurements, the C&GS pressure-recording tide gage (bubbler gage) monitored the free surface elevation. This device registers the variation of the sea surface pressure head, as transmitted hydrostatically from a submerged sensor fastened to the southeast leg of the BBELS. The bourdon type pressure gage is coupled to and moves the ink pen of a single-

channel strip chart recorder (manufactured by Esterline Angus Corp.,
Indianapolis, Indiana), giving a continuous record of the tide level. This
strip record was hand-read, providing digitized amplitude values (cm) ob-
tained at equi-time spaced intervals of 1.8 ksec (30 minutes). These values
are tabulated in appendix C.

The first period of current observation (series I) extended from 29 April
through 8 May. The instrument sampling interval was set for 19 minutes with
a 1-minute film advance time, giving an effective sampling time of $\Delta T = 20$
minutes (1.20 ksec). The cylindrical current meter was suspended about 5 meters
beneath the sea surface by a 1.9 cm diameter nylon line, which was fastened
to the west end of the catwalk under the main BBELS housing (see figure IV-3).
The meter was counter-weighted at it base by a 10 kgm weight to provide added
stability and damping from the horizontal accelerations of the longer period
waves.

The record actually extended through 11 May (1000 hours); however, on the
afternoon or evening of 10 May, during a period of high winds and rough seas,
the instrument was lifted over one of the north diagonal pipe supports of the
tower. In this position, the instrument was quite close (within 2 meters) to
the northeast leg and within 1 meter of the surface at low water. Hence, the
meter would have experienced violent wave motions and produced data quite
incommensurate with the data at the original depth of 5 meters. The period
of reliable data was therefore considered to extend from 29 April (1300 hours)
through 8 May (1240 hours). A summary of the results is given in table IV-1.

Table IV-1. Long Term Current Measurements from BBELS: Series I (1964)

Dates and Time	29 April (1300 hours) through 8 May (1240 hours)
Mean Depth of Meter (m)	5
Sampling Period T (ksec)	765.6 (212 hours 40 minutes)
Sampling Interval T (ksec)	1.2 (20 minutes)
Total Data Points N	648
Mean Speed (cm sec^{-1})	14.1
Variance of Speed (cm^{2}sec^{-2})	29.5
Mean Azimuth (^{O}T)	290
Speed of Net Displacement Vector (cm sec^{-1})	6.0
Range of Speeds (cm sec^{-1})	4.9 - 36.6

The mean speed over the sampling period of 212.66 hours (765.6 ksec) was
14.1 cm sec^{-1}, with a standard deviation of 5.39 cm sec^{-1} and a range of values,
from 4.9 to 36.6 cm sec^{-1}. The speed of net displacement vector had a magnitude

of about 6 cm sec^{-1} and an azimuth of about 290°T. Three variables are plotted in figure IV-6 as a function of time: η , the height of the tide (upper curve); ς , the speed of the current (middle curve); and θ, the direction of the current (lower curve).

The time variation of the free surface level η is clearly governed by the semidiurnal tidal component M_2, whose period of 12.4 hours coincides with the mean period of the recorded oscillation (figure IV-6). The mean range for the period, which should be quite representative for year-round values, is of the order of 80-90 cm. However, there is evidence of a strong diurnal inequality (i.e., an alternating increase and decrease in amplitude), and of a long period constituent, which appears as a slow decrease in amplitude toward the middle of the record and as an increase toward the end. This latter component is probably the so-called fortnightly inequality (see Defant, 1958). The η portrays a sinusoidal pattern, which appears slightly steeper on the ebb than on the flood side. The diurnal inequality is relatively intense, giving as much as a 20 percent difference in amplitude between two consecutive periods. Also, the diurnal inequality appears to weaken as the lunar fortnightly modulation approaches a maximum. According to Defant (1958), one may classify this tide system between semidiurnal form and mixed (predominantly semidiurnal) form. A much larger sample would be required to establish the relative magnitudes of the semidiurnal constituents (i.e., M_2, S_2, N_2 and K_2) with respect to the diurnal components (i.e., K_1, O_1, P_1) and to the lunar fortnightly constituent M_f.

The current speed ς is quite variable; however, it displays oscillations that seem to correlate with ebbing and flooding intervals of η (figure IV-6). Velocity peaks tend to occur near the time of high water. The fluctuations of the tidal period, however, show a strong diurnal inequality. Oddly enough, the strongest current is associated with the minimum oscillation of η . This is particularly evident from 30 April to 3 May. Another interesting feature is the sharp drop in current speed after the maximum is obtained; e.g., at 1 May at 0930, 2 May at 1100, and 3 May at 1300.

The ς record contains relatively high frequency bumps, which appear to have periods ranging from 2 hours down to 20-40 minutes or less, and which fluctuate as much as 10-15 cm sec^{-1} within a 20-minute sampling interval. The data as plotted are 20-minute averages of speed and direction. Thus, the many small peaks displayed are suggestive of the still higher unresolved frequencies; i.e., above the Nyquist frequency - f_N of 0.4 cycle per kilosecond (0.025 cycle min^{-1}).

The current direction θ depicts clearly a semidiurnal anti-cyclonic (clockwise) rotation of the tide vector. The abrupt drop in the θ trace occurs when the flow shifts through 360°T, usually about one hour after high water. The current direction remains north for not more than an hour, then swings rapidly to the south (at one or two hours after high water) and proceeds to rotate clockwise almost linearly with time. Its direction is west (270°) at about mean low water and, rotating steadily, it reaches 360° again at high water plus one hour.
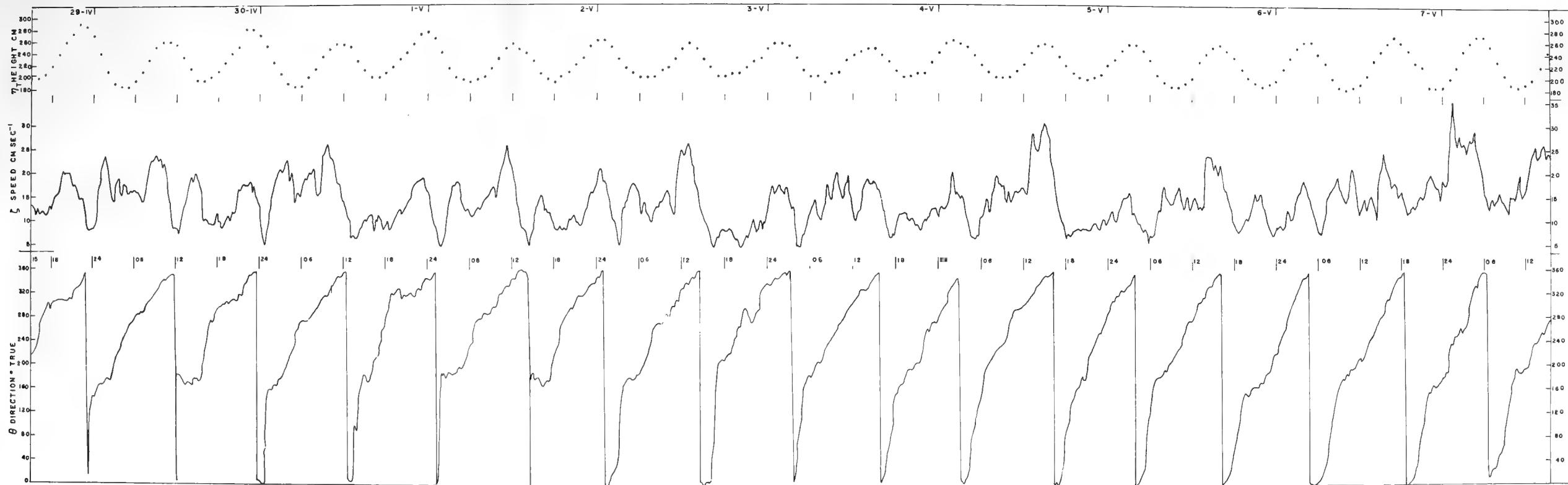
Current Direction, Current Speed, and Tide Height Plotted for Record I.

Figure IV-6

The speed and direction data (on punch-cards) were programmed on a Bensen Lehner electro-plotter, which provided a means of representing the Eulerian data on a progressive vector diagram (sometimes called a Lagrangian hodagraph diagram) depicting the head-to-tail addition of the current vectors for the entire sampling period (see figure IV-7). The digital computer program for this punch-card preparation is given in appendix D. The plot in figure IV-7 represents a graphical integration of the time variable velocity vector, which is displayed as its scaler components S and θ in figure IV-6. A consecutive pair of points in the XY plane defines a vector representing the average current speed and direction over a 20-minute interval. The figure could virtually represent a time sequence of the Eulerian velocity vectors, but not necessarily the pattern of flow at regions other than the BBELS. The head-to-tail path is indicative of the geometric pattern (or stream line) of the flow for a particle which is initially at the origin of the first vector and then moves with the local mass of water. The particle would indeed follow the vector path if the local mass of water moved as a solid, which, of course, is not the case. In the simple model of rectilinear tidal motion with no net displacement over the sampling period, this vector diagram would present a simple line of oscillation. For a rotating tidal current, in which the particles move in a circle with constant angular velocity, the head-to-tail vector diagram would appear as a circle with a period equivalent to the semi-diurnal tide.

The most obvious motion depicted by the progressive vector diagram is a mean flow moving to the WNW. The secondary motion displayed is a gross meandering pattern which oscillates roughly about the mean vector direction. During the period 29 April through 1 May, the mean flow tends toward the west. Then from 2 May through 6 May, the mean flow tends more to the north at about 310°-320°T. On 7 May a disturbance in the pattern causes the mean drift to shift more to the west.

The dominant oscillatory motions of the progressive vector diagram are displayed as cycloid-like meanders, the peaks of which show open loops or, occasionally, a closed spike. These are defined geometrically as prolate and ordinary cycloids, respectively. Throughout the period of observation, the rotational sense of the vector direction is clockwise or anti-cyclonic, as was inferred from the time record of θ .

The times of high water (obtained from the trace of η in figure IV-6 and marked with an H on the vector path) occur near the time that the peak of the cycloid is attained. In other words, the high water usually occurs just prior to a change in gross current direction from north to east.

The pattern of the time of high water marked on the progressive vector plot (figure IV-7) indicates a strong correlation of the tidal extremes with the pattern of the velocity vectors. For example, the time of low water occurs at the time of strongest flow to the west. This point occurs at the trough of the cycloid in the progressive vector diagram.

From the time of low water to the time of high water, the current flow is fastest and steadiest. In general, the flow is westward at low water, and slowly tends to rotate clockwise, attaining a northwest direction 4 to 4.5 hours after low water. At this point the swiftest current is found between 20 and 40 cm sec^{-1}. At low water plus 6.2 hours (i.e., at high water), the flow has decelerated and tends more to the north. At a point generally 20-90 minutes after the time of high water, the current slows to the minimum for the whole cycle, turns abruptly eastward, and continues to rotate anticyclonically to the south. The change in direction from north to south at the cycloid peaks usually occurs within a single 20-minute sampling interval. Once this southern component is attained, the speed gradually increases, as indicated by the spacing of the points in figure IV-7. As the time of low water draws nearer the current flow tends to decrease in magnitude while turning alowly to the west. At the time of low water the current is generally tending westward.

The anti-cyclonic current patterns in figure IV-7 show the influence of the coriolis deflection; indicating that the flow at BBELS, although tidally driven, has strong inertial tendencies. The progressive vector diagram is reminiscent of patterns obtained by Gustafson and Kullenberg during observations of suggested inertial motto currents in the Baltic Sea in 1933 (see Sverdrup, Johnson, and Fleming, 1942).

The current patterns must also be affected to some extent by the variations in wind conditions. During the period 29 April through 6 May, the winds were from the NE. These winds were caused by an unusual stationary high pressure system positioned off Nova Scotia. This resulted in NE winds and a seven-day period of fair weather. (Normally NE winds are caused by low pressure cyclones moving up the east coast, bringing rain and storm conditions). This high moved on after 6 May, and the winds shifted to the southwest on 6 and 8 May. Further studies on the time variability of various current vector components should reveal the effects of the wind.

This nine-day series of measurements revealed the gross tidal character at BBELS, and provided some basis for predicting the relationship of tidal amplitude with current speed and direction.

There is evidence, from the frequent spikes occuring in figure IV-6, that motions exist which may occur at frequencies of 0.5-1.0 cycle per hour or less. This intermediate frequency range was further examined by means of an auto-spectrum analysis (figure IV-8) of the equi-spaced speed data.

For the analysis, the time increments ΔT was 20 minutes (1.2 ksec), and the total lags m were 50. This gave a maximum lag of 60 ksec or a little less than 10 percent of the total data record. The number of data points was 648. Equation (III-9) gives the degrees of freedom DF as equal to about 26, which gives reasonably narrow confidence bands of spectral resolution. For DF = 26 (referring to figure III-3) the ratio is 1.36 above
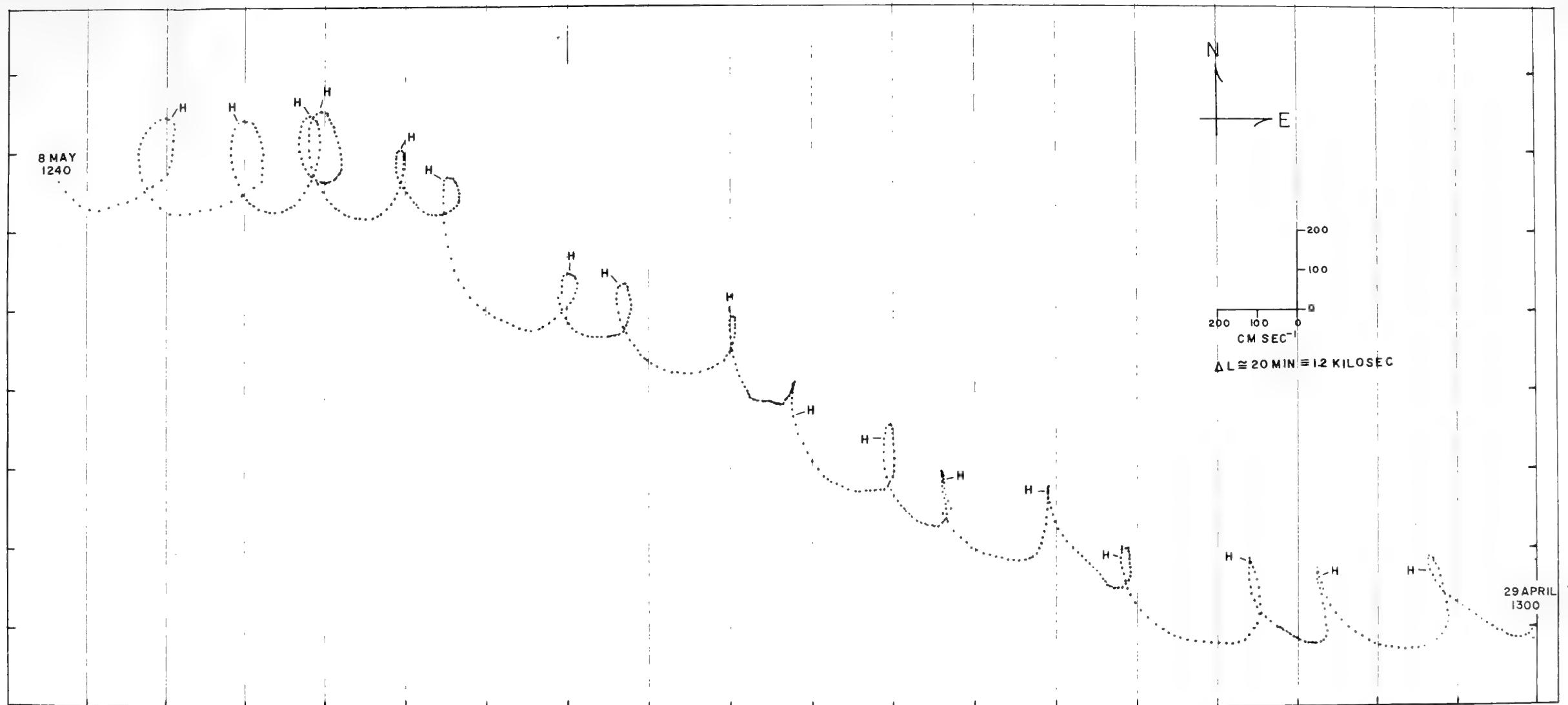
Progressive Vector Diagram of the Mean Current Vector at 20-Minute Intervals.

Figure IV-7

and 0.67 below the spectrum value to the 80% confidence limit spread. The range of the upper and lower limits is shown in figure IV-8 as a vertical bar indicated by R.

The frequency scale in figure IV-8 is in terms of millicycles per kilosecond (where 1 ksec = 16.67 minutes), which is abbreviated mcpks.

The integral under the curve (the variance) is found to be 29.49 cm^2 sec^{-2}. Most of the energy is associated with motions having frequencies below 85 mcpks or periods greater than 13 ksec (3.6 hours). Above 85 mcpks peaks occur at 105 mcpks (a period of 160 min) at 170 mcpks (98 min) and at 350 mcpks (49 min). There is a minimum in the curve at about 310 mcpks (a period of 79 min). The region from 310 to 405 mcpks contains motions depicted as the wiggles in the speed curve of figure IV-6. As an interesting comparison, the auto-spectra of the free surface tide level $\eta_{(t)}$ was computed and is shown in figure IV-9. Both curves are similar in shape and show peaking at the tide frequency. The speed function contains relatively more energy above the tidal frequency probably caused by the strong trend in the general variation in the mean flow over the nine-day sample.

During the period 24 November (1200) through 8 December (0920) 1964, a second series of current measurements was made from the BBELS. Series II allowed a more thorough investigation of the motions at BBELS than series I, since it involved both longer sampling periods and shorter sampling intervals. The same current meter system (Braincon histogram type) was employed and suspended as before from the west end of the catwalk at about 5 meters beneath the water surface.

For series II the histogram current meter was preset to sample for 4 minutes. Allowing 1 minute to advance the film, this gives a virtual 5 minute (0.3 ksec) sampling interval, compared to 20 minutes (1.2 ksec) for series I. During the 14-day sampling period, 4008 data points of current speed current direction, instrument tilt angle, and tilt direction were acquired. A supplementary record of tidal height $\eta_{(t)}$ was also obtained from the C&GS tide gauge. The data were processed at Braincon Corp. and in the NUWS computer laboratory in a fashion similar to that discussed for series I.

Figure IV-10 shows a small segment of the record of tidal height η (cm), current speed $\mathcal{S}$ (cm sec^{-1}), and current direction Θ ($^\circ T$) -- made from 24 November (1230 hours) to 25 November (1000 hours). The ordinate scales are identical to those in figure IV-6 for easy comparison. The time scale, however, is stretched to depict the greater density of points per unit time.

Comparison of series II data with series I data indicates very similar amplitude and phase relationships among the parameters η, $\mathcal{S}$, and Θ. These relationships were consistent throughout the long series II record. The η shows that maximum high water occurred about 1 hour after the maximum current $\mathcal{S}$ and also at the time of northward current direction Θ. The lesser peak of $\mathcal{S}$ occurring at high tide plus 4 hours (2400 hours) is clearly depicted on the series I record (figure IV-6).
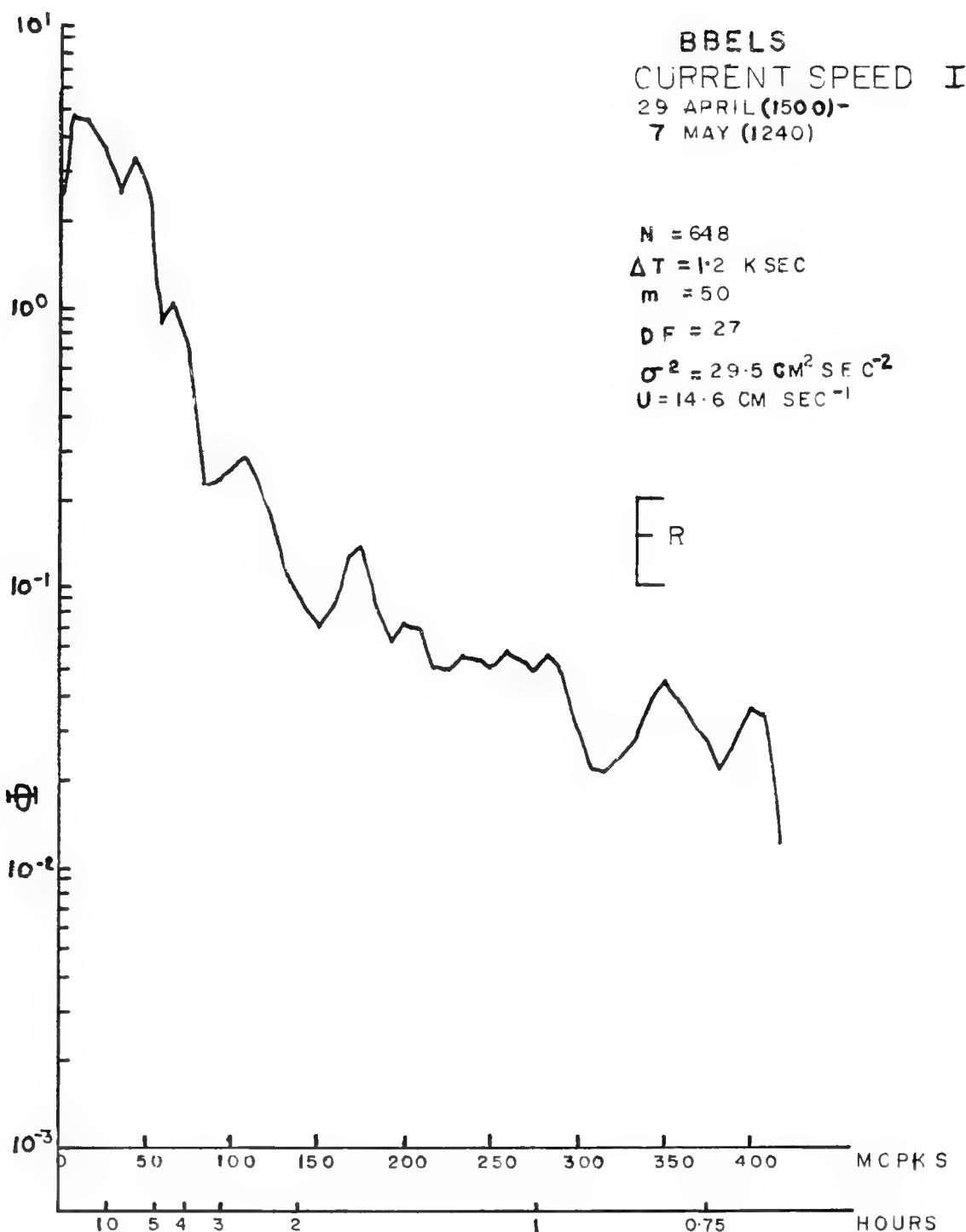
Auto–Spectrum of Current Speed During Record I.

Figure IV-8

BBELS
TIDE DATA (C&GS)
29 APRIL (1200) -
11 MAY (1200)
AUTO SPECTRA $\Phi_\eta(f)$

N = 577
ΔT = 0.5 HR = 1.8 K SEC
m = 50
D F = 23
σ^2 = 1.69.4 CM^2

R

12.5^h

10^3
10^2
10^1
10^0
10^{-1}

0   50   100   150   200   250   300 MCPKS

50 10   5 4   3   2   1.5   1.0   HOURS
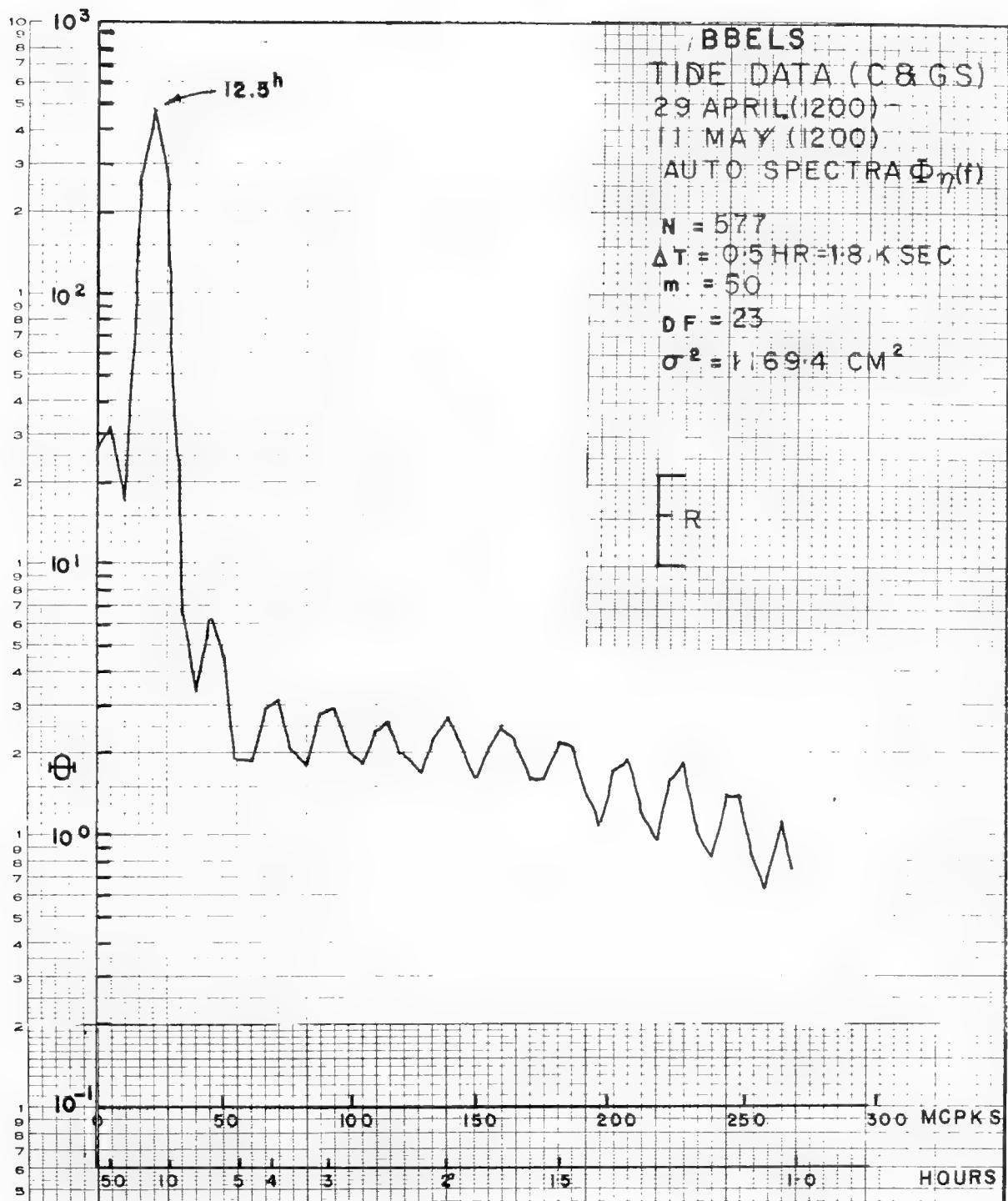
Auto-Spectrum of Tidal Gauge Data Obtained During Record 1.
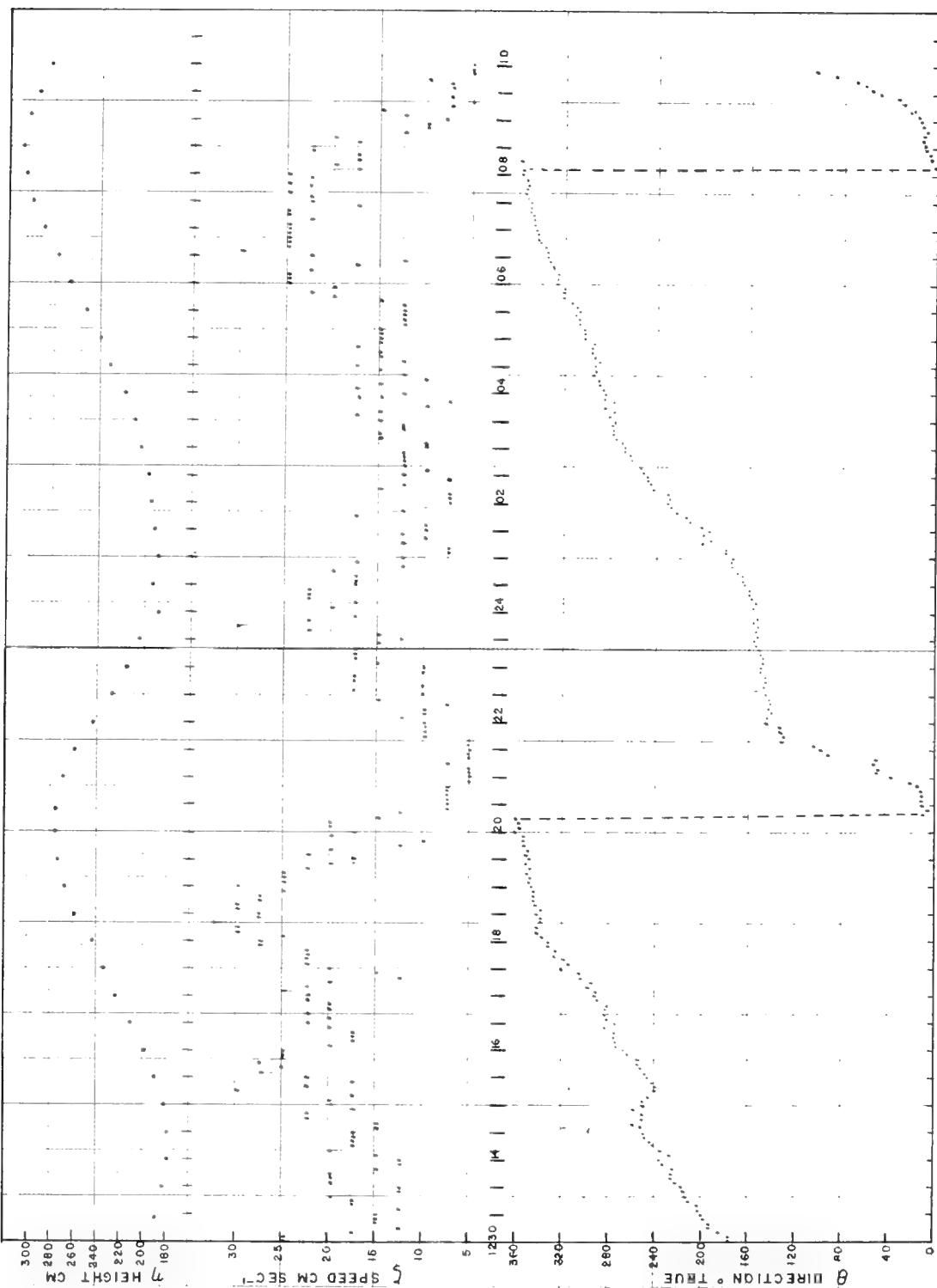
Figure IV-9

Current Direction, Current Speed, and Tide Height Plotted for Record 11.

Figure IV-10

The θ trace shows a rapid variation between 0 and 140°, followed by a leveling off for 2-3 hours, and then a gradual climb to 360°. The 5-minute samples do not indicate rapid or high frequency current direction variations. However, the current speed S, under this higher resolution (5 versus 20 minute sampling interval), still contains rapid oscillations.

Only certain incremental values of S occur. This is due to the resolution of the film reader, which can be read only to within 1°. The Savonius rotor calibration of the Braincon meter is 0.403° per centimeter per second for a 4-minute interval averaging time. Since the radarc on the film was read to the nearest whole degree, the resulting speeds occur only as multiples of 2.43 cm sec^{-1}. This limitation on the number of velocity values is due to the small angular displacement caused by the short integration time. Over longer sampling intervals the current variation appears more continous (see figure IV-6). For sampling over short intervals (5 minutes or less) the instrument could be improved by: (1) geering the rotor rotation to give a larger angular swing of the radarc per unit speed; and (2) using finer grained photographic film, together with an improved optical film reader to permit a reading of the radarc to fractions of a degree.

The speed trace S shows abrupt variations of 7-10 cm sec^{-1} occurring within 5-10 minutes. This explains the differing mean values of $\bar{u}$ (in table IV-3) for the wave measurements, which were taken at successive 5-10 minute intervals. The strongest current occurs while θ is varying most slowly, and conversely.

An auto-spectrum Φ_θ was generated to further examine motions having an ultra-tidal frequency; i.e., in the range $[$ 50 mcpks $< f <$ 1600 mcps$]$ or $[$320 min $> \tau >$ 10 min$]$. A sample containing 1000 points, from 24 November (1200 hours) through 26 November (2340 hours), was analyzed. The results are shown in figure IV-11. The ordinate scale is in terms of cm^{2}sec^{-2} per mcpks. The abscissa scale is in mcpks and hours.

The spectrum portrays a rather uninteresting pattern with most of the energy concentrated well above 200 mcpks. This undoubtedly is the influence of the 6 and 12-hour peak oscillations associated with the tape shown in figure IV-6. There are small peaks occurring at about 230 and 500 mcpks, and two other peaks at 1400 and 1600 mcpks. These four peaks are slightly larger than the 80 percent confidence range shown on the graph.

In general, the spectrum beyond 200 mcpks is approximately constant or white. This white energy is not negligible, however, for it constitutes about 31 percent of the total variance. The phenomenon of aliasing could be contributing energy from frequencies less than the Nyquist value of fn=1.677 mcpks (6 cycles per hour) to those frequencies from 250 mcpks up to fn.

In summary, these two series of measurements (I and II) show a predictable pattern of current speed and direction in relation to the free surface height of the tide. However, there occurs a relatively high frequency "noise" in the current speed S, which contains relatively large amounts of spectral energy
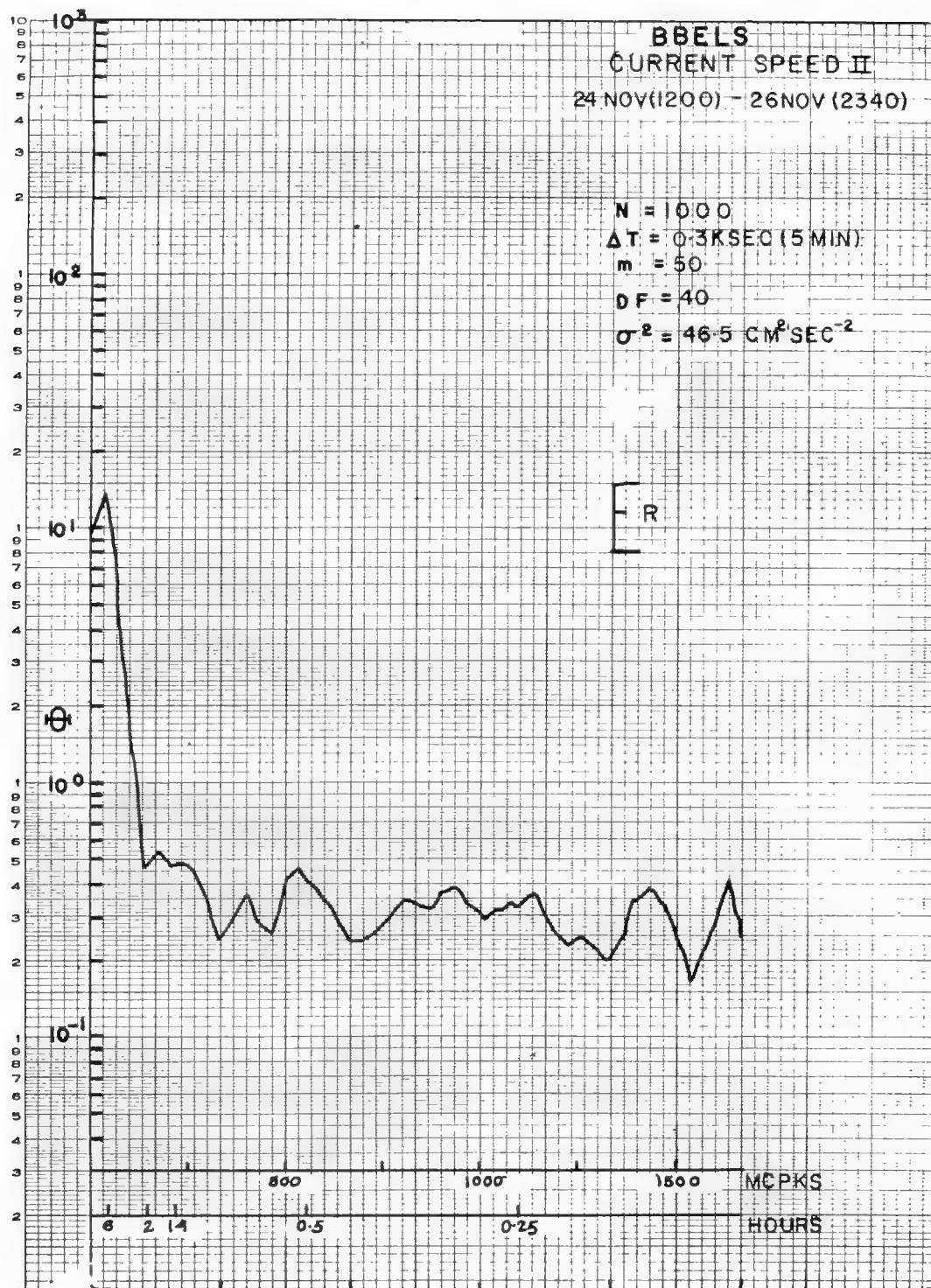
Auto–Spectrum of Current Speed for a Segment of Record II.

Figure IV-11

located in the range of periods of 10-15 minutes and less. These fluctuations or pulsations must be taken into account in the records of wave motions made over these suggested time periods.

Since the gross tidal currents are relatively predictable at the BBELS, a closer examination of them should reveal the causes of anomalies in the tidal pattern; i.e., the effects of wind upon the predominantly tidal and internal flow. Indeed, the BBELS facility could be of great use in the study of infra-tidal frequency motions.

Temperature Data -- The seasonal variation in the thermal structure exhibited in the vicinity of the BBELS is typical for a coastal region in the temperate zone. There are quite strong annual variations of water temperature caused by the interaction of the seasonably variable continental shelf water with the fresh water runoff from various rivers and bays north of the light station along the Massachusetts and Rhode Island coast (see figure IV-3). A data report on the seasonal distribution of oceanographic variables in Rhode Island Sound (which includes the location of BBELS) has been prepared by Shonting, Cook, and Wyatt (1966).

A gross picture of the thermal structure was obtained by making bathythermograph lowerings from the BBELS prior to each of the later series of wave measurements (BBELS numbers 11-16). A composite plot of the temperature profiles (figure IV-12) shows that isothermal conditions exist during the winter months, whereas the water tends to stratify during the late spring and summer. (The salinity stratification in the vertical is generally not intense enough to affect the stability of the water column in the region of BBELS.) The currents from Buzzards Bay and Vineyard Sound, mixing with the waters of Rhode Island Sound, apparently suppress temperature stratification in the region of the light station. Further westward, toward Block Island, much more intense stratification exists during the late spring and summer months (see Shonting and Cook, 1967).

Some seasonal surface temperatures for the BBELS location are shown in figure IV-13. The circles are taken from a monthly aerial survey (using an infra-red radiation thermometer) made during 1964 by the Sandy Hook Marine Laboratory and the Coast Guard under contract with NUWS. Due to inherent problems associated with this method (see Clark, 1964), the values are probably only reliable to within $\pm 1.5^{\circ}$C. Also, they do not accurately represent the water temperature a few centimeters below the ocean surface. The crosses in figure IV-13 indicate the surface temperature registered by bathythermograph observations taken at BBELS. The seasonal range of temperature is roughly $18-19^{\circ}$C. The minimum value occurs in late January, and the maximum in August.

Wind Measurements -- Observations of wind speed and direction were made aboard the BBELS during periods of wave measurements. During the first few series of wave observations, wind speed and direction readings were usually taken once or twice per hour. It was found from experience that, because of the relatively high variability in both the wind speed and direction, it was
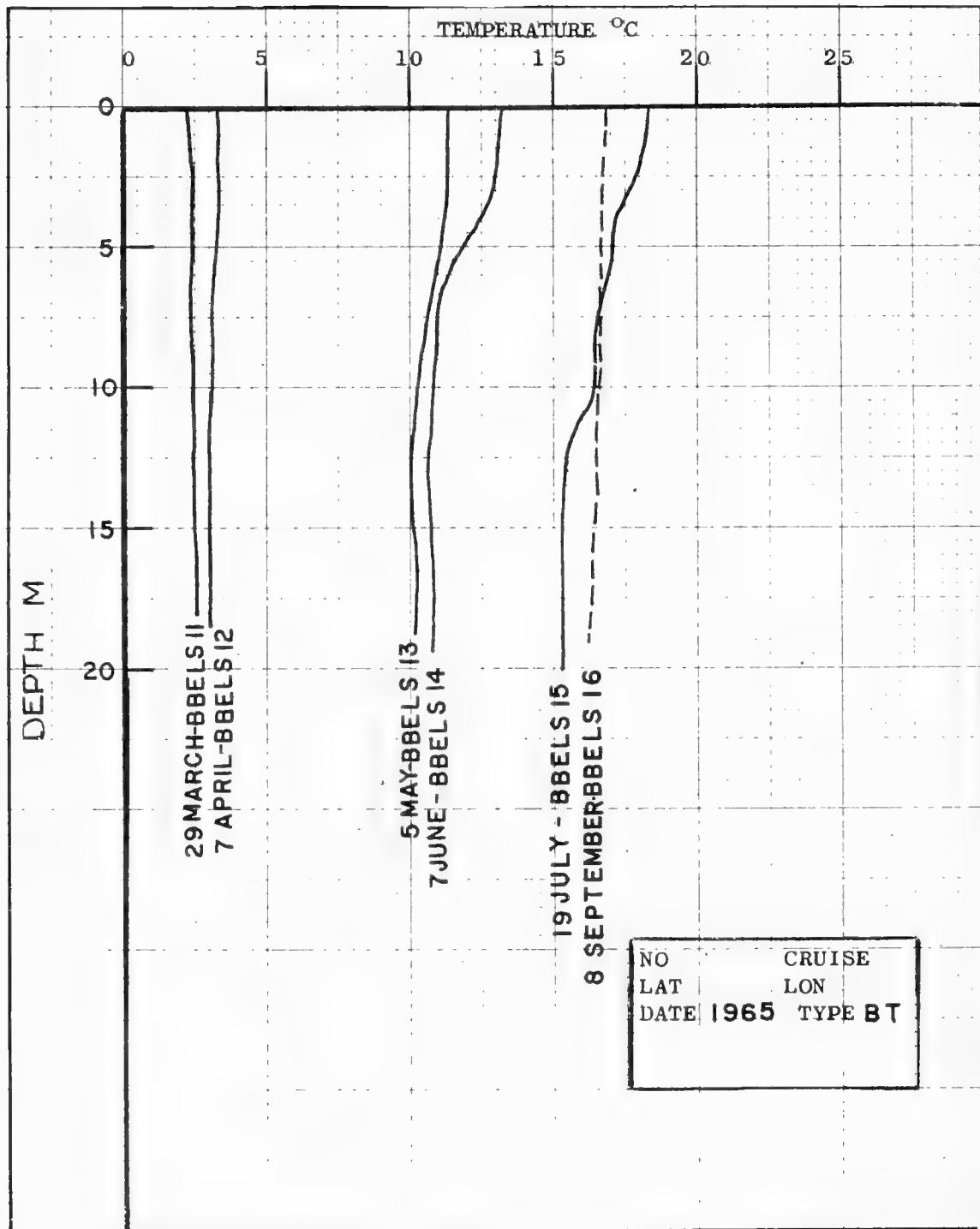
Bathythermograph Records Made at BBELS - March to September 1965.

Figure IV-12
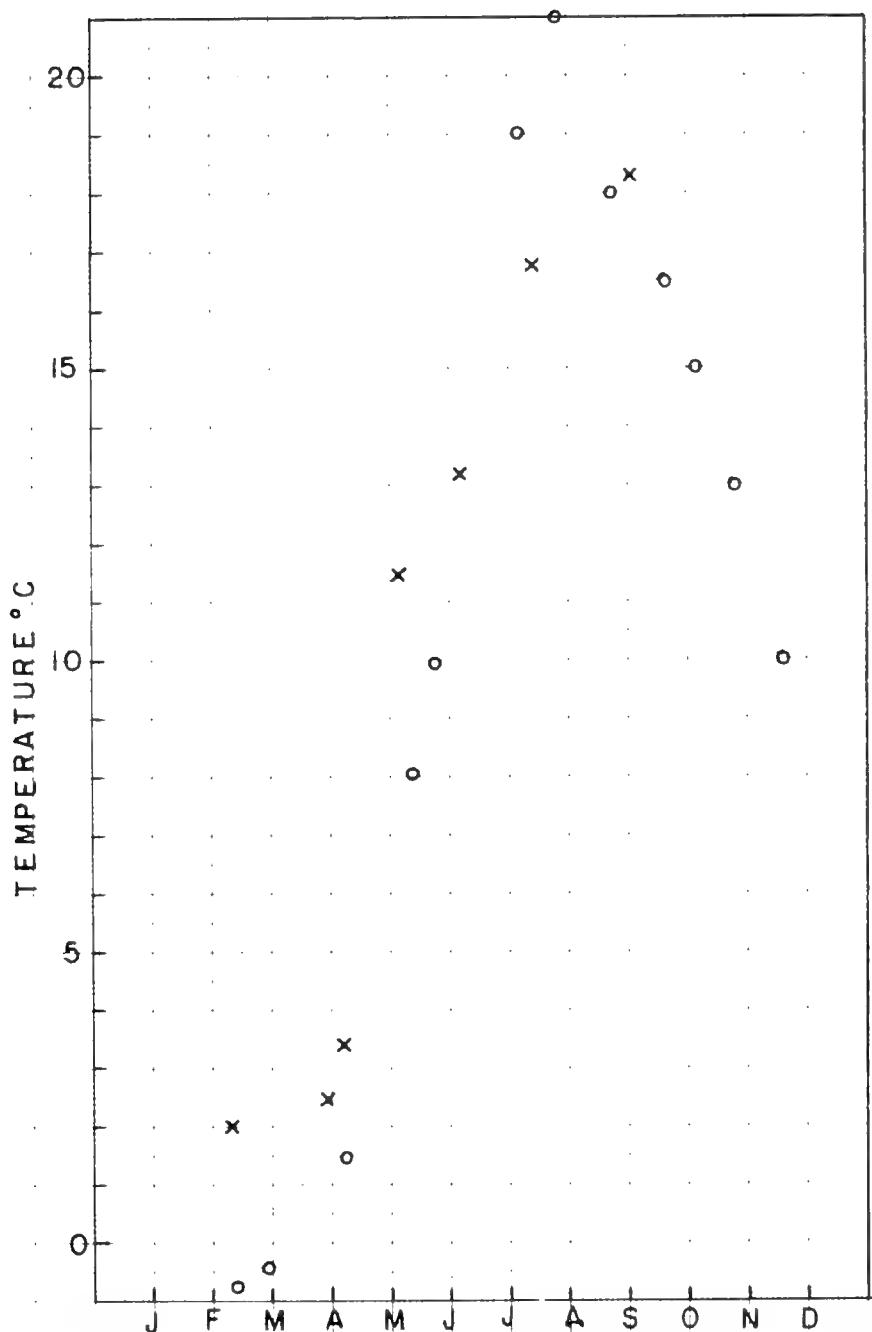
Gross Seasonal Variations in Surface Temperature Observed at BBELS.

Figure IV-13

desirable to monitor every few minutes, preferably at the time of each wave observation. Unfortunately, only spot observations were made, since equipment was not available to record the wind velocity continuously.

The wind speed and direction were recorded for BBELS series 4, 7, 8, 9, 10, 11, 12 and 13 from an anemometer system owned by the Weather Bureau (model F420) and permanently mounted on the light station. The instrument (manufactured by the Electric Speed Indicator Co., Cleveland, Ohio) is provided with a pair of visual readout dials mounted in the tower communications room. The speed is registered in knots, and the direction in degrees true. The unit is mounted off the northeast corner of the helicopter landing deck as shown in figure IV-4. The anemometer is fastened about 1 meter above a rail on the catwalk that extends out from the top deck of the tower at a height of 22 meters above the water. Unfortunately, the position of mounting is about 25 meters directly north-northeast of the beacon column. The column is about 2.5 meters in diameter at the base, but widens to about 5 meters above to provide for the beacon housing section. The tower must certainly affect the anemometer measurement when the wind is from the SSW and south. Fortunately, winds were from the west or southwest during most of the wave observations.

The BBELS wind measuring system was checked out by a Weather Bureau technician in August of 1964 and was found to be working properly. However, during the winter and spring of 1964-1965 it was suspected that system accuracy was becoming degraded, probably due to bearing wear. This was indicated by a loud squeaking of the cup mounting shaft as it whirled in the wind. During the series BBELS 14 on 9-10 June 1965, a comparison check was made of the BBELS anemometer system with a newly acquired portable anemometer system (Type C, 1400, built by the Belfort Instrument Co., Baltimore, Maryland). The output of this portable system provides a continuous analog voltage of wind speed; but, in contrast to the BBELS system, the wind direction is indicated by an array of eight wind direction lights whereby, at best, one can estimate the wind direction to within $22.5°$. The portable unit, having an indicated error (for wind speed) stated by the manufacturer to be within ± 0.4 m sec^{-1}, was sensitive and accurate enough to evaluate any gross speed error in the BBELS system.

This study, using the portable anemometer system, was made for two reasons: (1) to detect any gross biasing of the BBELS anemometer speed sensor observable within the limits of the accuracy of the portable unit; and (2) to determine any difference in the observed wind speed when measured from the upwind side of the tower deck as compared to measurements from the northeast side of the tower deck.

During periods of westerly winds, it was found that when the portable system was mounted at the same level as the BBELS system (2 meters above the upper deck), first at the windward and then at the leeward side, there was negligible difference in the indicated mean wind speed. Hence, for practical purposes, it was assumed that, for westerly winds at least, the BBELS anemometer was capable of measuring accurately the approximate wind speed and direction at

at its fixed location. However, the most desirable location for a wind speed indicator would be either on the west side of the tower, or high enough on the beacon column to have an unobstructed view of the wind field.

When the portable system was placed adjacent to the BBELS system, a consistent discrepancy showed up in the speed readouts of the two systems. Wind speed values were recorded simultaneously on 8 and 9 June 1965, and the results are plotted in figure IV-14. The BBELS system was clearly biased toward lower speeds of about 2.4 m sec^{-1} as the correlation graph indicates. The direction sensing records were comparable for the two systems.

The biasing of the BBELS anemometer was reported to the Coast Guard on 10 August 1965, whereupon the unit was replaced with a new F420 system within a week. This, however, did not solve the problem of the errors in wind speed records already made during the wave measurements taken from August 1964 through June 1965. It was decided to attempt a rough correction on this potentially biased wind data, based upon the assumption that the error in the BBELS anemometer system increased linearly from the time of the system checkout in August 1964. A straight line was drawn through the points (see figure IV-14), assuming a linear relationship between the two systems. The slope of the line is close to unity, but a clear ordinate intercept is produced. Therefore, it was assumed that whatever was wrong with the BBELS system was only affecting the threshold velocity--or, in effect, the ordinate intercept. The linear time variability equation of conversion was determined in the following manner. The line in the graph may be represented by:

$$V_N = V_B + I(t) \; ; \qquad (IV\text{-}2)$$

where V_N is the desired corrected wind speed, and V_B is the recorded wind speed. $I(t)$ is the ordinate intercept, which increased with time. Assuming that the ordinate intercept increased linearly from August 1964 to August 1965, one may write the following equation for the time period of one year:

$$V_N = V_B + \left(\frac{N-1}{12}\right) I_1 \; ; \qquad (IV\text{-}3)$$

where N = the month (i.e., 1, 2, ...12) and I_1 is the biased wind speed if the calibration bias changed linearly with time for one year ($I_1 = 3.2$)

$$V_N = V_B \; ;$$

and for the tenth month (June 1965)

$$V_N = V_B + 2.4 \text{ (m sec}^{-1})$$

87
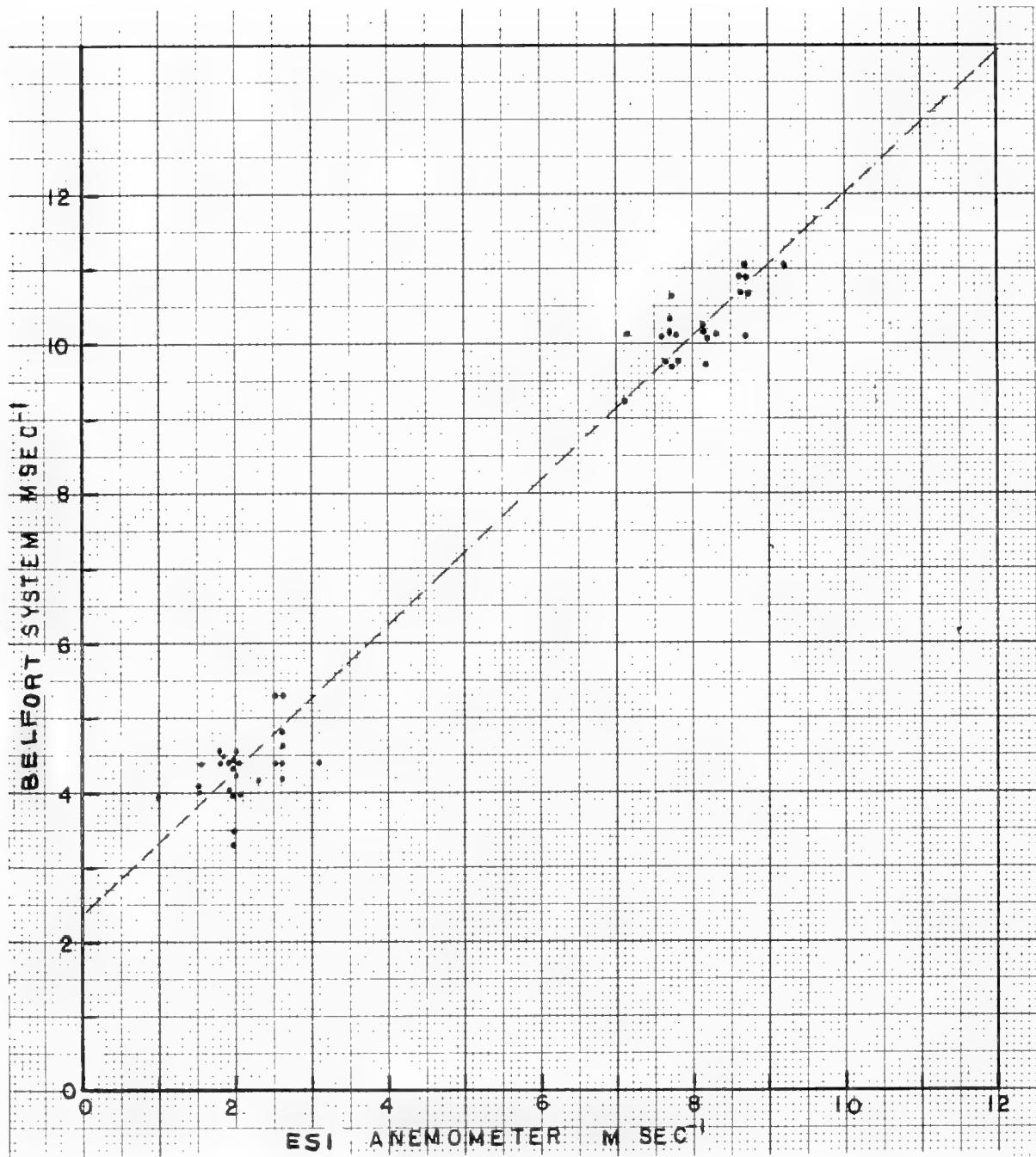
Wind Speed Readout of the Belfort Portable Anemometer System Compared with
the BBELS Anemometer Readout.

Figure IV-14

These corrections were applied to the recorded wind data between the periods of August 1964 and June 1965. Although the method is admittedly crude, since the deterioration of the calibration of the BBELS anemometer probably occurred in a non-linear fashion, this correction was considered to be better than none at all.

All wind observations made after June 1965 were obtained from the Belfort system mounted on the windward side of the tower (in all cases, the west side); hence, no correction was applied to these data. Wind data associated with the wave meter observations (including corrected data from the BBELS anemometer) are tabulated with the wave data in table IV-3.

Wave Meter Observations

During the period 30 March 1964 through 9 September 1965, sixteen series of experimental measurements of surface wave motions were made from the BBELS using the various wave meters discussed in chapter II. Ten of these series were thoroughly analyzed, providing 124 individual measuremtns. (Most of these are discussed in chapter V.) For convenient reference, table IV-2 lists the various experiments and the instruments used.

Methods of Making Measurements -- It should be emphasized that these experiments were of an exploratory nature and were designed to evaluate both the instruments and the methods of using them. As the experiments proceeded, innovations were made in both the mounting and the method of suspension of the ducted meters.

The original intent, in making wave measurements from the BBELS, was to provide a rigid support for the wave meters. However, a proposal to fabricate a rigid vertical beam mount, which would be supported by the horizontal cross member pipe located about 4 meters above the water on the west side of the BBELS (see figure IV-4), was considered unsatisfactory in at least four respects:

1. There is no easy access to the bottom legs for mounting the beam supports. Furthermore, the bottom cross members often become flecked with oil dripping from the upper storage tanks, which affords slippery pipe walking.

2. Provision for lowering and raising the instrument for measurements at various subsurface depths would be overly difficult.

3. The range of depths would be limited by the length of the vertical beam.

4. Beam mounting would place the instrument quite close to the diagonal side members and to the main legs of the tower.

These anticipated difficulties with a rigid mount made it advisable to try to suspend the wave meter by means of cables from the catwalk of the BBELS (beneath the housing). A pyramidal suspension system, involving the use of counterweights, could be tended from readily accessible points on the upper platform and would require no climbing around on the narrow and slippery

Table IV-2. Wave Measurements made at Buzzards Bay Entrance Light Station Using the Various Wave Meter Systems

SERIES	DATE	INSTRUMENT USED	DATA OBTAINED	PURPOSE OF MEASUREMENTS
BBELS-5	27 Apr 1964	OMDUM II	u, w simultaneously at various depths	1. Test OMDUM II. 2. Compare u with w at various depths. 3. Measure depth attenuation of u and w.
BBELS-7	5 Aug 1964	OMDUM II	u, w simultaneously at various depths	1. Test out new guy system. 2. Measure depth attenuation of u and w.
BBELS-8	7 Dec 1964	OMDUM III	u, w simultaneously at various depths	1. Test new meter OMDUM III. 2. Examine stability with 5 kgm weight.
BBELS-9	26 Jan 1965	OMDUM III	u, w simultaneously at various depths	1. Examine relative magnitudes of u and w. 2. Because of wind variation, obtained observations of wave changes.
BBELS-11	29-30 Mar 65	LIMDUM I	w at various depths	1. Observe 24-hour variation in wave motions caused by weather changes.
BBELS-12	7 Apr 1965	OMDUM III		1. Examine stability with 15 kgm weights.
BBELS-13	25-26 May 65	OMDUM III	u, w at various depths	2. Make measurements in heavy seas.
BBELS-14	8-9 Jun 1965	LIMDUM I OMDUM III	w1, w2 at various depths	1. Test out vertical anchored guy.
BBELS-15	19-20 Jul 65	LIMDUM I		1. Examine motions associated with long swells superposed on wind waves.
BBELS-16	7-8-9 Sep 65	LIMDUM I (u) OMDUM III		1. Examine variation in OMDUM III response with various angles θ between u meter and wave direction.

lower cross pipes. Moreover, a wire suspension system could be lowered and raised with ease, providing sampling at many depths over a relatively short time span. Also, with a main suspension guy lead from the west side of the catwalk, instrumentation could be positioned relatively far out from the legs and cross members. This is because of the large overhang of the catwalk. The vertical projection to the water of the west end of the catwalk is about 5 meters from the nearest diagonal support pipes and about 12 meters from either of the main west legs. This is a much greater horizontal distance than could have been provided by any feasible rigid support requiring bracing to the horizontal cross pipe.

In spite of these favorable attributes of a suspended system, there was a degree of uncertainty about how the perturbations of the waves would affect the suspended meter. There is, after all, no substitute for having a current meter fixed rigidly in inertial space.

As with most new techniques for scientific measurements, the method of wave measurement became more refined as experience was gained. Essentially, three successive modifications of the suspension system were used on the BBELS.

Figure IV-15 shows the arrangement of the suspending cables and the associated hardware for support of the wave meters. (The insert in figure IV-15 depicts the simple electrical circuitry.) The wave meters--either in the OMDUM configuration (shown in figure II-15) to measure u and w simultaneously, or the LIMDUM configuration (shown in figure II-17) to measure spatially separated pairs of w's or u's--are affixed to a vertical rod (shown in the figures). This rod, in turn, is fastened to the horizontal mounting rod of the suspension system in the manner shown in figure IV-16. Welded to the horizontal rod is a vertical piece of L-stock about 18 cm in length. The vertical instrument rod fits into this L-stock and is held rigid by two stainless steel hose clamps.

A counterweight was suspended on a 4-meter-long wire pennant from the bottom of the vertical instrument rod. The weight consisted of from three to six 2 kg sash weights lashed together. To each end of the horizontal mounting rod, which is about 3 meters in length, was attached a stabilizing guy as shown in figure IV-15. These guys led to the handrail stanchions on the northwest and southwest corners of the BBELS (main level - exterior walkway). The main support cable was shackled on to the top pad eye in the vertical instrument rod (figure IV-16). On the same shackle was attached the back guy, which led eastward to the center of the catwalk beneath the platform housing.

The main support cable, which was used to raise and lower the entire wave meter system, was led through a meter wheel fastened to the handrail at the end of the catwalk, and then to the hand winch fastened to the grating floor of the catwalk (see figure IV-17). The east, west, and back guys were stainless steel wire rope 2.4 mm in diameter. The main support cable and the anchored guy (when used) were stainless steel wire rope 6.3 mm in diameter.
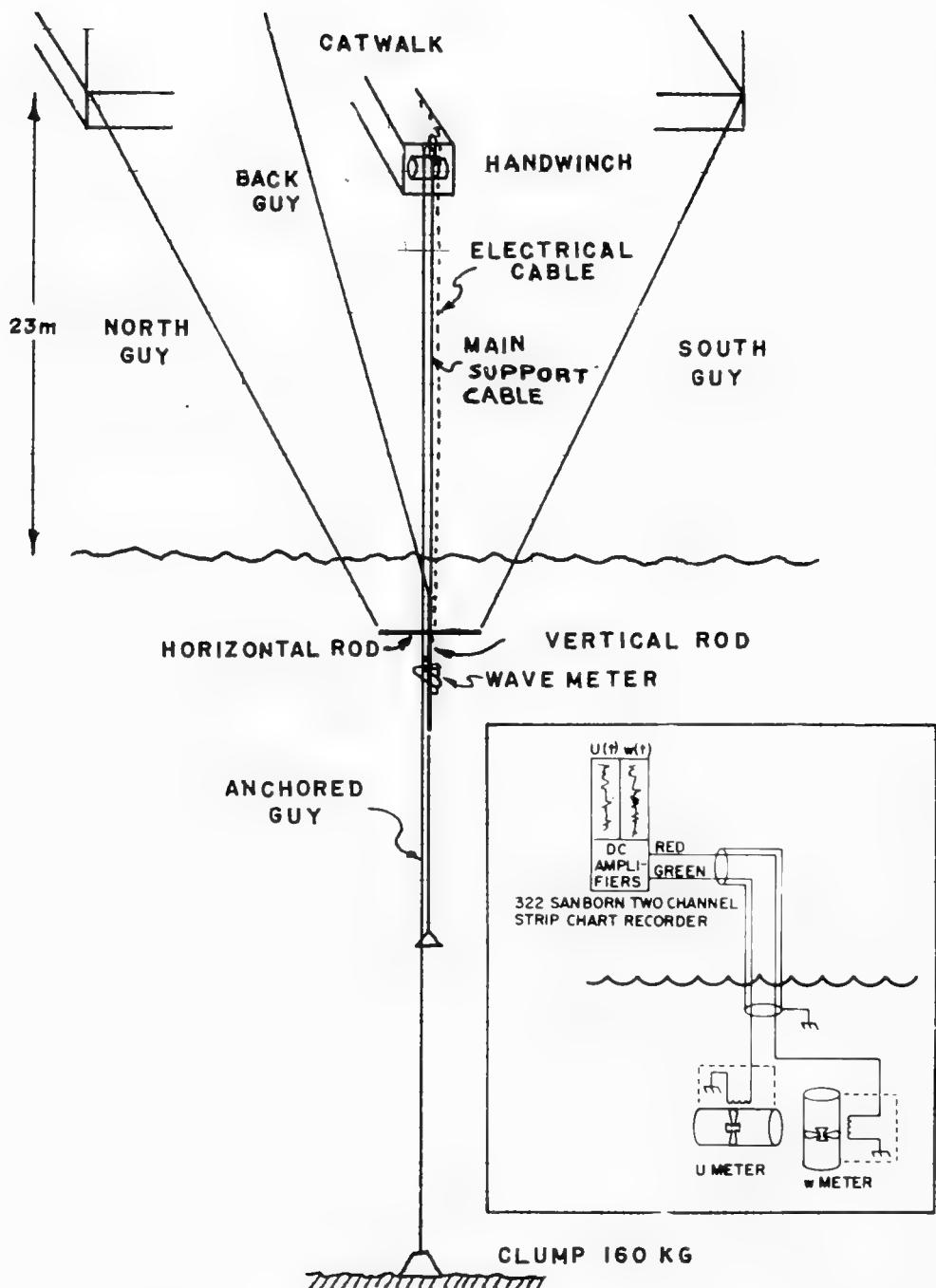
Wave Meter Suspension System on BBELS (Insert: Electrical Schematic of Wave Meter System).

Figure IV-15

MAIN
SUPPORT
CABLE

BELDEN
CABLE

BACK GUY

TAPE

SPLICE

HORIZONTAL
ROD

CLAMPS

SINGLE PIN
CONNECTORS

VERTICAL
INSTRUMENT
ROD
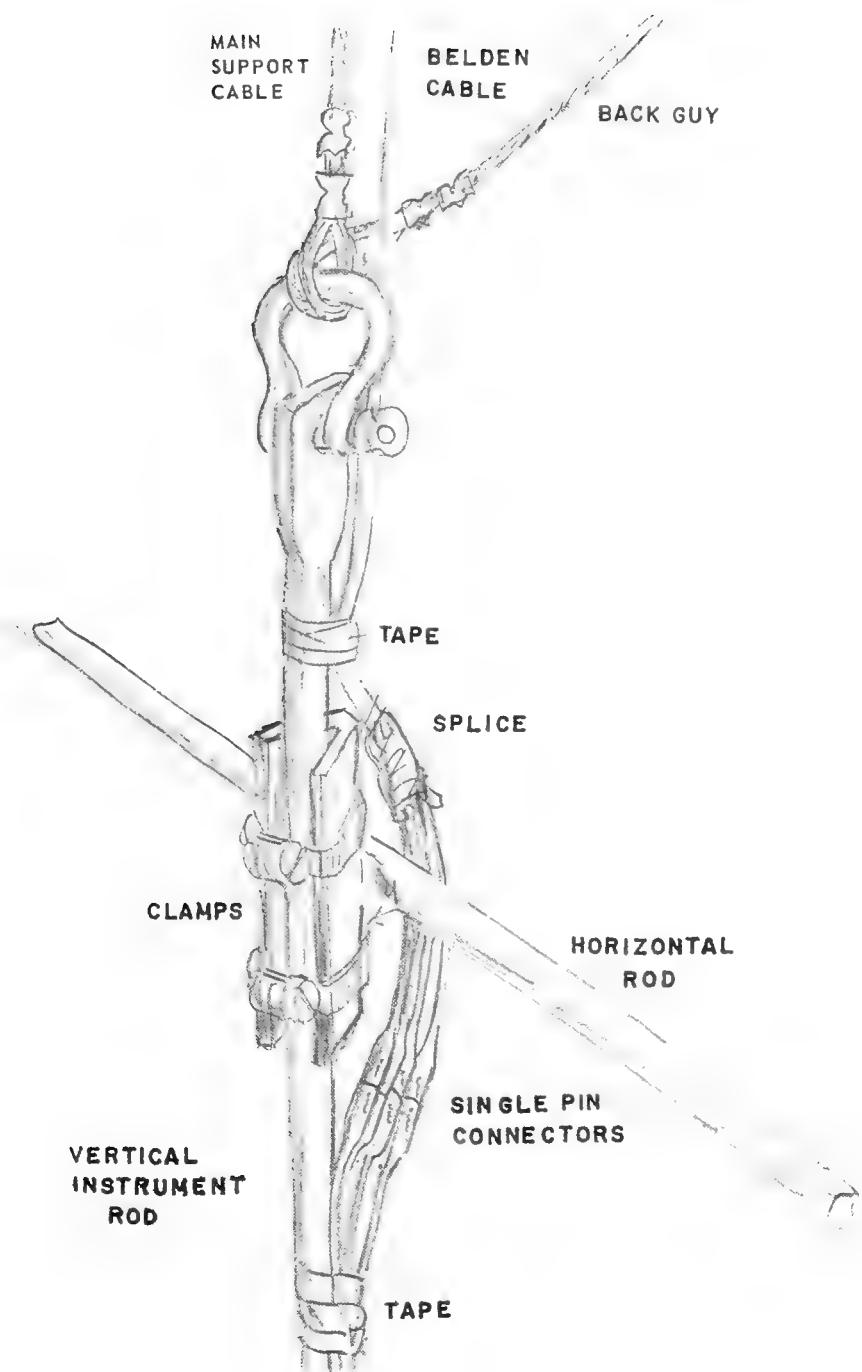
TAPE

Coupling of Main Support Cable and Electrical Cable

Figure IV-16

Hand Winch and Anchored Guy Termination Mounted on BBELS Catwalk

Figure IV-17

The four electrical leads from the wave meters were taped to the vertical instrument rod (see figure IV-16). The four single-pin male connectors mated with female connectors, which, in turn, were spliced to the four-conductor, shielded, neoprene-jacketed cable made by the Belden Manufacturing Co., Chicago, Illinois). The cable above the splice was securely taped to the vertical instrument rod, leaving sufficient slack so that, if a strain were accidently taken on the electrical cable, the connectors could not unplug. The Belden cable was led upward parallel with the main support cable to the catwalk rail, and then inboard and up to the 722 Sanborn two-channel system in the BBELS laboratory.

This system was used for the wave measurements listed as BBELS-5, 7, 8, 9, 10, 11, 12, and 13. The BBELS-5 measurements were made without the benefit of a back guy. The measurements listed as BBELS-14, 15, and 16 were made with an additional anchored guy shown in the figure IV-15. This guy led from the rail adjacent to the meter wheel vertically to a 160 kg lead clump set on the bottom. A tension of about 50 kg was drawn on this anchored guy by means of a turnbuckle led from a pipe fastened to the catwalk rail (see figure IV-17).

The vertical rod supporting the wave meter was fastened to the anchored guy by means of messengers used in tripping Nansen bottles. The two messengers were placed on the anchored guy. Each was fixed to the vertical instrument rod, one above and one below the meter, with stainless steel hose clamps. The meter system was then lowered, allowing the two messengers to slide down the anchored guy. (See figure IV-18.)

In practice, the wave meter was fastened to the main support cable and, with the north, south, and back guys slack, lowered while the Belden electrical cable was payed out. When the meter reached the desired depth beneath the wave troughs (registered on the meter wheel), the north and south guys were pulled taut, thus keeping the main support cable vertical, and excess slack was taken out of the electrical cable. Then the back guy was tightened to bring the horizontal rod firmly positioned at the apex of the inverted pyramid formed by the four guys. Much care was taken to keep equal tension on the south and north guys so as not to tilt the suspended system.

The method of suspending the LIMDUM I system (used to measure simultaneous vertical velocities at two levels) was much simpler, since complete horizontal stability was not necessary for determinations of the vertical motions. Also, a slight rotation of the system about the vertical rod axis should not affect the w measurements. For LIMDUM I observations of the vertical velocity component w, only the single main support cable was used. During BBELS-11, a northeast storm occurred, and a series of vertical velocity measurements were made from the east end of the catwalk (which, at the time of measurement, was the windward side of the BBELS).

For measurements with LIMDUM I of the horizontal velocity component u, the suspension involving all guys was used, since the (horizontal) meters had to be fixed with respect to the azimuth angle in the direction of the waves (see figures II-10 and III-4).

West View of BBELS Showing Catwalk -
OMDUM III System Fixed to Cross Bar at Bottom Center

Figure IV-18

Data Presentation -- The results of each series of partical velocity obser-
vations made at the BBELS using the OMDUM II, OMDUM III, and LIMDUM I systems
are summarized as efficiently as possible in table IV-3. The total observations
made with these instruments aboard BBELS represent about one-half million inter-
polated velocity values. Hence, because of space limitation, no effort was made
to list either raw or interpolated velocity data in the presentation of results.
The uninterpolated data is on file at NUWS, and it is planned to place them on
file at the National Oceanographic Data Center, Washington, D.C.

The statistical analysis of all wave records is presented as a tabulation
in appendix B in the form of computer printout listings. This statistical
analysis consists of the various parameters discussed in chapter III. Also
in appendix B are the individual plots of auto-spectra pertaining to each
series of wave measurements. Other plots are presented in chapter V as they
relate to the material discussed.

Table IV-3 summarizes the more important results of the wave observations
aboard the BBELS. Also included are environmental observations relating to
wind, sea, and tide. This table should be used in conjunction with the statis-
tical analysis computation listings and the auto-spectra plots, both of which
are included in appendix B. The following is a brief explanation of the indi-
vidual parameters in table IV-3.

1. Serial: This is the sequence number which, for a given set of
observations, is given in sequence.

2. Depth: The estimated depth of the instrument below the mean
trough level. This value is estimated to within ± 0.1 meter. The Roman
numeral following the depth value indicates the measurement (first, second,
etc.) at that depth.

3. Date: Date(s) of observations.

4. Time Span: The approximate times of starting and finishing
observations.

5. DF: The number of degrees of freedom for the statistical estimates
based on chi-square distribution.

6. N: Number of interpolated data points.

7. $\bar{u}$, $\bar{w}$: Mean values of $u(t)$ and $w(t)$ as defined by equation (III-11).

8. σ_u^2, σ_w^2: Variances of the records of $u(t)$ and $w(t)$ (also indicated
in the text as $\overline{u'^2}$ and $\overline{w'^2}$).

9. $\overline{u'w'}$: The covariance function at zero lag $\phi_{uw}(o)$, given by
equation (III-25).
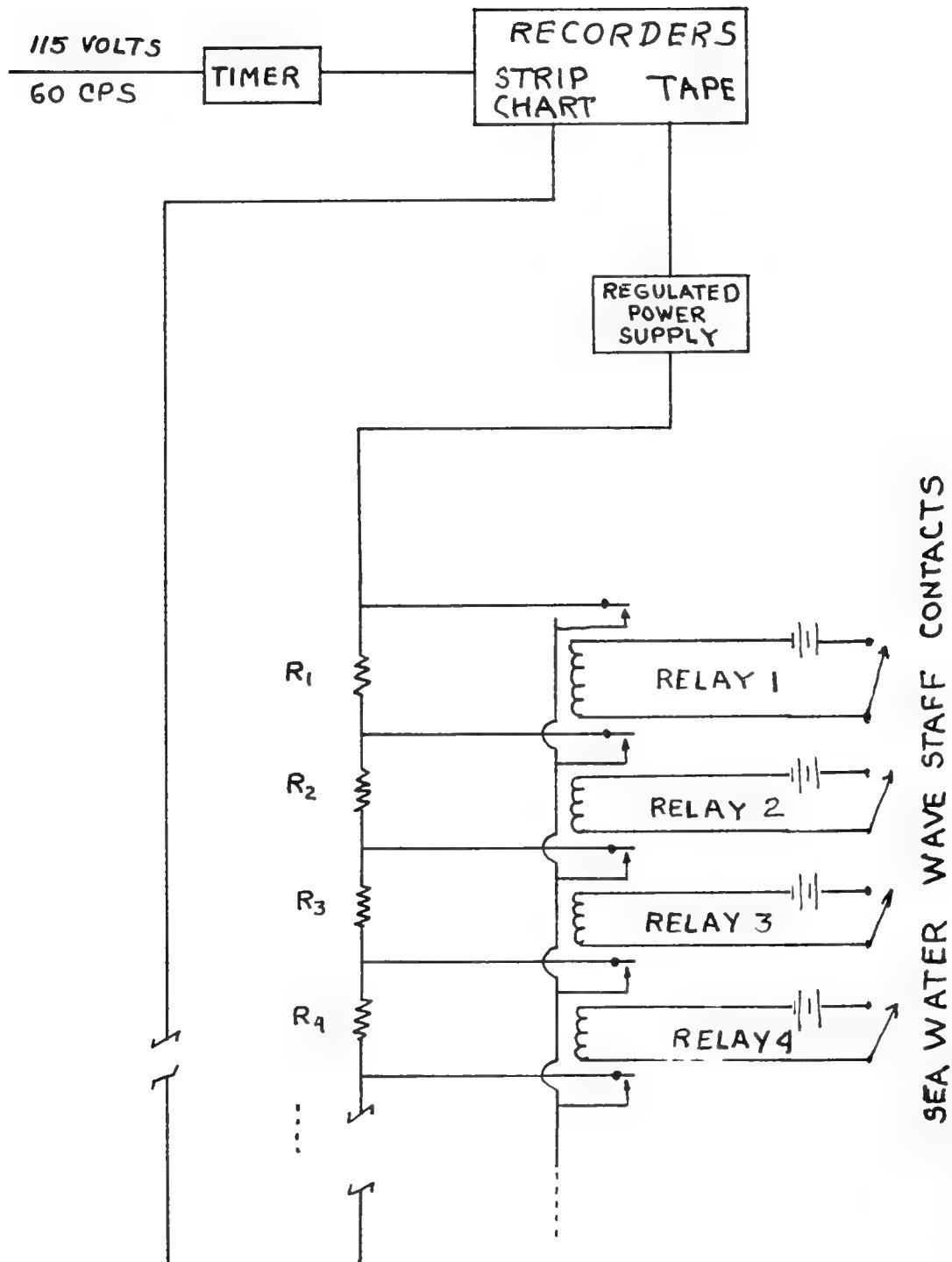
Corps of Engineers Wave Staff System (Schematic Diagram).

Figure IV-19

10. r: The linear correlation coefficient defined by equation (III-29).

11. L,H,T: The (eye) estimate of the wave length, wave-height, and period of the wind waves (sea) and swell. These values are only indicated as a guide, and are by no means an accurate statistical estimate of the parameter.

12. Θ: The estimated direction of the wind waves (sea) and swell.

13. Wind: Wind speed (m sec^{-1}) and direction from which it is blowing.

14. D: Doubtful data.

NOTE: For BBELS-5 and 7, the number of lags M = 32; for all other series, M = 50.

Wave Gauge System Observations

The Coastal Engineering Research Center (formerly the Beach Erosion Board) maintains aboard the BBELS from March through September a relay type step resistance wave gauge. This instrument provides a record of the height of the free surface, designated by $\eta(t)$, at a fixed location in the ocean. During the months of operation, the wave gauge is programmed to record η for specific time intervals during the day. Unfortunately, during most of the wave meter observations (spring and summer of 1965), the wave gauge was inoperative because of biological fouling problems. However, some wave staff records were obtained during or near the time of wave meter measurements, which allowed a rough comparison of the two wave monitoring systems.

The wave gauge operates on the principle of an electrolyte (sea water) completing an electrical circuit between a power supply and a relay coil, which (when engaged) bypasses a fixed resistance. Figure IV-19 is a schematic representation of this system. Switching of the relays 1, 2, 3 . . . occurs in sequence when the free surface mades contact with copper contacts linearly spaced on the vertical staff. As the relays are made, the resistances R_1, R_2, R_3 . . . are eliminated from the circuit, and the voltage on the recorder increases proportionally. Thus, as the water level rises and falls with the passing waves, the voltage V(t) fluctuates, presenting (with proper calibration) a linear voltage analog of the time-variable free surface oscillation $\eta(t)$.

The actual wave staff containing the copper contacts was fastened to the south side of the southeast leg of the BBELS. The staff is composed of nine sections, each 153 cm long. The copper contacts on the bottom three sections are 7.5 cm apart, whereas on the top six sections the contacts are 30.5 cm apart. This spacing arrangement permitted relatively high resolution for waves of average and a lower resolution for the larger waves. This recording system was housed in the laboratory of the BBELS. The recording was done on both an ink-pen strip chart recorder and on a magnetic tape recorder system.

The Coastal Engineering Research Center (CERC) has developed an analog spectrum analyzer (see Caldwell and Williams, 1963) that abstracts the wave data from magnetic tape having a recording speed of 1.27 cm min^{-1}. Samples of 10 minutes are generally made. The tape is scanned by a tape-reading device (at a speed of 160 cm sec^{-1}) which contains a set of band-pass filters and detectors for continuous automatic sweeping of the record at chosen frequencies. These filters range from 2 cycles sec^{-1} to 200 cycles sec^{-1}. Since the data tape is played back into the detector at a much higher speed, the original signal frequency increases by a factor of 7,500. Thus, a 0.5 cps (2 second period) signal on the tape appears as a 3,750 cps signal to the scanner. From an electronic point of view, it is much easier and less expensive to fabricate narrow bandwidth filters to work in high frequency ranges (i.e., a few kilocycles sec^{-1}) than in the relatively low frequencies peculiar to ocean waves (i.e., below 3 cps). By artificially increasing the frequency of the wave gauge signal, a signal is produced which is quite amenable to narrow and accurate bandpass filtering . The analog spectrum analyzer breaks the signal, and the signal squared, into their Fourier component frequencies by electronic filtering in a range of bandwidths. The system then produces an automatic plot of the voltage analog of the average wave height, and of the average squared wave height, against the real frequency.

No effort has been made in the preceding brief summary to discuss in detail the complexities of the CERC analog spectrum analyzer. According to workers at CERC (Williams, 1964), it is difficult to predict how auto-spectra obtained by the Tukey digital method (discussed in chapter III) will compare with the analog spectra. A rough comparison of spectra obtained by the CERC spectrum analyzer with spectra from digital methods is given by Mobarek (1965). From actual comparison, together with some empirical reasoning, Mobarek arrives at factors for converting the "squared average" analog spectrum of the CERC analyzer to the digital Tukey spectrum. Mobarek's reasoning is worth examining.

The analog spectrum analyzer provides the spectra of the wave height distribution, whereas the digital analysis provides the spectra contribution to the variance of the wave amplitude. Hence, the analog spectra are large by a factor of four.

Because of the manner of integrating and averaging the spectral energy over frequency, the energy per unit bandwidth of the digital method is not automatically equivalent to the energy per unit bandwidth over which the averaging is done in the spectrum analyzer. In the digital method, the energy in the harmonics about a certain frequency band is integrated, and this sum is depicted as existing at the center of the band. On the other hand, the spectrum analyzer sums up energy over a 0.027 cycle sec^{-1} interval. Thus, the spectral energy must be made equivalent for a unit frequency sampling interval. For the wave motion spectra a frequency resolution of $\Delta f = (2m\Delta T)^{-1}$ was used. When $m = 50$ and $\Delta T = 0.2$ second, $\Delta f = 0.050$ CPS. The energy spectrum of the analog computer can therefore be made commensurate with the digitally computed spectrum by multiplying the analog spectrum function by the ratio of $(0.050)(0.027)^{-1}$ or 1.9.

Finally, with respect to the relationship of the two spectra associated with the spectral smoothing of averaging function, as observed from actual plots, the spectrum analyzer seems to over-estimate the values of the spectral densities by a factor of "about 3".

Fourteen wave height auto-spectra made with the CERC Laboratories analog computer were compared with spectra of wave particle motions recorded over the same period (this series was BBELS-12 recorded on 25-26 May 1965). Comparison of the analog wave height data with the digitally derived spectra was difficult because of differences in frequency bandwidth studies. The band of spectral estimates defined by having $\Delta T = 0.2$ second and $m=50$ gives a spectral range of 0-2500 mcps, whereas the bandwidth of the analog spectra was roughly 0-300 mcps. This lower frequency range was chosen because the CERC workers are more interested in resolving low-frequency swell than wind waves. The spectral curves were converted from English to metric units and the appropriate factors (arrived at by Mobarek) were applied to produce the plots shown in the appendix B (figures WS-1 to WS-14).

The absolute values of the spectra may be somewhat inaccurate, since there appears to be some arbitrariness in deciding the factors for conversion from analog to digital spectra. However, the curves do permit a rough comparison of the position of the maximum spectral energy. The shifts in the spectra can be compared with spectra variations depicted in the spectral records of BBELS-13.

For a direct comparison of the Tukey analysis with the CERC analog process, two wave staff records on paper strip charts were obtained and processed at the NUWS computer laboratory (using a $\Delta T = 0.2$ second). The auto-spectra curves are shown in appendix B in figures WS-15 and WS-16. The spectra are also listed in appendix B. The relation of this data to the wave motion is discussed in chapter V. It was planned to obtain the CERC spectra of these two records, but it was learned later that the magnetic tape system was inoperative while the paper tape records were being made. Hence, a direct simultaneous comparison of the two spectra was not possible.

Table IV-3. Master Tabulation of Wave Data — TM No. 377

D = Doubtful data

SERIAL	DEPTH m	DATE	TIME SPAN	DF	N	u $cm\ sec^{-1}$	σ_u^2 $cm^2\ sec^{-2}$	$\bar{w}$ $cm\ sec^{-1}$	σ_w^2 $cm^2\ sec^{-2}$	$\overline{u'w'}$ $cm^2\ sec^{-2}$	r	SEA L m	H cm	T sec	θ	SWELL L m	H cm	T sec	WIND $m\ sec^{-1}$
BBELS-5 OMDUM II																			
001	0m I	4/27/64	1135-1138	56	888	-39.5	117	-1.8	1368	114.9	0.28	7-15SW	50-80	3	SW	No visible swell			6.8 WSW
002	1m I	"	1145-1148	56	888	-32.3	78	-1.5	889	49.9	0.19	"	"	"	"		"		6.8 WSW
003	2m I	"	1155-1158	56	888	-33.1	70	-1.2	558	67	0.35	"	"	"	"		"		6.8 WSW
004	4m I	"	1255-1257	18	288	-30.2	12	-3.9	186	-14.1	-0.30	"	"	"	"		"		6.9 WSW
005	3m II	"	1305-1308	55	876	-30.8	30	+1.2	279	+11.6	0.13	"	"	"	"		"		6.9 WSW
006	2m II	"	1312-		-	-	57		401	+0.9	0.00	"	"	"	"		"		6.9 WSW
007	1m II	"	1320-1323	56	888	-35.3	64	-1.0	622	+50.0	0.19	"	"	"	"		"		6.9 WSW
008	0m II	"	1330-1333	55	876	-33.4	80	-0.8	890	-5.2	-0.02	"	"	"	"		"		6.9 WSW
BBELS-7 OMDUM II																			
009	0.5m I	8/5/64	1021-1026	55	1328	-25.7	366	-8.5	1182	-145.2	-0.22	10-15	100-130	3-4		No swell			7.5 SSW
010	7m I	"	1112-1116	50	1340	-16.2	20	-1.8	128	-0.8	-0.11	"	"	"		"			7.9 SSW
011	10m I	"	1127-1132	50	1356	-20.5	21	+1.1	61	+1.6	+0.11	"	"	"		"			7.4 SSW
012	1.5m I	"	1144-1200	50	1386	-16.2	90	-2.1	586	-71.7	-0.31	"	"	"		"			7.2 SSW
013	10m III	"	1309-1314	53	1328	-10.9	7	+6.2	37	+0.73	+0.05	"	"	"		"			5.4 SSW
014	9m I	"	1319-1324	49	1218	-9.8	5	+3.8	55	-0.24	-0.05	"	"	"		"			5.4 SSW
015	8m I	"	1328-1333	45	1129	-9.3	18	+5.3	59	+7.7	-0.24	"	"	"		"			5.4 SSW
016	6m I	"	1348-1353	51	1266	-12.7	10	-3.5	81	+2.3	+0.08	"	"	"		"			5.7 SSW
017[D]	4m I[D]	"	1409-1414	51	1264	-12.0	16	-15.3	22[D]	-0.46	-0.03	"	"	"		"			6.3 SSW
018	3m II	"	1417-1422	41	1061	+0.3	159	+3.2	371	-0.17	-0.01	"	"	"		"			6.4 SSW
019	2m I	"	1426-1431	60	1490		223		455	-105.7	-0.33	"	"	"		"			6.4 SSW

Table IV-3. Master Tabulation of Wave Data (Continued)   TM No. 377

SERIAL	DEPTH m	DATE	TIME SPAN	DF	N	$\bar{u}$ cm sec⁻¹	σ_u^2 cm² sec⁻²	$\bar{w}$ cm sec⁻¹	σ_w^2 cm² sec⁻²	$\overline{u'w'}$ cm² sec⁻²	r	SEA L m	SEA H cm	SEA T sec	θ	SWELL L m	SWELL H cm	SWELL T sec	WIND m sec⁻¹
BBELS-8 OMDUM III																			
020	1m I	12/7/64	1310-1315	50	1245	+21.6	189	+6.4	348	6.4	0.03	2-4	20-40			Slight swell			5.0 WNW
021	0.5m I	"	1324-1329	63	1576	+16.8	354	+7.3	701	-46.9	-0.09	"	"			"			5.0 WNW
022	2m I	"	1337-1342	54	1359	+13.7	240	+2.9	251	76.7	0.31	"	"			"			5.0 WNW
BBELS-9																			
023u	0.5m I	1/26/65	1145-1150	54	1341	-5.5	555	+0.3	739	-333.5	-0.52	5	10	30	SSW	50		5-6	3.8 ESE
Complete re-reading of 023u raw data																			
023ur	0.5m I	"	1145-1150	54	1341	-5.5	570		709	-337.9	-0.52	"	"	"	"	"	"	"	"
024u	0.5m II	"	1224-1229	37	918	+3.2	490	+2.7	892	-261.7	-0.40	"	"	"	"	"	"	"	5.1 SE
025u	2m I	"	1235-1240	62	1365	+11.4	444	+4.6	493	-202.4	-0.43	12	30	30	S	50		5-6	5.8 SE
OMDUM III corrected data from above																			
024	0.5m II	"	1224-1229	37	922	+3.1	415	+2.5	824	-216.2	-0.37	"	"	"	"	"	"	"	"
025	2m I	"	1235-1240	62	1562	+10.9	391	+4.5	430	-169.8	-0.41	"	"	"	"	"	"	"	"
BBELS-10 OMDUM III																			
026	0.5m I	3/3/65	1141-1146	58	1443	-26	43.5	-8.1	73.0	5.4	0.10	2-3	5-10	0.5		10-20	10-20	5	1.7-2.0 NE
027	3m I	"	1242-1252	62	1549	-25.6	14.8	-5.8	16.7	0.8	0.05	"	"	"		Slight			0.5 ENE
028	3m II	"	1256-1306	93	2320	-17.7	9.3	+1.5	50	+3.0	+0.14	"	"	"		"			0.5 ENE
029	1m I	"	1340-1350	71	1764	-18.6	18.8	+3.7	68	8.9	0.25	5-10	"	"		10	10	5	1 W
BBELS-11 LIMDUM I																			
030	0.5-2m I	3/29/65	1622-	38	974			-1.1 / +0.3	1289 / 684		0.92	15-20	100-120	3-4	⌐ E / ENE-E	No visible swell	"		10.2 ENE
031	0.5-2m II	"	1630-	14	339			-1.1 / +0.2	1616 / 731		0.95	"	"	3-4	ENE-E	"			10.7 E
032	0.5m III	"	1713-1716	26	646			-1.7	1062			(Very short crests noted, steep waves)				"			11.0 ENE

u = uncorrected   r = reread   94B

Table IV-3. Master Tabulation of Wave Data (Continued)   TM No. 377

SERIAL	DEPTH m	DATE	TIME SPAN	DF	N	$\bar{u}$ cm sec⁻¹	σu^2 cm² sec⁻²	$\bar{w}$ cm sec⁻¹	σw^2 cm² sec⁻²	$\overline{u'w'}$ cm² sec⁻²	r	SEA L m	H cm	T sec	θ	SWELL L m	H cm	T sec	WIND m sec⁻¹
033	0.5m IV	3/29/65	1715-1720	45	1130			-2.8	1034			15-20	100-120	3-4	E	No visible swell			11.0 ENE
034	2m I	"	1734-1739	58	1458			-0.2	487			"	"	"		"			
035	3m I	"	1748-1753	59	1486			-0.9	306			"	"	"		"			10.0 ENE
036	1.5m I	"	1803-1808	64	1600			+2.5	538			"	"	"		"			9.7 ENE gusty
037	2.5m I	"	1820-1825	52	1297			-0.6	335			"	"	"		"			9.6 ENE
038	4m I	"	1832-1837	56	1438			-0.6	222			"	"	"		"			9.4 ENE
039	5m I	"	1845-1849	64	1600			+0.5	102			"	"	"		"			9.3 ENE
040	3.5m I	"	1851-1855	40	992			-0.9	192			"	"	"		"			9.2 ENE
041	4.5m I	"	1900-1905	55	1380			-1.7	194			"	"	"		"			9.2 ENE
042	6m I	"	1906-1911	64	1600			+0.6	115			"	"	"		"			9.0 ENE
043	7m I	"	1928-1933	64	1600			+0.9	79			"	"	"		"			8.7 ENE
044	5.5m I	"	1934-1939	57	1417			-0.3	91			"	"	"		"			9.0 ENE
045	6.5m I	"	1942-1947	58	1459			+0.5	79			"	"	"		"			8.3 ENE
046	8m I	"	1950-1955	60	1500			-0.1	70			"	"	"		"			8.2 ENE
047	2m II	"	2000-2005	54	1360			+0.1	415			"	"	"		"			7.4 ENE
048	0.5m V	"	2009-2013	34	847			-2.5	686			"	"	"		"			7.3 ENE
049	0.5m VI	"	2158-2203	40	1007			-3.0	742			"	"	"		"			5.2 NE
050	2m III	"	2204-2211	78	1938			-0.1	347			"	"	"		"			5.1 NE
051	2m IV	3/30/65	0010-0015	57	1425			-0.8	286			15-20	130	3-4		No visible swell			5.1 NE
052	0.5m VII	"	0022-0027	47	1168			-3.7	761			"	"	"		"			5.2 NNE
053	0.5m VIII	"	0440-0445	56	1401			+1.5	337			"	"	"		"			9.0 WNW
054	0.5m IX	"	0810-0815	59	1480			-4.6	508			"	"	"		"			10.9 WNW
055	2m V	"	0826-0831	55	1295			+1.8	309			"	"	"		"			10.7 WNW

Table IV-3.   Tabulation of Wave Data (Continued)

SERIAL	DEPTH m	DATE	TIME SPAN	DF	N	$\bar{u}$ cm sec⁻¹	$\sigma_u{}^2$ cm² sec⁻²	$\bar{w}$ cm sec⁻¹	$\sigma_w{}^2$ cm² sec⁻²	$\overline{u'w'}$ cm² sec⁻²	r	SEA L m	SEA H cm	SEA T sec	SEA θ	SWELL L m	SWELL H cm	SWELL T sec	WIND m sec⁻¹
056	2.0m VI	3/30/65	1023-1030	62	1537			-0.8	474			Seas heavy-confused. Cross trains. 15-20	130	3-4	WNW	No visible swell			13.8 WNW
057A	0.5m X	"	1036-1040	40	1001			-5.1	1265			"	"	"	"	"			14.0 WNW
057B	"	"	1040-1047	12.8	1070			-2.9	1133.1			"	"	"	*	"			
058	0.5m XI	"	1129-1131	30	768			---	952			"	"	"	"	"			14.7 WNW
059	2.0m VII	"	1134-1137	50	751			+2.9	486			"	"	"	"	"			14.6 WNW
060	2.5m II	"	1140-1144	58	1445			---	476			"	"	"	"	"			15.5 WNW
061	1.0m I	"	1155-1158	29	733			---	970			"	"	"	"	"			15.3 WNW
062	1.5m II	"	1159-1203	49	1232			-3.8	859			"	"	"	"	"			15.2 WNW
063	3.0m II	"	1205-1208	43	1080			---	296			"	"	"	"	"			15.4 WNW
064	3.5m II	"	1212-1216	31	768	plot missing			287			"	"	"	"	"			15.3 WNW
065	2.0m VIII	"	1218-1221	45	1132			-3.9	419			20-25	150-120		WNW	No visible swell			15.0 WNW
066	2.5m III	"	1226-1229	42	1055			---	471			"	"	"	"	"			15.1 WNW
067	4.0m II D	"	1234-1238	40	1008			-1.4	462 D			"	"	"	"	"			15.2 WNW
068	4.5m II	"	1241-1244	35	885			---	312			"	"	"	"	"			17.0 WNW
069	3.0m III	"	1245-1251	42	1059			+0.5	228			"	"	"	"	"			17.0 WNW
BBELS-12 OMDUM III																			
071	0.2m II	4/7/65	1235-1238	23	585	+4.5	33	+0.1	75	-7.0	-0.14	4	15		SSE	10	20		4.4 E
072	0.2m III	"	1243-1248	62	1551	+9.4	20	+0.1	86	-3.3	-0.08	4	15		SSE	7	20		5.4 ESE
073	10.0m I	"	1316-1320	53	1327	16.0	3.5					3-4	10-15			Slight			4.5 ESE
074	0.6m I off bottom	"	1354-1359	48	1202	16.75	3.9					3-4	10-15			Slight			4.5 ESE
075	1.0m II off bottom		1415-1417	25	629	+12.5	8.4		0	0	0								
076	5.0m off bottom	"	1440-1443	35	883	+17.5	3.1		0	0	0	3-4	10-15			3-4		Slight	5.4 ESE

D = Doubtful

Table IV-3. Master Tabulation of Wave Data (Continued)

TM No. 377

SERIAL	DEPTH m	DATE	TIME SPAN	DF	N	$\bar{u}$ cm sec⁻¹	σ_{u^2} cm² sec⁻²	$\bar{w}$ cm sec⁻¹	σ_{w^2} cm² sec⁻²	$\overline{u'w'}$ cm² sec⁻²	r	SEA L m	H cm	T sec	θ	SWELL L m	H cm	T sec	WIND m sec⁻¹
BBELS-13 OMDUM III																			
077	1.0m I	5/25/65	1705-1709	58	1294	-20.1	129	+0.4	964	+68.8	+0.20	15-25	100-120	4-5	SSW	No visible swell			17.2-16.2 SSW/SW
078	1.5m I	"	1714-	62	1540	-19.8	103	+0.1	957	-23.2	-0.07	"	"	"	"	"			"
079	2.5m I	"	1740-1745		1461	+16.0	51	-0.7	669	+20.2	0.11	"	"	"	"	"			13.2-16.2 SW/SSW
080	2.5m II	"	1747-1752	61	1532	-13.9	42	-2.6	573	-27.5	-0.18	"	"	"	"	"			17.2-16.2 SSW/SW
081	1.0m II	"	1828-1833	65	1636	-11.3	201	+1.2	878	-48.2	-0.12	"	"	"	"	"			18.2 SW/SSW
082	1.0m III	"	1835-1840		1304	12.4		-3.2		-87.3	-0.16	30	110-140	4-5	"	"			18.2 SW/SSW
083	4.0m III	"	2016-2020	67	1684	-13.6	90	-8.5	424	-20.9	-0.11	15-20	110-120	4-5					16.0 SW
084	4.0m IV	"	2034-2037	29	723	-10.8	133.2	-7.2	468.9	-29.9	-0.12	15-20	"	"					12.2 WSW
085	4.0m VI	5/26/65	0008-0011	29	719	-5.2	228.0	0.9	362	-41.9	-0.15								10.15 SSW/SW
086	4.0m VII	"	0552-0557	59	1470	-5.4	83.4	-6.4	156.6	+3.2	0.03	10-20	60-80	6					7.2-9.7 WSW
BBELS-14 LIMDUM I-W																			
087	0.0-2.0m II	6/7/65	1403-1408	56	1408			-3.2 1.6	397.4 870.8		0.74	20	100-120	4		No swell			7-9 SW/SSW
088	0.0-2.0m III	"	1412-1417	64	1618			-3.4 -6.0	541 166		+0.69	"	"	"		"			8 SSW
089	1.0-3.0m I	"	1433-1438	59	1482			0.3 -2.9	395.1 203		0.77	"	"	"		"			7-9 SW/SSW
090	2.0-4.0m I	"	1454-1459		1395			-1.8 3.1	253 145		0.79	"	"	"		"			7-9 SW/SSW
091	3.0-5m I	"	1502-1508	57	1413			-1.4 -2.6	196 128		+0.71	"	"	"		"			10 SSW
092	4.0-6.0m I	"	1511-1517	52	1299			-3.0 -3.6	126 79		+0.70	"	"	"		"·"			10 SSW
093	5.0-7.0m I	"	1520-1525	33	1330			-2.0 -0.1	79 66		+0.52	"	"	"		"			10 SSW/SW
094	6.0-8.0m I	"	1539-1545	56	1402			0.1 3.0	85 57		+0.58	"	"	"		"			10 SSW
095	7.0-9.0m I	"	1553-1558	56	1387			-1.1 +0.0	69 50		+0.42	"	"	"		"			9-10 SSW/SW
096	8.0-10.0m I	"	1604-1609	31	1278			-1.6 +3.6	49 36		+0.24	"	"	"		"			10 SSW/SW

Table IV-3. Master Tabulation of Wave Data (Continued)   TM No. 377

SERIAL	DEPTH m	DATE	TIME SPAN	DF	N	$\bar{u}$ cm sec^{-1}	σu^2 cm^2 sec^{-2}	$\bar{w}$ cm sec^{-1}	σw^2 cm^2 sec^{-2}	$\overline{u'w'}$ cm^2 sec^{-2}	r	SEA L m	H cm	T sec	θ	SWELL L m	H cm	T sec	WIND m sec^{-1}
097	9.0-11.0m I	6/7/65	1613-1618	57	1422			+4.9 +2.1	45 23		+0.16	20	100-120	4		No visible swell			9-10 SSW/SW
098	2.0-4.0m VI	"	2228-	68	1706	+4.2	118.5	4.2 3.1	211.0	115.5	0.73	2-3	Confused			No swell			7-9 SSW
099	1.0m IV	6/7/65	2357-0008	52	2296	-18.6	89	+1.4	528	-21.8	-0.10	20	100-120	4		No visible swell			7 SSW
100	2.0-4.0m VII	6/8/65	0010-0015	54	1345	- 3.4	115.4	-1.1 -3.4	163.0		0.54	10-15	100-120	3.5-4		No swell			7 SSW

OMDUM III

SERIAL	DEPTH m	DATE	TIME SPAN	DF	N	$\bar{u}$ cm sec^{-1}	σu^2 cm^2 sec^{-2}	$\bar{w}$ cm sec^{-1}	σw^2 cm^2 sec^{-2}	$\overline{u'w'}$ cm^2 sec^{-2}	r	SEA L m	H cm	T sec	θ	SWELL L m	H cm	T sec	WIND m sec^{-1}
101	0.0m I	6/8/65	1411-1415	50	1262	+30.0	257	+1.5	953	-162	-0.33	20	100-120	4		No swell			5.4 ESE 7-9 SW/SSW
102	0.5m I	"	1420-1424	45	1136	31.4	158.3	1.3	688.9	-117.2	-0.36	"	"	"		"			7-9 SW/SSW
103	1.0m I	"	1428-1432	42	1039	36.2	117.7	-1.2	402.6	-78.0	-0.36	"	"	"		"			7-9 SW/SSW
104	1.5m I	"	1435-1439	41	1022	37.2	72.0	-2.4	243.6	-49.7	-0.38	"	"	"		"			7-9 SW/SSW
105	2.5m I	"	1450-1454	58	1461	+15.5	51	-0.7	669	+20.2	+0.11	"	"	"		"			9-10 SSW
106	3.0m I	"	1457-1501	46	1143	+18.9	16	-2.2	186	- 6.9	-0.13	"	"	"		"			9-10 SSW
107	3.5m I	"	1508-1512	51	1267	+30.4	41	-3.7	132	-36.1	-0.49	"	"	"		"			9-10 SSW/SW
108	4.5m I	"	1524-1528	42	1038	+23.3	20.4	-4.4	112.8	-19.1	-0.4	10-15	100-120	3.5-4		No swell			11-12 SSW
109	5.5m I	"	1539-	37	918	18.3	16.4	-4.8	68.3	- 3.1	-0.1	"	"	"		"			11-12 SSW
110	6.5m I	"	1553-1557	45	1136	31.4	77.8	1.3	7.79	-11.5	-0.36	"	"	"		"			11-12 SSW

BBELS-15 LIMDUM I

SERIAL	DEPTH m	DATE	TIME SPAN	DF	N	$\bar{u}$ cm sec^{-1}	σu^2 cm^2 sec^{-2}	$\bar{w}$ cm sec^{-1}	σw^2 cm^2 sec^{-2}	$\overline{u'w'}$ cm^2 sec^{-2}	r	SEA L m	H cm	T sec	θ	SWELL L m	H cm	T sec	WIND m sec^{-1}
111	0.0-2.5m I	7/19/65	1922-1929	83	2068	+6.1 +3.1	547 186				+0.69					Swell radiating from 170° T			7.5 W
112	0.0-2.5m II	"	1940-1951	80	2013	+1.7 +3.2	-188 210					3-4	10-20			50-75	70-110	8-10	7.5 W
113	0.0-2.5m III	"	2003-2009	68	1705	-3.5 6.9	475.6 215.6				-0.76	5-9	20-30			50-75	70-110		7.0 WSW
114	0.0-2.5M IV	"	2201-2209	62	1555	+26.4 +24.2	135 83				0 71	10-30	30-70			Long swell from 170° T			2.6 NW
115A	0.0-2.5m V	""	2400-0008	97	2422	-12.7 - 9.1	121.1 41.2				-0.12					"			3.0 N/NW
115B	0.0-2.5m V*	7/20/65	0930-0934	32	86	-21.0	98.3									"			4.4 N
116	1.0-3.5m I	"	1234-1237	25	628	-28.32 -28.45	72 49				+0.10	3-6	10-20			20-30	40-50		7.0 WSW

* 2.5m channel out

Table IV-3. Master Tabulation of Wave Data (Continued)

SERIAL	DEPTH m	DATE	TIME SPAN	DF	N	ū cm sec⁻¹	σ u² cm² sec⁻²	w̄ cm sec⁻¹	σ w² cm² sec⁻²	u'w' cm² sec⁻²	r	SEA L m	SEA H cm	SEA T sec	θ	SWELL L m	SWELL H cm	T sec	WIND m sec⁻¹
117	2.0-4.5m I	7/20/65	1241-1244	22	552	-28.1 / -28.2	76.2 / 45.7				0.52					Long swell from 170° T			2.6 W
118	3.0-5.5m I	"	1252-1255	26	649	-27.0 / -26.5	59.7 / 41.7				+0.38	3-6	10-20			Long swell from 170° T			2.6 W

BBELS-16 OMDUM III B

SERIAL	DEPTH m	DATE	TIME SPAN	DF	N	ū cm sec⁻¹	σ u² cm² sec⁻²	w̄ cm sec⁻¹	σ w² cm² sec⁻²	u'w' cm² sec⁻²	r	SEA L m	SEA H cm	SEA T sec	θ	SWELL L m	SWELL H cm	T sec	WIND m sec⁻¹
119	1-3.5m VII	9/8/65	0200-0207	74	1849			+0.4 / -0.9	158 / 84		-0.46								
120	0.5m I (255°)	"	1340-1346	28	702	-19.7	57	+0.4	256	-7.6	-0.06	3-5	10-20		SSE	Slight			4.2 W
121	0.5m II (270°)	"	1350-1357	49	1227	-19.8	66.1	+0.6	266.1	-10.3	-0.1								3.5 W
122	0.5m IV (315°)	"	1420-1425	55	1374	-18.4	38	-0.9	278	-11.2	-0.11	4	20			No visible swell			4.2 W
123	0.5m VI (330°)	"	1431-1436	46	1152	-12.9	39.4	-1.2	250.8	-15.1	0.15	1	10						4.6 WSW
124	0.5m VII (345°)	"	1441-1446	48	1205	-13.3	30.3	-2.3	239.2	-5.2	-0.06	4-5	30						5.3 WSW

B = Directional spectrum studies.

94G

.

CHAPTER V

RESULTS AND DISCUSSION

The large amount of wave meter data gathered at BBELS makes it difficult to examine it all in detail in the remaining pages. Moreover, the intention here is to present brief discussions on the most meaningful aspects of the data in the hope of deriving some basic information and, perhaps more importantly, of demonstrating the potential of this new approach to the study of surface waves and their energy relationships.

Velocity Data

General Characteristics - Before examining the velocity data, it is worthwhile to note that the electrical output of the wave meters can be used to present a graphic or analog picture of wave motions. The wave meter record, a sample of which is shown in figure II-7, represents a train of voltage pulses generated by the impeller magnets moving by the induction coil of the meter. As explained in chapter II, the amplitude of the pulse should be proportional to the current speed. This amplitude modulation property is graphically demonstrated in figure V-1 (A and B). Shown are raw wave records of the LIMDUM I wave meter recorded at chart speeds of 5 mm sec^{-1} (Record A) and 1 mm sec^{-1}(Record B). The records were made on 20 July 1965 at BBELS, with the LIMDUM I system configured to measure simultaneously the horizontal velocities u_m and w_m (see equation III-55). On this day, there was an exceptionally large swell radiating from the south. This swell had an estimated height of about 50 cm and wave lengths of over 50 meters. The winds were light from the NE at 2-3 m sec^{-1}. The u meters were spaced with a vertical separation of 2.5 meters and were aimed at about 170°T - directly into the swell.

The top and bottom traces of each record represent the upper u meter (at 0.0 m) and the lower u meter (at 2.5 m), respectively. The polarity of the voltage pulses on the bottom trace of the A record was reversed; i.e.; the oscillations of both u channels should be in phase. The polarity is correct for the bottom trace of the B record.

The motions caused by the passage of the long swell are excellently portrayed, appearing as the 5-7 second undulations produced by the amplitude modulation of the voltage output. The wave motions at the two levels are of similar phase, and the damping effect on the amplitudes of the horizontal component of the wave motions with depth is evident.

The amplitude bias downward in the B record is caused by the superposition of the observed mean tidal current flowing northward in the positive sense (appearing downward on the chart). At the time of the A record, the tidal current was weak, and bias does not appear.
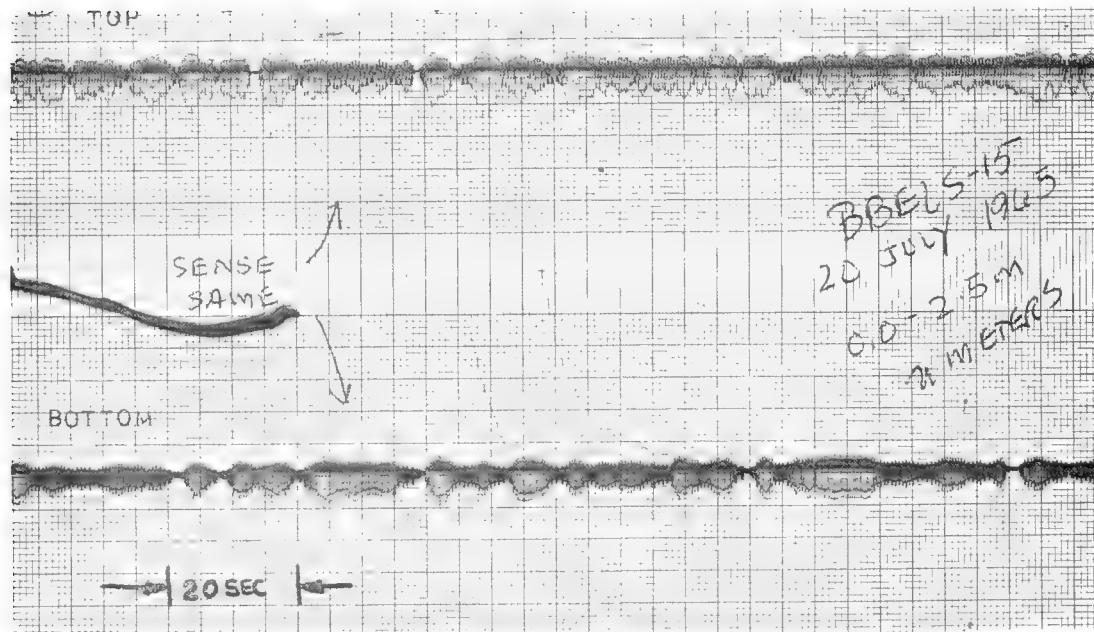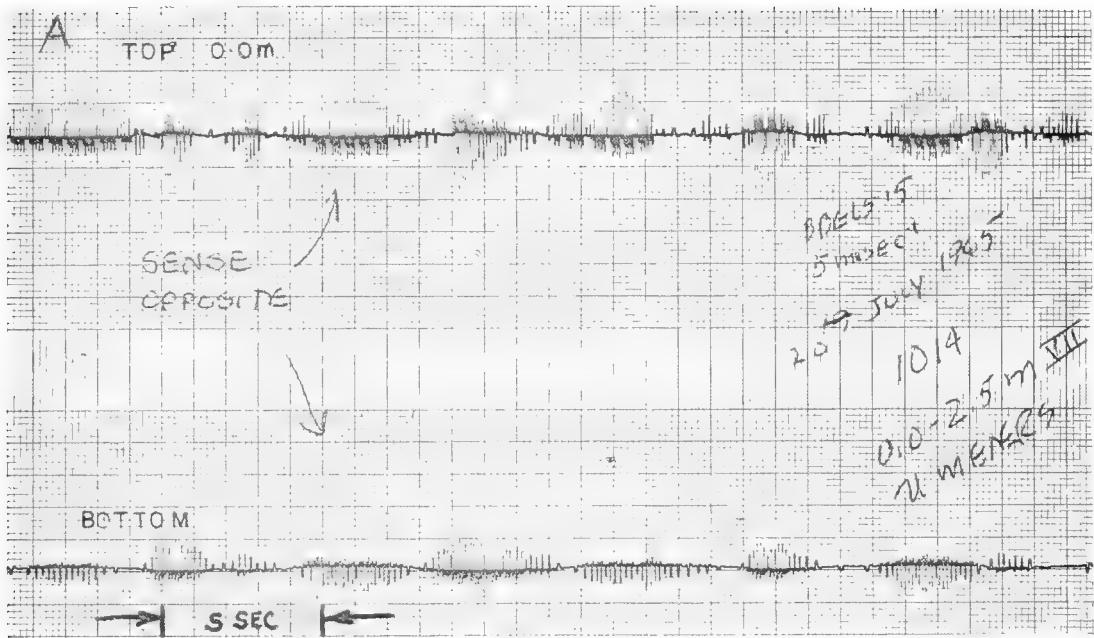
Recorded Traces of LIMDUM I Output – Chart Speed of 20mm Sec^{-1} (Upper Traces)
and 5mm Sec^{-1} (Lower Traces)

Figure V-1

The heights of the induced voltage pulses are not equal; thus, periodic gaps occur in the otherwise smoothly scribed sinusoidal-like oscillations. The jagged effect could easily be eliminated by careful placement of each magnet within the impeller to give identical voltage amplitudes for a given speed.

Figure V-2 is a 38-second segment of processed velocity data abstracted from the record of serial 023 (BBELS-9, 0.5 m I), where the orthogonally mounted wave meter (OMDUM III) was used to obtain a simultaneous u and w record - shown by solid and broken lines, respectively. The data points used were interpolated at the usual 0.2-second intervals. The wind was from the ESE at about 3.0 - 4.5 m sec^{-1}, and there was a well-defined swell running from the south (see table IV-3 for other information on this record). Also present were small waves building up with the increasing wind from the SE. The u sensor of the wave meter was aimed directly at the oncoming swell.

The long period undulations of the u and w traces in figure V-2 vary from 7 to 10 seconds. The gross oscillations of the u and w components demonstrate a phase shift of approximately 90° (to be expected) between the two wave motion components; i.e., corresponding to sine and cosine-like motions. The increase in the amplitude of the motions toward the end of the trace, similar to the increase in the heights of a train of swells, is probably due to the beat of two or more dissimilar frequencies of waves. The velocity patterns are quite jagged, showing that higher frequency wind wave motions (which were observed) were superimposed on the swell. This becomes evident when examining the auto-spectra of these observations.

Figure V-3 shows a 38-second section of the record from serial 025 (BBELS-9, 2.0 m I). Here again, as with the record of 023, there is a similar periodicity and out-of-phase relationship between the u and w traces; however, the short jagged peaks are not so prevalent. This is consistent with the fact that at deeper depths the higher frequency motions become filtered.

In general, figures V-2 and V-3 show that the gross amplitudes of these orthogonal velocity components are roughly equal. This is important to note because often this was not the case with the OMDUM measurements. Figure V-4, for example, shows a plot of a 38-second u and w trace from serial 120 (BBELS-16, 0.5 m I) during a period of moderate swell from the SSE and small seas (see table IV-3). The u meter of the OMDUM III system was aimed into the wind waves from the west. The mean horizontal current was about 20 cm sec^{-1} moving westward against the wind waves.

Figure V-4 shows a strong inequality in the amplitudes of the u and w traces. The vertical velocity w shows strong oscillations having amplitudes two to three times those of the u component. The u component oscillates about the negative d-c bias caused by the tide current and never actually changes direction (crosses the zero axis). Closer eamination of the motions shown in figure V-4 reveals that the relatively high frequency oscillations (2-3 second period) occurring in the u trace are identifiable on the w trace (A and A', B and B', etc.). Note
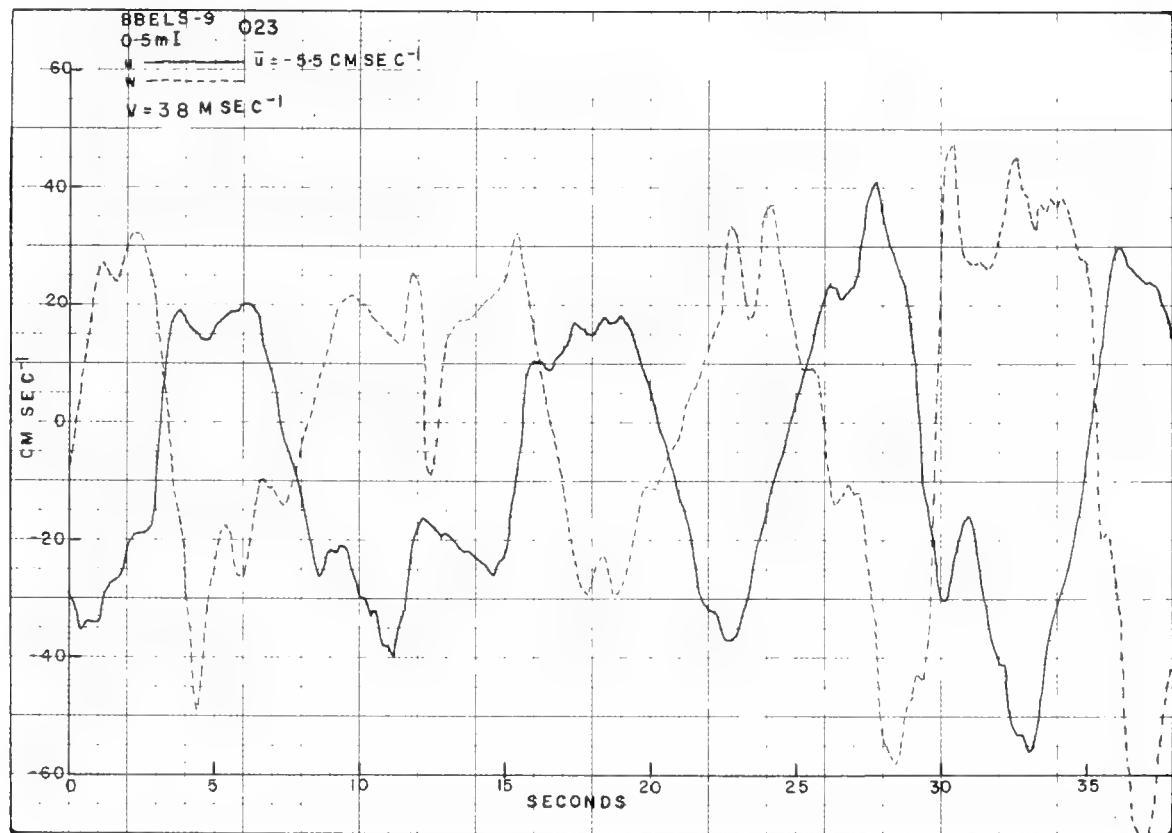
Segment of Interpolated u and w Data from OMDUM III (BBELS-9, Serial 023, 0.5 m I).

Figure V-2
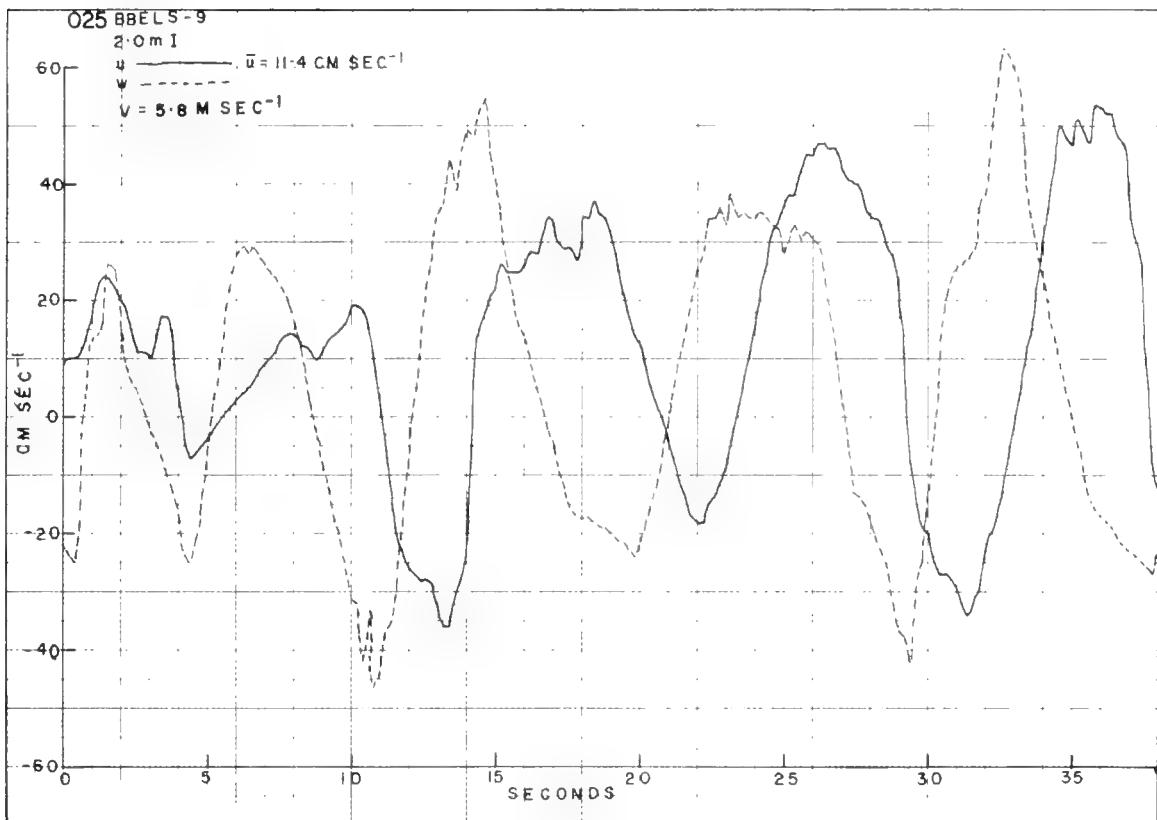
Segment of Interpolated u and w Data from OMDUM III (BBELS-9, Serial 025, 2.0m I).
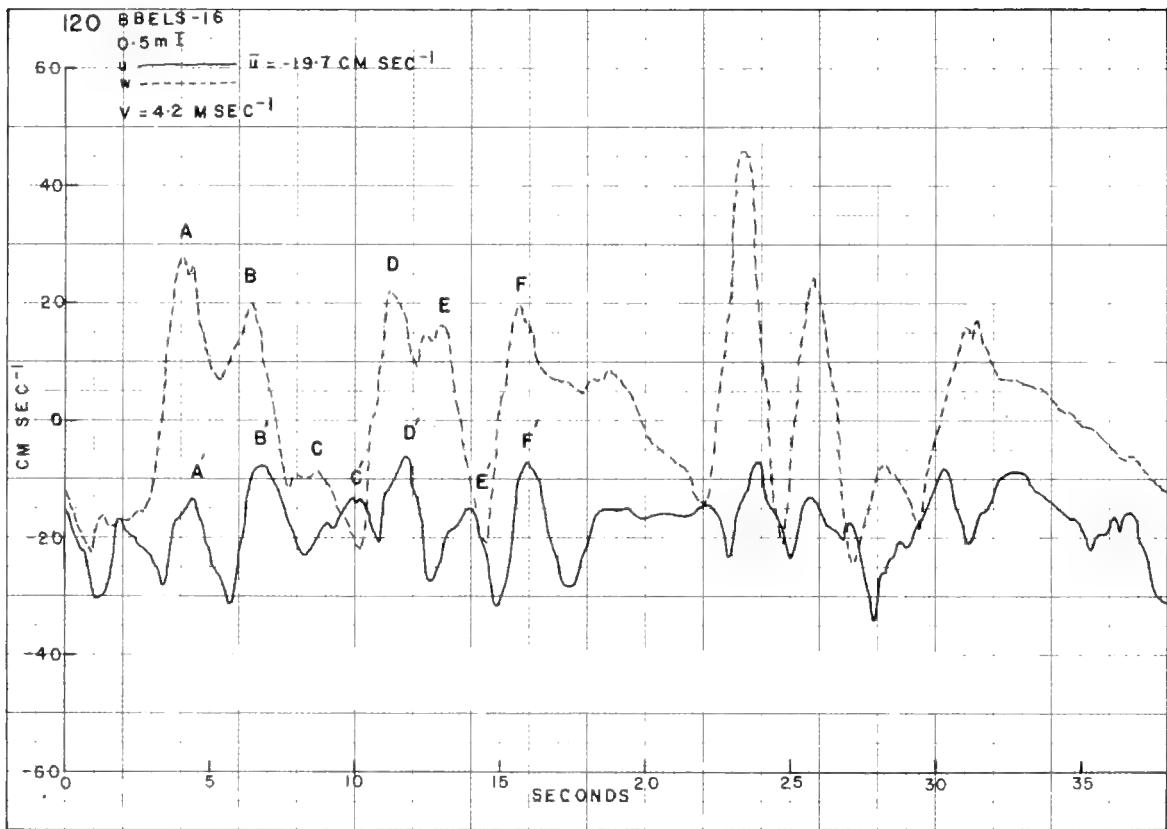
Figure V-3

Segment of Interpolated u and w Data from OMDUM III (BBELS-16, Serial 120, 0.5m I).

Figure V-4

also that these higher frequency motions are phase shifted similar to those of serial 023 and 025 (figures V-2 and V-3). However, the w trace clearly contains a strong lower frequency component having an estimated period of from 5-7 seconds.

The last sample record (figure V-5) was made using LIMDUM I, measuring w at depths of 0.0 and 2.0 meters. During this record from serial 086 (BBELS-14), winds were 8.0 m sec^{-1} from the SSW and no swell was observed.

Comparison of the 0.0-meter record (top) with the 2.0-meter record (bottom) indicates a high degree of positive correlation (or in-phase motion) between the observed motion at the two levels. The attenuation of the motion with depth is also evident in the amplitude differences of the two traces. There is also evidence of what appears to be a beat effect (from 5 through 25 sec) occurring on both records.

The velocity data portrayed in figures V-2 through V-5 would seem to indicate that the time variation of Eulerian wave velocities measured at a point is not particularly sinusoidal. The velocity functions appear rather to have somewhat flattened crests with abrupt slopes and jagged narrow troughs. It is interesting to note that this is roughly the inverse description generally given of the profiles of waves (e.g., Kinsman 1960). This odd shape associated with the velocity functions might result from some property of the wave meter. This does not seem to be the case, since the OMDUM II system faithfully reproduced an impressed sinusoidal oscillation simultaneously registered by an accelerometer (see figures II-3 and II-4). However, some further examination of possible distortion of the wave motion patterns by the wave meter seems called for at this point.

It will be recalled (see chapter II) that the OMDUM III system has a threshold velocity of about 7-8 cm sec^{-1}. This means that no output is registered when the speed of flow through the cylinder is less than this value; thus, a gap is periodically produced in the data as the wave motions oscillate. On the other hand, a high concentration of data points is produced in regions of high absolute velocity (this is shown in figure III-8). However, with interpolation, a uniform distribution of data points (as a function of time) is obtained. The velocity data were sampled at high enough frequencies to provide proper resolution, so that the plot of the interpolated velocity data should provide a reliable picture of the velocity (see figure III-8). This is particularly true since the velocity functions appear to change rapidly as they pass through zero, whereas they linger at the higher absolute values (vis., a boxcar signal as the extreme case). Hence, over the whole record relatively few sub-threshold data points have to be interpolated.

From examination of the actual velocity traces, it becomes obvious that, in order to properly compare the various records and individual u and w motions, one must progress further to the analysis of the variances and spectra.

Variances of the Observed Wave Motions - The results of the series of measurements made in Narragansett Bay (discussed in chapter IV) indicated a strong
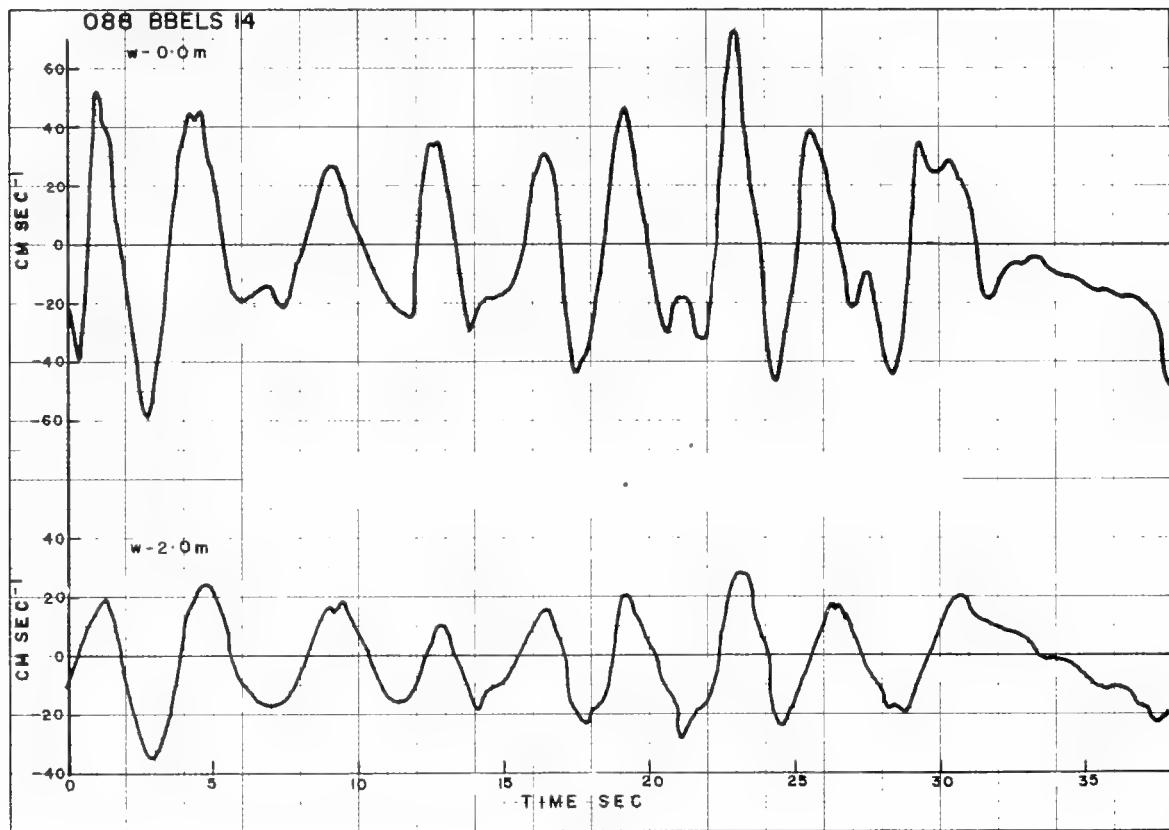
Segment of Interpolated Vertical Velocity Data from LIMDUM I (BBELS-14, Serial 086, 0 & 2m III).

Figure V-5

inequality between the amplitude of fluctuations of the u and w components $(\sigma_u^2 = 22.3$ cm^2 sec^{-2}, as opposed to 62.9 cm^2 sec^{-2} for $\sigma_w^2)$. The reason for this inequality is not clear, since one might expect that the variances of the vertical and the horizontal velocity components would be approximately equal for "deep water" waves, the motions of which suggest quasi-circular orbits (see equations (II-9) and (II-10)).

In examining the OMDUM velocity data from the first few observations from the BBELS, it was found that the same disproportion between variances generally occurred. A comparison of the variances of u and w for the various measurements is provided by table V-1. The table lists the ratios and square roots of the ratios of the variances of the u and w components (the latter being equivalent to the ratio of the standard deviations of the amplitudes of the velocity fluctuations). Also listed are: the mean horizontal velocity $\bar{u}$; the sea state judged from visual estimates of wave structure, using the definitions in table II-2; the instruments used; and the method of support of the instruments (see chapter IV).

It is evident that the more stable the suspension system, the more nearly equal the variances become (ratio σ_u/σ_w approaches unity). One might conclude that the wave forces upon the meters bias the measurement of the relative magnitudes of the two velocities. Note also that the OMDUM III instrument has about one-half the cross-sectional area of OMDUM II, which would reduce drag. Hence, it appears that as the waves pass the suspended instrument, the u measurement tends to be biased by oscillation of the meter in the x direction.

It appears from table V-1 that, during higher mean horizontal velocity $\bar{u}$ (absolute value), the ratio R_A tends to be smaller, suggesting that the mean current flow may be a counteracting phenomenon tending to dampen the instrument response to fluctuations of u. However, maximum value of R_A is 0.978, and most of the values are well below 0.8. Also, the Narragansett Bay measurements (rigid suspension system) and those from BBELS-14 and 16 (most stable suspension system) do not produce exceptionally high ratios.

This disproportion between the amplitudes of u and w was somewhat discouraging when the first observations were analyzed, since it seemed to cast doubts on all data obtained with the wave meters. Further examination of the spectra of the data indicated that, although the accuracy of the u data was rendered somewhat questionable by the non-rigid mounting of the instruments, other explanations of the unequal variances were plausible, and that the two-dimensional motions seemed, in general, to be well portrayed.

There is no a priori evidence that one must obtain equal variances for observed component wave motions. Some insight into the potential differences that might be expected in the statistics of u and w can be obtained by examining factors which may be used to distinguish horizontal from vertical motions.

Eckart (1955), in discussing fluid motion, defined a "random oscillation" flow as distinct from a "random drift". To visualize this, let L be the time

Table V-1. Comparison of the Variances of u and w.

SERIES		σ_u^2/σ_w^2	σ_u/σ_w	$\bar{u}$	*SEA STATE	INSTRUMENT	SUPPORT
Narragansett Bay		0.354	0.595		2	OMDUM II	Rigid beam
BBELS-5			R_A=0.315				
0m I	001	0.085	0.294	-40	3	OMDUM II	
1m I	002	0.087	0.296	-32	3	OMDUM II	
2m I	003	0.125	0.353	-33	3	OMDUM II	North guy
4m I	004	0.063	0.252	-30	3	OMDUM II	South guy
3m II	005	0.109	0.330	-31	3	OMDUM II	5 kgm weight
2m II	006	0.141	0.375		3	OMDUM II	
1m II	007	0.102	0.319	-35	3	OMDUM II	
0m II	008	0.089	0.298	-33	3	OMDUM II	
BBELS-7			R_A=0.522				
7.0m I	010	0.153	0.391	-16	2	OMDUM II	
10m I	011	0.342	0.585	-21	2	OMDUM II	
1.5m I	012	0.153	0.391	-16	2	OMDUM II	
10m III	013	0.194	0.440	-11	2	OMDUM II	North guy
9m I	014	0.082	0.287	-10	2	OMDUM II	South guy
8m I	015	0.306	0.553	- 9	2	OMDUM II	Back guy
6m I	016	0.124	0.352	-13	2	OMDUM II	7 kgm weight
4m I	017	0.774	0.863	-12	2	OMDUM II	
3m II	018	0.429	0.655	0	2	OMDUM II	
2m I	019	0.490	0.700		2	OMDUM II	
BBELS-8			R_A=0.805				North guy
1m I	020	0.528	0.726	22	2	OMDUM III	South guy
0.5m I	021	0.505	0.711	17	2	OMDUM III	Back guy
2.0m I	022	0.957	0.978	14	2	OMDUM III	10 kgm weight
BBELS-9			R_A=0.844				North guy
0.5m I	023	0.751	0.867	6	1	OMDUM III	South guy
0.5m II	024	0.549	0.741	3	1	OMDUM III	Back guy
2.0m I	025	0.901	0.949	11	1	OMDUM III	10 kgm weight
BBELS-14							
1m IV	099	0.169	0.410	-19	3	OMDUM III	
							North guy
							South guy
							Back guy
BBELS-16							Anchor guy
0.5m I	120	0.222	0.471	-20	1	OMDUM III	7 kgm weight

*Sea state values are taken from table II-2.

R_A = average ratio (σ_u/σ_w) for series.

variable displacement vector of a particle from a fixed point in the XZ plane, given by:

$$\mathbb{L} = \mathbb{i}\, L_x + \mathbb{K}\, L_z \, .$$ (V-1)

The velocity at an instant of time is given by:

$$\frac{d\,\mathbb{L}}{dt} = \mathbb{V} = \mathbb{i}\,\frac{dL_x}{dt} + \mathbb{K}\,\frac{dL_z}{dt} \, .$$ (V-2)

Eckart defines a "random oscillation" as that motion existing when $\mathbb{V}$ remains approximately constant as $|\mathbb{L}|^2$ increases indefinitely. On the other hand, a "random drift" exists when $|\mathbb{L}|^2$ increases indefinitely with time, although the variance of the velocity $\overline{|\mathbb{V}|^2}$ remains constant. When Eckart made this distinction, he may not have been thinking specifically of ocean wave motions; but particles in ocean waves fulfill each criterion, depending upon which coordinate one chooses to observe. For example, along the Z axis the motion is definitely bounded; i.e., $\overline{L_z^2}$ is approximately constant over short periods (for stationary conditions). In other words, the variance of the amplitude of the orbital motions is approximately unchanging during a period ranging from a few minutes to a few hours. Thus, in the vertical, there is a random oscillation condition. Note also that for short periods:

$$\overline{\left(\frac{dL_x}{dt}\right)^2} \cong 0 \, .$$ (V-3)

In the X direction, the situation is different. The value of $\overline{L_x^2}$ is, in general, always increasing with time. This is due partly to the actual continuous displacement peculiar to surface waves, but mainly to a mean flow of tidal current and perhaps wind drift. Also, over short periods:

$$\overline{\left(\frac{dL_x}{dt}\right)^2} \cong CONSTANT.$$ (V-4)

The reason for considering these definitions is to indicate the degree of anisotropy of the wave motions. It may reasonably be assumed that, over the period of measurement, there will be zero mean vertical motion. However, the mean horizontal motion will usually be non-zero, caused by slowly oscillating or meandering currents that contribute to the u (but not to the w) velocity data. The statistics of the random oscillation for vertical motion w(t) should be simpler to interpret than those for horizontal motion u(t), since the latter function can have strong contributions of a random drift nature. Hence, for a given time interval of

measurement, the concept of mean value and stationarity, so important to spectrum evaluation, has more significance when applied to w(t) observations than to u(t). The random oscillation mode of a fluid is thus more amenable (than a random drift process) to examination by a Eulerian time series measurement. For example, it is easier to measure and interpret a spectrum of wave heights than it is to measure and interpret a spectrum of ocean currents.

The estimate of the two-dimensional components in the XZ plane of a particular wave train is rendered difficult in another respect. The u component detector has been shown in calibrations to be sensitive to the direction of flow. This can be clearly seen in measuring the u and w components of a uniform train of ocean waves. Assume in figure V-6A that the output of the motion detector or current meter is proportional to the cosine of the angle θ between the azimuth of the detector and the direction of the waves. Now, if u_0 is the amplitude of the horizontal velocity component function oscillating both in time and space, then its value is a function of the azimuth of the detector and is given by:

$$u(\theta) = u_0 \cos\theta . \qquad \text{(V-5)}$$

The variance obtained will be:

$$\sigma_u^2(\theta) = \overline{u_0^2 \cos^2\theta} \qquad \text{(V-6)}$$

The variance is proportional to the wave energy, so that the spectral functions would have a similar relationship to θ. On the other hand, the response of the vertical motion detector will be independent of the value of θ, or:

$$\sigma_w^2 \qquad = \text{constant.} \qquad \text{(V-7)}$$

The essential difference here (shown in figure V-6B) is that the particle subjected to random oscillation is virtually bounded along the Z coordinate by the interplay of pressure forces, gravity, and, to a lesser extent, shear stresses. Particles experiencing random drift move in a less predictable way, with much weaker shear and pressure forces acting upon them in a somewhat random manner. A fairly sophisticated interpretation may therefore be required to explain observed differences between the two velocity records. As an example, if both a swell and a wind wave motion are present, and if the swell is not moving in a coincident direction to the wind wave (at which the horizontal sensor has been aimed), then the swell motion plus the wind wave motion are detected by the vertical sensor. However, some of the horizontal flow component of the swell is filtered out.

Figure V-4 appears to bear out this analysis. The u meter of the OMDUM III system was aimed at the wind waves coming from the west. The result is that small
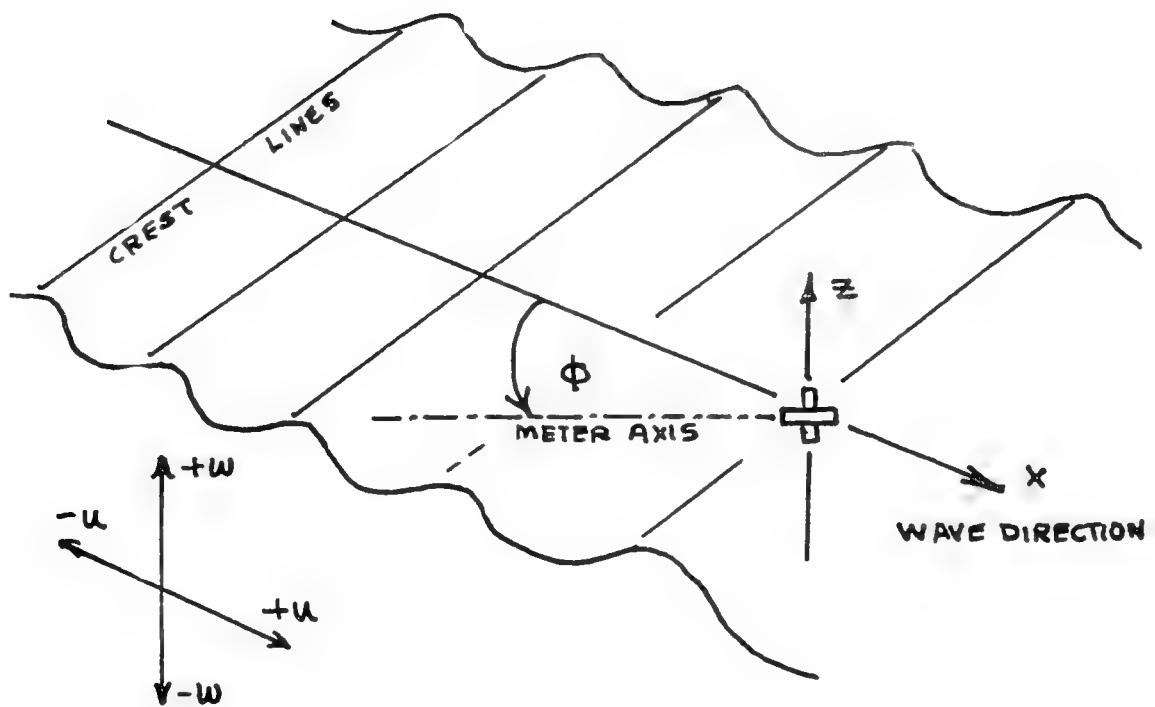
Orientation of the OMDUM System.

Figure V-6A
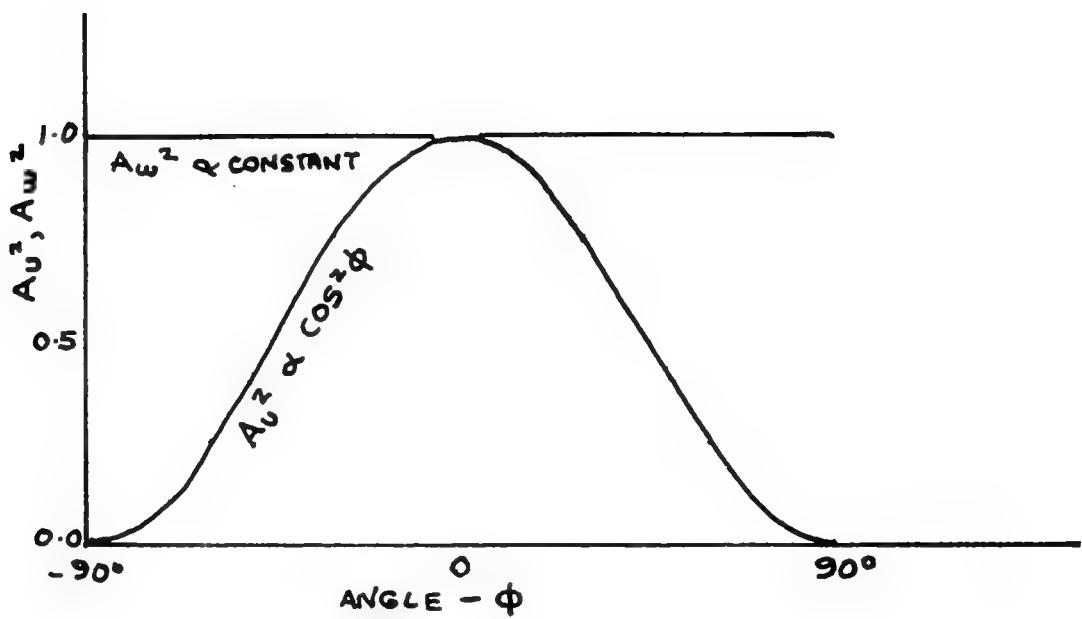
Relationship of A_u^2 and A_w^2 with Θ.

Figure V-6B

wind waves are recorded in the u direction, but no swell is indicated; whereas the w meter indicates both sea and swell. Since the swell frequencies, which generally occur below 200 mcps, do contribute substantially to the total variance (up to 50 percent in cases of high swell conditions), this directionality aspect could contribute strongly to the inequality of the u and w variances. Also, the relative contribution of swell to the variance increases with depth because of the strong attenuation of the higher frequency wave motions.

Finally, the disproportion of variances could be partly explained by a diminution of σ_u^2 caused by the u meter not "seeing" certain horizontal wave components that contain substantial energy but are traveling in off-angle directions. Also, the potential biasing effects of wave-induced motion on the suspended wave meter system cannot be ignored. For it appears that the more stable suspension systems, when coupled with a reduction in drag of the wave meters, do allow more accurate measurements. Further discussion of the angular response of the wave meters with respect to swell and wind waves is given later in this chapter.

Distributions of Wave Velocity Samples - Workers studying surface elevation statistics have considered the question of the probability distribution of the free surface function η (t) at some fixed point in the ocean. Their reasoning is that, if the waves observed are formed by many contributions from unrelated forces and at different times, one can assume that the elements of the Fourier components making up the function η (t) are statistically independent. Thus, the distribution should be Gaussian or normal. This assumption has been considered by Pierson (1955), and by Pierson, Neumann and James (1955), among others.

The Gaussian time probability distribution is written as:

$$P(\eta) = \frac{1}{2\pi\sigma_\eta^2} \, e^{-\frac{\eta'^2}{2\sigma_\eta^2}} \; ; \qquad \text{(V-8)}$$

where, as usual, η' is the instantaneous deviation from the mean $\bar{\eta}$. This probability distribution is uniquely determined when the mean and variance of a set of data are known.

Kinsman (1965), inquiring into the distributions of wave data, presents an analysis of 24 capacitance pole wave measurements made several years earlier (Kinsman, 1960). Kinsman made plots of the characteristic frequency distributions from free surface records of η (t) spaced 0.2 second apart. (This spacing was used because the spectra of the records show no appliable energy at frequencies greater than 2500 mcps; i.e., the Nyquist frequency for the 0.2-second sampling rate.) These distributions showed a positive tail raised slightly above the Gaussian, and a negative tail slightly below. Kinsman saw the skewness toward high values as compatible with the observed fact that the surface waves he measured were not symmetrical, but had relatively longer and flatter troughs and sharper and more peaked crests. However, the overall deviation from a Gaussian distribution was very small.
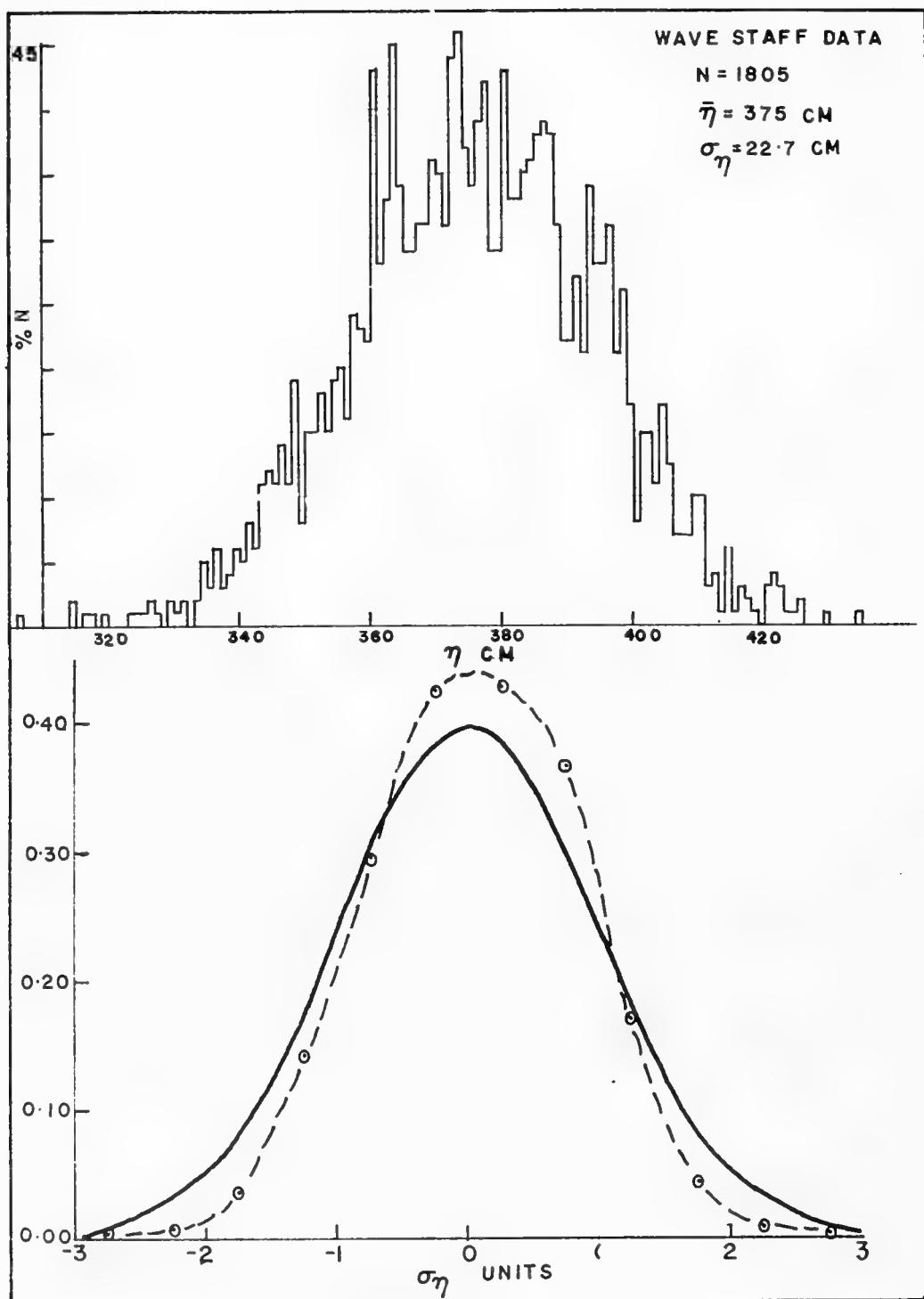
Frequency Sort of Wave Staff Data (Upper Plot) and Comparison with the Gaussian (Lower Plots).

Figure V-7

It is of interest to examine (as Kinsman did) the amplitude distribution of wave velocity components measured with the wave meters. The relationship of the probability distribution of wave velocity components may indicate some interesting assymetric or nonlinear characteristics of the wave motions. Further, it is well to determine the approximate distributions of the wave meter data, since strong deviations from Gaussian (e.g., extremely lopsided distributions) would tend to detract from the physical meaning of the variance and its associated spectra.

Before looking at the velocity sample distribution, let us examine a free surface distribution from a record of $\eta(t)$ made with the CERC wave staff (discussed in chapter IV) mounted on BBELS. The record was made on 9 June 1965 from 0000 to 0006 hours. During this period the wind velocity was 7 m sec^{-1} from the SSW. A copy of the original analog record was obtained and digitized at 0.2-second intervals using the NUWS Telerecordex film reader. For the sample, N = 1805, the mean $\overline{\eta}$ = 375 cm, and the variance σ_{η}^2 = 516 cm^2, giving a standard deviation σ_{η} = 22.7 cm.

The histogram sort of values of η at 1 cm increments is shown in the upper plot of figure V-7. The ordinate is proportional to the number of values N or percent of population of η which occurred within each height interval designated on the abscissa. The general pattern of the distribution appears roughly symmetrical about the mean. A closer look indicates, however, that the upper side (above 375 cm) falls below the Gaussian, whereas the lower side (below 375 cm) may fall above it.

The best way to examine the distribution is to follow a procedure used by Kinsman (1960). This analysis entails a 1/2 σ_{η} frequency sort of the data. Figure V-7 (lower plot) shows the percentage of population within 1/2 σ_{η} intervals. The solid curve is the classical Gaussian distribution curve. The broken line connecting the circles serves only to suggest the actual η distribution. The experimental curve is similar to the Gaussian, although the curve tends to fall below the Gaussian on the lower side and is skewed toward higher values near the peak.

In figure V-8 the frequency distribution of the wave heights is expressed as a cumulative percent ordinate versus the excursion from the zero (mean $\overline{\eta}$) wave height in units of standard deviation σ_{η}. The straight line entered is the Gaussian. From these plots it would appear that this wave record, like those of Kinsman (1960), is substantially Gaussian except for skewing toward the extreme values.

Turning now to some velocity data distributions; figure V-9 (upper plot) shows a frequency sort of the vertical velocity values w from serial 057 (BBELS-11, 0.5 m χ). For this sample N = 2088 and σ_w = 34.6 cm sec^{-1}. The distribution appears to be bi-modal, with the peaks occurring symmetrically at about ± 15-20 cm sec^{-1}. The lower plot in figure V-9 compares the overall distribution with the Gaussian. The experimental curve (broken lines) seems to be somewhat over-populated at the ± 0-1 σ_w values. This effect may be caused by the peaks in the actual data histogram (upper plot). Figure V-10 is the cumulative frequency plot of the w velocity distribution shown in figure V-9. The behavior closely follows the Gaussian (straight line) except for higher positive velocity values.
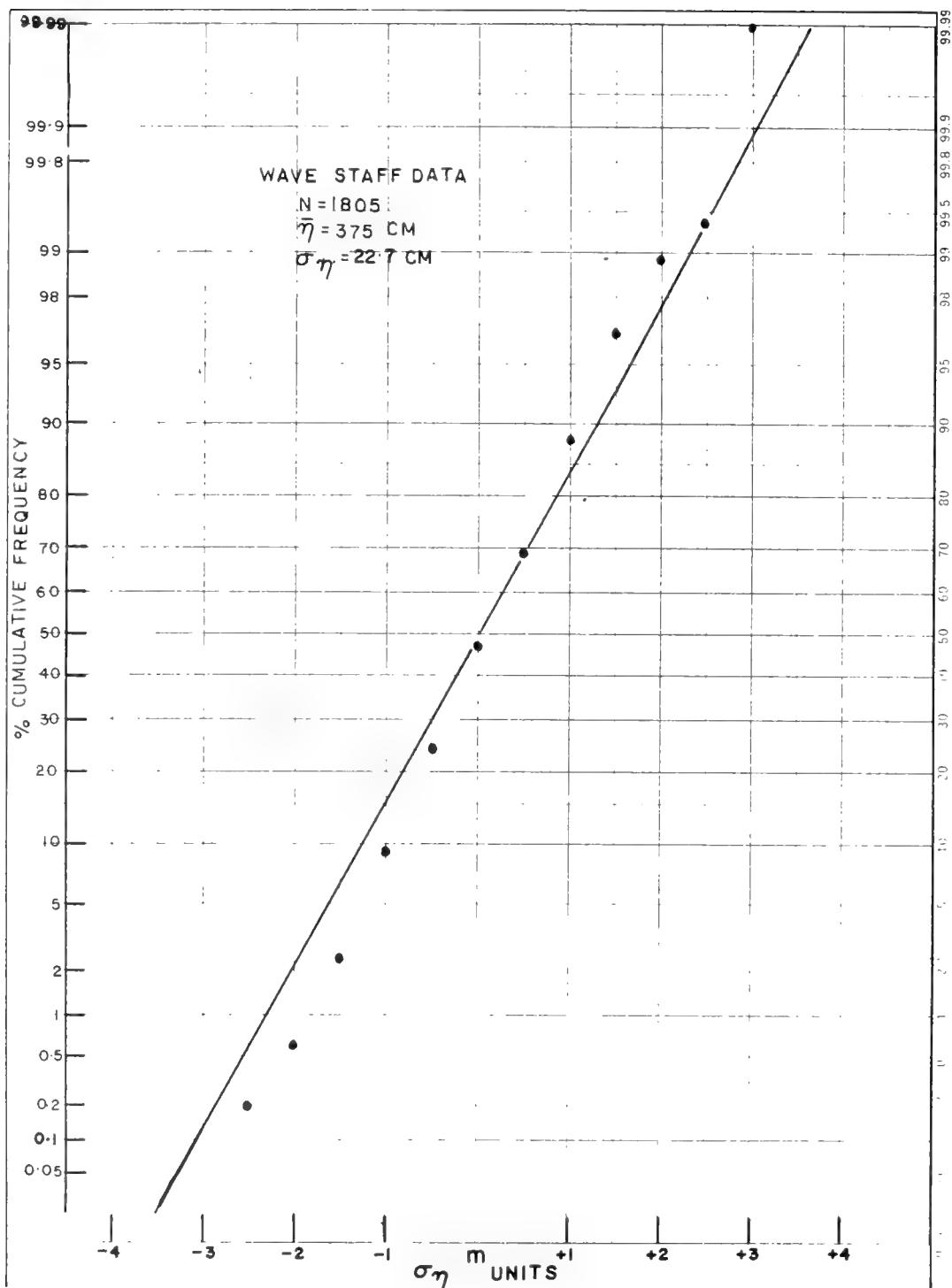
Cumulative Frequency Sorts of Wave Staff Data.
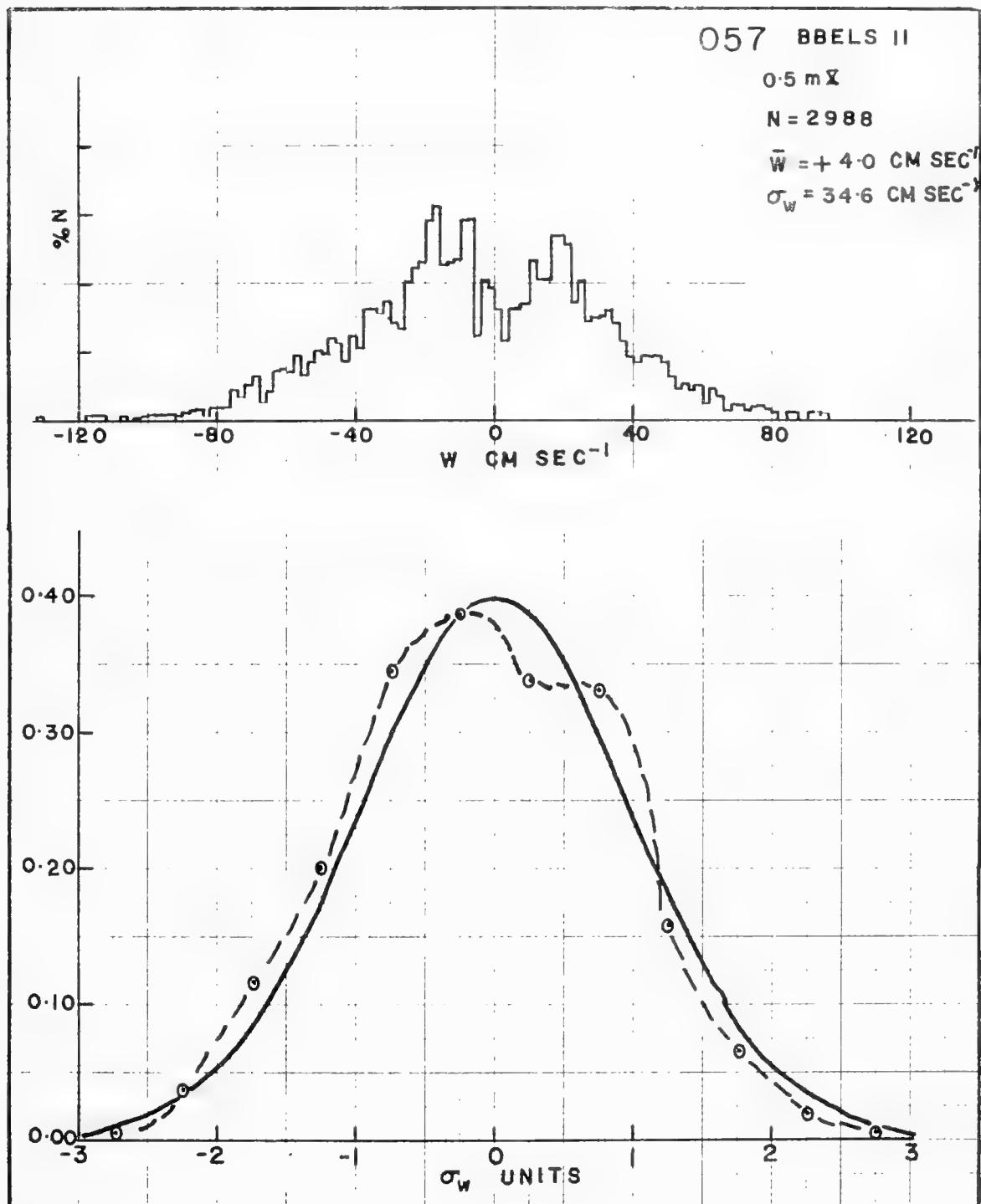
Figure V-8

Frequency Sort of Vertical Velocity Data (BBELS-II, Serial 057, 0.5m)
and Comparison with the Gaussian (Lower Plots).
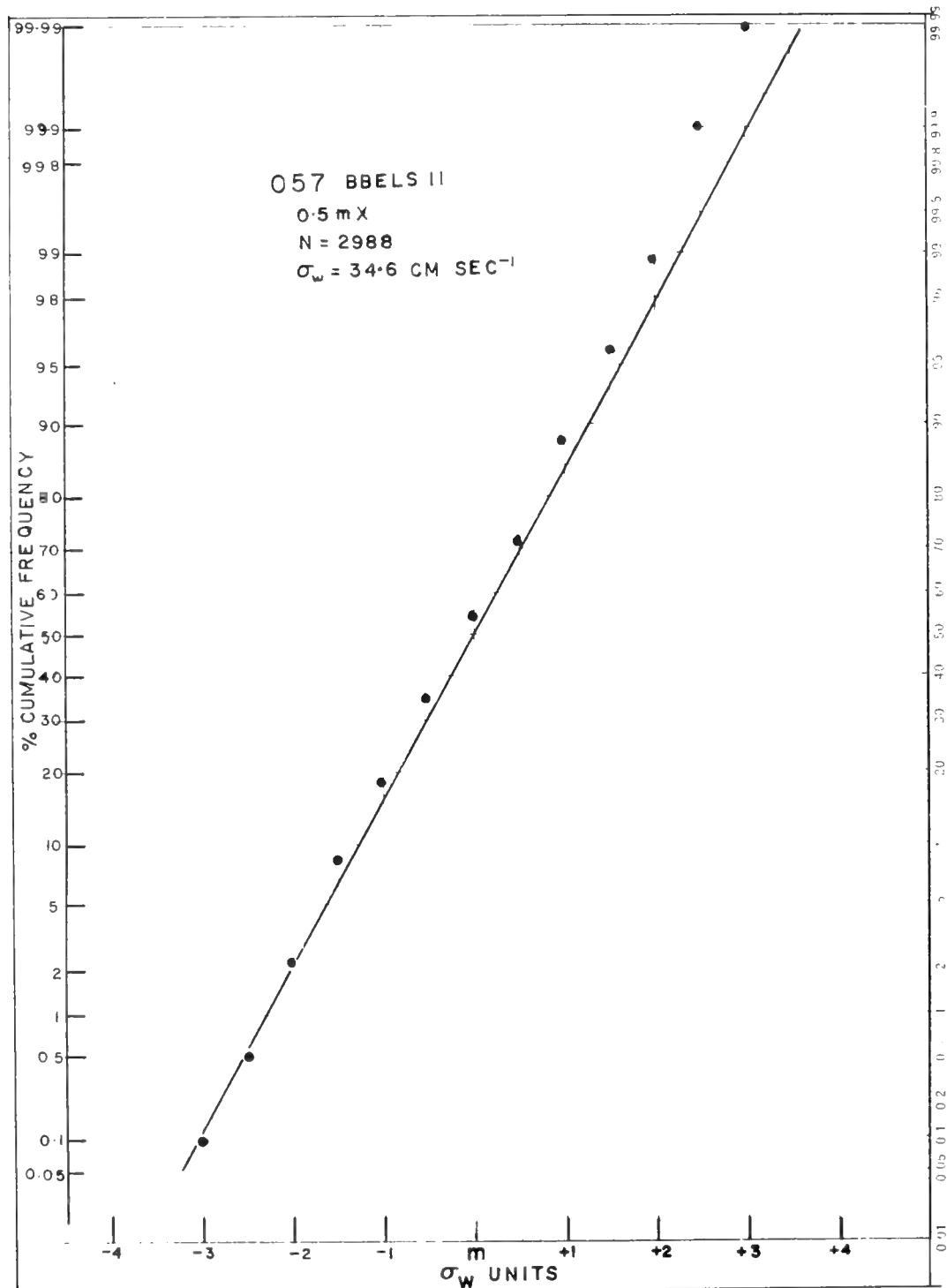
Figure V-9

Cumulative Frequency Sort of Vertical Wave Velocity Data (BBELS-II, Serial 057).

Figure V-10

Figures V-11 and V-12 (upper graphs) show histogram sorts of serial 055 (BBELS-11, 2m V) and serial 038 (BBELS-11, 4m II) for a 2 cm sec^{-1} sorting interval. The same bi-modal character occurs, with an apparent minimum at velocity values below about 5 cm sec^{-1}. Because of the coarseness of the 1/2 σ_w interval, the lower curves in figures V-11 and V-12 do not show a bi-modal shape. However, a gross distortion appears in the distribution, as compared to the Gaussian.

The explanation for the distortion of the velocity sample distribution seems obvious. It was noted earlier that the ducted cylinders of the wave meters (used in the OMDUM III or LIMDUM I configurations) have a threshold velocity of about 7-8 cm sec^{-1}. Thus, there are times (evident in figure III-9) when the wave motion does not exceed the threshold velocity. Since the impellers do not rotate, no signal is provided. The interpolation program fills in this information gap with linearly interpolated velocities. If the wave motion, after having fallen below the detectable velocity, again rises above it (in the same sense or direction); then the interpolation program provides a supply of linearly interpolated velocity values between the two points where the wave meter stopped and resumed sensing motion. Thus, a disproportionately large number of near-threshold velocity values are produced in the data. These interpolated velocities are produced in place of the actual lower velocities, which are undetectable. Note that when there is a zero crossover (change of sense), the interpolation process probably gives a much less distorted velocity distribution. This is because, in passing through zero, the velocity values are constantly changing to the next actual velocity value (see figure III-2).

A velocity null followed by motion in the same sense can therefore cause trouble. At greater depths, where the motions are slower, this effect is amplified (see figures V-11 and V-12). Statistically, the null velocity situation would occur with equal probability upward (+w) or downward (-w). The histogram produced would therefore show a bi-modal distribution, with peaks at or near the threshold velocities. By increasing the range of the sorting interval (e.g., from 2 cm sec^{-1} to 5 cm sec^{-1}), the distribution would, perhaps, appear more Gaussian. The question arises as to how closely one should attempt to resolve the data in order to judge the data distribution. The sorting interval can always be resolved (for a finite sample) so that only one (or less) data point falls in each interval. This, of course, produces a meaningless distribution.

The null velocity situation, however, does not seem to be the whole story. For one thing, the maxima that occur in serial 057 (0.5 m depth) are centered well above the threshold velocity of 7-8 cm sec^{-1}. Also, in the interpolated velocity traces in figures V-2 through V-4, the regions of variation from positive to negative velocities (or vice versa) seem small compared with the time spent at the large velocity magnitudes.

The hypothesis that the waves should be Gaussian is based on the assumption that the free surface function η can be represented (as an approximation) by a quasi-infinite number of independent Fourier components, having a quasi-infinite number of wave heights and frequencies. In reality, however, the ocean is not random to the extent that one cannot distinguish relatively organized systems of waves (either wind-generated waves or swell) among much clutter.
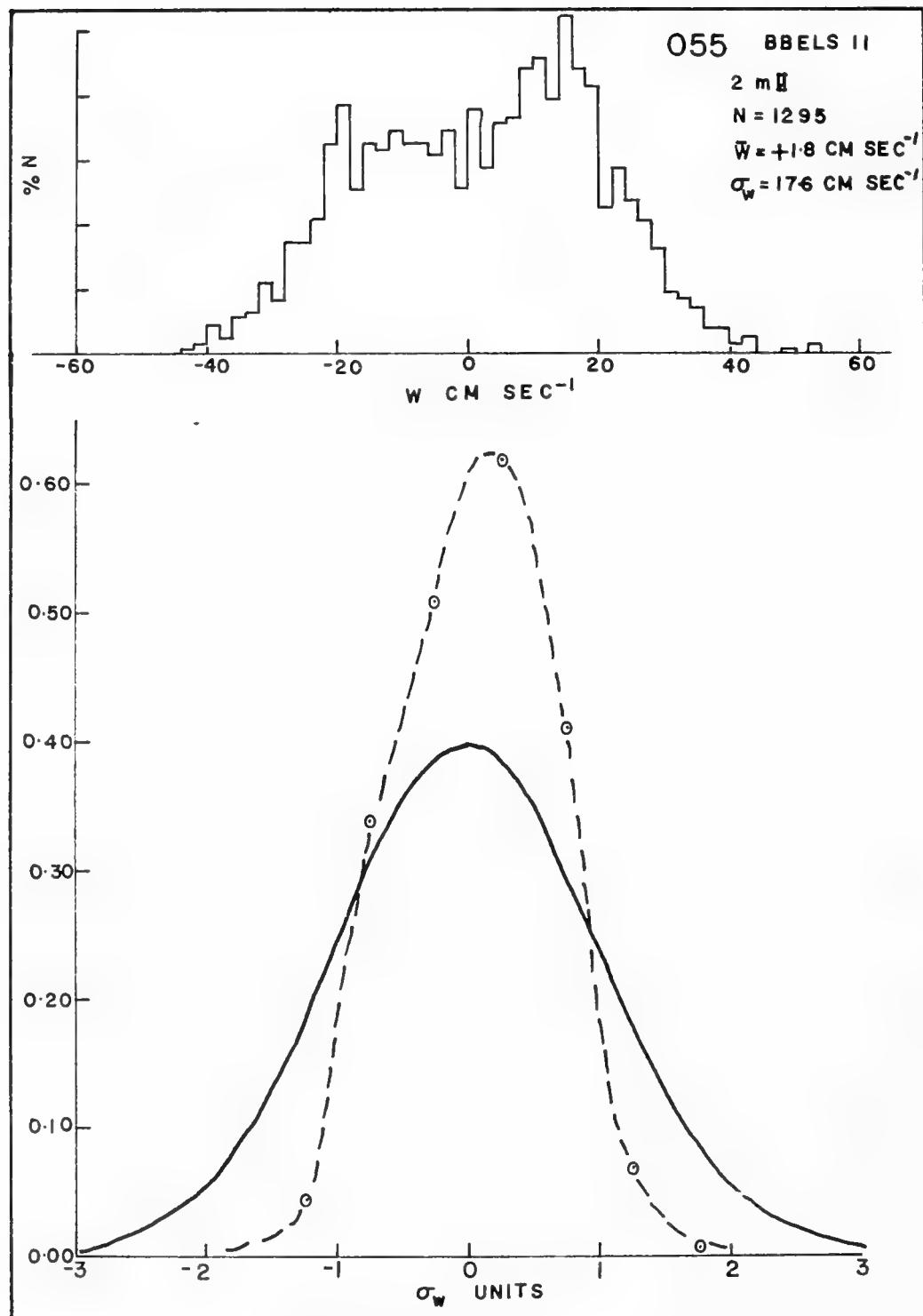
Frequency Sort of Vertical Velocity Data (BBELS-II, Serial 055, 2.0m) and Comparison With the Gaussian (Lower Plots).

Figure V-11
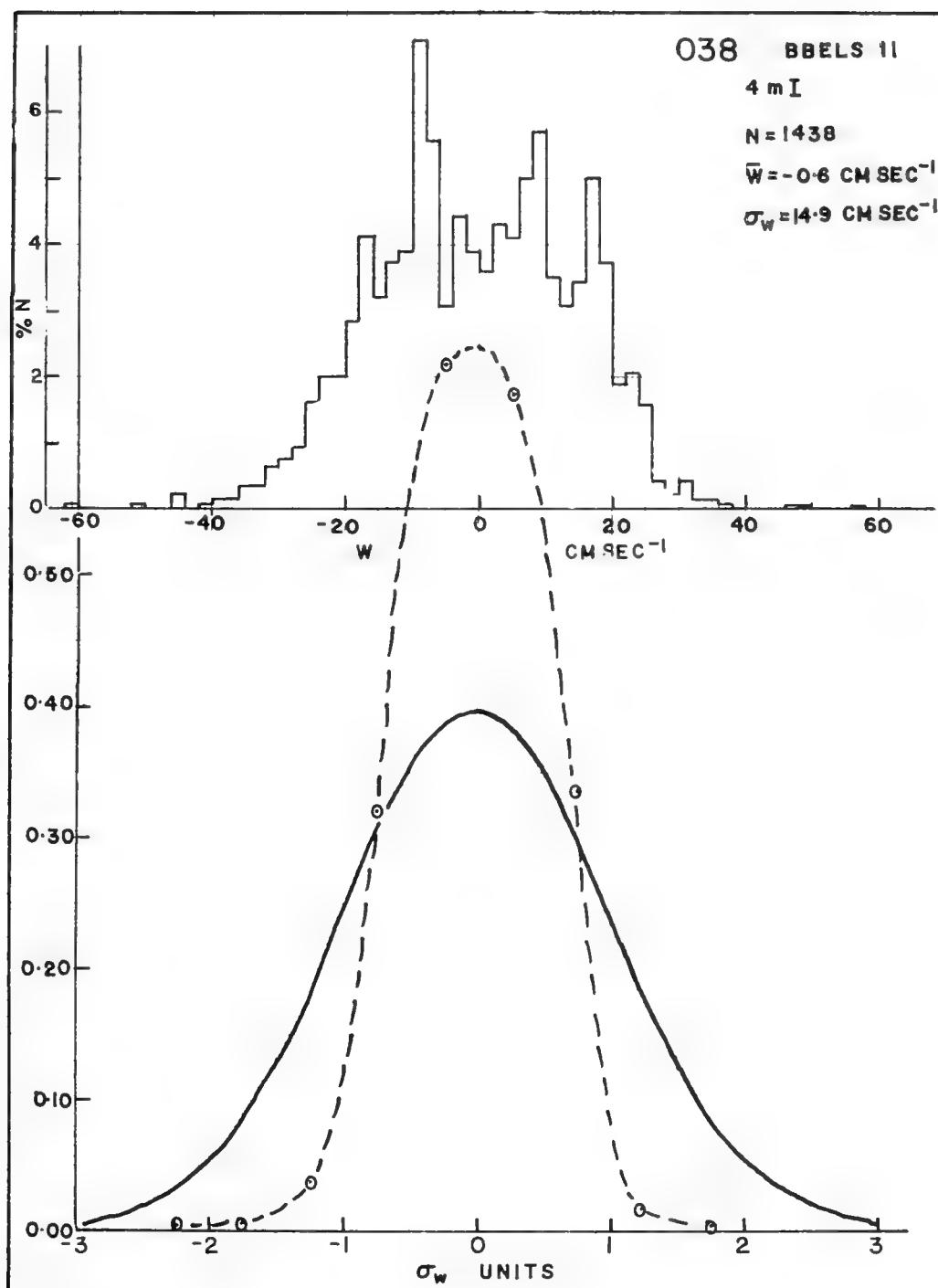
Frequency Sort of Vertical Velocity Data (BBELS-II, Serial 038, 4.0m) and Comparison with the Gaussian (Lower Plots).

Figure V-12
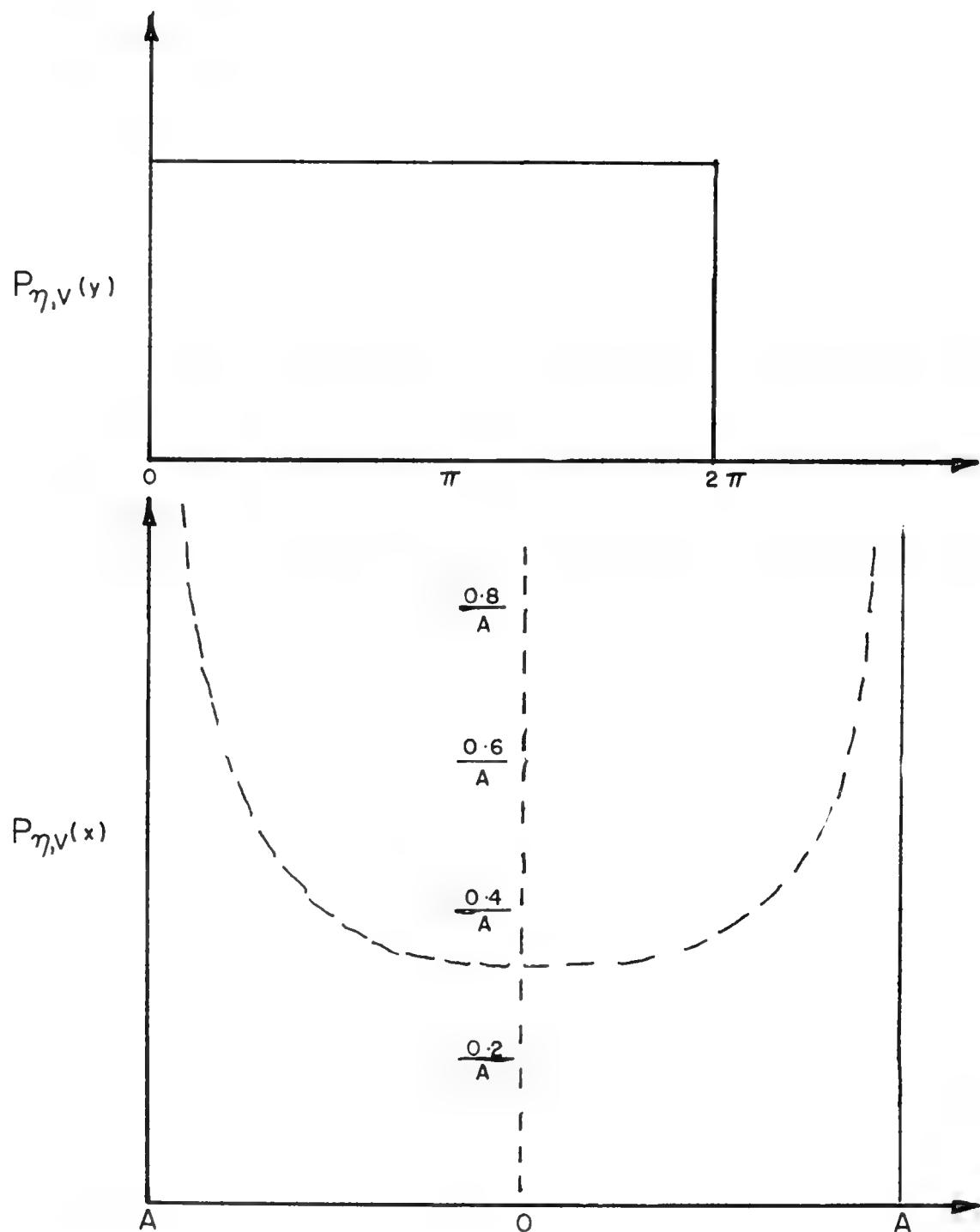
Flat Probability Distribution of the Phase Angle Function (Upper Trace) and
Probability Distribution of the Amplitude Function (Lower Trace) of Ocean Waves
with Random Phase.

Figure V-13

For the sake of argument, assume an ocean with a large system of ideal, small amplitude, sinusoidal waves propagating in the same direction. The waves are of identical wave length, wave height, and frequency, but all are of random phase. What then is the probability distribution of the height of the free surface level $\eta(t)$, or of the magnitude of a velocity component $v(t)$, when measured at a fixed location? If the density of the phase angle given by $P_{\eta,r}(\gamma)$ is uniform (i.e., has equal probability of occurring anywhere within the range 0, 2π, as shown by the upper plot of figure V-13); then, with classical sinusoidal waves, the probability density of the amplitude A or the velocity function u (given by $P_{\eta,r}(x)$) will be as depicted in the lower plot of figure V-13. (See appendix A.) This distribution is far different from the Gaussian in that the maximum values occur at the peaks of the waves.

Applying this argument to the case of real waves: if there is a dominant class amongst the myriad of waves present (represented by a peak in the spectra), a class with similar heights, frequencies, and wave lengths, but of random phase; then there will be a tendency to produce a maximum in the distribution function associated with either the velocity or the free surface functions of the waves. This maximum would occur on the $\sigma_{\eta,r}$ scale around the mean amplitude value of the particular function.

In short, if there are in the ocean a quasi-infinite number of waves of all frequencies, amplitudes, and wave lengths, such an assortment of waves has an approximate Gaussian distribution function. If, on the other hand, there is a dominating sub-group of waves having similar parameters, their distribution function tends to appear like $P_{\eta,r}(x)$ in figure V-13. This latter effect would produce a net distribution that is symmetric about the mean, but with a bi-modal tendency as shown in figures V-9, V-11, and V-12 (upper histograms).

Velocity Auto-Covariance Spectra

The spectrum analysis of the wave particle velocity records can, with proper interpretation, present the most meaningful part of the data analysis. Not only can the auto-spectra of the time series records help in the interpretation of the physical processes being studied, but they can often reveal something about the reliability of the data and of the instrument used to obtain it.

Auto-spectra plots of the wave observations and tabulations of the statistical data are presented in appendix B. Along with table IV-3, which summarizes both the statistical and environmental data for each observation, these should provide ample information for reference.

For purposes of orientation, examine first a typical auto-spectrum - serial 069 (BBELS-11, 3m III) made 30 March 1965. This auto-spectrum Φ_w (see plot P-069 in appendix B) is of the vertical velocity component w measured at about 3 meters below the trough level. It was computed using 1059 data points with M = 50 lags. A logarithmic ordinate is used in the appendix B plots to show the frequency contribution over the whole range of measured spectral density. The ordinate Φ_w is in units of $cm^2 \ sec^{-2}$ per unit frequency bandwidtn. In this case, if M = 50
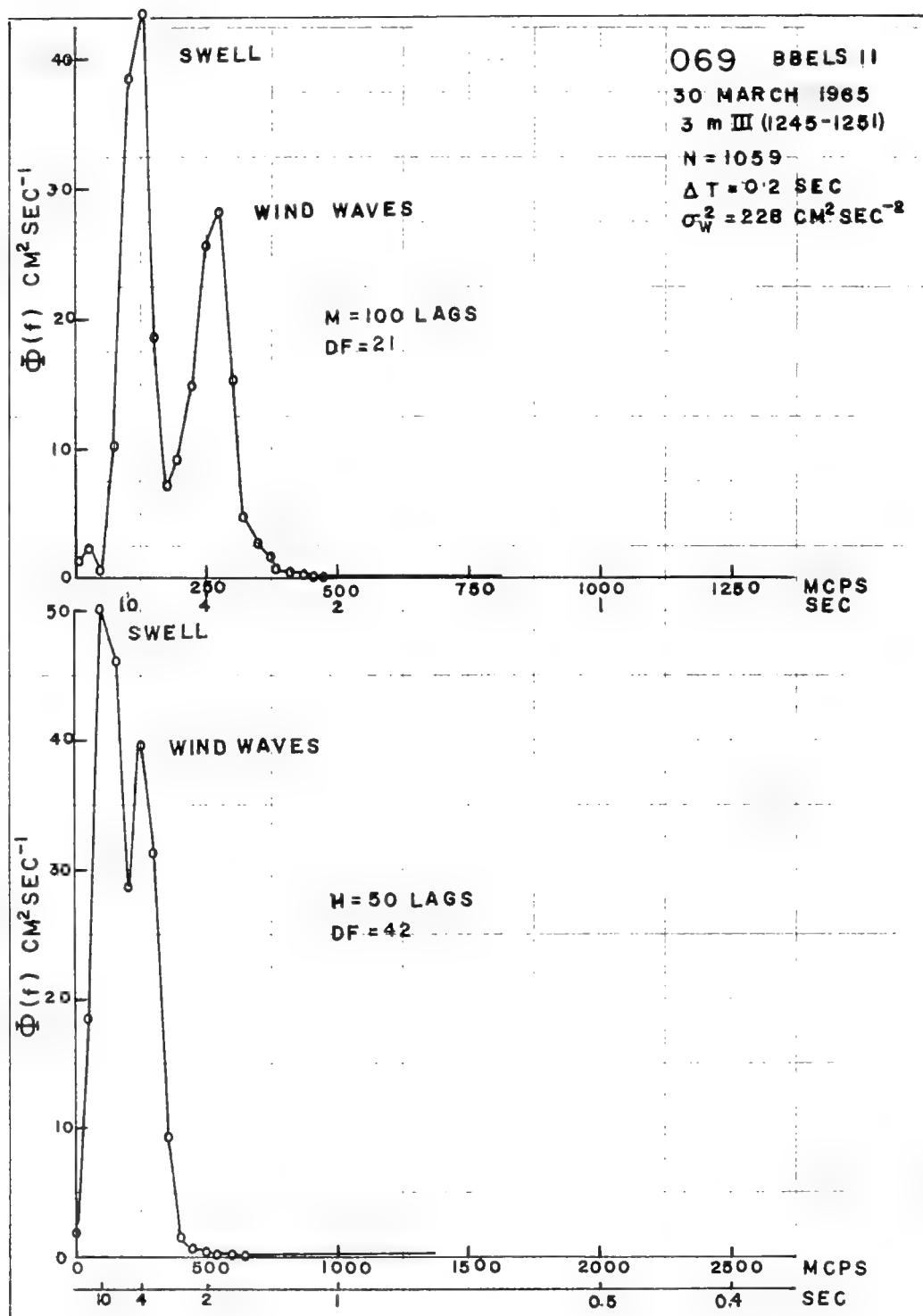
Auto-Spectra for M=50 and M=100 Lags (BBELS-II, Serial 069).

Figure V-14

lags and ΔT = 0.2 second; then, according to equation (III-6), the frequency band upon which each of the 50 spectral density estimates is centered (i.e., the frequency resolution) is 50 mcps. Thus, the units of Φ_ω are in $cm^2\ sec^{-1}$. The abscissa is shown as units of frequency, in millicycles per second (mcps), and period (sec). Using equation (III-10), the number of degrees of freedom DF = 42. From the confidence limit plot of figure III-3, the range of the 80 percent confidence limits lies below 1.38 and above 0.73 times the value obtained. The vertical bar (shown on each graph) delineates the range R of the 80 percent confidence limits when the middle crossline is placed on the curve. This is best done using a pair of dividers.

Since ΔT = 0.2 second and M = 50, the limiting frequency or Nyquist frequency f_n is given by equation (III-2):

$$f_N = \frac{1}{2\Delta T} \quad = \quad 2500 \text{ mcps.}$$

The frequency of resolution Δf is given by equation (III-4):

$$\Delta f = \frac{1}{2M\Delta T} = 50 \text{ mcps.}$$

The spectrum displays two peaks, at frequencies of 100 and 250 mcps (10 and 4 sec periods). The energy is concentrated in the band between 50 and 500 mcps.

The use of a logarithmic ordinate provides equal resolution at all ranges of the values of Φ_ω. Because of this effect, there is a distortion in the relative magnitudes of the energy distribution with frequency. To illustrate this: Φ_ω for serial 069 was plotted using a linear ordinate (see figure V-14, bottom graph). Observe the strong damping of the higher frequency energy on the linear scale. The two peaks stand out more than in the logarithmic plot of serial 069 (in appendix B).

To resolve more highly the low frequency range from 250 to 500 mcps, one need only apply the relationship in equation (III-4), increasing the number of lags M. By letting M = 100, the frequency range is resolved into twice as many divisions (i.e., Δf = 25 mcps) over the same range from 0 - 2500 mcps. The new spectrum is produced in figure V-14 (upper curve). For convenience, the f scale has been stretched out and cut off at 1250 mcps, since negligible energy lies beyond. The two peaks are much more clearly defined. Now the peaks occur at about 125 and at 275 mcps, or at about 9.0 and 3.6 second periods.

This increase in resolution cannot be obtained indefinitely by increasing M values. One must keep equation (III-10) in mind. With the degrees of freedom DF = 21, the upper and lower ratios for 80 percent confidence are now 1.40 and 0.64, respectively (figure III-3). These values can be considered near enough to
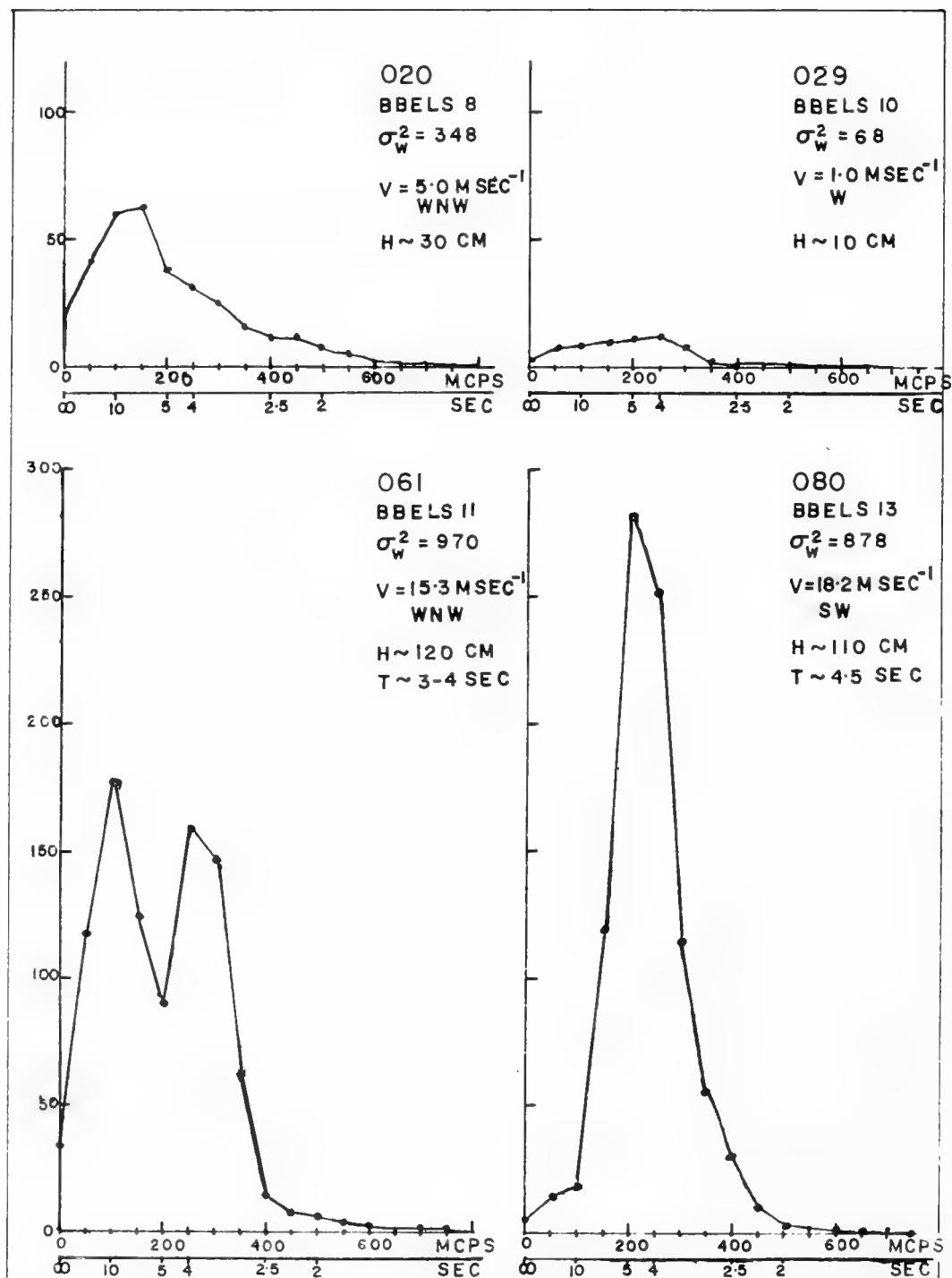
Auto-Spectra $\emptyset_w$ for Various Wind and Wave Conditions.

Figure V-15

unity to give credence to the spectrum plot. However, if DF becomes less than 10, the confidence limit bands broaden rapidly.

Before discussing some of the spectra of the individual series of observations, let us examine some typical auto-spectra associated with different wind-sea conditions. Figure V-15 shows four spectra of the vertical velocity w measured at one meter below the trough level of the waves.

A linear ordinate scale is used, in lieu of a log scale, to better show the gross variations of the energy distribution. The frequency scale was cut at 800 mcps, since beyond 600 mcps the energy is below an order of magnitude of the peak values. The variances (cm^2 sec^{-2}) and wind velocity (cm sec^{-1}) are listed on the graphs for comparison. Values of the estimated height H and a period T of the wind waves are also given. These last two quantities were estimated visually from the BBELS catwalk (some 17 m above the waves), using a "seaman's eye" and a stopwatch. The estimates must be considered extremely crude and only suggestive of the wave conditions present.

The spectra in figure V-15 reveal a strong correlation of the auto-spectra and their integrated areas (the variances) with the gross wind speeds and sea conditions. Peaks in the spectra generally occur at frequencies coinciding with those of the visually observed waves.

By far the most wave energy occurs below 400 mcps (above 2.5 sec period). This "cutoff" effect may be caused by the instrument; but, more probably, it is a real effect, since the response time of the impellers was shown (in chapter II) to be greater than 10^4 mcps, or less than 0.1 second period. The interpretation of the slope of $\Phi(f)$ with f near the cutoff range is discussed later in this chapter.

Another interesting effect is the occurrence of the double peaks in the 061 plot as compared to the single peak in 080, whereas the total energy is roughly equal. In 061 the winds from the WNW were fetch-limited (see figure IV-3) and steadily increasing in speed. Just prior to this WNW wind, a NE storm had passed, generating longer than usual waves from the open sea to the SW. On the other hand, when the 080 observations were made, the SW wind had been blowing many hours, and the seas tended to be fully developed. However, no swell was observed, and the 080 spectrum appears to portray fully developed but locally originated wind waves (sea).

The disproportion between the variances of the u and w velocity components in the waves (discussed in the previous section) shows up distinctly in the plots of the auto-spectra pairs (Φ_u and Φ_w). The curves in appendix B show strong variations in the values of Φ_u and Φ_w for BBELS-5 and 7 at all depths measured.

In BBELS-5 (serial 001, 002, 005, and 008) the u spectra contain double peaks located at about 250 mcps (4 sec) and 400 mcps (2.5 sec), whereas the w spectra have only a single peak at about 200 to 250 mcps. This same effect of a double peaking of Φ_u also occurs in most of the BBELS-7 plots.

The Φ_u spectra generally display more energy at frequencies above 1000 mcps (see 002 through 008). The spectra of Φ_u and Φ_w in serial 001 and 002 appear to demonstrate the selectivity of swell and sea. The energy of Φ_w is lumped in the range from 100 to 700 mcps, whereas the Φ_u energy is highly damped in this frequency range. This gap in the Φ_u energy could be caused partially by the swinging of the suspended meter in response to the dominant frequency of the waves. Such a resonant oscillation could highly damp the impeller response to the u velocity fluctuation by tending to follow (give with) the back and forth motions. However, it was suggested earlier in this chapter that the difference in the variances of the horizontal and vertical motion components could be caused by the directional characteristics of the OMDUM systems.

All spectra show strong attenuation of energy with depth, especially at frequencies above 600 - 700 mcps. This is discussed later in this chapter.

The auto-spectra of BBELS-8 and 9 (serial 020 through 025) were made using the OMDUM III system, which was kept more stable in the water by a more elaborate guy system (than in BBELS-5: see table V-1). These records show similarly shaped auto-spectra that are unlike the previous (001-019) records. Also, the variances are more nearly comparable in magnitude (see table V-1). The curves of Φ_u in BBELS 8 and 9 appear in profile very similar to Φ_w, except for a constant flat (frequency independent) filtering over the whole range. Note also that both Φ_u and Φ_w attenuate about the same with increasing frequency. It appears from BBELS-8 and 9 that the u and w meters were sensing and recording similar types of motions, although the energy per unit bandwidth was consistently higher for Φ_w than for Φ_u.

The BBELS-12 observations (7 April 1965) permit a comparison of the spectra associated with motions at the surface and near the bottom. Serial 071 and 072 were obtained with OMDUM III at 0.2 meter below the wave troughs. For 071 (1235-1238) the wind was from the east at 4.4 m sec^{-1}. For 072 (1243-1448) the wind was from the ESE at 5.4 m sec^{-1}. During this period the waves were small, with an estimated height of about 20 cm. The variances, corresponding to the low sea state, are also small (see table IV-3). The Φ_u, as usual, falls much below Φ_w. The low values of $\bar{w}$ (0.1 cm sec^{-1}) for both observations indicate good vertical positioning of the w meter.

In the afternoon, two deep measurements were made using OMDUM III at 1.0 and 5.0 meters above the bottom. The spectra of these deep measurements (P. 075 and 076 in appendix B) show no indication of the surface wave motions. No spectra of the w component is shown, since no vertical motion was detected at either level. This indicates that no motions attained the threshold velocity of OMDUM III - about 7-9 cm sec^{-1}.

The variance σ_u^2 was 3.13 cm^2 sec^{-2} at 5.0 meters off the bottom and 8.4 cm^2 sec^{-2} at 1.0 meter off the bottom, indicating a higher degree of turbulence near the bottom. The value of $\bar{u}$ at 5.0 meters was +17.5 cm sec^{-1}; $\bar{u}$ at 1.0 meter was +12.5 cm sec^{-1}. One would expect that if turbulence were being generated near the bottom, a mean vertical shear would exist in the horizontal flow. It

is thus tempting to speculate that these data show evidence of interaction between a tidal current and the sea bottom, producing both a mean shear $\partial \bar{u} / \partial z$ and a gradient of turbulent energy. However, the existence of such a gradient is not certain; since $\bar{u}$ was not measured simultaneously at the two depths, but over a 20-minute time lag. These measurements do demonstrate the use of the ducted meters to study the bottom turbulence.

The problem of assuming stationarity in the time series records was discussed in chapter III. Ideally, in a purely stationary process:

$$\frac{\partial}{\partial t} \Phi(f) = 0 \quad \text{AND} \quad \frac{\partial}{\partial t} \int_0^{f_N} \Phi(f) df \cong \frac{\partial \sigma^2}{\partial t} \cong 0 ; \qquad (V\text{-}9)$$

where the frequency range from 0 to f_N covers the region of interest. One way to estimate the degree of stationarity in a process is to make a relatively long record, divide it into smaller subdivisions, and examine their spectra. The degree of similarity of the auto-spectra and a comparison of the variances would be indicative of the stationarity of the whole record. During BBELS-11, a single record was made at 0.5 meter for 11 minutes (see table IV-3, 057A and 057B). From this record, which contained 3,300 data points at 0.2-second intervals, two sub-samples were abstracted: the first had 1001 points, and the second 1070 points. The auto-spectra Φ_w are shown in figure V-16. The degrees of freedom DF for both samples was about 42. Referring to figure III-3, the ratios of 80 percent confidence limits are above 0.74 and below 1.29 with respect to the average value. This amplitude is shown in figure V-16. Examination of spectra and visual observation of sea and wind conditions indicated that the 5-10 minute sampling period of wave motions should be relatively unaffected by gross time variations in the wave structure. Sudden wind shifts did occur, but these were unusual and were well-monitored as they happened.

Short period fluctuations in the horizontal current were also found to occur at BBELS (see chapter IV). This phenomenon, although not visibly affecting the wave structure, can affect the spectra; especially the u(t) spectrum. Because of this, it is reasonable to assume that in the OMDUM (u,w) record, w(t) has a higher degree of stationarity than u(t).

Auto-Spectra of Off-Angle Wave Measurements - Calibration of OMDUM III for off-angle response (see chapter II) was done with a simulated steady flow in the towing tank. This simulated motion was not very wave-like. Because of this, an attempt was made to roughly imitate the off-angle test in actual wave conditions at the BBELS.
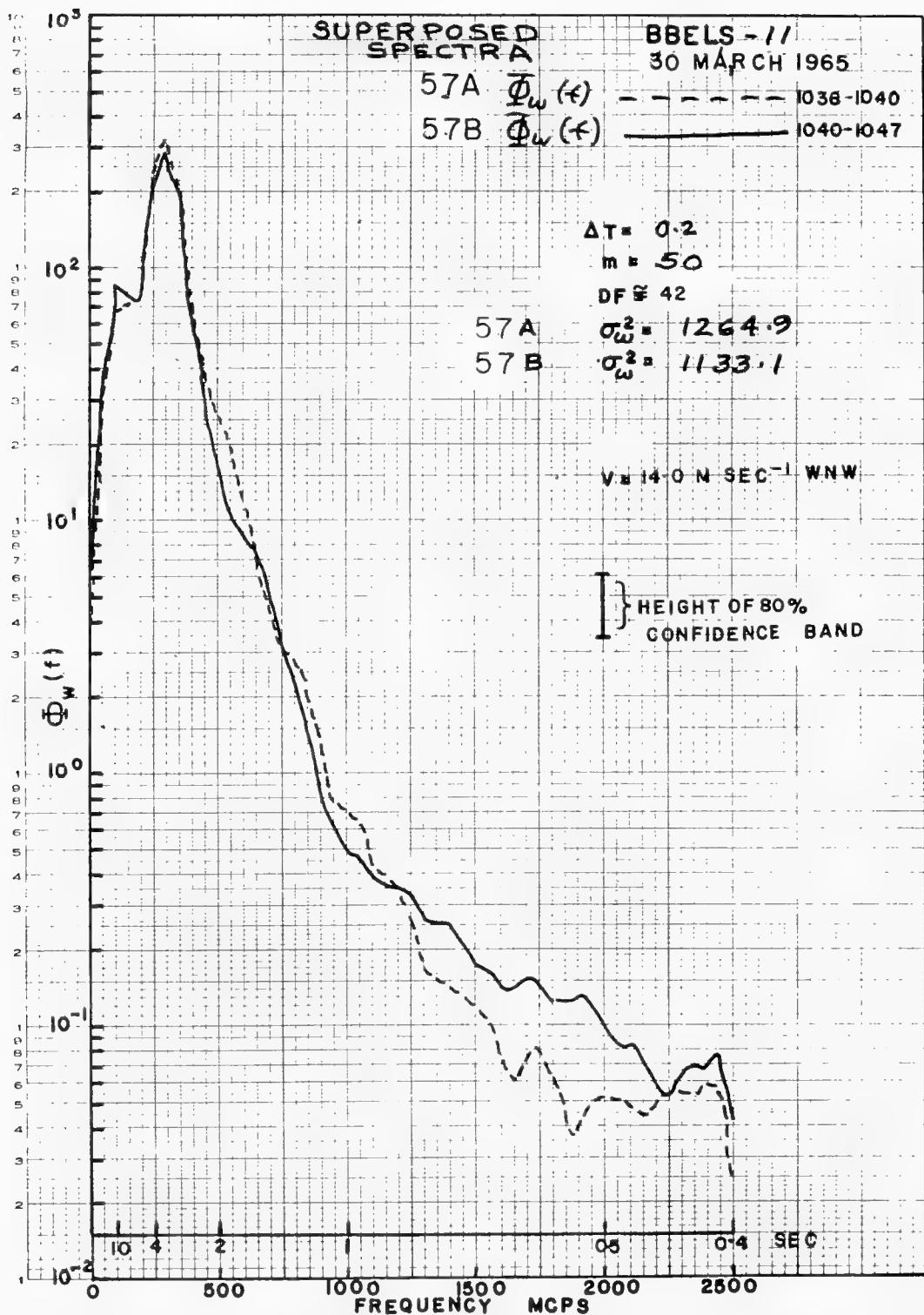
Auto-Spectra of Two Segments of a Single Wave Observation (BBELS-II, Serial 057-A and 057B).

Figure V-16

The experiment was made during BBELS-16 (7 September 1965). The u meter was aimed at different angles of attack (Θ) from the on-coming wind waves (see figure V-6A). With the meter placed at a depth of 0.5 meter, simultaneous records of u and w were made at about 0°, 20°, 50°, and 80° from the observed wind wave direction. The data (serial 120 - 123) are listed in appendix B.

During the period of measurements (1340 through 1436 hours), the winds were light, ranging from 3.5 m sec^{-1} to 4.6 m sec^{-1}, and varied in direction from W to WSW. Unfortunately, the low wind speed and the variability did not provide a very consistent (i.e., stationary) wind wave field. In general, over the 56-minute period of measurements, the wind waves were quite small and short-crested, having a maximum height of from 25 - 30 cm and a wave length of 3 - 5 meters.

Prior to the observations (at 1000 hours), a gentle swell was observed radiating from the SSE (155° T). At 1410 the presence of swell was indeterminate. After the period of observations (at 1900 hours), a slight swell was again observed from the south, having a height of about 20 cm and a wave length from 20 - 40 meters.

The auto-spectra for four of the records (serial 120 - 123) are shown in figure V-17. The Φ_u and Φ_w are depicted as broken and solid lines, respectively. The angle Θ, the time interval of measurement, the mean $\bar{u}$ component (cm sec^{-1}), wind speed V (m sec^{-1}), and the variances σ_u^2 and σ_w^2 are shown above the spectra curves.

The w spectra Φ_w exhibit a dominant low frequency peak (A) at about 100 mcps (6.6 sec), and a lesser peak at 400 mcps (2.5 sec). The heights of the two peaks (A and B) remain at about the same value throughout the series; except in serial 121, where a sharp rise is noted in peak B. (This is also reflected in the Φ_u spectrum.)

The u spectra Φ_u likewise display dominant peaks at 100 mcps (A') and 400 mcps (B'); however, the relative magnitudes of A' and B' are sharply contrasted with A and B. In serial 120 (with $\Theta \cong 0°$) A' is smaller in magnitude than B'. Serial 121 shows relative amplification of both B and B', probably caused by a local change in the wind wave conditions (i.e., a non-stationary effect). Serial 122 and 123, however, display a continuous decrease in B', whereas A' tends to increase. In serial 123 ($\Theta \cong 80°$) the Φ_u curve is a crude mirror image of the Φ_u curve in serial 120 ($\Theta \cong 0°$). The low frequency peaks A and A' are attributed chiefly to a gentle swell. Although not always visible (the visual observation at 1410 hours indicated no swell), this swell was apparently present during the entire sampling period. The B and B' peaks in the curves are probably associated with the observed small (and rather confused and non-stationary) wind waves. The spectral densities and variances σ_u^2 and σ_w^2 at the 0.5 meter depth are quite low, as would be expected with the low wind speeds (e.g., compare these curves with the 0.5 meter depth spectra of serial 023 U and 024 in appendix B).

Assume then the presence of a small swell running from about 175°T and of small wind waves normal to this direction (i.e., at about 250°T). With the u meter
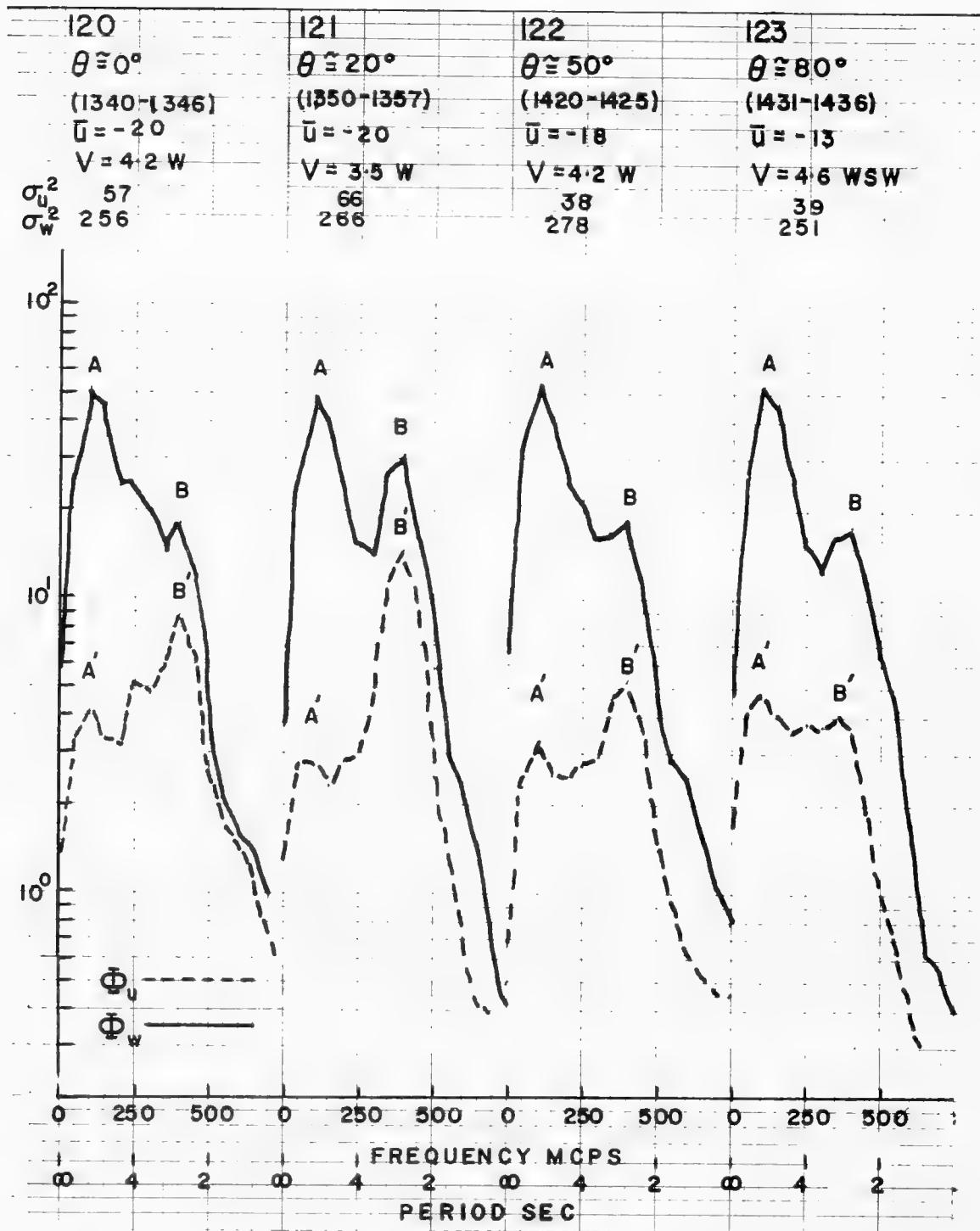
Auto-Spectra of Velocity Components for Various Values of Θ.

Figure V-17

aimed approximately at the wind waves (as in serial 120), one would expect little or no change in the total spectral curve of Φ_w as the meter is rotated. On the other hand, as Θ is varied from $0°$ to $90°$ (see figure V-6A), the swell peak of Φ_u (A') should increase and the wind wave peak (B') should decrease with respect to each other. This is shown, at least qualitatively, in the curves (figure V-17). Peak A remains about the same from 120 through 123, whereas A' starts off relatively small, drops off slightly, then increases from 121 through 123. Peak B, although fluctuating, remains roughly constant; whereas peak B' shows strong attenuation, especially from 121 to 123.

The variance σ_w^2 displays approximately constant values (within 6-8%) over the four measurements. On the other hand, the horizontal variance σ_u^2 displays a general decrease (associated with the decrease in the high frequency wind wave peak B'), which is further evidence of the damping out of the wind wave perturbations as the u meter axis rotates to larger values of Θ.

Quantitatively, little can be stated with regard to the directionality response of the u component meter. In general, it appears to behave as one would expect with respect to the cosine law approximation described in chapter II. Further tests should be made in more fully developed seas and under more steady wind conditions to better assess the directionality response of the OMDUM type wave meter.

Comparison of the Auto-Spectra of Wave Motions with Those of Free Surface Oscillations - The Coastal Engineering Research Center (CERC) wave staff system on the tower afforded an opportunity to compare some free surface wave records η (t) with the particle motion records produced by the wave meters. Comparison of the auto-spectra is not easy; since the CERC records are analyzed on an analog computer (discussed in chapter IV), which renders to the spectra certain biasing idiosyncrasies not found in the digital Tukey spectra.

The auto-spectra plots of the CERC free surface observations are given in appendix B. Two BBELS-13 wave observations (serial 077 and 080) at 1 meter depth were made almost simultaneously with CERC observations WS-4 and WS-5. Figure V-18 shows the auto-spectra Φ_u and Φ_w for both BBELS observations. Below the wave meter curves are superimposed traces of the two wave staff spectra (WS-4 and WS-5). The frequency scales (abscissas) are identical for both sets of curves. The ordinate on the left (cm^2 sec^{-1}) refers to the 077 and 080 curves; the ordinate on the right (cm^2 sec) refers to the Φ_η spectra. This is a difficult comparison to make, since the low frequency spectral resolution is obviously much higher for the free surface spectra than for the wave motion spectra. The peaks of the Φ_η spectra are much narrower and fall unquestionably at 200 mcps (5 sec). The Φ_w spectra reach a maximum between 200 mcps (5 sec) and 250 mcps (4 sec). The Φ_u spectra show peaks (at the higher frequency) at about 250 mcps.

Because of the incompatability of the CERC analog versus the Tukey digital spectrum analysis, a comparison of Φ_η with Φ_w was not very productive.
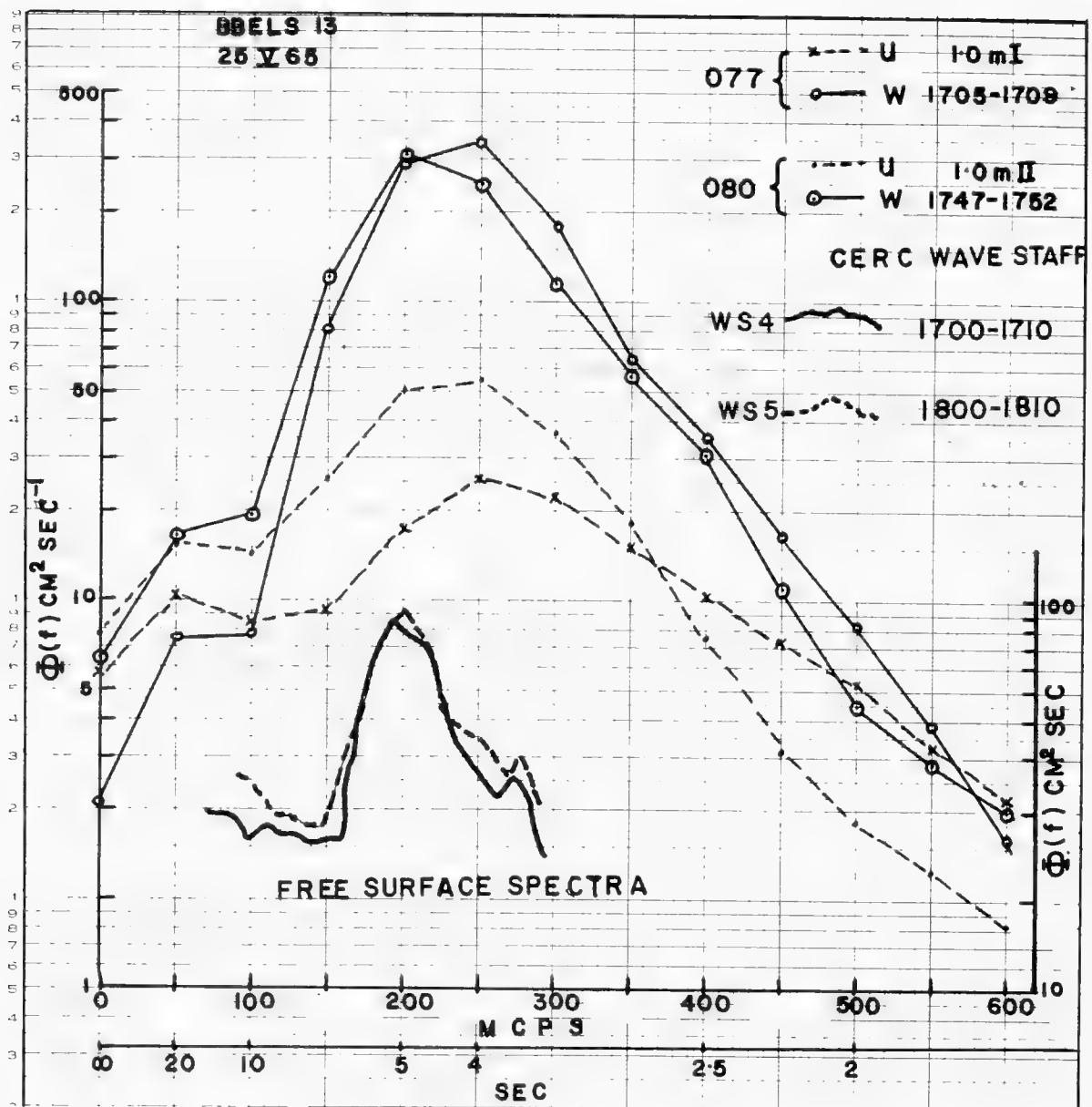
Auto-Spectra of Recorded Wave Motions $\emptyset_u$ and $\emptyset_w$ Compared with Free Surface Observations $\emptyset_n$ Obtained with an Analog Spectrum Analyzer.

Figure V-18

Most obvious is the fact that there is information in the spectrum range up to 1000 mcps (and possibly higher) which is apparently filtered in the CERC spectrum analysis procedure.

As noted in chapter IV, two CERC wave records were obtained and processed digitally, producing the spectra WS-15 and WS-16 in appendix B. These spectra appear quite similar to the wave motion spectra, mainly because of the increase in frequency range up to 2500 mcps.

An OMDUM III record (BBELS-14, serial 106, 3.0 m I) made on 8 June 1965 at 1457-1501 was compared to the wave staff record WS-15 made at 1600-1610. The auto-spectra are shown in figure V-19, where Φ_w (cm^2 sec^{-1}) and Φ_η (cm^2 sec) are plotted on the same ordinate scale. The spectra up to 500 mcps (2-second period) are very similar. The Φ_w appears to decrease much faster than the Φ_η function from 500 to 1200 mcps. Since the OMDUM III w(t) record was made at a depth of 3.0 meters, the accompanying attenuation of high frequencies with depth is undoubtedly reflected in the spectrum. Beyond this, Φ_η seems to whiten and remain constant. The peaks at 250 mcps (4 sec) stand out, and even the small peak at 50 mcps is comparable in the two spectra. Since two different quantities are being compared, not much can be concluded regarding the relative slopes of the two spectral densities.

True similarities between the auto-spectra of free surface wave records and wave particle motion records could best be identified if a record of w(t) made very near the surface were available for comparison. This is because of the strong damping of the high frequency surface motions with depth. The wave staff can detect high frequency motions (the limiting frequency being the natural response of the wave staff detector and recorder) which are completely "raw" and unfiltered; whereas the wave meter lying beneath the free surface detects motions which are subjected to a "low pass" filter that increases exponentially with depth. Unfortunately, no near-surface w(t) records were made near the time of the WS-15 and WS-16 records. However, the long period, low frequency motions do appear similarly represented by each spectrum in figure V-19, which indicates a certain similarity between wave particle motions and free surface motions.

Vertical Distribution of Wave Energy

The classical theory of surface wave motion predicts that the amplitude, velocity, and acceleration of particles in surface waves all decrease rapidly with depth. The decrease of motion is exponential in nature. This is demonstrated by equations (II-4) through (II-12), which apply for the cases of short and intermediate waves.

The experiences of divers and submariners attests to this attenuation of surface wave motion with depth. There is, however, little quantitative evidence. An excellent discussion of this matter is presented by Wiegal (1964). In considering the engineering aspects of wave forces on submerged objects, Wiegal presents studies and data regarding the attenuation of wave pressure forces determined both in the laboratory and in situ.
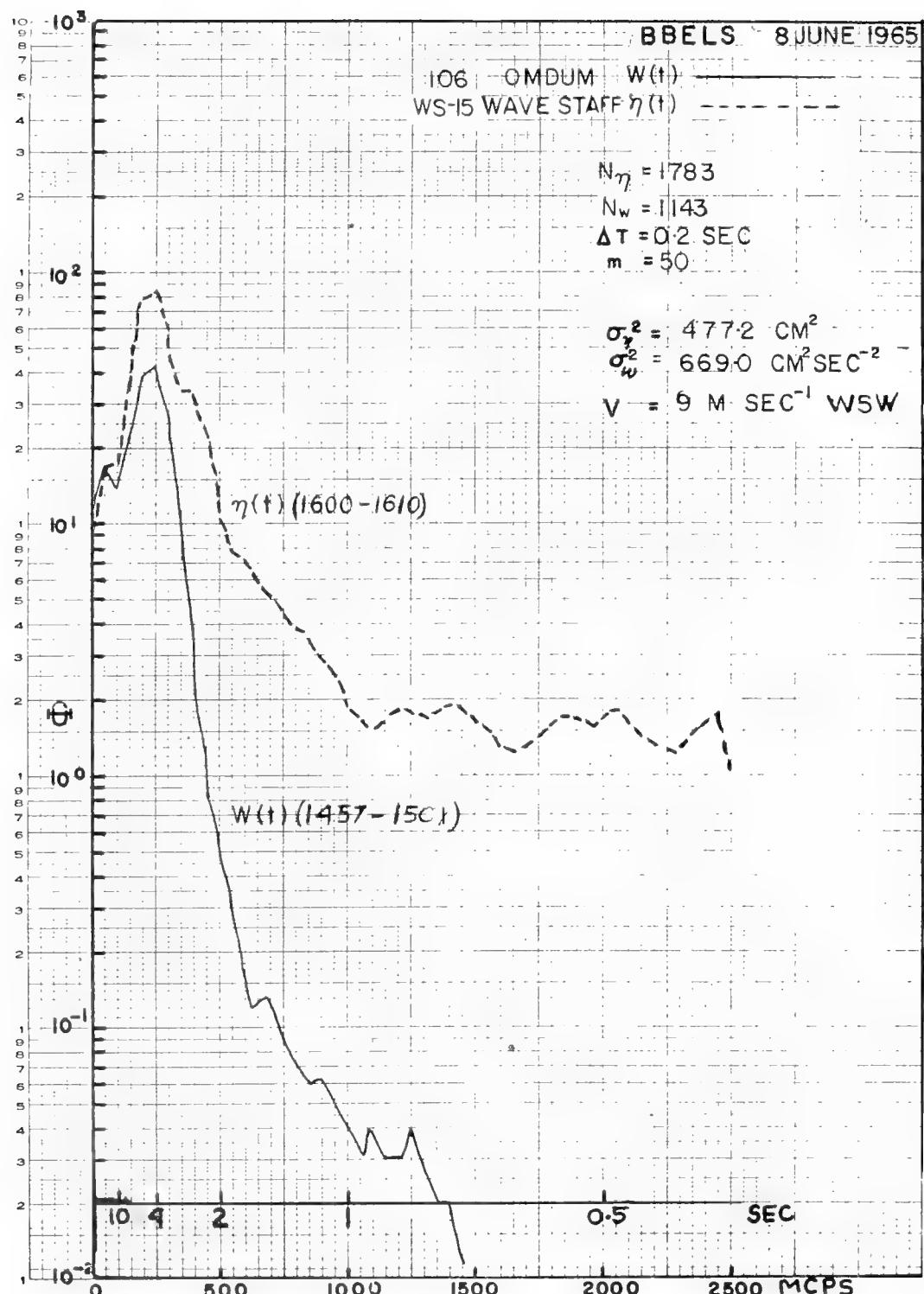
Auto-Spectra of Free Surface Elevation η and Vertical Motion w.

Figure V-19

The wave meter systems (OMDUM and LIMDUM), when suspended from the BBELS platform at various depths beneath the free surface, permitted some interesting observations of the vertical gradient of wave motion. Four sets of observations from BBELS are particularly valuable for an examination of this phenomenon.

BBELS-5 Observations - The first series of wave measurements reported herein (BBELS-5) produced relatively crude results. The suspension system was untried, and less attention was paid to precise positioning of the wave meter system than in later experiments. However, in some respects the results of BBELS-5 were quite meaningful. Two factors contributed favorably to this series of measurements: (1) wind and sea conditions were relatively constant during the sampling period; and (2) the sequence of observations was made over a short time interval (less than two hours). Both factors should lend credence to the desired assumption of stationarity, thus permitting a better comparison of individual observations. The results provided a vivid picture of wave motion attenuation with depth. Before considering this aspect, a brief review of the general experiment may be helpful.

The OMDUM II system was suspended without the benefit of a back guy (discussion of suspension systems is given in chapter IV). As usual, the u meter was aimed in the upwind (up-wave) direction. For convenience, the observations of BBELS-5 are divided into two series, A and B (see appendix B). The former were taken between 1135 and 1257 hours, and the latter between 1305 and 1333 hours. (Results of the measurements are given in table IV-3).

Referring to the table IV-3, the mean values of the horizontal component $\bar{u}$ indicate a fairly steady flow moving in an up-wind direction at about 30-40 cm sec^{-1}. The mean vertical velocity component $\bar{w}$ ranges from -3.9 to +1.2 cm sec^{-1}. In general, there is a non-zero value obtained for the mean vertical velocities. This effect cannot be attributed to the vertical tidal velocity since, for the 100 cm tide range at BBELS, the maximum vertical velocity component would be less than 0.1 mm sec^{-1}. The chief cause is probably that the vertical w meter was tilted slightly off-vertical during the measurements. When the $\bar{w}$ values are large, there is reason to doubt the records. The majority of the $\bar{w}$ values obtained were of the order of $\pm$ 1.5 cm sec^{-1}, which is not considered excessive.

The variance of the u values is roughly one-tenth that of the w values. From this discrepancy in the variances and, as will be seen, from the auto-spectra curves of the u and w components, there is reason to doubt the horizontal stability of the suspension system used in BBELS-5 and 7 observations. Since the u component shows such strong damping, the discussion based on these data is concentrated on the statistical properties of w.

Figure V-20 shows the plot of the variance σ_w^2 as a function of depth for both A and B series of BBELS-5 (triangles). The attenuation is clearly of an exponential nature, with the variance σ_w^2 decreasing by about one-half every 2 meters. This exponential decrease is illustrated by the solid and broken lines drawn through the triangles. The linear relation of the semi-logarithmic plot is indicative of a genuine exponential relationship.
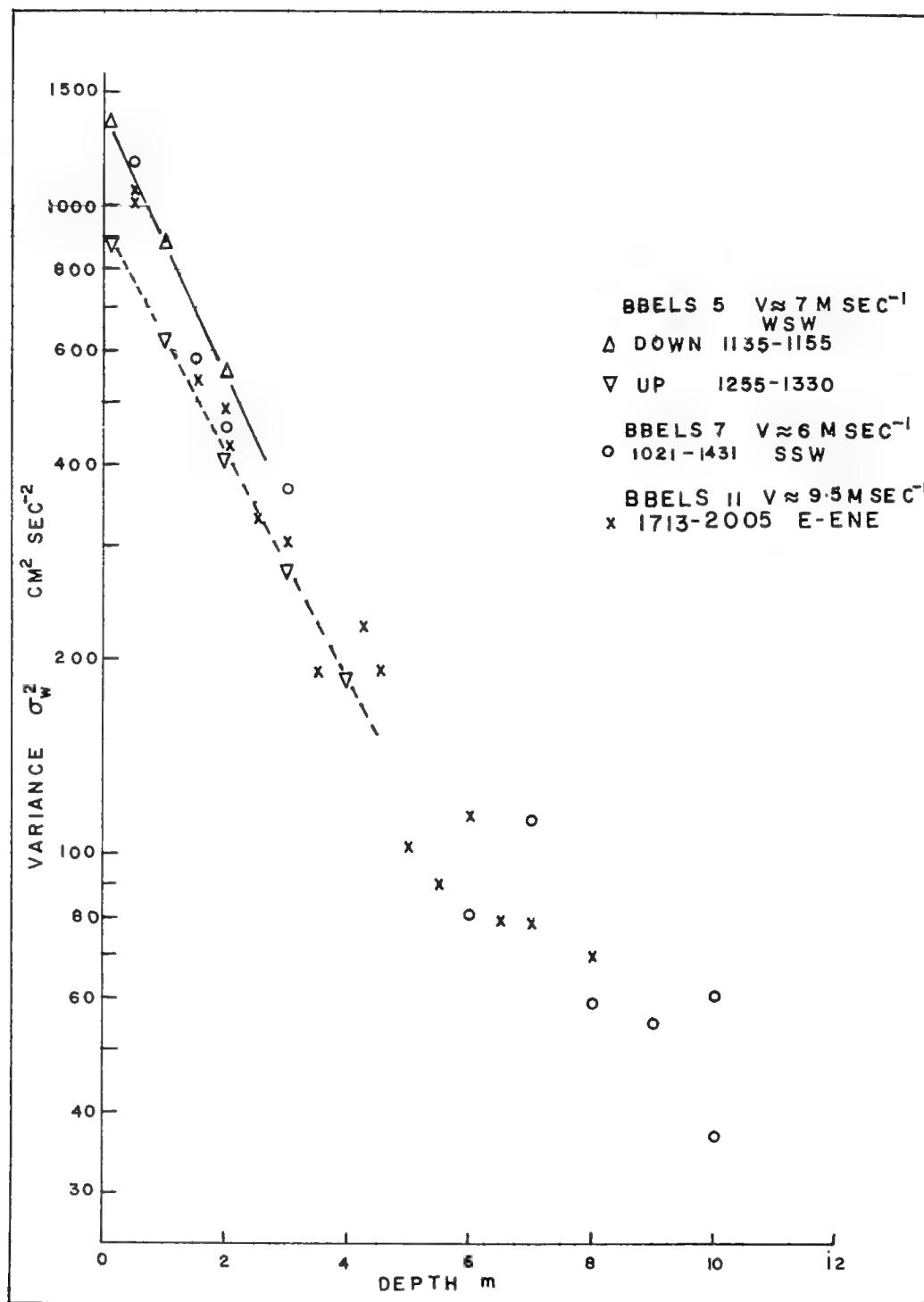
Distribution of Variance σ_w^2 as a Function of Depth from BBELS-5,7, and 11 Observations.

Figure V-20

The auto-spectra provide the best illustration of the depth attenuation of wave motions. Figure V-21A shows the composite auto-spectra Φ_w for four depths (series A) as a function of frequency (mcps). The time of the start of each observation is given next to the depth value. This family of four curves clearly demonstrates the attenuation of the wave motion with depth. The curve for zero meters (wave trough level) shows a strong peak at about 250 mcps (4 sec), which is undoubtedly associated with the wind waves. This is followed by a sharp attenuation to about 1000 mcps (1 sec). Beyond this point the energy tends to flatten out and fluctuate up to the Nyquist frequency (2500 mcps).

The characteristic curves form a family showing strong but unequal attenuation at all frequencies. There is a distinct "reddening" with depth of the dominant peak of each curve; e.g., the peak shifts from 250 mcps (4 sec) at the surface to about 150 mcps (6.6 sec) at a depth of 4 meters. This illustrates the "low pass filter" effect mentioned earlier in this chapter.

Irregularities in the spectral curve occur in the higher frequency range (beyond 750 mcps), particularly at the 4-meter depth. These fluctuations of the spectral density at high frequencies are less meaningful than at lower frequencies, and could be caused by "noise" inherent in the spectrum computations and highly magnified in the logarithmic presentation.

Figure V-21B shows the spectra of the horizontal component u for series A of BBELS-5. There is a striking difference between the two functions Φ_u and Φ_w. The Φ_u function indicates a marked decrease of energy below 1000 mcps (compared to Φ_w). Again, however, there is strong attenuation at all frequencies, except below 200 mcps at depths of 2.0, 1.0, and 0.0 meters. The strongest decrease in spectral density occurs between 0.0 and 1.0 meter, and between 2.0 and 4.0 meters. The 0.0 meter curve clearly displays two peaks - at 100 mcps (10 sec), and at about 400 mcps (2.5 sec). The other three curves indicate the same low frequency peak at 100 mcps, but the secondary peak (strongly attenuated) is evident only at 1.0 meter depth.

Figure V-22A shows the vertical velocity spectra for series B taken between 1305 and 1333. The 4.0 meter curve from series A is repeated, since (for convenience) it is considered timewise to be the end of series A and the beginning of series B. Here again is a clear indication that the spectral energy at all frequencies shows a strong attenuation with depth.

Comparison of figure V-21A with V-22A indicates strong similarities between the spectral functions at any given depth. Specifically, the curves for 0.0 m I and 0.0 m II show remarkable similarity, with the major peak at 250 mcps (4 sec) and similarly located minor peaks at 1100 mcps and 2000 mcps.

The curves for the function Φ_u of series B (figure V-22B) again show peak values that are much smaller than those for the corresponding vertical velocity spectra Φ_w. The 0.0 m II curve displays a double peak (similar to that of the 0.0 m I curve in series A), one peak occurring at 200 mcps and one at 350 mcps. Also, there is a similar sharp decrease in energy, at the higher frequencies,
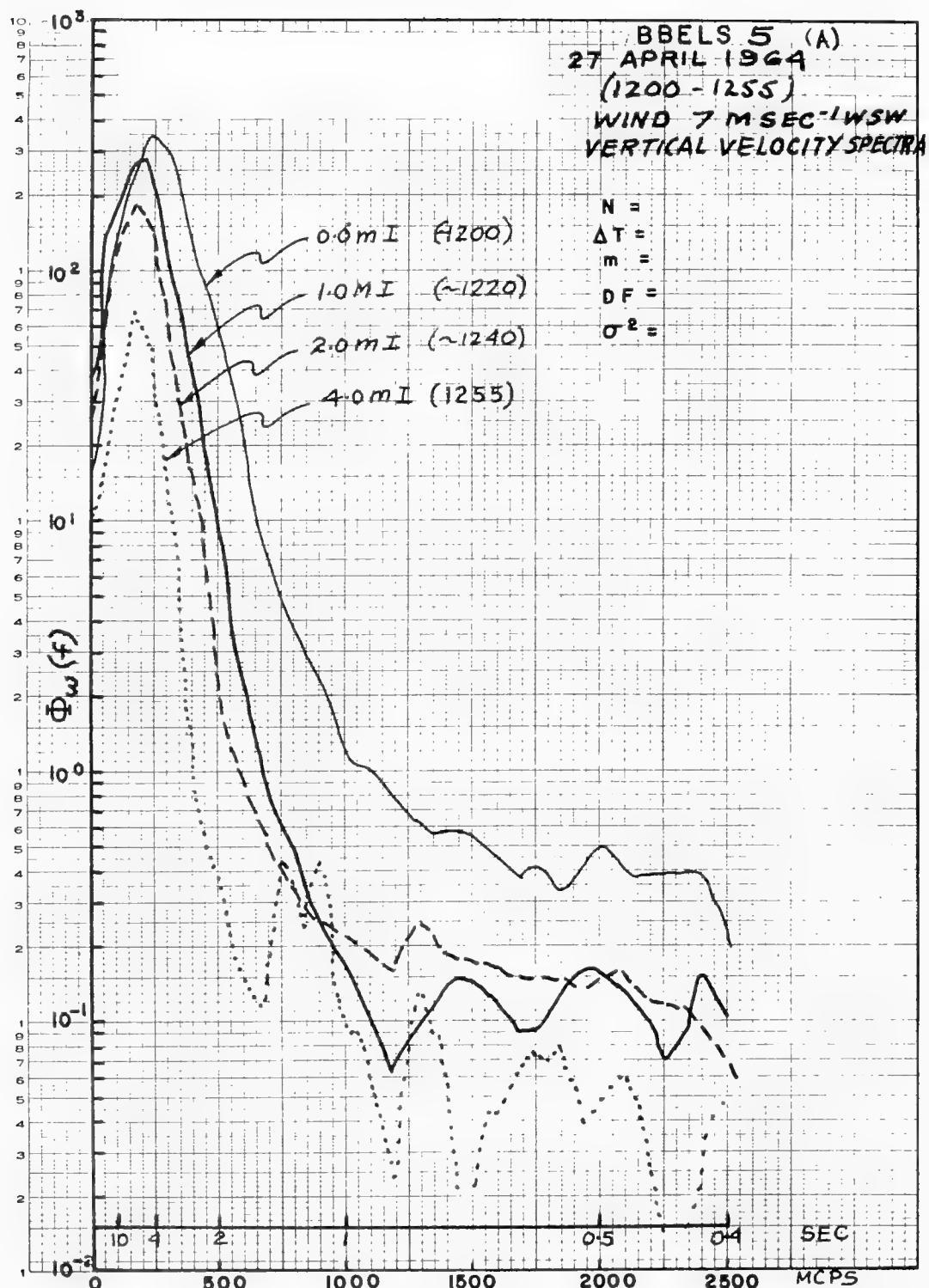
Auto-Spectra $\emptyset_w$ as a Function of Depth for BBELS-5 (1200-1255).

Figure V-21A

Auto-Spectra $\emptyset_u$ as a Function of Depth for BBELS-5 (1200-1255).

Figure V-21B

Auto-Spectra ϕ_w as a Function of Depth for BBELS-5 (1305-1330).

Figure V-22A

Auto-Spectra ϕ_u as a Function of Depth for BBELS-5 (1305-1330).

Figure V-22B
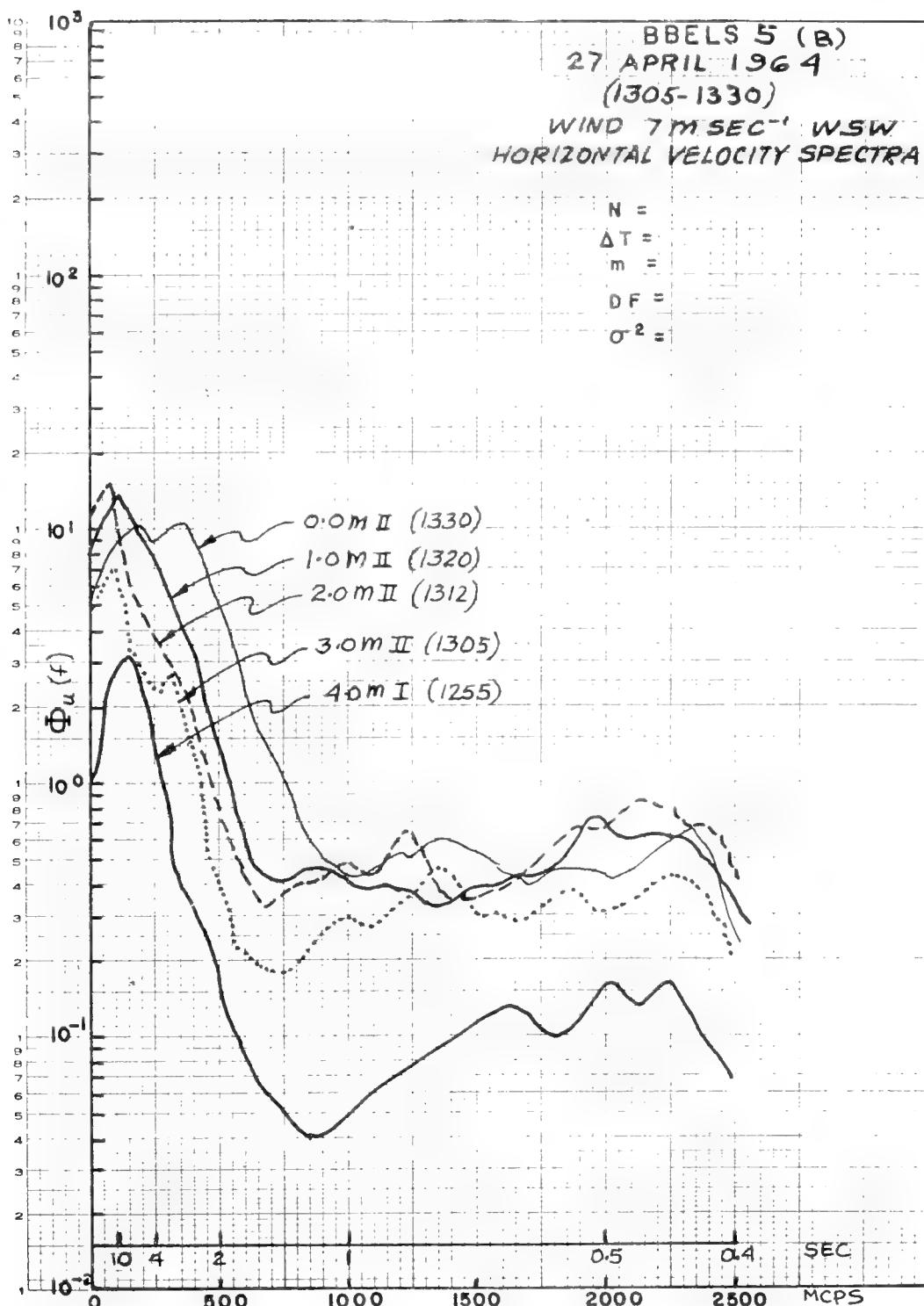
from 3 to 4 meter depths. Above 1000 mcps, the curves (except for 4.0 m I) remain between 0.2 to 0.8 cm^2 sec^{-1}. The w spectra curves, however, continue to decrease beyond 1000 mcps.

The corresponding spectral curves for both sets of observations (A and B) show strong similarities. The gross differences between the curves of Φ_u and Φ_w are also similar in each case. The similarities in the spectra indicate the degree of stationarity of the statistics of the observed motions during the sampling period, whereas the consistent reproduction of the dissimilarities between the w and u spectra indicates the inherent precision (or repeatability) of the wave meters - even though these dissimilarities may be partly caused by the wave meters themselves.

BBELS-7 Observations - The set of observations designated as BBELS-7 was made using the OMDUM II wave meter. An additional guy leading from the meter support rod back to a point in the center of the tower was utilized in an attempt to gain horizontal stability. This new pyramidal configuration (see figure IV-17) was used in conjunction with a heavier (25 kgm) counterweight, giving this system more horizontal and vertical stability than that for BBELS-5 measurements.

Unfortunately, this series of observations (of u and w at various depths) was made over a 6-hour period. Thus, even though wind conditions remained fairly constant at 6-8 m sec^{-1} from the SSW, it is difficult to assess the degree of stationarity over so long a period.

The results of the statistical analysis of the data are summarized in the table IV-3. The distribution of the variances of the vertical velocity component with depth is shown as circles in figure V-20. They were placed along with the data from BBELS-5 because the wind and sea state values were roughly equivalent. Indeed, both sets of data form a relatively narrow envelope.

The values of σ_w^2 are generally 2 to 5 times larger than σ_u^2; however, the difference in these values is not so great as with BBELS-5. The values of $\bar{u}$ range from -25.7 cm sec^{-1} at about 1024 hours to 0.3 cm sec^{-1} around 1420 hours. There are also a few disturbingly large values for $\bar{w}$; namely, at 0.5 m I, 10.0 m III, 8.0 m I and at 4.0 m I. At this last level, $\bar{w}$ = -15.3; hence the spectrum, which also looked doubtful, was discarded.

Five of the auto-spectra of the vertical velocities are shown in figure V-23A. These spectra cover a wide range of depths, from 0.5 meter down to 10.0 meters. Clearly, most of the high frequency wind wave energy (above 500-600 mcps) has been filtered at depths of 7 meters and beyond. The spectral peaks, as with the BBELS-5 curves, show a definite "reddening" with depth - from 300 mcps (3.3 sec) at 0.5 meter down to 50 mcps (20 sec) at a depth of 10 meters.

Figure V-23B shows a family of horizontal velocity spectra at depths ranging from 2.0 to 10.0 meters. Here again there is evidence of attenuation of spectral energy with depth. The 2.0 m I curve displays a strong wind wave peak at 250 mcps (4 sec), with a secondary peak at about 50 mcps. The other curves (6.0 m I,
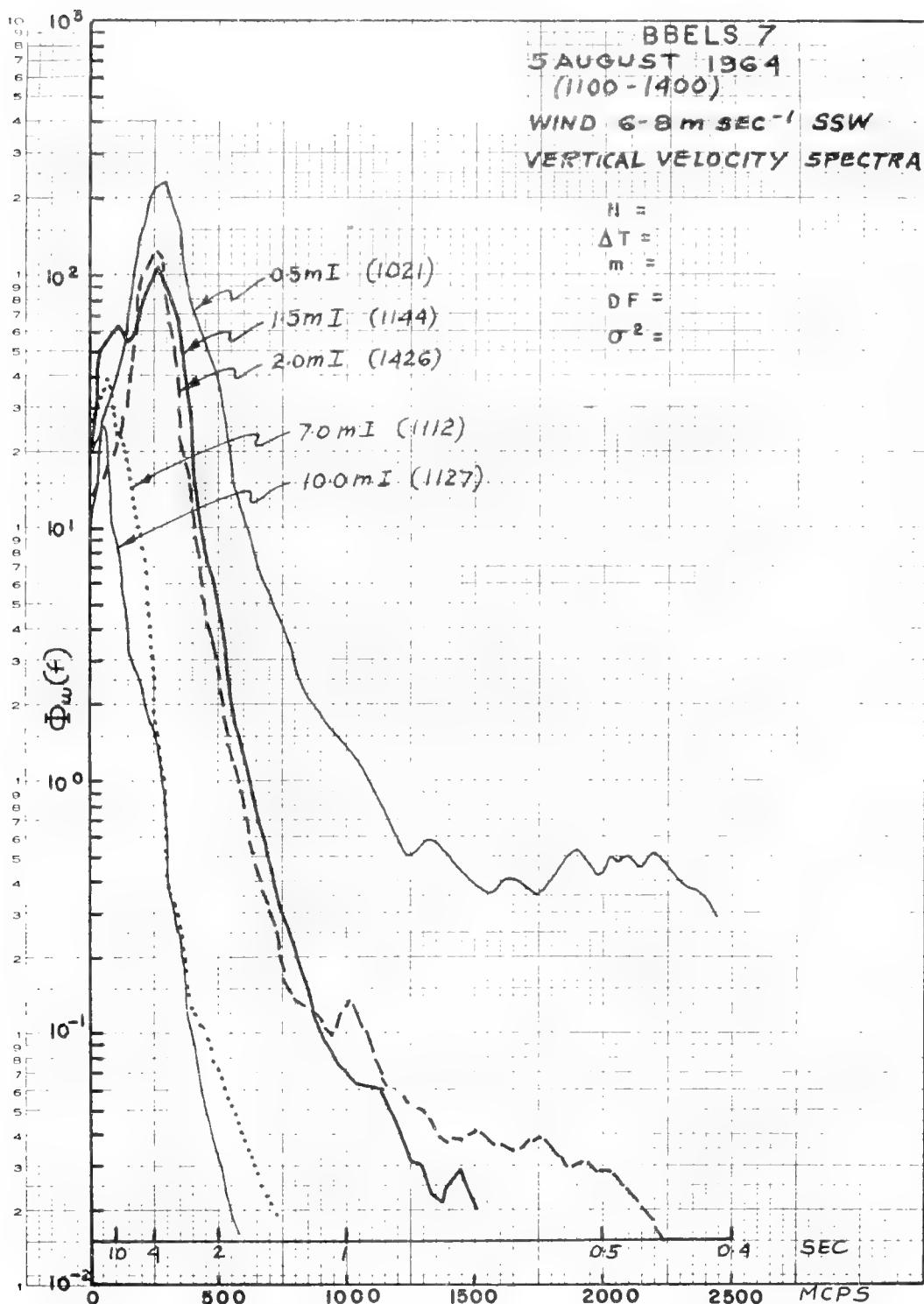
Auto-Spectra ϕ_w as a Function of Depth for BBELS-7.

Figure V-23A

Auto-Spectra ϕ_u as a Function of Depth for BBELS-7.

Figure V-23B
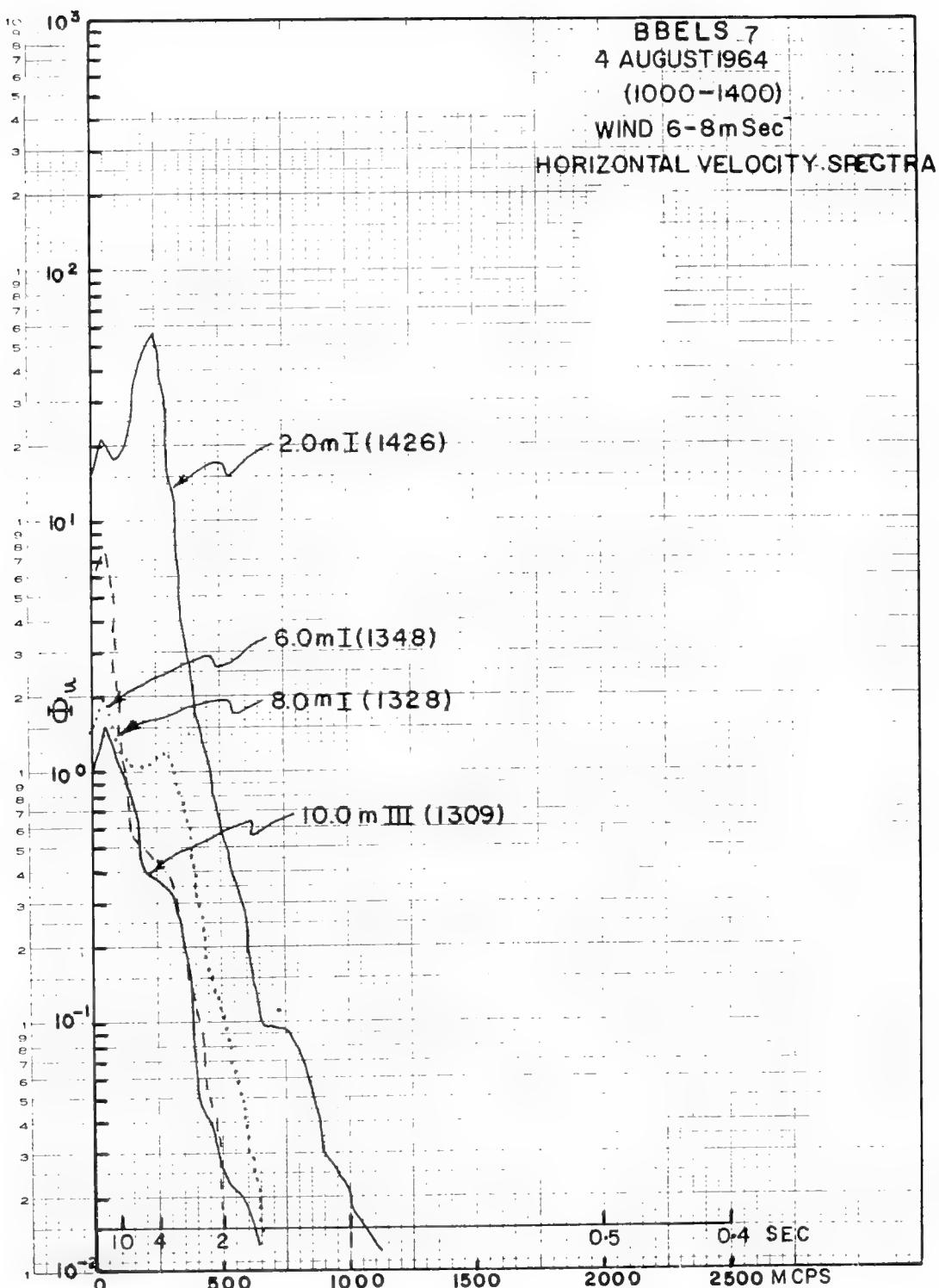
8.0 m I, and 10.0 m III) display clear double peaks, which are obviously attenuated with depth.

The 8.0 m I peak at 50 mcps exceeds the 6.0 m I peak; but in the range of the wind wave frequencies (above 150 mcps) the 6.0 m I curve lies consistently above the 8.0 m I curve, as would be expected.

BBELS-11 Observations - The BBELS-11 observations of 29 and 30 March 1965 were made to study the 24-hour variation in wave energy at various depths. This aspect of the observations is discussed later in this chapter.

During the period between 1713 and 2005 on 29 March, sixteen observations were made of the vertical velocity w (using the LIMDUM I system) over a depth range from 0.5 meter to 8.0 meters below the mean wave trough level. The vertical separation of the two cylinders was 1.5 meters.

Because of recorder pen failure, only one channel could be used; hence, w was not measured at the two depths simultaneously. Instead, the leads of the upper and lower w meters were alternately connected to the usable recorder channel.

The results of this sequence of observations (serial 032-047) are listed in table IV-3. The winds varied from E to ENE and averaged about 9.5 m sec^{-1}. The variances are plotted (crosses) in figure V-20. The distribution of σ_w^2 is very similar to that for BBELS-5 and 7. The surface intercept (at 0.0 m) appears to be at about 1400-1500 cm^2 sec^{-2}. As with BBELS-5 and 7, the exponential attenuation of σ_w^2 with depth is indicated by the linearity of the log plot.

The thin envelope of points in figure V-20 indicates that the two different wave meters produce similar wave data under similar wind and wave conditions. Hence, the fundamental designs of the OMDUM II and LIMDUM I systems (even though each has different calibration curves, probably different drag coefficients with respect to wave motions, and different geometries) would seem to be capable of detecting faithfully the gross oscillatory motions in waves.

BBELS-14 Observations - The BBELS-14 observations were made on 7 June 1965, using the LIMDUM I system (configured as shown in figure II-17). The purpose of these observations was to measure the vertical velocity component w simultaneously at two vertically separated points in the manner shown by figure III-4. For this purpose, the LIMDUM I system did not need to be fastened to the horizontal rod with its north, south, and back guys, as was necessary with the OMDUM systems. The LIMDUM I system was simply suspended by the main support guy and counter-weighted with a bottom pennant attached to six sash weights having a combined weight of about 18 kg. The ducted meters were spaced 2.0 meters apart, and observations were made at various depths. The simultaneous measurements at two different depths supplied particularly good data on how the variance of the wave motion varied with depth. The statistical results of these observations are given in table IV-3.
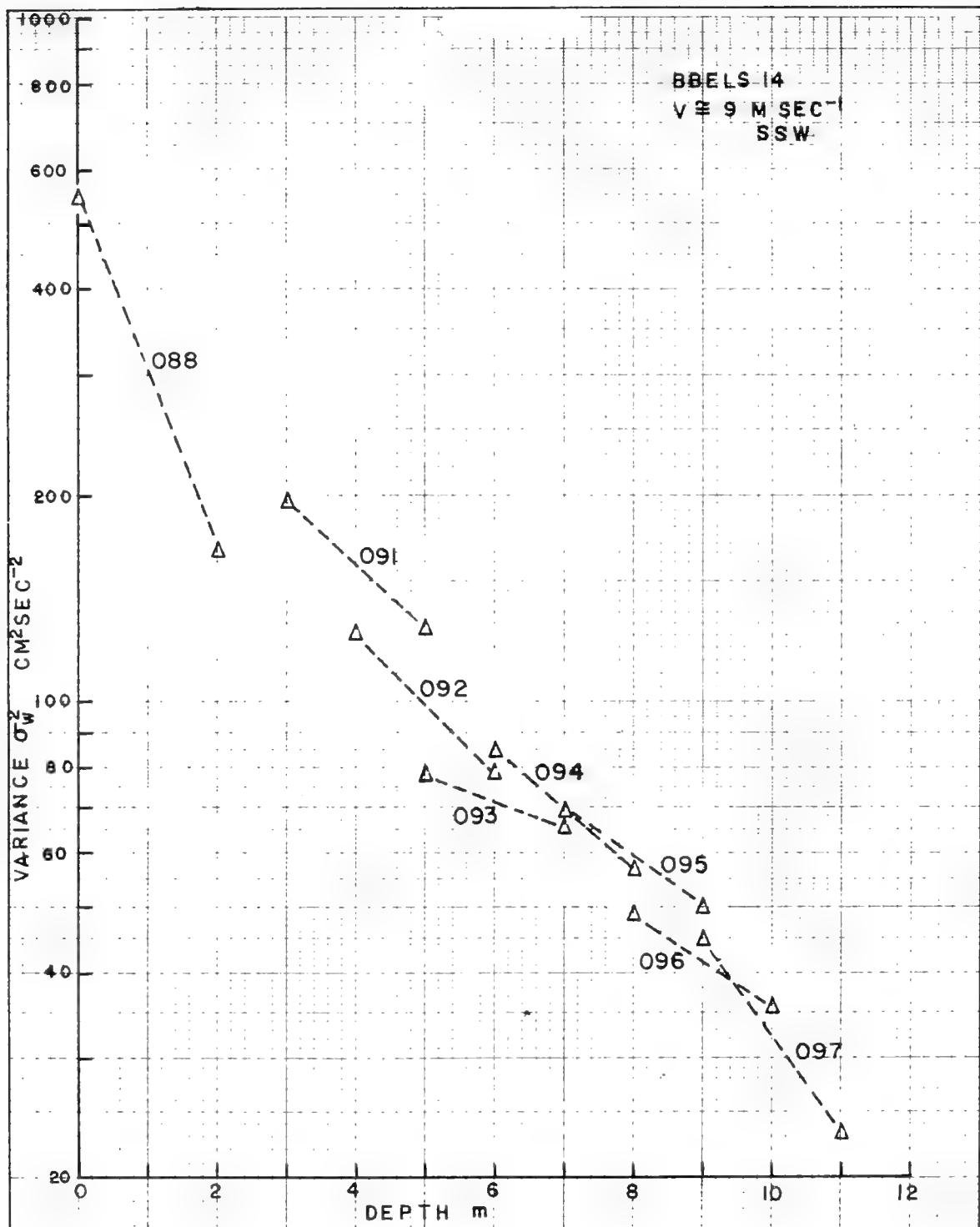
Observed Variances σ_w^2 as a Function of Depth (LIMDUM I-BBELS-14).

Figure V-24

Figure V-24 is a plot of the variances $\sigma_w{}^2$ (obtained for eight pairs of measurements) as a function of depth. The broken lines connect the variances of the simultaneously measured pairs. The wind speed was about 9-10 m sec^{-1} from the SSW during this sampling period (from 1412 to 1618).

These values show a similarity to the plots from BBELS-5 and 7 in figure V-20, which is indicative again of an exponential decrease in the variance of wave motion components with depth.

Figure V-25 depicts the superposition of some of the various auto-spectra from BBELS-14. The uppermost curve (0.0 m) shows two peaks: a major one at about 250 mcps (4 sec), and a lesser one at 50 mcps (20 sec). The curves for the deeper observations show a strong decrease in energy. Note the "reddening" of the 250 mcps peak at the surface to 150 mcps (6.6 sec) at a depth of 9 meters. Above 100 mcps each curve, in the order of ascending depths, consistently falls to the right of the preceding one, and thus shows a progressively larger energy content proportional to the area under the respective curves.

Note in table IV-3 the linear correlation coefficient r between the two w values. This number is, in a sense, a spatial correlation coefficient for w_1 and w_2 at a fixed vertical distance apart, and is defined for this case in chapter III. If one considers the fluctuations at two points z_1 and z_2 in the field of wave motion, the correlation between w_1 and w_2 will, in general, vary with the magnitude of the distance $z_2 - z_1 = h$. One would expect the correlation to diminish as h increases. This suggests a method of defining a length that may be associated with an eddy size. If r (h) is the correlation coefficient between the fluctuations at points separated by a distance h, a length L can be defined by the relation

$$L = \int_0^\infty r(h)\,dh \qquad ; \qquad (V\text{-}10)$$

provided, of course, the integral converges. For a real turbulent regime this will be the case for h greater than some finite length; i.e., beyond some length the spatial correlation r, for all practical purposes, vanishes. The length L, called the "scale of turbulence" (see Sutton, 1953, or Hinze, 1959), represents the average size of eddies or the length scale of the fluctuation, but without any strict definition of the model of an eddy.

For the experiments made with the LIMDUM I system, the separation is fixed; and the correlation coefficient is measured as a function of the depth. From equation (V-10), it follows that:

$$\frac{\partial L}{\partial z} = \int_0^\infty \frac{\partial}{\partial z} r(h)\,dh . \qquad (V\text{-}11)$$
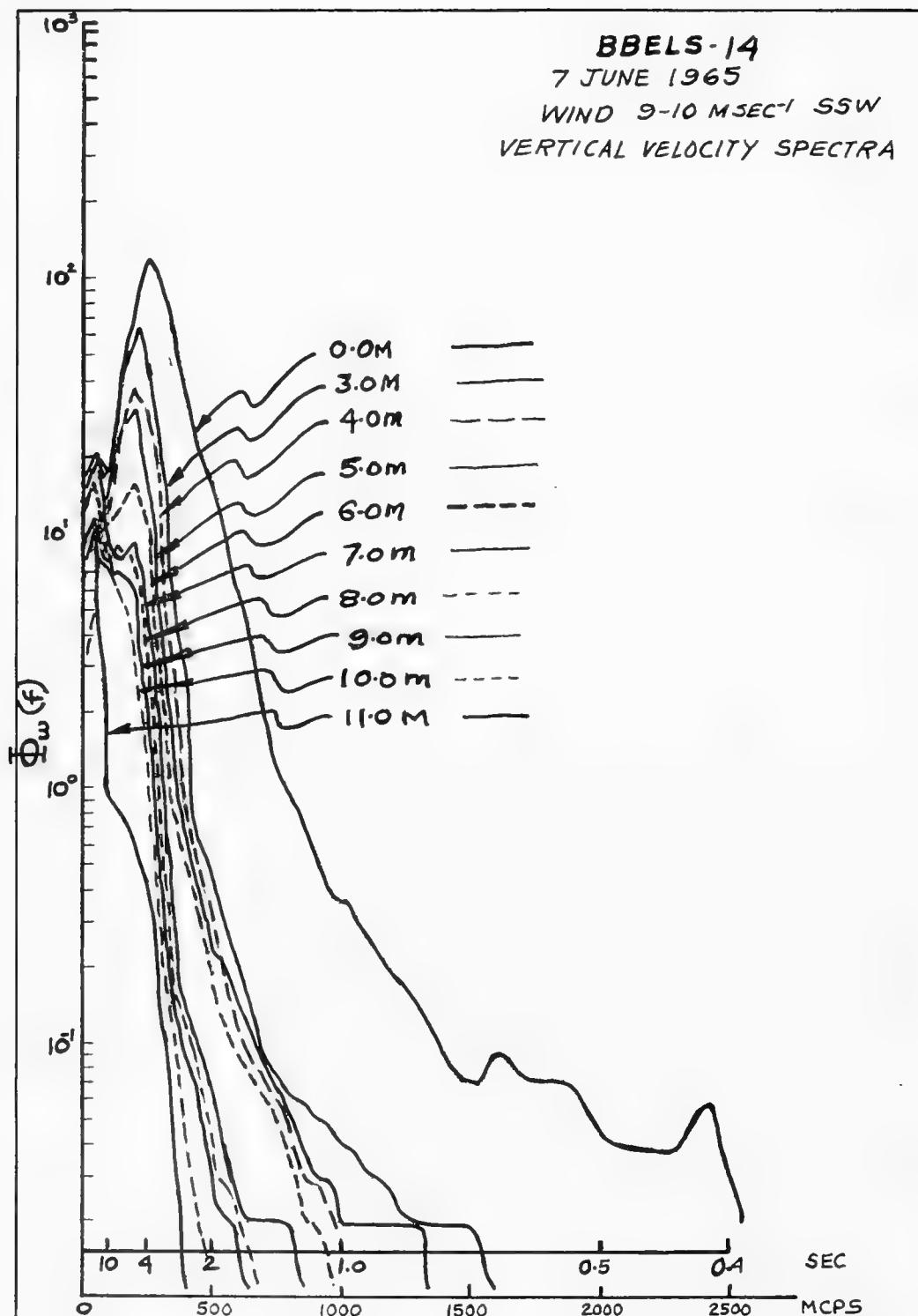
Variation of the Auto-Spectra $\emptyset_w$ with Depth (BBELS-14).

Figure V-25

Thus, the vertical gradient in the correlation coefficient is proportional to the vertical gradient of the eddy scale with depth. Figure V-26 shows the correlation coefficients plotted as a function of depth. The arrows indicate the depth of the upper and lower velocity sensor and the distance of separation (h = 2 m). For the particular wave conditions existing at the time, the correlation between 0 and 5 meters is quite constant at about 0.7. At depths below 5 meters, the coefficient drops off rapidly (and apparently quite linearly) to a value of 0.16 at a depth of 10 meters. The spatial correlation for a 2-meter separation indicates that eddy motions associated with the waves vanish at about 12 meters.

Comparison of Kinetic and Potential Wave Energy - Specific examples have been given of the decrease of the variance of wave motion with depth. The generality of the results from BBELS-5, 7 and 14 are indicated in figures V-27 and V-28, in which the variances of the horizontal and vertical velocity components taken from each BBELS observation (i.e., BBELS 5 and 7-16; all listed in table IV-3) are plotted as a function of depth. The numbers represent the numerical values of the wind speed (in m sec^{-1}) observed at the time of each measurement. The wind speed values were used in an attempt to relate the variance distribution to wind intensity. Further discussion of this aspect is given later.

Referring to the horizontal variance σ_u^2 in figure V-27, the general tendency is for the variance to decrease with depth; but there is much scatter and even a few spurious values. The primed sevens (7') represent the data from BBELS-7. As was indicated previously, the BBELS-7 data were obtained without the back guy; hence, it was felt that this particular set of measurements would be potentially biased (by waves tending to move the meter and bias the horizontal response). And indeed, this group of observations does tend toward lower values than are indicated by the majority of the remaining points.

A more well-defined relationship is shown in figure V-28, where the vertical variances are plotted against depth. The circled values are from BBELS-11; where, within one hour, a sudden wind speed increase and direction shift occurred. These values should therefore not be judged on the same basis as the other points. This is because the new waves generated by a sudden shift of wind are not produced instantaneously but require time to build up. Thus, at a given instant, the wave structure is not necessarily commensurate with the intensity of the wind field (see Pierson, Neumann and James, 1955). The other values, in general, were obtained in fully developed seas under fairly constant wind conditions.

The numerical values of wind speed were used on the plot to see if the higher wind speeds produced higher variances for a given depth. This is not too well shown in the σ_u^2 plot (figure V-27), probably because not enough (reliable) data points were available. The vertical variances (figure V-28) better exhibit this relationship, particularly at depths between 0 and 2.5 meters. Thus, for a given depth, the wind speeds tend to increase as one moves up the ordinate (i.e., with increasing variance magnitude). At depths beyond 5 meters, however, the relationship becomes uncertain.
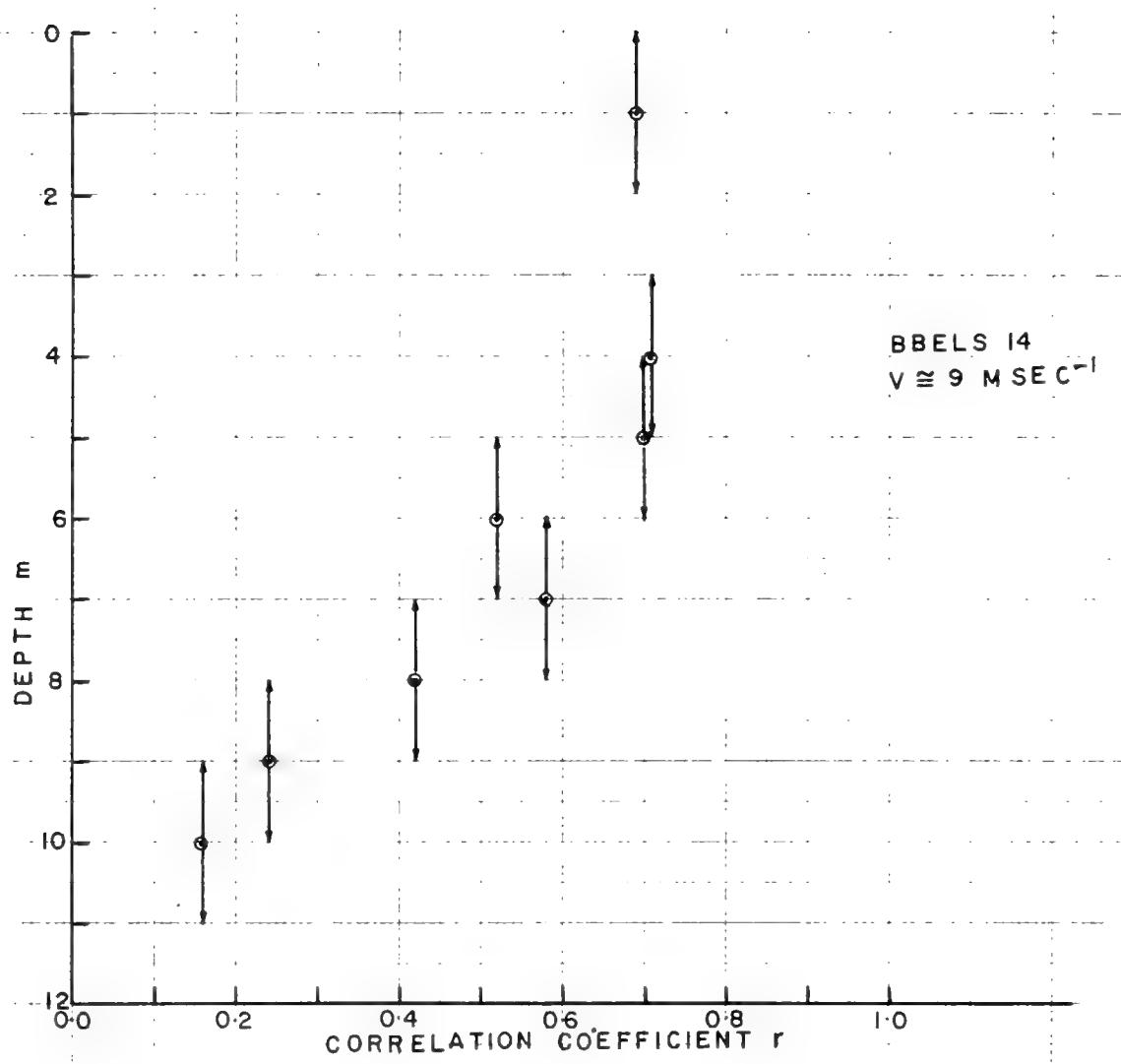
Change in Spatial Correlation Coefficient r with Depth (BBELS-14).

Figure V-26
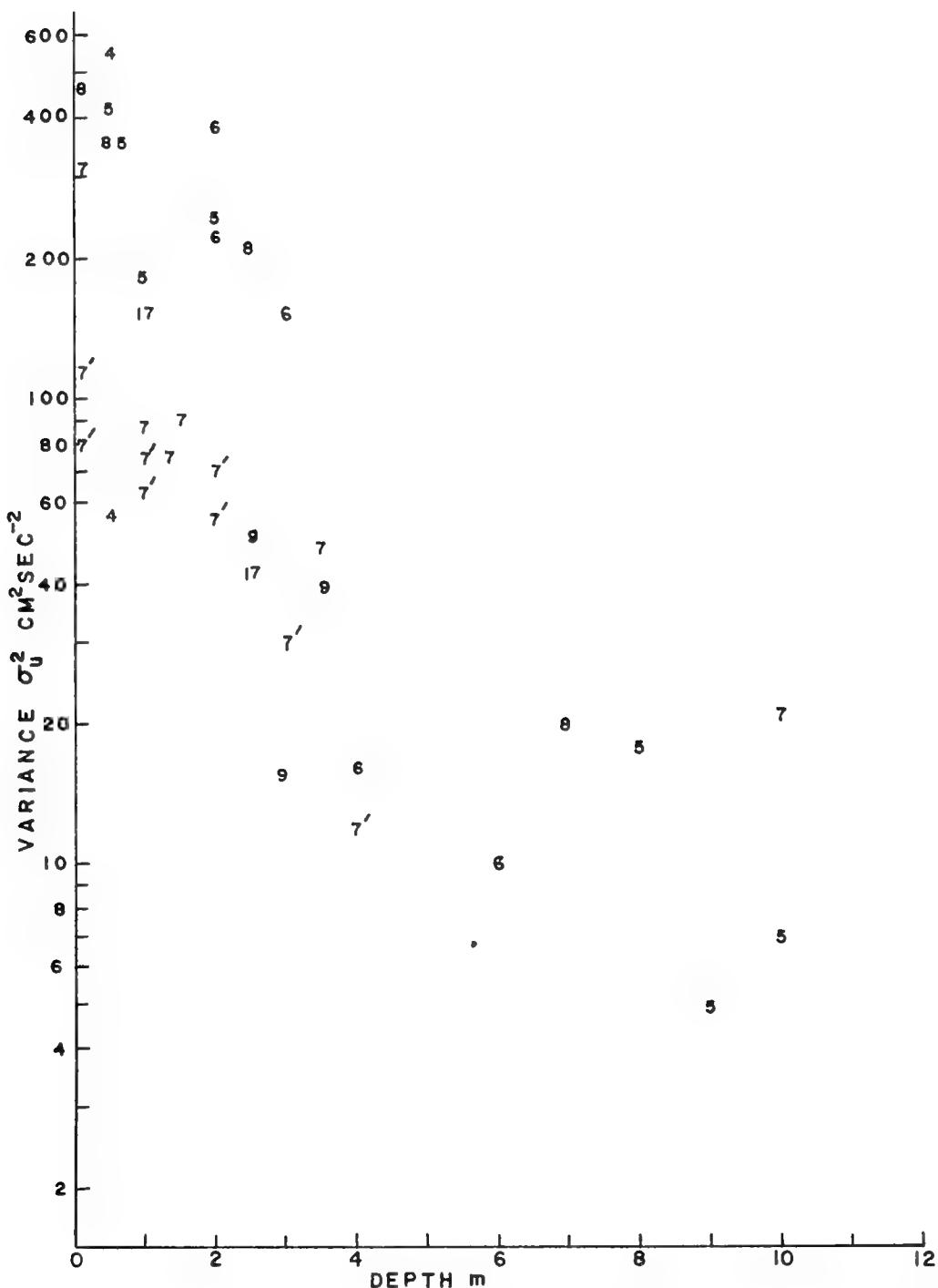
Distribution of Variances σ_u^2 for all BBELS Observations as a Function of Depth and Ambient Wind Speed.
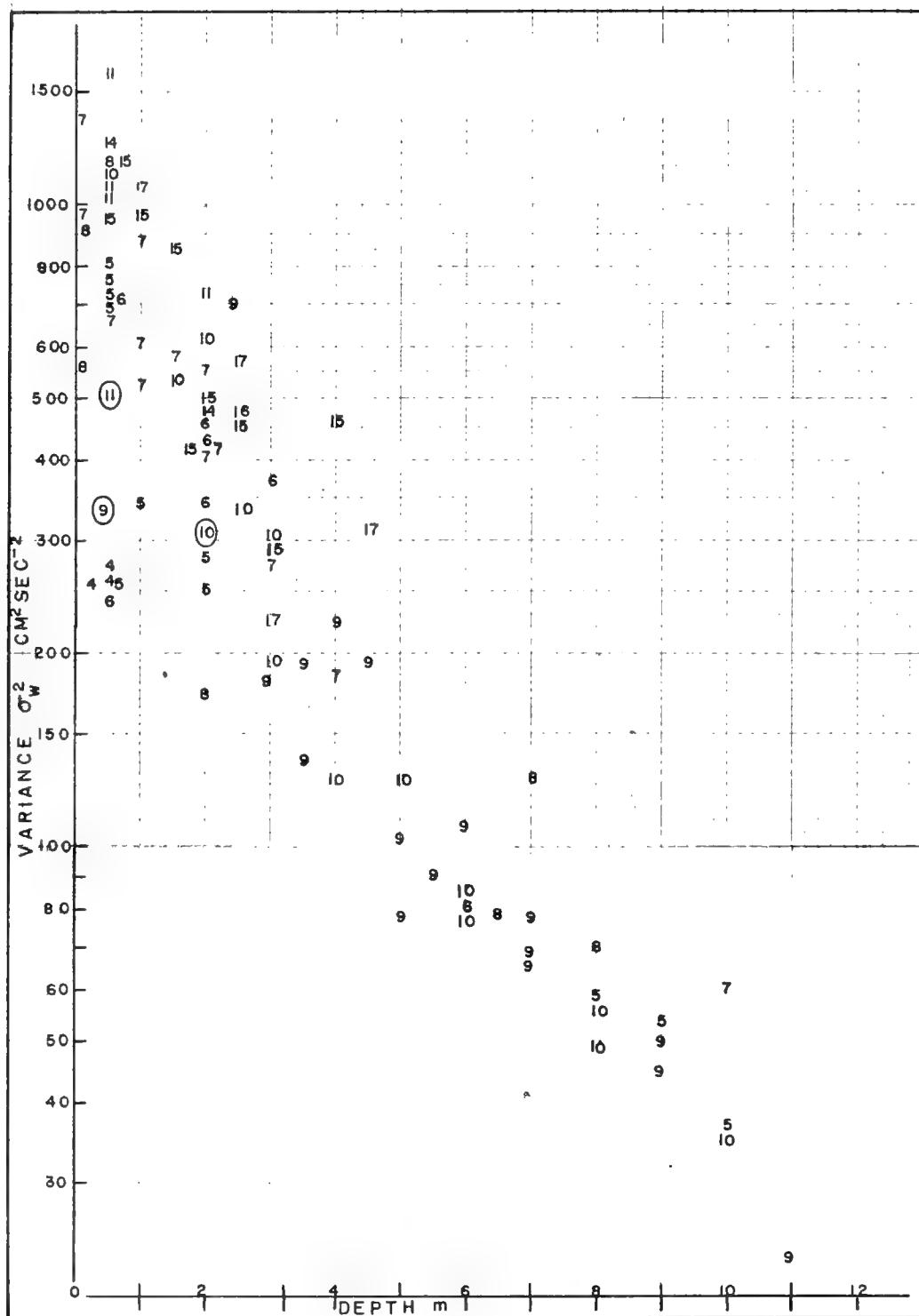
Figure V-27

Distribution of Variances σ_w^2 for All BBELS Observations as a Function of Depth and Ambient Wind Speed.

Figure V-28

Discounting the group of primed sevens in the σ_u^2 plot (figure V-27), the average slope of the envelope of variances for each velocity component is very similar. Further, if one considers the slopes of those variances associated with comparable wind speeds (i.e., for speeds of 5, 6, 7 and 8 m sec^{-1} in each plot), the abscissa and ordinate intercepts are quite similar in each case - roughly 11-12 meters and 400-800 cm^2 sec^{-2}, respectively.

It is of interest to compare the measured variances with the theoretical values obtained from the vertical velocity function of a classical trochoidal wave (see, for example, Proudman, 1953). This function is given as a third order approximation of a trochoidal wave:

$$\omega_T'(x_0, z, t) = -\frac{2\pi A}{T}\left[1 - \frac{5}{2}\left(\frac{\pi A}{L}\right)^2\right] e^{\frac{2\pi z}{L}} \sin 2\pi\left(\frac{x_0}{L} - \frac{t}{T}\right); \quad (\text{V-12})$$

where $\omega_T'(x_0, z, t)$ is the deviation of the theoretical vertical velocity component about a zero mean, A is the amplitude of the wave, T is the period, and L is the wave length. The coordinate x_0 is a constant, indicating that the measurements are being made at a fixed horizontal position but at various depths z.

A trochoidal wave is preferable to the traditional sinusoidal type wave, since the former is perhaps more representative of actual ocean waves. Also, the trochoidal system is derived by assuming a realistic ratio of wave amplitude to wave length, whereas the sinusoidal wave is derived by assuming a vanishingly small amplitude.

The theoretical variance function is defined as:

$$\overline{\omega_T'^2} = \sigma_\omega^2 = \frac{K}{T_s} \int_{-T_s/2}^{T_s/2} \sin^2 2\pi\left(\frac{x_0}{L} - \frac{t}{T}\right) dt \quad ; \quad (\text{V-13})$$

where

$$K = \frac{4\pi^2 A^2}{T^2}\left[1 - \frac{5}{2}\left(\frac{\pi A}{L}\right)^2\right]^2 e^{\frac{4\pi z}{L}} \quad , \quad (\text{V-14})$$
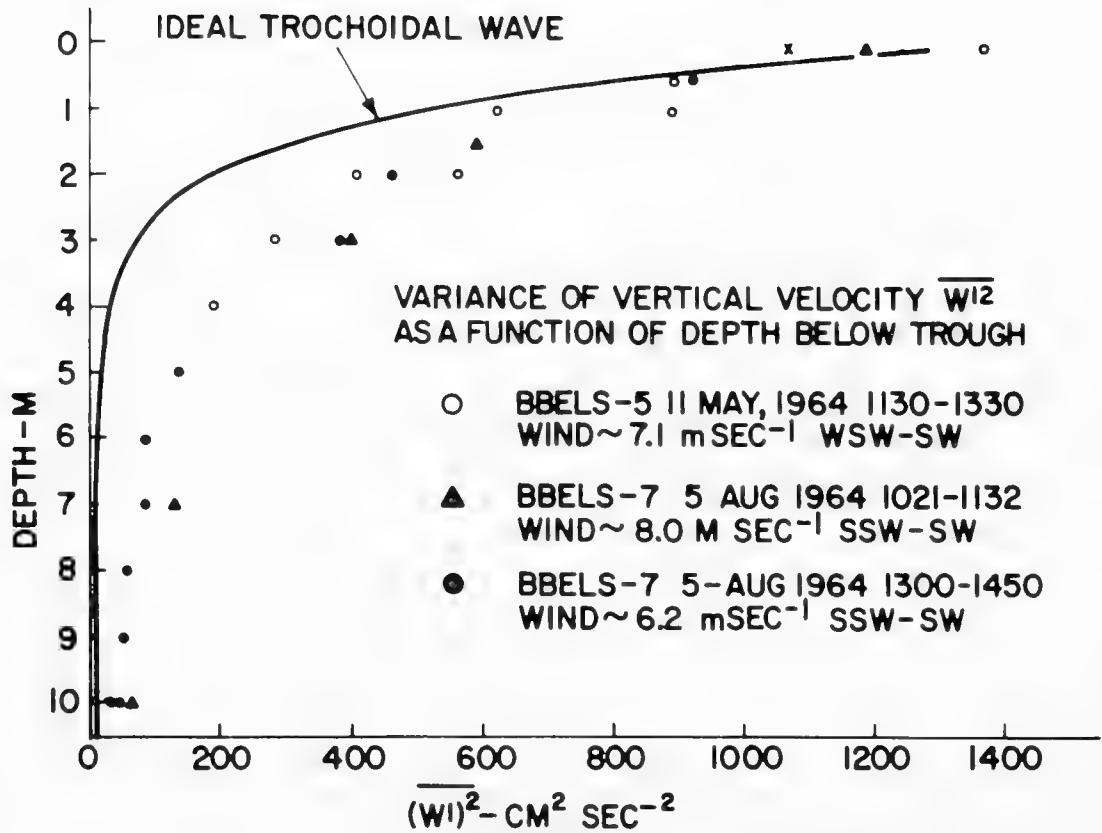
Observed Distribution of Variance $(w')^2$ vs Depth Compared with an Ideal Trochoidal Wave.

Figure V-29

and T_S is the period over which the time average is made.

Integrating equation (V-13) gives:

$$\overline{w_T'^2} = \frac{K}{2} + \frac{KT}{2\pi T_S} \sin 4\pi \left(\frac{x_0}{L} - \frac{t}{T}\right)\Bigg|_{-T_S/2}^{T_S/2} . \qquad \text{(V-15)}$$

Since $T_S \gg T$, the second term of the expression may be neglected. Thus:

$$\overline{w_T'^2}(z) = \frac{2\pi^2 A^2}{T^2}\left[1 - \frac{5}{2}\left(\frac{\pi A}{L}\right)^2\right]^2 e^{\frac{4\pi z}{L}} . \qquad \text{(V-16)}$$

The evaluation of equation (V-16) is somewhat arbitrary, since precise information is lacking of the parameters T, L, and A. In order to compare the depth attenuation of the theoretical variance of the trochoidal wave with the observed variance as a function of depth, one must evaluate the coefficient of the exponential term in equation (V-16). The somewhat arbitrary values of the wave parameters were based on visual observations made at the time of measurements and on the sea state chart (table II-2) derived from statistical observations by Marks (1964). The variance calculated from equation (V-16) at zero depth is about 1100 cm2 sec-2, using the following values: wave length L = 18.0 m; period T = 4.0 sec; and amplitude A = 30 cm.

This curve is plotted as a solid line in figure V-29, along with the variance-depth distribution from BBELS-5 and 7. The surface value of variance is somewhat arbitrarily chosen, since the values of the parameters can only be estimated. However, the curve clearly displays rapid depth attenuation. Below 1.5 - 2 meters, the theoretical values of variance fall off much faster than do the measured values. This seems plausible, since the sinusoidal oscillations of the classical waves transfer no momentum downward due to the absence of any Reynolds stresses (i.e., turbulent diffusion). On the other hand, ocean waves cannot be completely irrotational; and, by their very nature, they serve to transfer turbulent energy statistically downward. This is evidenced by the residue of variance existing at depths well below 4-6 meters (see figures V-27 and V-28).

Essentially, the observed variance function characterizes only the gross motional fluctuations in the waves. The lower limit of the size of the eddies

contributing to the variances is determined largely by the physical dimensions of the turbulence meter. The meters used were 15 - 18 cm in diameter. Eddy structure of this dimension or smaller, although perturbing the highly responsive impellers, would probably present a highly biased effect or a smearing of the high frequency motions because of the complex interaction of the meter geometry with the water flow through and around it.

The residual variance at deeper levels may therefore be caused by the interaction of the mean horizontal tide flow with the meter, artificially generating turbulence about the meter which is then registered. The calibration tests, however, did not support this interpretation for steady or slowly varying flow up to at least 115 cm sec^{-1}. As discussed in chapter II, there was no vertical impeller response for a series of horizontal flow calibrations.

A further examination of the observed vertical distributions of the variances, as they pertain to the distribution of wave energy, seems called for. For better interpretation, the variances σ_u^2 and σ_w^2 can be indicated by their equivalents $\overline{u'^2}$ and $\overline{w'^2}$; where u' and w' are the deviations from the mean $\bar{u}$ and $\bar{w}$ (see equation (III-12)). Appendix A shows that the terms $\rho \overline{u'^2}$ and $\rho \overline{w'^2}$ represent dynamic pressures (or normal stresses), expressed in dynes cm^{-2}, acting in the direction of the respective velocity fluctuations u' or w'. If a dynamic pressure (force per unit area) is integrated over a depth D, normal to this area, this integral represents the turbulent kinetic energy contained in a volume of unit cross section and depth D. A similar integration can be done using the mean values $\bar{u}$ and $\bar{w}$, giving the volume integral of the kinetic energy associated with the mean motion. For example, the total kinetic energy of a volume of water bounded by the free surface $\bar{\eta}$ and the depth D (and of unit cross section) may be given by:

$$ E_{KT} = \frac{1}{2}\rho \int_{\bar{\eta}}^{-D} (\bar{u}^2 + \bar{w}^2)dz + \frac{1}{2}\rho \int_{\bar{\eta}}^{-D} (\overline{u'^2} + \overline{w'^2})dz \qquad ; \qquad \text{(V-17)} $$

$$ \underset{A}{\qquad\qquad\qquad\qquad} \underset{B}{\qquad\qquad\qquad\qquad} $$

where E_{kt} is in units of erg cm^{-2}. Integral A is the kinetic energy associated with mean motion; integral B is the kinetic energy associated with the turbulent or wave-induced oscillatory motions.

In the problem of two dimensional wave motion, $\bar{w} = 0$ and $\bar{u}$ is the mean

current. The upper limit of integral B in equation (V-17) is the mean free surface $\bar{\eta}$, which is located at $Z = 0$. Thus, the turbulent kinetic energy associated with two-dimensional wave motion is:

$$E_{kw} = \frac{1}{2} \rho \int_{0}^{-D} \left(\overline{u'^2} + \overline{w'^2} \right) dz \qquad (V\text{-}18)$$

From the wave measurements, distributions of $\overline{u'^2}$ and $\overline{w'^2}$ are available as a function of depth (see table IV-3); hence, the numerical integration of equation (V-18) can obtain estimates of E_{kw}.

Six sets of BBELS wave observations were used to calculate the integral E_{kw}. The results are given in table V-2, which lists the wind velocity V (cm sec-1), the depth of numerical integration D (m), and E_{kw} (erg cm^{-2}). The other parameters are discussed later.

Note that for BBELS-5 and 7, the OMDUM II system obtained both u and w at various depths; hence, equation (V-18) was used to estimate E_{kw}. For BBELS-11 and 14, however, the LIMDUM I system obtained only values of w. The following integral was used for these calculations:

$$E'_{kw} = \rho \int_{0}^{-D} \overline{w'^2} \, dz \qquad (V\text{-}19)$$

It is assumed that in equation (V-18):

$$\overline{u'^2} \simeq \overline{w'^2} \qquad (V\text{-}20)$$

This assumption is certainly not unreasonable in dealing with surface waves, for which, classically, equation (V-20) holds. In fact, it may turn out that equation (V-20) is a better assumption than using the experimentally obtained $\bar{u}$, which intuitively seemed too small. If equation (V-19) is used in all calculations of E_{kw} (i.e., discarding $\bar{u}$ completely), the E_{kw} integrals will be roughly 10-20 percent larger than values obtained using equation (V-18). These numerically integrated estimates of E_{kw} are approximations and should be considered as merely indicative of the order of magnitude of the wave turbulent kinetic energy. The E_{kw} values thus obtained are similar in magnitude to wave energies tabulated by Stewart (1961) for similar wind conditions.

TABLE V-2

Comparison of Wave Kinetic Energy Estimated by Vertical Integration of the Variances of the Wave Motions with Estimates of Wave Potential Energy Inferred from Wave Heights and Wave Lengths Utilizing Data from Marks (1964).

Series Components Measured	Wind Speed $(m\ sec^{-1})$	Depth E_{kw} $(erg\ cm^{-2}$ $x\ 10^5)$	L (m)	$H_m/2$ (cm)	$E_p(H_m/2)$ $(erg\ cm^{-2}$ $x\ 10^5)$	H(L) (cm)	$E_p(H_L)$ $(erg\ cm^{-2}$ $x\ 10^5)$
BBELS-5 (u,w)							
(001-004)	6.8 WSW	1.82	10.5	38.	1.77	37	1.68
(004-008)	6.9 WSW	1.32	10.5	38	1.77	37	1.68
BBELS-7 (u, w)							
(009-016)	6.7 SSW	1.67	12.5	53	3.44	44	2.37
(018-019)							
BBELS-11 (w)							
(032-047)	9.5 ENE	4.10	12.5	55	3.71	65	5.18
(057A, B, 058, 069)	15 WNW	6.07	17.5	65	5.18	65	5.18
BBELS-14 (w)							
(088, 091-097)	9.6 SSW	3.21	20	55	3.71	79	7.65

In the classical theory of progressive surface waves, the total wave energy per unit horizontal area is given by (see Lamb, 1945):

$$E_T = g \rho A^2 \quad ; \qquad \text{(V-21)}$$

where g = 980 cm sec^{-2}, ρ is the density of sea water, and A is the amplitude of the wave (equal to half the wave height, H/2). The kinetic energy E_k of the wave equals the potential energy E_p, or:

$$E_K = E_P = \frac{E_T}{2} \qquad \text{(V-22)}$$

It is worthwhile to attempt to evaluate E_p using average values of the observed wave heights. During the BBELS observations, visual estimates were made of wave height (H) and wave length (L), and these are listed in table V-2. The values obtained are manifestly very subjective, and statistical interpretation of them is difficult.

Consider first the wave height observations. What was actually done was to scan the sea surface from the lower catwalk (shown in figure IV-18), located some 18 meters above the water, and to estimate the distance from the visible crests to the trough. This method of observation gives approximate values of maximum wave height Hm, but it is difficult to derive anything more than rough estimates of the average wave height (see Pearson, Neumann, and James, 1955).

A somewhat arbitrary decision was made to define the "average wave height" as 0.5 Hm, and these values are listed in table V-2. Using these Hm/2 values and equation (V-21), the estimates of wave potential energy, designated E_p (H/2), were obtained. These estimates range from 1.77 to 5.18 X 10^5 erg cm^{-2}. They are very similar in magnitude to the kinetic energy values (E_{kw}). Note that in BBELS-11 E_p (H/2) shows a similar increase with the respective values of E_{kw}. In view of the crudeness of the instrumentation and the obvious shortcomings of both the data and perhaps its interpretation, the similarity of E_{kw} with E_p (H/2) is startling.

It may reasonably be objected that the choice of using average wave heights of 1/2 Hm was made so as to produce similar magnitudes of E_{kw} and E_p (H/2). Let us therefore estimate the mean wave height by another method. Note in table IV-3 that values were recorded of wave length. These were somewhat more accurate than wave height, since the distance between the main west legs of the BBELS (15 m) could be used as a reference. From the observed values of wave length L, inter-polated values of average wave height (designated by $\bar{H}$) were obtained using table II-2 (from Marks, 1964). These values are tabulated as H(L) in table V-2, and are very similar to those for Hm/2. Values of corresponding potential energy, designated as E_p ($\bar{H}$), are shown in the last column of table V-2. These values of E_p ($\bar{H}$) are still similar to both E_{kw} and E_p (H/2) in most cases.
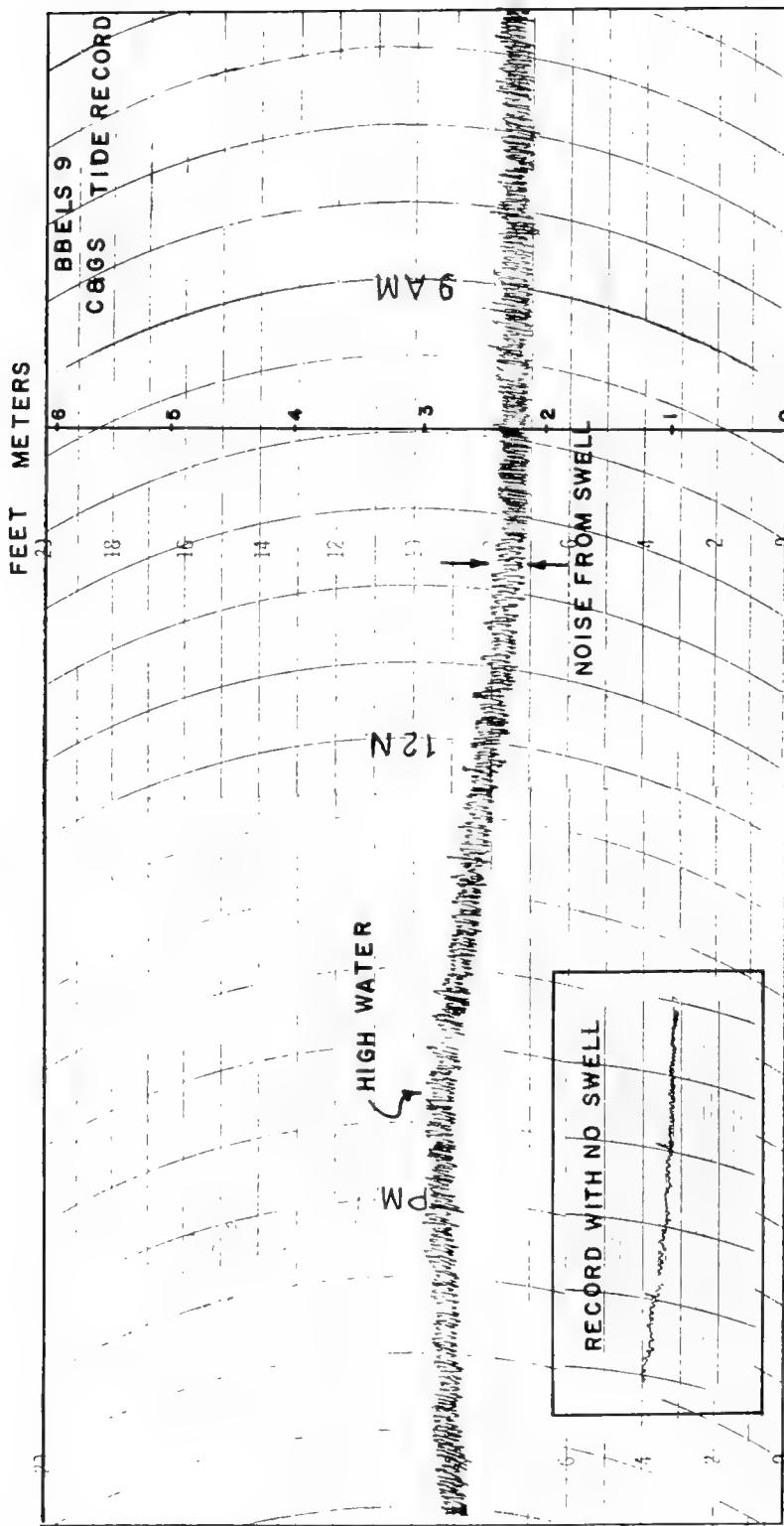
Tide Record at BBELS Showing Swell Oscillations.

Figure V-30

In conclusion, it has been shown that the values of estimated potential energy of waves are similar to the values of wave kinetic energy estimated from direct measurements of u and w within the waves. Obviously, the value of E_p in equation (V-21) is sensitive to the value of A; hence, error in choosing A values could vary E_p by as much as a factor of 4. However, the important point is that $E_p(H/2)$ or $\bar{E}_p(\bar{H})$ are of the same order of magnitude as E_{kw} estimated from actual measurements. This not only lends credence to the wave measurements and techniques, but suggests that a real equipartitioning of wave potential and kinetic energy occurs in the ocean.

Short Term Changes in Wave Energy

Wind Wave Build-up - Usually, when making a series of wave measurements, the total time involved was short enough so that the wave and wind conditions were relatively constant (i.e., stationary). This was desirable for comparison of observations at different depths. However, during observations made on 26 January 1965 (serial 023 and 024 of BBELS-9), a build-up of sea conditions was visually observed, which was corroborated by the time variation in the auto-spectra of wave motions observed at 0.5 meter depth.

The measurements were made using the OMDUM III system (with three guy wires) suspended from the west side of the tower. The u meter was aimed at 180°T, with the original intention of observing the unusually strong swell radiating from the south.

Two sets of 5-minute observations were made. The first (023) started at 1145 hours; the second (024) at 1224 hours. The oceanographic and meteorological conditions are listed in table IV-3. At 1147 the wind was recorded at 3.7 m sec^{-1} from the ESE. Between measurements, the wind steadily increased until at 1245 it was recorded at 5.8 m sec^{-1} from the SE. The seas observed at 1145 were slight, but became perceptibly larger as the wind speed increased. The well-defined swell observed throughout the observation period had wave lengths of about 30 meters, wave heights of about 50 cm, and periods of 5-6 seconds.

The tide gauge system aboard the BBELS (discussed in chapter IV) served in this case as an indicator of the strong swell. Figure V-30 shows the tide gauge trace for the period of BBELS-9 observations. The swell appears as high frequency "noise" on the trace. For comparison, a section of a record with little or no swell is shown in the insert at lower left of figure V-30.

The indicated swell height on the tide chart is about 20 cm, which is some-what less than the visually estimated height of 50 cm. Thus, it appears that swell motions are somewhat damped by the tide gauge system, but are still of low enough frequency so as not to be completely filtered out. With small cost, a minor modification could be made in the time response, enabling the tide gauge to record swell along with tide height over long periods.
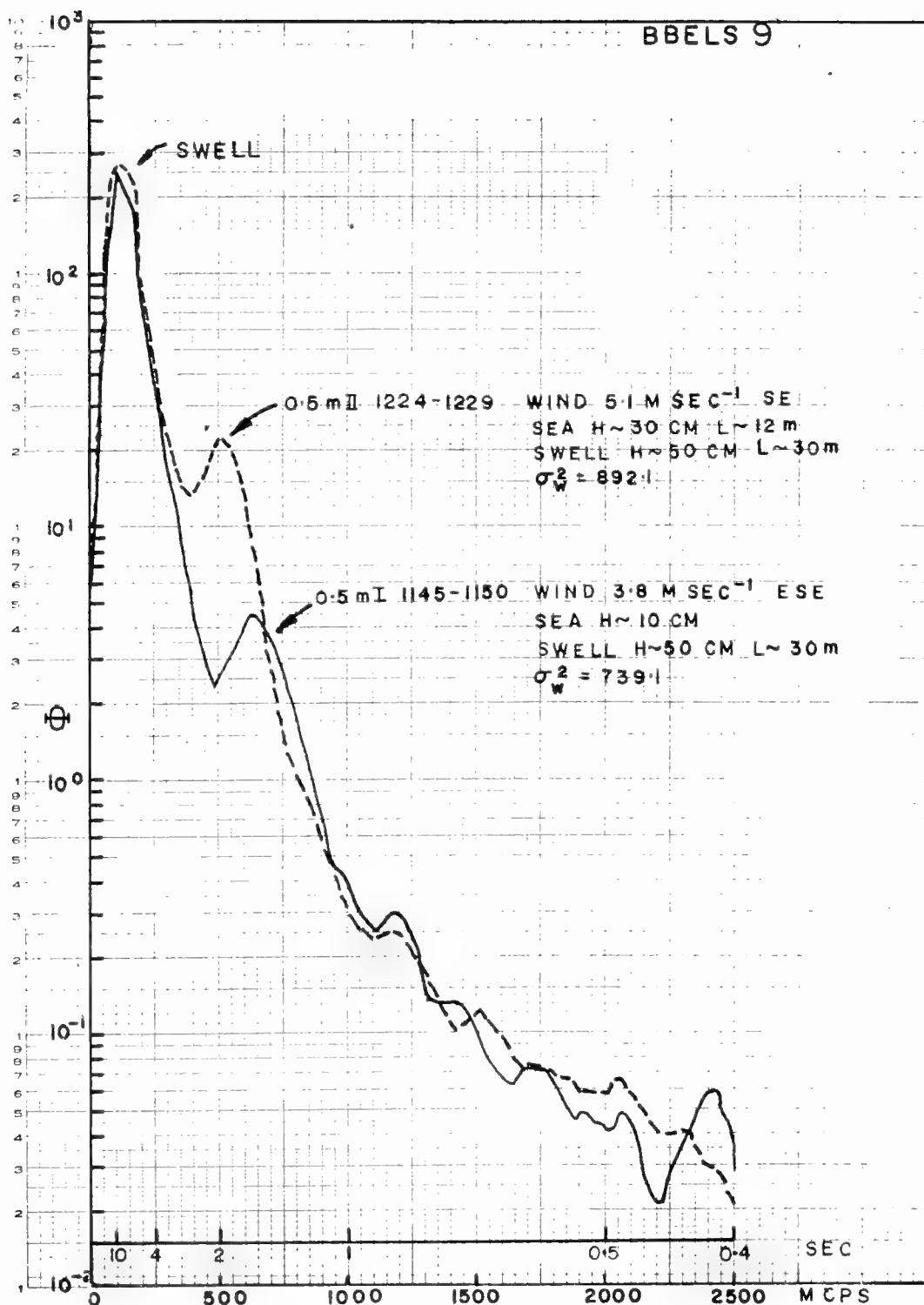
Superimposed Time Lapse Auto-Spectra of Vertical Velocity Components
(BBELS-9 Uncorrected Data).

Figure V-31A

Referring to table IV-3, the mean horizontal down-wave flow component $\bar{u}$ varied from -5.5 to +3.2 cm sec^{-1} between the time of serial 023 and 024. Low tide occurred at about 1030 hours. According to the relationship between tide height η and current direction θ shown in figure IV-6, at the time of the wave measurements (from 1145 to 1229), the current should have been changing from 180° to about 280°. Since the u meter was aimed at 180°, the predicted current change agrees with the observations.

Interestingly enough, the values of σ_u^2 and σ_w^2 are more nearly equivalent than in any other BBELS observations at 0.5 meter depth (see table V-1, showing the ratios σ_u^2 / σ_w^2). The variances for 2.0 meters are about equal.

The auto-spectra for u and w from serial 023 (0.5 m I) are shown in appendix B. The curves exhibit two peaks, one centered at 100 mcps (10 sec) and a lesser one at 600-650 mcps (1.7 sec). Although the Φ_u curve falls slightly below the Φ_w curve at all frequencies, the spectra are similar in shape. A third minor peak is displayed by Φ_w at about 1200 mcps (0.85 sec).

The auto-spectra for the second 0.5 meter observation (serial 024) are also shown in appendix B. Two dominant peaks are again displayed. The highest energy peak again occurs, for both Φ_u and Φ_w, at 100 mcps (10 sec). Clear secondary peaks are exhibited at about 500 mcps (2 sec); however, the Φ_u peak falls farther below the Φ_w value than in the 023 observation.

The auto-spectra for 2 meter depth (serial 025) are shown in appendix B. Again the dominant peak occurs at 100 mcps (10 sec), where the curves for each spectral component are essentially identical. Below 200 mcps (above 5 sec), Φ_u slightly exceeds the value of Φ_w . At about 400-500 mcps, a slight step or plateau is depicted by the Φ_w curve and, to a lesser extent, by Φ_u . This inflection appears to be a vestige of the secondary peaks of the spectra from the 0.5 meter measurements (serial 023 and 024).

Inspection of the auto-spectra of the three observations indicates that by far the greatest energy content lies in the low frequency swells appearing in the spectra in the region from 100 mcps (10 sec) to 250 mcps (4 sec). The secondary peaks in the auto-spectra occurring at 500-700 mcps (2.0-1.7 sec) are probably manifestations of the small wind waves radiating from the SE super-imposed upon the long swells from the south.

In view of the wind and sea build-up during the observations, it is of interest to directly compare the spectra of serial 023 (0.5 m I) with 024 (0.5 m II). Figure V-31A displays the superposed auto-spectra of the vertical velocity components. Most striking is the similarity of the curves except in the frequency band from 350 mcps (2.8 sec) to 900 mcps (1.1 sec). In this region, there is a contrasted and overall "reddening" and energy increase displayed by the 0.5 m II spectrum relative to that of the 0.5 m I. The peak of 0.5 m I at 650 mcps (1.7 sec) attains 4.6 cm^2 sec^{-1}; whereas the corresponding 0.5 m II peak, which has shifted to 500 mcps (2.0 sec), attains 23 cm^2 sec^{-1} — a five-fold increase in spectral density.
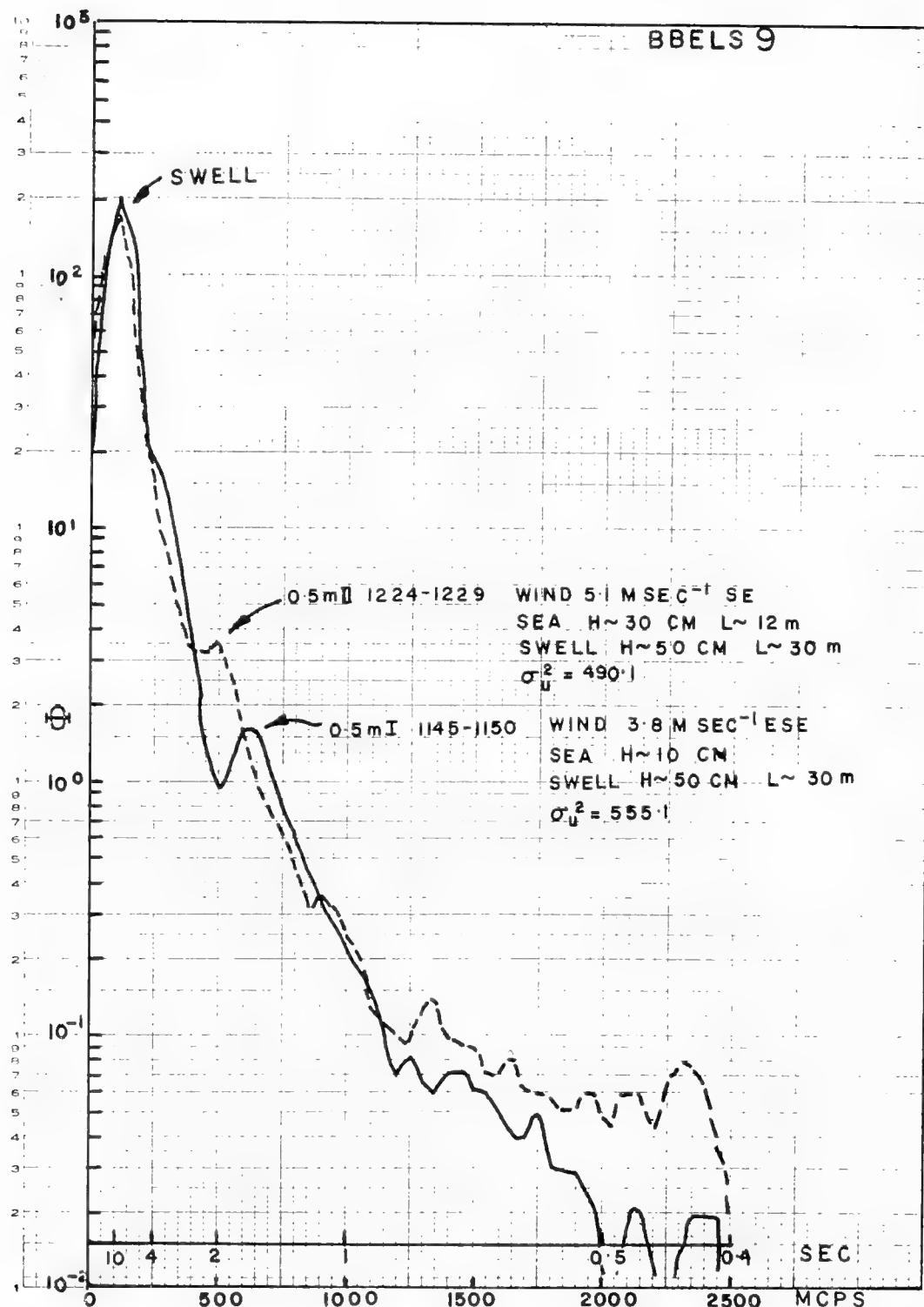
Superimposed Time Lapse Auto-Spectra of Horizontal Velocity Components
(BBELS-9 Uncorrected Data).

Figure V-31B

Figure V-31B displays the build-up of the horizontal energy spectra at similar frequency bands. The change in secondary peak frequency is identical with that observed in the vertical spectra. The spectral density is 1.6 cm^2 sec^{-1} at 650 mcps (1.7 sec) for 0.5 m I, and attains a level of 3.5 cm^2 sec^{-1} at 500 mcps (2.0 sec) for 0.5 m II — only a two-fold increase.

Thus, there is evidence of a build-up of the wind-wave spectrum bands produced by the increasing winds. However, the low frequency swell (at 100 mcps) shows essentially no change between the 0.5 m I and 0.5 m II observations.

There are several small high frequency peaks above 1000 mcps (1.0 sec). The most notable peak occurs in the pairs of vertical velocity curves (figure V-31A) at about 1200 mcps (0.83 sec). This peak shows no change of position in the two curves. This may indicate a resonant fluctuation in the flow through the meter, which could be somewhat independent of the wave conditions.

The BBELS-9 observations thus show direct evidence of energy being added by the wind to the motions of the sea surface. This energy input is very frequency dependent. The wind-imparted wave energy also tends to move to a lower frequency range with the passage of time.

The relationships of the variances and spectra of the three observations (023, 024, and 025) further demonstrate the ability of the OMDUM III system to respond to the two-dimensional wave motion components in the direction in which the system is aimed. The u meter was pointed directly into the oncoming swell from the south (whereas the wind waves were from the SE). As a result, the curves for Φ_u and Φ_w tend to be very similar for the low frequency range from 0 to 250 mcps. The greatest differences between the u and w spectra occur in the frequency range around 500 mcps (2 sec). This may very well be due to the u meter being directed some 45° away from the path of the high frequency wind waves, whereas the w meter would respond fully to the w component associated with the wind waves. Moreover, the OMDUM III tends to respond fully to both the u and w components associated with low frequency swell. (Note that this is similar to the effects discussed earlier in this chapter.)

Wave Energy During Changing Wind Conditions - The longest and one of the more interesting series of observations was BBELS-11, made on 29 and 30 March 1965. Wave observations were made over a 24-hour period in order to observe changes in wave motion statistics as the wind (and hence, the wave conditions) changed. It was intended to use the LIMDUM I system arranged to measure w at two depths with a 1.5 meter vertical separation. As explained earlier, a pen of the two-channel recorder burned out shortly after measurements began; and, since no spares were available, the work was continued using one recorder channel. The LIMDUM I was placed at a certain depth, and each meter was recorded in succession on the single usable channel.

A total of 39 observations were made at various depths from 1622 hours on 29 March through 1251 hours on 30 March (see table IV-3). The statistical analysis listings and the plotted auto-spectra for each record of w are presented in appendix B (serial 030-069).
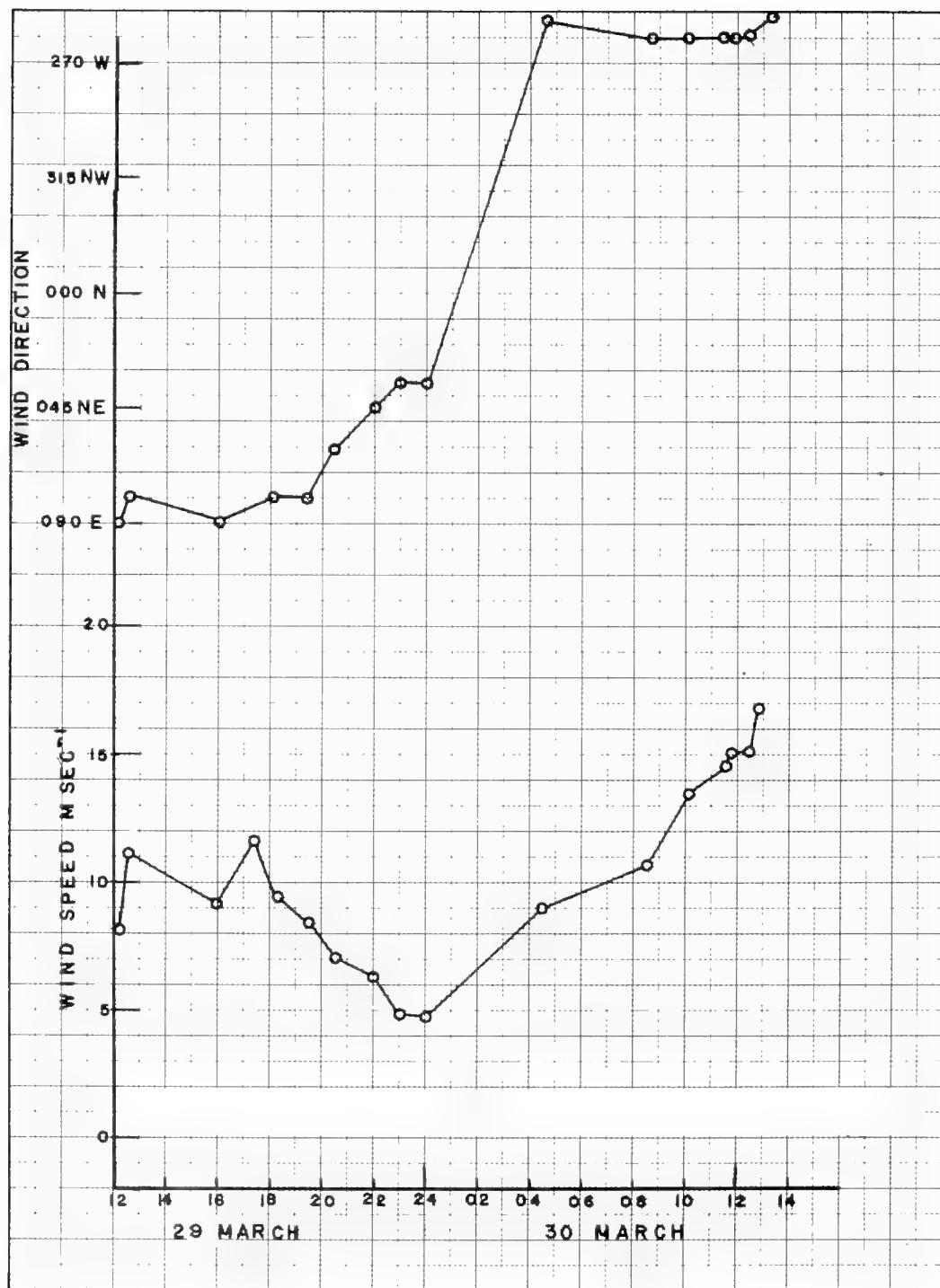
Wind Speed and Direction During BBELS-II Observations.

Figure V-32

It was hoped that, during the period of observations, some definite variation would occur in the wind field, permitting observation of reflected changes in the waves. Shortly after the helicopter trip to BBELS at 1500 hours on 29 March, a northeast blizzard commenced. Strong ENE winds and snow continued through midnight. Wind speed and direction for the entire sampling period are plotted in figure V-32. The winds from 1200 to 1800 hours on 29 March were from the east at about 9-12 m sec^{-1}. The winds abated to about 5 m sec^{-1} and shifted to the NE by 2400 hours. The snow ceased at about 0200 hours on 30 March. By 0400 the wind had shifted rapidly around to WNW at about 9 m sec^{-1}, and the skies were clear. From 0400 on, the winds remained from the west to WSW, but the wind speed steadily increased, attaining 17 m sec^{-1} by 1300 hours.

During the first 12 hours of observations, the wind waves naturally were out of the east and ENE - from Buzzards Bay. The LIMDUM I system was therefore placed on the east side of BBELS and suspended from the end of the catwalk (see figure IV-4). This was done to avoid measuring waves from the leeward side of the tower. As soon as the winds shifted to the WNW after 0400 on 30 March, the LIMDUM I system was moved to the usual position on the west side of BBELS (see figure IV-18).

Nine observations, all made at 0.5 meter beneath the wave troughs, were chosen as representative of conditions during each phase of weather variation. The auto-spectra Φ_w for this sequence are shown in figure V-33. Greater resolution of the lower frequencies was obtained by computing these spectra using M = 100 lags, in lieu of the 50-lag resolution used in the plots of appendix B. Also, a linear ordinate of spectral density (cm^2 sec^{-1}) is used to emphasize the high energy peaks. The abscissa lists both frequency (mcps) and period (sec). The time of sampling, wind velocities, and the variances are shown for reference.

The first three spectra (030, 031, and 032) display large variances in excess of 1000 cm^2 sec^{-2}. Strong bands of spectral energy occur from 150-350 mcps (12.9- 6.6 sec), with peaks at about 250 mcps (4 sec). Since observation 031 was only a one-minute sample, there is large uncertainty in the variance and spectral estimate.

Even with relatively high ENE winds of 10-11 m sec^{-1}, the wave frequencies are concentrated at 250 mcps. Winds of 10-11 m sec^{-1} from the S or SW (where there is an "infinite" fetch) produce waves having spectral peaks between 150-200 mcps (4.0 - 6.6 sec), as shown by figure V-15 (spectrum 080). The waves portrayed in spectra 030-032 are probably "fetch limited" because of the land masses directly to the east (see figure IV-3), and are therefore of relatively high frequency.

Observation 048 indicates a drop in wind speed. The spectrum now shows two peaks; the highest at 300 mcps (3.3 sec) and the lesser one at about 200 mcps (5 sec). The variance value has decreased sharply to 686 cm^2 sec^{-2}. The lower frequency peak may be attributed to longer period swell-like waves generated away from the local area. The spectrum of these waves could have been masked by the strong wind waves depicted by 030, 031, and 032.
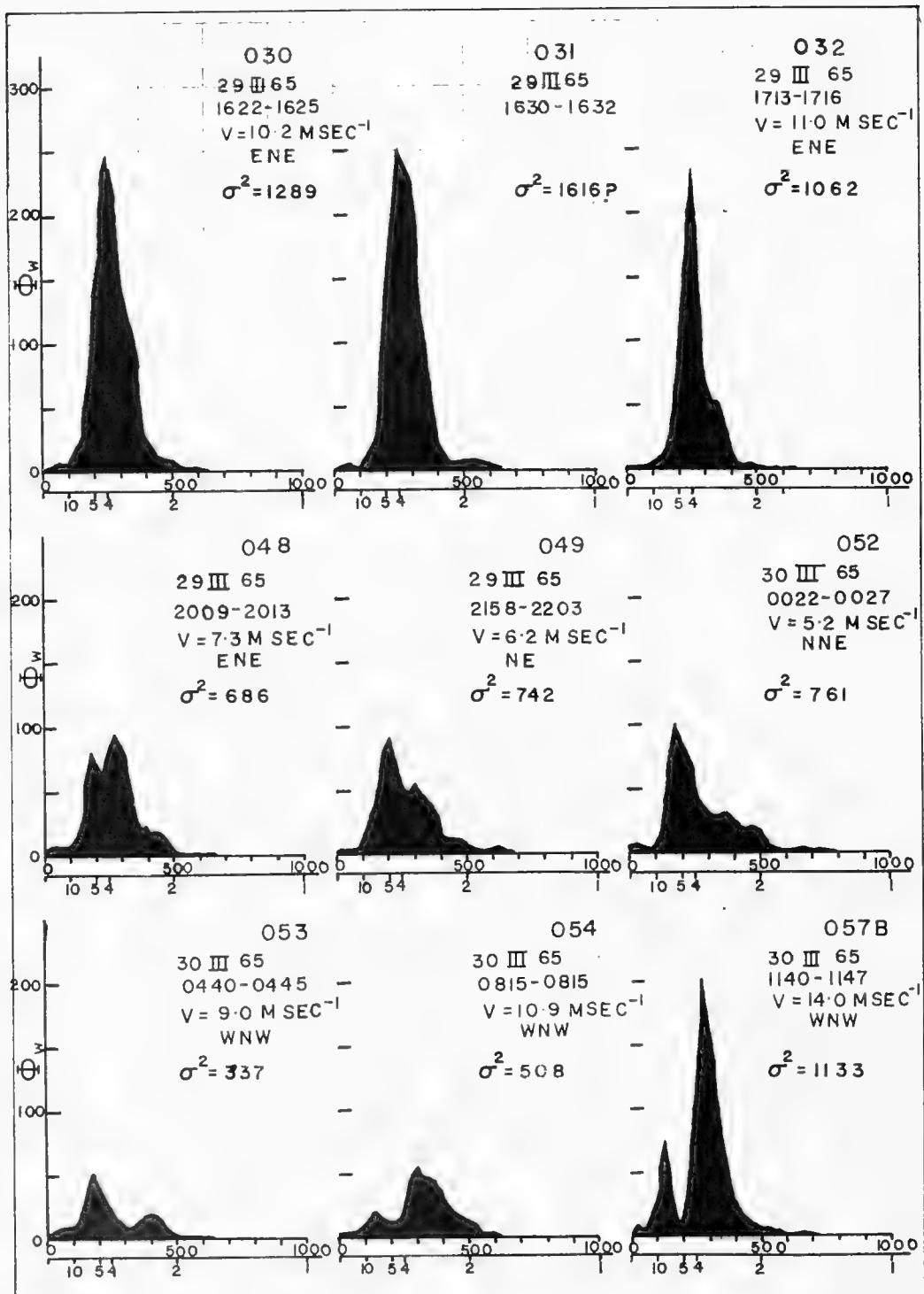
Time Variation of $\emptyset_w$ Due to Wind Conditions (BBELS-II, 0.5 m).

Figure V-33

Spectrum 049 shows a further decrease in wave energy along with lower wind speed. The low frequency peak (200 mcps) seen in 048 is still present and relatively unchanged, whereas the high frequency peak at 300 mcps has decreased markedly. In 052, where the winds have dropped to 5.2 m sec^{-1} and shifted more northerly, the high frequency peak (still at about 300 mcps) is still smaller. The low frequency peak remains about the same as 049. Comparing 048, 049, and 052, it appears that the energy between 250 and 500 mcps was rapidly attenuated as the wind decreased and shifted to a more northerly direction.

By 0440 hours on 30 March, the wind was from the WNW at about 9.0 m sec^{-1}. The 053 spectrum shows that the low frequency peak at about 200 mcps has been suppressed relative to the three previous spectra. The original band centered at about 300 mcps has vanished, and a new peak has formed at about 400 mcps. This latter peak is probably associated with the new wind waves generated by the freshening WNW winds.

The 054 auto-spectrum shows a further suppression of the low frequency peak. There is, however, an increase in the height of the band associated with wind waves, which now is centered at about 350 mcps.

By 1140 hours (serial 057 B) the winds attained a speed of 14.0 m sec^{-1}. The large wind waves are commensurate with the large variance of 1133 cm^2 sec^{-2}, and show up clearly as a strong spectral pedestal centered at about 300 mcps. There is a much smaller peak at 150 mcps. Actually, two sets of waves were observed, one from the NW and another from the west. The latter waves were apparently generated over the lower fetch (see figure IV-3). They are therefore of lower frequency and have far less energy than the freshly developed waves related to the high WNW winds. Note the similarity of the larger peak of 057B with the peak of 032, both of which are attributed to relatively short-fetch wind waves generated by relatively high winds.

The BBELS-11 observations showed gross variations in the characteristic auto-spectra of vertical wave motions. An attempt has been made to relate the spectral shifts to observed wind and wave variations. The preceding commentary of cause-and-effect is only a suggested simplified explanation of what is obviously a very complex geophysical phenomenon.

It was suggested earlier in this chapter that the variance, when measured as a function of depth, can serve as an indicator of the vertical distribution of kinetic energy associated with the wave motions. With this concept in mind, let us examine the time-variable distribution of $\overline{\sigma_w}^2$ obtained in BBELS-11.

Figure V-34 shows the distribution of the variance $\overline{\sigma_w}^2$ (in cm^2 sec^{-2}) as a function of depth and time. It is instructive to compare this figure with figure V-32. Between 1600 and 1800 hours on 29 March, the 0.5 meter and 2.0 meter variances are both relatively large (exceeding 1000 cm^2 sec^{-2} and 450 cm^2 sec^{-2}, respectively). The winds at this time were about 9-12 m sec^{-1}. From 1700 hours on 29 March through 0500 hours on 30 March, both the 0.5 meter and 2.0 meter variances display an overall decrease with time. This effect

Time-Depth Variation of Vertical Motion Variance from BBELS-II Data.
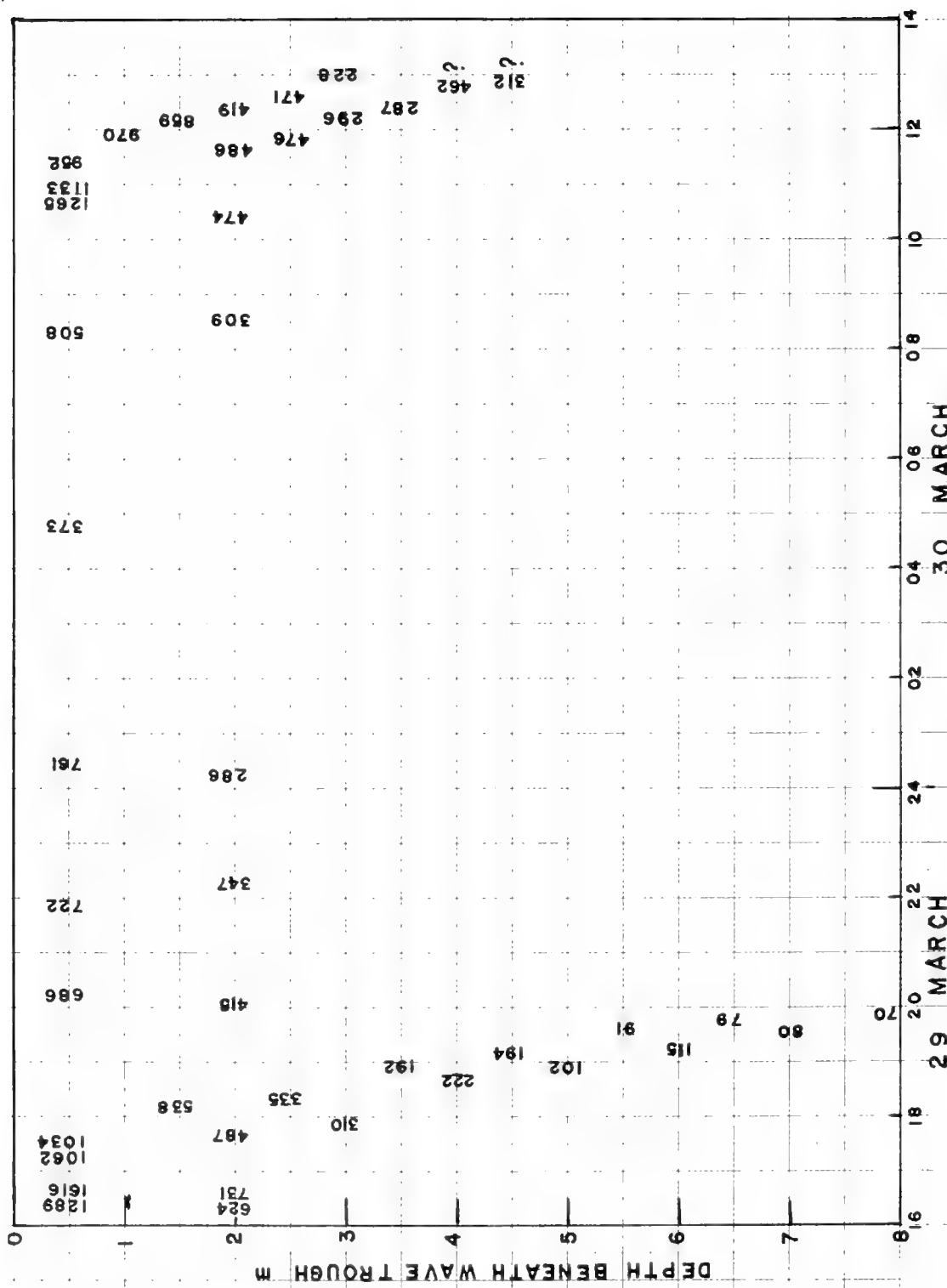
Figure V-34

closely follows the variation in wind speed, which has decreased from 12 m sec^{-1} at 1800 hours to 4.9 m sec at 2400 hours. Note that at the point of minimum 0.5 meter variance (373 cm^2 sec^{-2} at 0445), the wind has freshened to about 9 m sec^{-1} but is from the west. Waves generated by this wind are directly opposed to waves generated by winds only 4 hours earlier. The minimum variance is clearly associated with this wind shift. From 0815 to 1145 hours on 30 March, the 0.5 meter and 2.0 meter variances begin to increase. Starting at 2400 hours, the wind speed steadily increased to 12 m sec^{-1} by 1300 hours.

Thus, there is a plausible correlation between the wind velocity and the statistics of wave motions at BBELS. However, a word of caution regarding the quantitative evaluation of the variances and the amplitudes of the auto-spectral functions. It has been shown that the amplitude of the wave motions falls off exponentially with depth, and that the attenuation is strongest for the higher frequencies. In view of this, relatively small errors (of 10-15 cm) in the depth positioning of the wave meter could produce relatively large errors in the variances and perhaps bias the spectrum. The BBELS tide range is about 90 cm. Therefore, for long time measurements at a "fixed" depth, the wave meter must be adjusted as the tide rises and falls. This was attempted during the BBELS-11 series; however, it was a relatively crude adjustment and some inaccuracy in the σ_w^2 estimates may have resulted. The maximum depth error is estimated at about 10 cm. This error, according to the variance attenuation curves in figures V-20 and V-24, is equivalent to a 10-15 percent error in the variance. This effect could not be responsible for the gross variance changes at a given depth shown in figure V-34. Truly, these observations show real energy changes in the wind-wave regime.

Equilibrium Range of Wave Spectra

It has been suggested that because of wave energy inter-relationships, the auto-spectra of the free surface elevation Φ_η should display, at some specific region of the spectrum, a functional relationship with frequency (see Phillips, 1958). This region of the spectrum is termed the "equilibrium range" because wave motions associated with frequencies in the range are saturated; i.e., they can hold no more wind-derived energy, hence there occurs a continuous outflow of spectral energy in this region. It is believed that this saturation occurs because the physical characteristics of the water limit the slope and height (and, therefore, the potential energy) of waves of a particular frequency.

Consider the behavior of the energy spectrum Φ_η for relatively high frequencies. The physical parameters governing behavior of the spectrum in the higher frequency ranges and those governing the surface stability must be gravity -g, wind speed v, and some roughness parameter as $\overline{\eta'^2}$ to govern the gross form drag of the waves. However, for the limiting stable configuration of the wave profile, the acceleration of a particle at the wave crest is -g. Using the dimensional relationships of Bridgman (1956), let us consider a possible functional relationship of the free surface spectra Φ_η with the frequency.

By definition (see chapter III):

$$\Phi_\eta = \frac{1}{2\pi} \int_{-\infty}^{\infty} \langle \eta(t)\, \eta(t+\tau) \rangle\, e^{2\pi i f \tau}\, d\tau\,; \qquad \text{(V-23)}$$

having units of cm^2 sec (L^{2}T; where L = length, and T = time).

On an entirely dimensional basis:

$$\Phi_\eta = Q\, g^A\, f^B = L^2 T\,; \qquad \text{(V-24)}$$

where Q, as in equation (II-26), is a dimensionless constant.

Equating (V-23) to (V-24) and solving for A and B:

$$\Phi_\eta = Q\, g^2\, f^{-5}\,. \qquad \text{(V-25)}$$

Equation (V-25) can be assumed to hold for waves whose frequencies are somewhat lower than those of waves in which surface tension (in lieu of gravity) is the important restoring force (i.e., capillary waves). If ρ is the density, c the phase speed, T_S the surface tension, and k the wave number, then, for large k values (small wave lengths):

$$\frac{f}{k} = c(k) = \left[\frac{g}{k} + \frac{T_s k}{\rho}\right]^{1/2} \cong \left[\frac{T_s k}{\rho}\right]^{1/2}\,. \qquad \text{(V-26)}$$

Since for deep water waves the phase speed is c(k) = $\left[g/k\right]^{1/2}$, then for the upper limit of the equilibrium range:

$$f \ll \left[\frac{4\rho g^3}{T_s}\right]^{1/2}\,. \qquad \text{(V-27)}$$

The lower limit is indicated by the fact that, although the functional variation with f in equation (V-25) is monotonic (i.e., ever-increasing for larger values of f), there is in the real waves at any instant a maximum of the spectral energy. Thus, equation (V-25) must obviously fail where spectral maxima occur.

It is not clear on theoretical grounds just where the lower limit of the equilibrium range should be found; however, Pierson (1959) offers evidence that in sharply peaked spectra the equilibrium range can only begin at frequencies greater than twice the frequency of the maximum spectral peak.

Workers have provided evidence that the slopes of the auto-spectra of the free surface function η (t) do, indeed, approximate the f^{-5} relationship indicated in equation (V-25). This has been shown by Phillips (1958), Burling (1959), Kinsman (1960), and Kinsman (1964).

If there really exists an equilibrium range where the free surface spectra are functionally related to the frequency, then this phenomenon should also be evident in the particle velocity spectra. The classical free surface function η (t) at a fixed horizontal position is associated as follows with the deep water wave velocity functions, given by equations (II-5) and (II-6):

$$ z = \eta(t) = \frac{H}{2} \cos \sigma t . \qquad \text{(V-28)} $$

It has been demonstrated that the observed wave motions are roughly similar to classical wave motions, at least with respect to approximate phase relationships of the u and w wave components (see figures V-2 and V-3). It is therefore reasonable to assume that the same forces affecting the spectral behavior of η (t) would likewise influence the motions u(t) and w(t). Moreover, since the value of $\overline{\eta'^2}$ and $\overline{u'^2}$ and $\overline{w'^2}$ are directly associated with the potential and kinetic wave energies, their spectra should be related to similar dynamic effects in the waves.

According to Kinsman (1960), there should be a relatively constant decrease in spectral energy with increase in frequency in the region somewhat above the maximum peak energy. Also, it was inferred that a saturated spectral region occurs irrespective of the absolute peak heights or wind speeds, assuming only that a minimum of wave energy is available to form the equilibrium range.

Figure V-35 shows five auto-spectra of the vertical velocity component w measured at 0.5 meter depth. Wind conditions varied from 5.2 m sec^{-1} (serial 052) to 14.0 m sec^{-1} (serial 057B). The variances are shown in the upper right corner. Although both the peak values and the frequencies of peak location vary considerably, the values and slopes of Φ_w are very similar in the frequency range from 500 mcps (2 sec) through 800 mcps (1.25 sec). These curves are suggestive of an equilibrium range in the wave velocity spectra.

To explore any functional relationship of Φ_w to f, a cursory examination was made of some specific spectra of the vertical motions from BBELS-11. The first set of observations (030, 031, 032, and 033) was made over the period 1622 to 1720 hours on 29 March 1965, at a depth of 0.5 meter. During this period (see table IV-3) the winds were 10-11 m sec^{-1} from the ENE, and the seas were probably fully developed because of the ENE fetch limit (see figure IV-3).
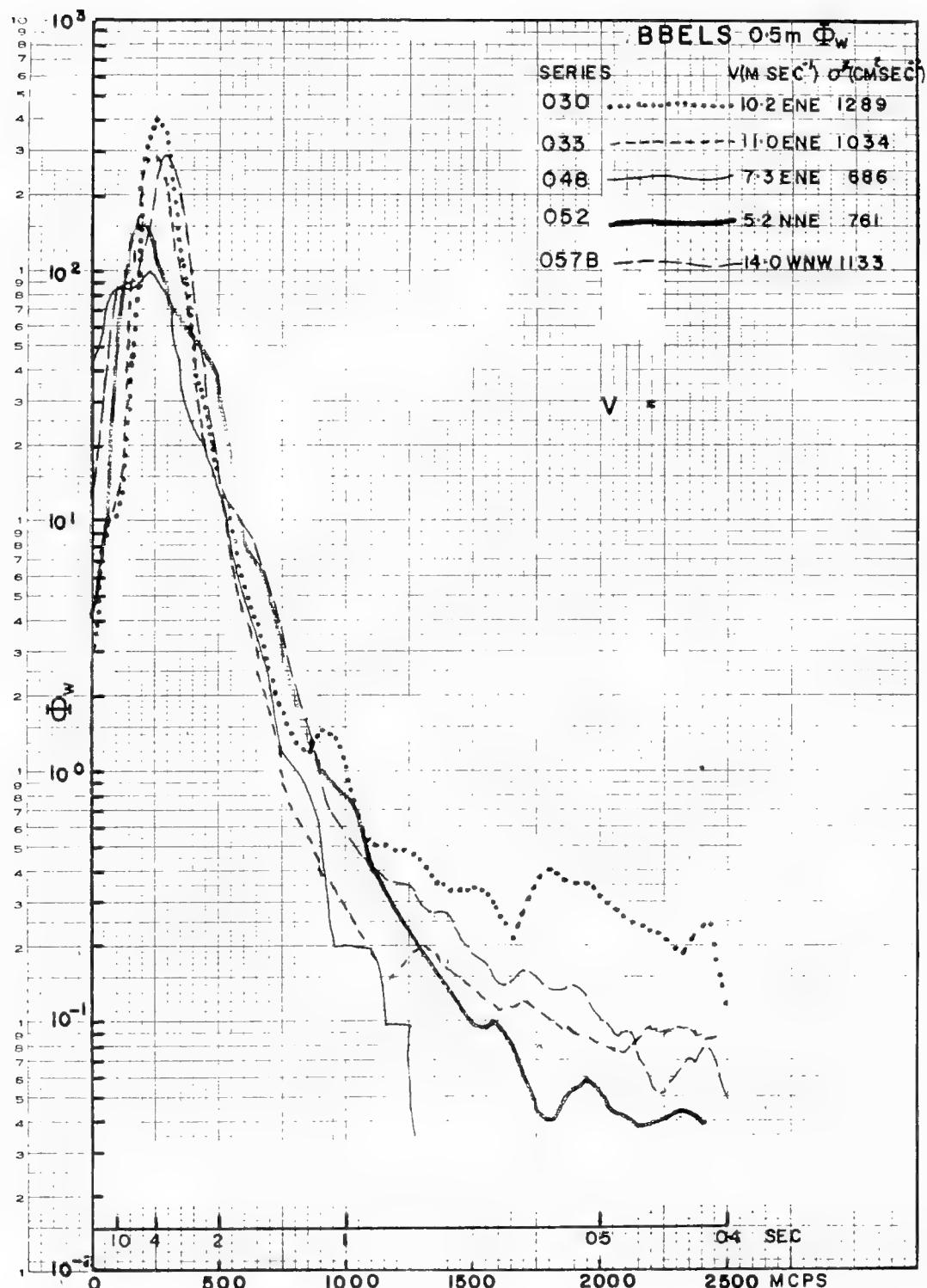
Auto-Spectra of Vertical Velocity at Various Wind Conditions (BBELS-II, 0.5 m).

Figure V-35

Since the high frequency region of the auto-spectrum was of primary interest, the values of Φ_w (listed in the appendix B) were averaged over 50-mcps increments from 250 to 1000 mcps. Weighted values of the spectral energy were then plotted (figure V-36) as a function of frequency (following the method of Burling, 1959). The weighting is in terms of various powers of the frequency (f^n). The curves indicate that the slope of Φ_w for $250 \lesssim f \lesssim 1000$ mcps appears to vary as f^{-5}, since:

$$\left[\Phi_w\right] f^5 \cong \text{CONSTANT.} \qquad (V-29)$$

Another group of BBELS-11 observations were examined for the f^n slope relationship - the average spectra for serial 048, 052, 054, 057A, 057B, and 058. These observations were at 0.5 meter depth between 2009 hours on 29 March and 1137 hours on 30 March 1965. The winds varied over this period from 7.3 m sec^{-1} ENE to 14 m sec^{-1} WNW. Examination of the spectral plots in appendix B shows a similarity in the values of Φ_w between 300 mcps and 1500 mcps and in the up-frequency slope of the function. Figure V-37 shows the average auto-spectra (weighted by f^n) as a function of frequency. The curve for Φ_w f^5 (triangles) appears to be quite independent of frequency over the range from 400 mcps to 1300 mcps. A slight rise in the curve beyond 1300 mcps indicates, perhaps, a transition.

The wave particle motion spectra display a clear functional relationship to frequency which is similar to that of the free surface spectra Φ_η . The concept of the equilibrium range of spectra can now be further examined in the light of these findings.

Consider the visible phenomena of wave generation. When the wind blows over calm water, the first response in the sea surface is the production of high frequency capillary waves having wave lengths of a few millimeters. In a rather continuous manner, progressively larger waves are formed, which become less and less governed by surface tension forces, but tend to propagate in response to gravity. At any given instant during this wave generation process, an auto-spectrum may be associated with the wave motions. The spectrum is continuously changing with time, since the process, at this stage, is not stationary. With time, the maximum energy peak gradually moves down-frequency. For a given wind speed and other associated parameters, a stabilization now occurs within a certain frequency range. Within this certain band no more energy can be permanently added; i.e., it has become saturated.

Figure V-38 shows an idealized auto-spectrum of the free surface variable Φ_η or the wave velocity component $\Phi_{u,w}$. The two peaks associated with swell and wind waves are shown at f_{ms} and f_{mw}, respectively. The equilibrium range is divided into the inertial subrange and the dissipation range. The dissipation range is associated with the high frequency turbulence visualized as small scale eddies and white caps. All wave energy is eventually dissipated in this range, either by breaking waves in the open sea or by the formation of breakers on the
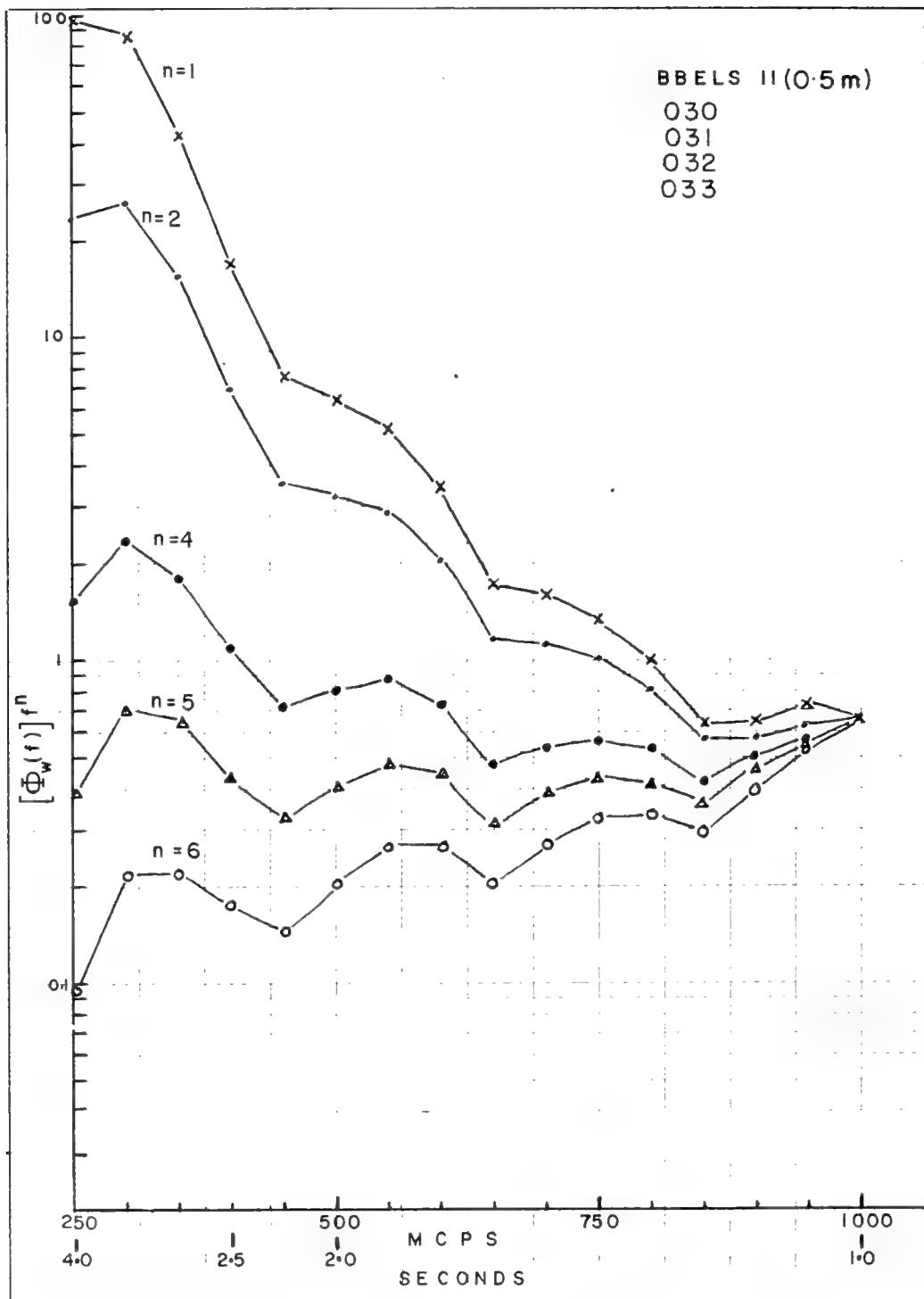
Individual Auto-Spectra from BBELS-II Data (Weighted by F^n) as a Function of Frequency.

Figure V-36
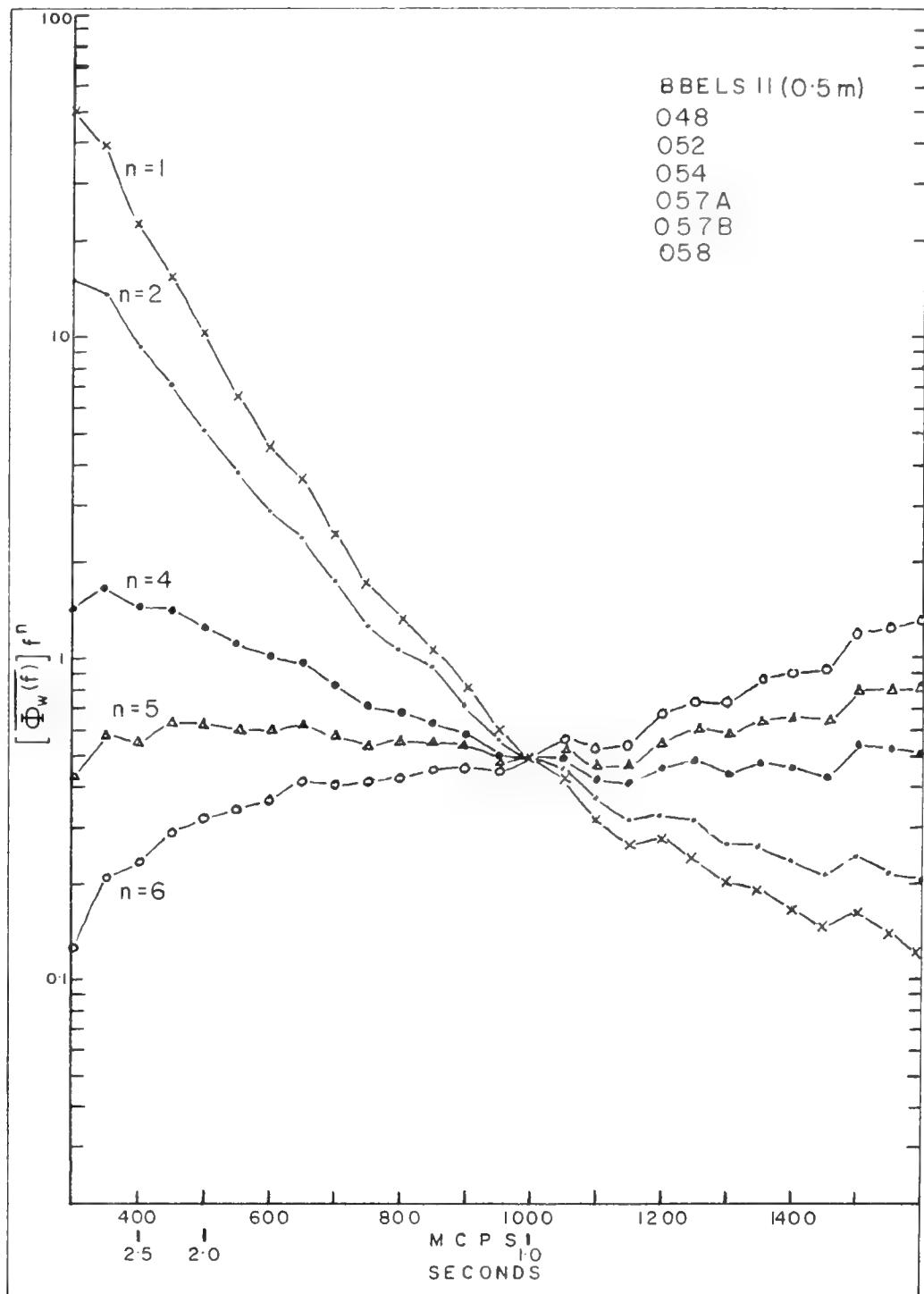
An Average Auto-Spectrum from BBELS-II Data (Weighted by F^n) as a Function of Frequency.

Figure V-37
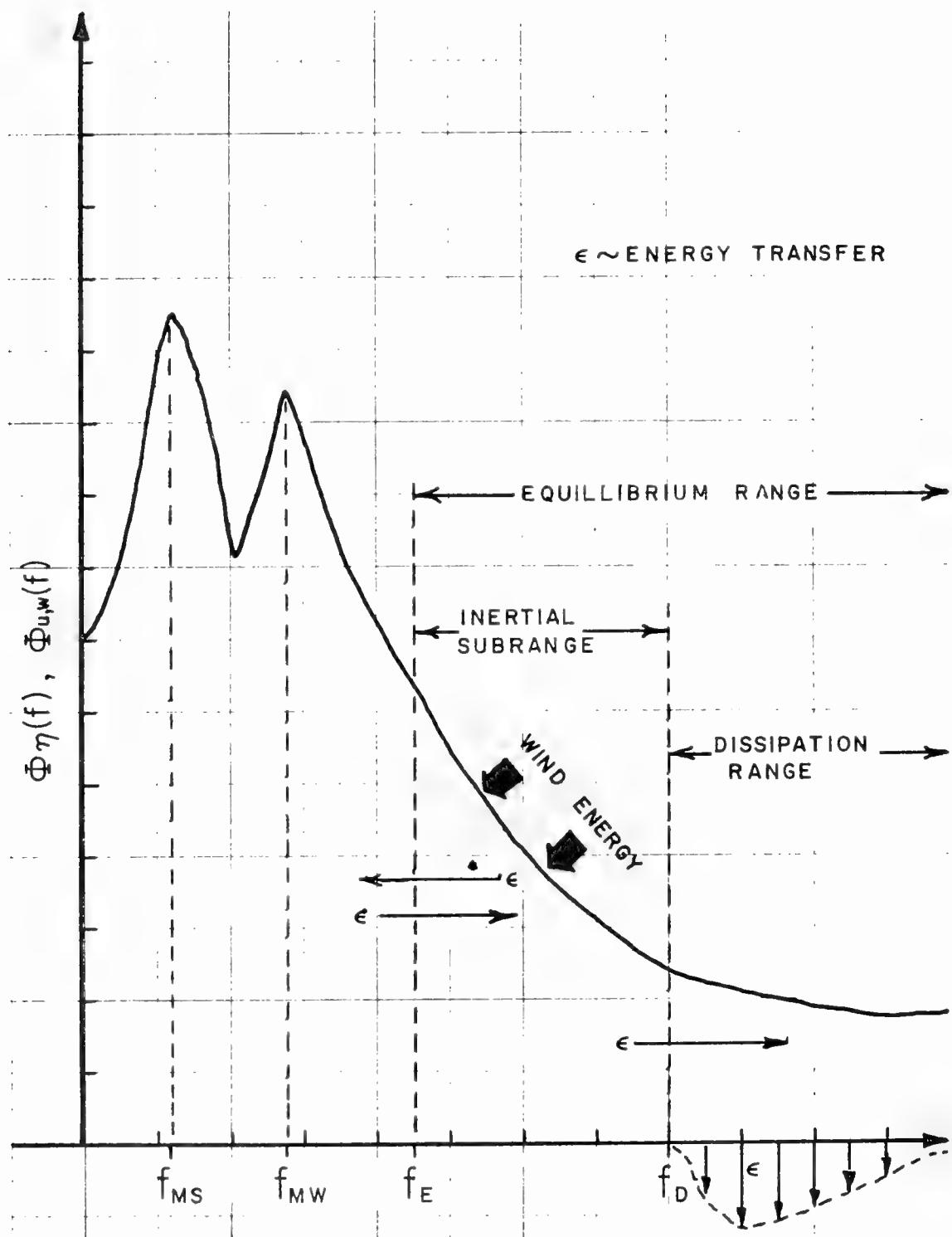
Idealized Wave Spectrum Displaying Various Spectral Ranges.

Figure V-38

beach. The inertial subrange is the frequency domain containing the wave motions most closely associated with the response of the sea surface to the wind stress. Thus, the inertial subrange can be thought of as a window (analogous to the green house effect) where wave energy is channeled into the system. Saturation occurs when waves of frequencies f (where $f_E \leqslant f \leqslant f_D$) attain the maximum height and slope. Then, because of purely physical properties of the water responding under gravity, breaking occurs, providing a new flow of energy into the dissipation range ($f_D \lessdot f$).

On the other hand, there is a continuous flow of energy from the inertial subrange to lower frequencies. This transfer has been aptly termed a "red shift" phenomenon by Starr (1961). Starr shows that wave energy tends to move down-frequency because of the inter-relationship of the rate of transport of wave momentum with respect to energy. Evidence of this red shift phenomenon is obvious in the ocean. The previously mentioned transition from smaller (higher frequency) to larger (lower frequency) wind waves and, of course, the occurrence of swells generated from wind waves: both manifestly exhibit the transfer of wind energy through wind waves into low frequency swell.

It is the wave motions governed by gravity that are capable of projecting energy to lower frequencies; i.e., energy in the inertial subrange. Motions in the turbulent dissipation range or in the capillary wave range, which are governed by viscosity and surface tensions, do not contribute energy to lower frequencies. For example, capillary waves observed on the surface of the ocean (i.e., the cat's paws) vanish almost immediately as the puff of wind subsides. On the other hand, it is suggested (but not proven) that, when swells enter a region of fresh wind blowing in the same direction as the swells, they do not directly gain wind-imparted energy within the frequency band of the swells. This would be an important measurement to make, since it would further justify the existence of an equilibrium range of energy.

Munk (1947) suggested that certain phenomena associated with the air-sea interface, such as wave structure and white caps, wind stress estimates, sea gull soaring, and evaporation data, seemed to point out discontinuities at a critical wind speed of about 7 m sec^{-1}. He also considered theoretical evidence related to the Kelvin Helmholtz stability criteria (Thompson, 1871), and predicted instability for winds exceeding 6.5 m sec^{-1}. Munk alludes to the point at which cresting occurs as the transition point. Beyond this point the quasi-laminar stable boundary flow of air over the water is eradicated by the onset of air turbulence at the sea surface, which is reflected by similar turbulent and breaking conditions in the surface of the water.

The very nature of an equilibrium range is the embodiment of a true non-linear process; i.e., the interaction of motions of different frequencies to effect energy transfer as depicted in figure V-38. If the wave generating process were viewed as a linear system; then, as energy is added to each frequency component, this component would grow independently of adjacent frequency ranges. In this case, the function associated with the wave process could be represented by the infinite series given by equation (III-1). But the observed phenomena of
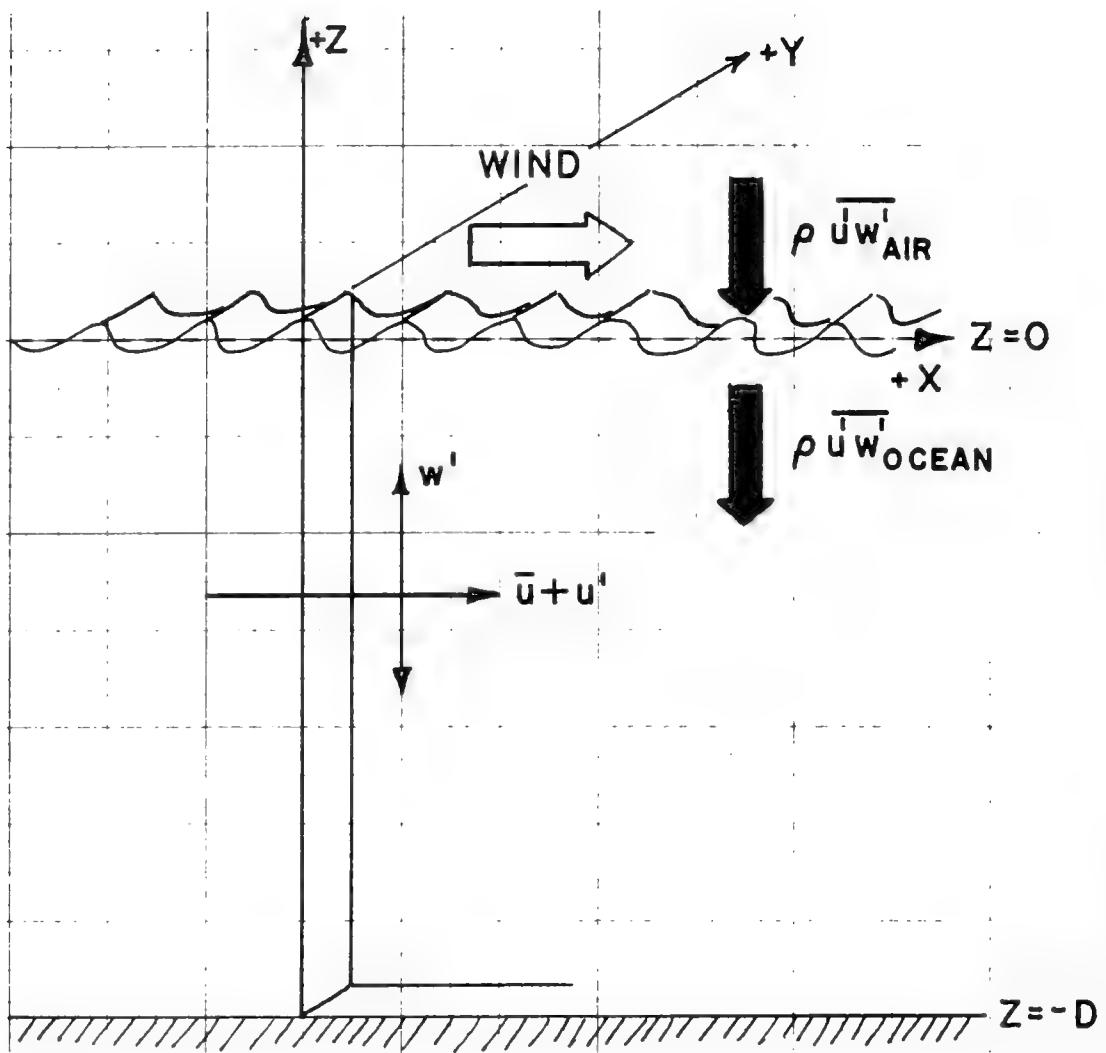
Schematic Diagram of Air–Ocean Interaction Phenomena.

Figure V-39

wave generation indicate that a linear system is not very well suited to describe the energetics of wind waves.

Reynolds Stresses in Ocean Waves

Certain quantitative features of the dynamic energy content of the surface layer have been depicted through analysis of the wave meter observations. Space variable and time variable distributions of turbulent kinetic energy and their accompanying spectra have been portrayed and associated with wind wave conditions. A more important and more difficult question remains to be considered. What deductions can be made regarding momentum and kinetic energy transport through and within the regime of the ocean surface wave motions?

Consider first the application of Eulerian wave particle velocity measurements in describing the momentum flux within the dynamic regime of wind wave motions. A simple intuitive model can be used to consider the flow of momentum. Assume a volume of ocean bounded at the surface by $Z = \overline{\eta}(t) = 0$ and at the bottom by $Z = -D$, and having a unit width in the Y direction. Assume also a steady wind that generates wind waves in the positive X direction as shown in the figure V-39. The wind blowing across the surface exerts a mean stress on the water. Now a mean stress can occur only if there is a mean vertical shear of horizontal velocity between the wind and the water surface. Likewise, the stress exerted at the surface must couple with the subsurface water, giving rise to a mean velocity gradient and an internal flow of horizontal momentum.

What then are the dynamics of motion occurring at a point just below the surface waves that are being subjected to the stress of the wind? Assume, at this point, that a Reynolds stress does exist, given by:

$$\tau = -\rho \overline{u'w'} \; ; \tag{V-30}$$

where ρ is the density of sea water, which is assumed constant.

The Reynolds stress function may be interpreted in two ways: as the time averaged horizontal shear stress or force existing across a unit horizontal area, or as a downward flow of horizontal momentum through a horizontal unit area per unit time.

Thus, assuming the proper measurement of u' and w' at a given point, the Reynolds stress delineates the shear stress, and hence the direction and magnitude of the flow of momentum imparted at the sea surface.

To better visualize this, consider a thin horizontal slab, of thickness δz and of unit width in the Y direction, situated within the water volume (see figure V-39). If $-\rho \overline{u'w'}$ is the momentum flux per unit horizontal area, then

$$- \frac{\partial}{\partial z} \rho \overline{u'w'} \, \delta z$$

represents the net force per unit area acting in the horizontal direction on the slab.

If the slab is moving in the X direction at a velocity $\bar{u}$, then

$$- \bar{u} \frac{\partial}{\partial z} \rho \, \overline{u'w'} \, \delta z \qquad \text{(V-31)}$$

represents the work done on the slab per unit area per unit time.

It follows that

$$- \bar{u} \frac{\partial}{\partial z} \rho \overline{u'w'} \qquad \text{(V-32)}$$

is the time rate of work on a unit slab by stresses per unit horizontal area.

For a finite volume

$$- \int_{z_1}^{\bar{\eta}} \bar{u} \frac{\partial}{\partial z} \rho \, \overline{u'w'} \, dz \qquad \text{(V-33)}$$

represents the rate of work done on the slab of thickness z_1 bounded on the top by the free surface ($\bar{\eta} = 0$) and on the bottom by the plane z_1 (a constant). Integral (V-33) may be written as:

$$- \int_{z_1}^{0} \frac{\partial}{\partial z} \bar{u} \, \rho \overline{u'w'} \, dz + \int_{z_1}^{0} \rho \overline{u'w'} \frac{\partial \bar{u}}{\partial z} \, dz \; . \qquad \text{(V-34)}$$

Integrating the first term directly gives:

136

$$+\bar{u}\, \rho \overline{u'w'}\Big|_{z_1} \; - \; \bar{u}\, \rho \overline{u'w'}\Big|_{z=0} \; + \; \int_{z_1}^{0} \rho \overline{u'w'}\, \frac{\partial \bar{u}}{\partial z}\, dz \qquad . \qquad (V\text{-}35)$$

$$\underset{A}{} \qquad\qquad \underset{B}{} \qquad\qquad \underset{C}{}$$

Terms A and B represent the transfer of mean flow kinetic energy derived from the stress on the upper and lower boundaries. Term C is the rate of transformation of kinetic energy of turbulent motions into or out of the mean flow energy.

The physical interpretation of equation (V-35) is illustrated by figure V-39. The first two terms represent the transfer of mean flow energy at the mean free surface $Z = \bar{\eta} = 0$ and at $Z = Z_1$. Term A would normally vanish for Z_1 values below the wave motion regime, since the u' and w' values diminish rapidly with depth. If $Z_1 = -D$ (i.e., at the bottom), the interaction of the mean flow with the bottom roughness elements could provide a disturbance of the flow, but $\bar{w}'$ in term B would essentially vanish. By evaluating the mean motion and the Reynolds stresses at the levels $Z = 0$ and $Z = Z_1$, one can determine the net flux of mean energy through these boundaries.

Equation (V-35) is derived directly from the Navier-Stokes equations for turbulent flow (see appendix A). Other terms, which are brought about by the viscous effects, can be neglected. In the absence of mean motion and, similarly, in the absence of a mean shear, no energy can be transferred from the boundaries.

It can therefore be argued that in a motionless volume of water subject to a surface wind stress, the surface, being a fluid, must in time respond to this stress, giving rise to some sort of a mean flow. This vertical distribution of the stress and mean flow are the determining factors controlling the amount of turbulent energy transformed into (or out of) the mean flow. Thus, the increase of mean flow energy supplied by terms A and B in equation (V-35) will, in time, force an increase in the shear $\partial \bar{u}/\partial z$ in term C. This term may then increase in magnitude until it approximately balances the influx terms A and B. The result is a steady state condition, where incoming mean energy at the boundaries is converted to eddy or wave energy.

The magnitude and direction of the stress-induced mean motion is usually smaller than the motions of tides or gross geostrophic flows. This explains the sparsity of pure wind-induced current measurements. A system such as the Gulf Stream may also gain mean kinetic energy and momentum from the contributions of the air/sea boundary stress which has been integrated over large portions of the ocean during long periods of prevailing winds through horizontal processes.
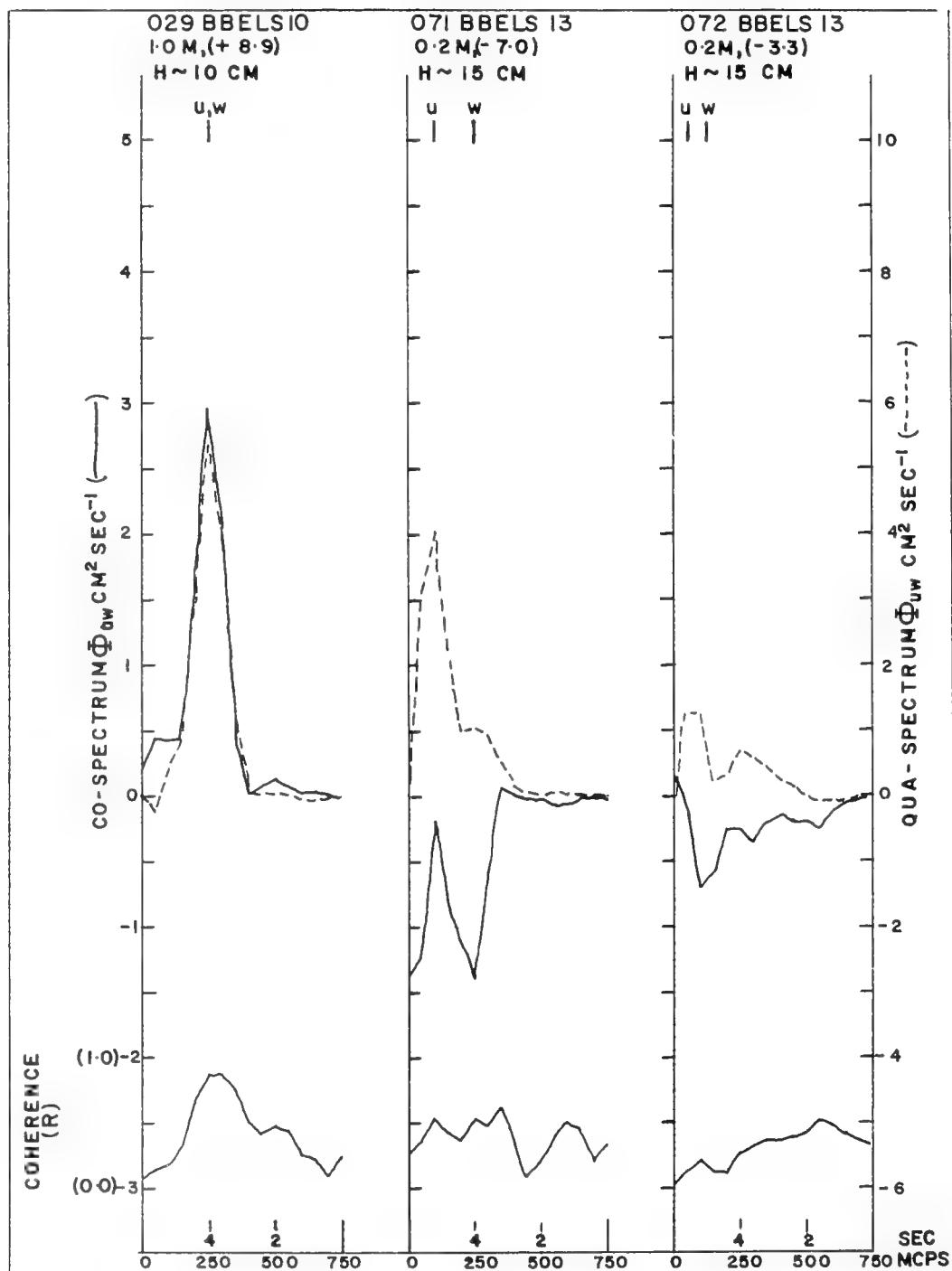
Cross-Spectra and Coherence for Serial 029, 071, and 072.

Figure V-40

Covariances and Cross Spectra of Wave Motions

As discussed in chapter III, estimates were made of the covariances and cross spectra of the u and w components of speed measured with the OMDUM II and OMDUM III wave meter systems. All statistics are listed in table IV-3.

The u and w data obtained with the OMDUM III system are more reliable because the system was subjected to a relatively thorough calibration and was used with the most stable suspension available (see table V-1).

Table V-3 summarizes the u, w BBELS observations obtained with the OMDUM III system. In these measurements, the u and w vector components lie in the vertical plane normal to the crests of the wind waves (as depicted in figure II-10). Listed in this table are: depth D, mean horizontal velocity $\bar{u}$, covariance $(\overline{u'w'})$, linear correlation coefficient r, wind speed V, and estimated maximum wave height H.

In table V-3 there is a relatively wide range of values of $\overline{u'w'}$, from +27.5 to -162 cm^2 sec^{-2}, the algebraic mean being -25.3 cm^2 sec^{-2}. Of the 28 records, 19 covariances were negative.

The magnitudes of the covariances seem to vary directly as the wind speed and wave height. The light winds and small waves occurring during BBELS-10 and BBELS-13 (071 and 072) observations are associated with relatively small covariances, whereas high winds and large waves occurring later during BBELS-13 (077 through 086) give generally large covariances.

There is also an indication that the covariance for given sea conditions decreases with depth. Attenuation of $\overline{u'w'}$ with depth is indicated in serial 102 through 110, but this relation is rather tenuous with regard to the other series.

The mean values $\bar{u}$ range from +37 to -26 cm sec^{-1}. The covariances do not appear related to either the magnitude or the sign of $\bar{u}$.

Statistics on the cross spectra of the u and w observations include both covariance spectra (co-spectra, abbreviated C_{uw}) and quadrature spectra (qua-spectra, abbreviated Q_{uw}). Listings of these data, together with the coherence R and phase angle PHI, are given in appendix B.

Representative co-spectra and qua-spectra from the observations listed in table V-3 are shown in figures V-40, V-41 and V-42. The co-spectrum axis is located on the left and the qua-spectrum axis on the right of the figures. The solid and broken lines represent C_{uw} and Q_{uw}, respectively. For convenience, the Q_{uw} scale is twice the magnitude of the C_{uw} scale.

Beneath the cross spectra is a plot of the coherence R. This quantity is the square root of the function defined by equation (III-29). Above each plot is the depth of the OMDUM III, the signed value of the covariance $(\overline{u'w'})$, and the
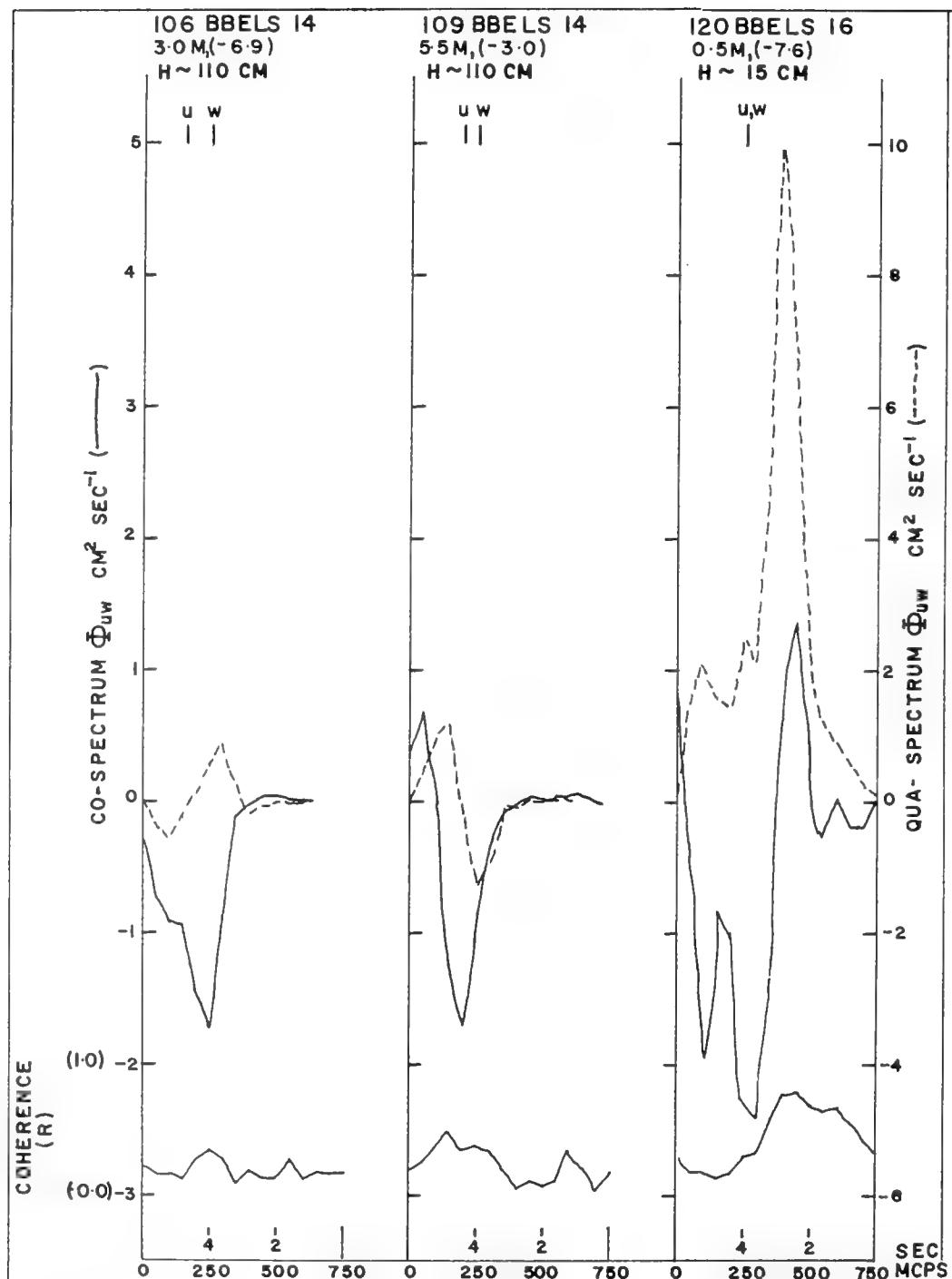
Cross-Spectra and Coherence for Serial 106, 109, and 120.

Figure V-41
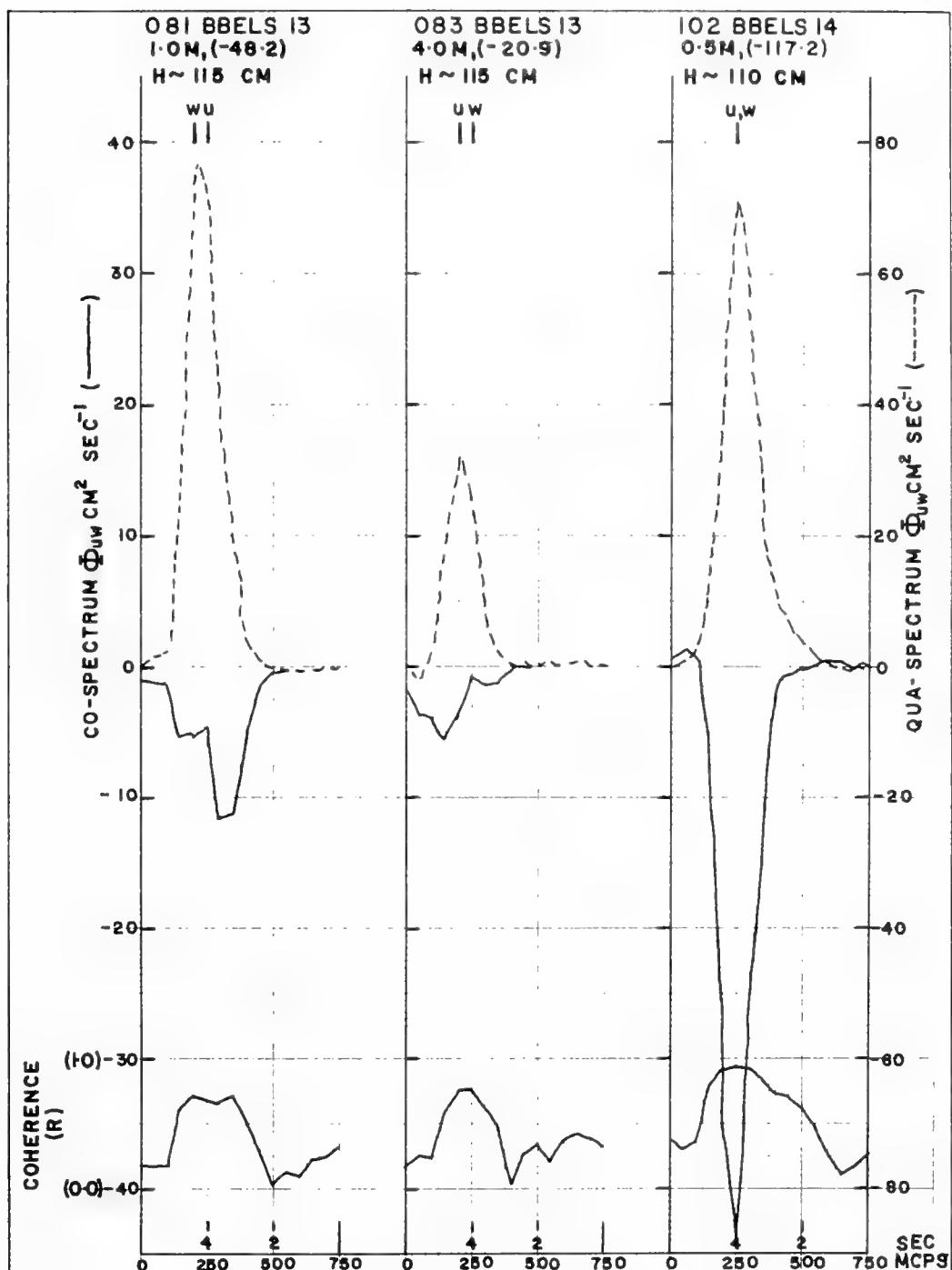
Cross-Spectra and Coherence for Serial 081, 083, and 102.

Figure V-42

Table V-3. Covariances and Supplementary Data Obtained
with OMDUM III System

Serial	Depth m	ū cm sec^{-1}	$\overline{u'w'}$ cm^{2}sec^{-2}	r	V m sec^{-1}	H cm
BBELS-10						
026	0.5	-26	+5.4	+0.1	1.8	10
027	3.0	-26	+0.8	+0.05	0.5	10
028	3.0	-18	+3.0	+0.14	0.5	10
029	1.0	-19	+8.9	+0.25	1.0	10
BBELS-13						
071	0.2	+5	-7.0	-0.14	4.4	15
072	0.2	+9	-3.3	-0.08	5.4	15
077	1.0	+20	-68.8	-0.20	17.2	110
078	1.5	+20	+23.2	+0.07	15.0	110
079	2.5	+16	+20.2	+0.11		110
080	2.5	+14	+27.5	+0.18	16.7	110
081	1.0	+11	-48.2	-0.12	18.2	115
082	1.0	+12	-87.3	-0.16	18.2	115
083	4.0	-14	-20.9	-0.11	16.0	115
084	4.0	-11	-29.9	-0.12	12.2	115
085	4.0	-5	-41.9	-0.15	12.2	115
086	4.0	-5	+3.2	+0.03	8.0	70
BBELS-14						
099	1.0	-19	-21.8	-0.10	7.0	110
101	0.0	+30	-162	-0.33	8.0	110
102	0.5	+31	-117.2	-0.36	8.0	110
103	1.0	+36	-78.0	-0.36	8.0	110
104	1.5	+37	-49.7	-0.38	8.0	110
105	2.5	+16	+20.2	+0.11	9.5	110
106	3.0	+19	- 6.9	-0.13	9.5	110
107	3.5	+30	-36.1	-0.49	9.5	110
108	4.5	+23	-19.1	-0.40	11.5	110
109	5.5	+18	- 3.1	-0.10	11.5	110
110	6.5	+31	-11.5	-0.36	11.5	110
BBELS-16						
120	0.5	-20	- 7.6	-0.06	4.2	15

approximate wave height H. The vertical bars with the letters u and w or u, w indicate the positions of the auto-spectra of the particular u, w pair (given in appendix B).

The cross spectra in figures V-40 and V-41 are representative of measurements made either near the surface during low sea state conditions (serial 029, 071, 072, and 120), or at depth during higher sea states (serial 106 and 109). Thus, the cross-spectral densities and the accompanying covariances have relatively small values. The data of serial 081, 083, and 102 (figure V-42) are derived from more intense wave conditions, and are associated with larger negative spectral densities and covariances.

Linear cross-spectral scales were used to avoid the difficulty of plotting curves having both positive and negative values on a logarithmic axis. These curves indicate that most of the cross-spectral energy is concentrated below 500 mcps (above 2 sec period).

The low energy observations in figures V-40 and V-41 show covariances ranging from +8.9 cm^2 sec^{-2} to -7.6 cm^2 sec^{-2}. These values are equivalent to the area between the curve (solid line) and the zero axis.

In general, the C_{uw} curves attain a maximum absolute value at a similar frequency position as the auto-spectra peaks. In the case where the covariance is negative, the C_{uw} peak is negative, and similarly for a positive covariance (see serial 029). The Q_{uw} curves in figures V-40 and V-41 tend to vary in their relationship with the curves of C_{uw}. Thus, serial 071, 072 and 106 indicate a quasi-mirror image relationship between Q_{uw} and C_{uw}; whereas serial 109 and 120 seem to display the C_{uw} peak shifted from the Q_{uw} peak. The coherence R displays maximum values at or near the indicated cross-spectral peaks. The stronger the cross-spectrum peaks, the greater is the magnitude of R.

Figure V-42, which displays the cross-spectra of higher energy wave systems, shows a much more clearly defined spectrum relationship. Both C_{uw} and Q_{uw} peak at the same frequencies as the auto-spectra. The Q_{uw} spectra show a much larger peak magnitude than the C_{uw}. The coherences corroborate the energy concentration at these wave frequencies, attaining values from 0.70 to 0.95. In general, the higher energy waves have clearly defined cross-spectra, whereas the low energy records exhibit small cross-spectral peaks and unstable patterns. A slight shift between the peaks of C_{uw} and Q_{uw} is shown by all cross-spectra except serial 029 and 102.

The co-spectra from the BBELS data are similar to the data from Narragansett Bay shown in figure IV-2. Although not shown, the Q_{uw} for the Narragansett Bay data also peaked strongly at the ambient wave frequency indicated by the auto-spectra.

The Q_{uw} function registers the degree of out-of-phase spectral energy associated with u and w (see chapter III). If the u and w velocity components were represented by a sin σt and a cos $\sigma' t$, respectively, then C_{uw} would be 0

for all frequencies, and Q_{uw} would display a maximum peak at the wave frequency σ^z . Thus, the tendency for a strong qua-spectrum is to be expected for ocean waves. The co-spectra C_{uw} should, on the other hand, be suppressed greatly. The large (and in general negative) covariance functions is indicative of a strong correlation between the u and w motions of the frequencies of the ambient wind waves.

The causes of the covariances and of the strong co-spectra of the u and w wave motions are difficult to assess. The covariances and cross-spectra are extremely sensitive to real (wave-induced) or artificial (instrument-induced) correlations. It is therefore desirable to examine possible sources (natural and artificial) which could contribute to the measured covariances of the wave motions.

Wave Models and Their Covariance Properties

A simple mechanism for transfer of wind-imparted horizontal stress or momentum downward through the wave regime was suggested earlier in this chapter. Such mechanisms are likely to be associated with the gross motions of the wind waves (see Shonting, 1964).

Results of the u,w observations have been presented in which relatively large (and generally negative) covariances were obtained. It is evident that instrument bias could contribute, at least partially, to the covariances. This biasing phenomena can be examined by constructing some artificial wave models.

It is instructive to consider some mechanisms associated with wave motions likely to exhibit covariance properties. Examine first the simplest motions of fluid particles moving in circular orbits in a progressive wave moving past a fixed point. Assuming that these waves are deep water waves, then the equations for the horizontal and vertical motions are given by (II-5) and (II-6). These may be rewritten as:

$$u' = A_z \cos \sigma t, \tag{V-36}$$

and

$$w' = A_z \sin \sigma t. \tag{V-37}$$

Here $A_z = \frac{H}{2} \sigma e^{kz}$

in equations (II-5) and (II-6); and $\sigma = 2\pi T^{-1}$, where T is the period of oscillation.

According to equation (III-24), the covariance of u' and w' is:

$$\overline{u'w'} = \frac{A_z^2}{T} \int_{-T/2}^{T/2} \cos\sigma t \, \sin\sigma t \, dt \, . \qquad \text{(V-38)}$$

This integration is represented graphically in figure V-43A (upper diagram). As shown by the shaded area beneath the time variable curve of $\overline{u'w'}$, the value of $\overline{u'w'}$ is zero when averaged over an integral number of wave periods or for a long record.

In the case of intermediate or shallow water waves, the orbits are elliptical, with the semi-minor and semi-major axes parallel to the Z and X axes, respectively. However, both the elliptical and the circular velocity functions have zero co-variances. Thus, the classical progressive wave, according to equation (V-30), has associated with it a zero Reynolds stress.

Turning now to consider a slightly different model, suppose that orthogonal wave motion components, measured at a fixed point, can be described by:

$$u' = A_u \cos\sigma t \, , \qquad \text{(V-39)}$$

and

$$w' = A_w \sin\left(\sigma t + \Delta\phi\right) \, . \qquad \text{(V-40)}$$

Here $\Delta\phi$ is a small phase shift between the orthogonal velocity components. The new covariance is given by:

$$\overline{u'w'} = \frac{A_u A_w}{T} \int_{-T/2}^{T/2} \cos\sigma t \, \sin(\sigma t + \Delta\phi) \, dt \, . \qquad \text{(V-41)}$$

Using trigonometric identities, this becomes:

$$\overline{u'w'} = \frac{A_u A_w}{2T} \int_{-T/2}^{T/2} \left[\sin(2\sigma + \Delta\phi) + \sin\Delta\phi\right] dt \, , \qquad \text{(V-42)}$$
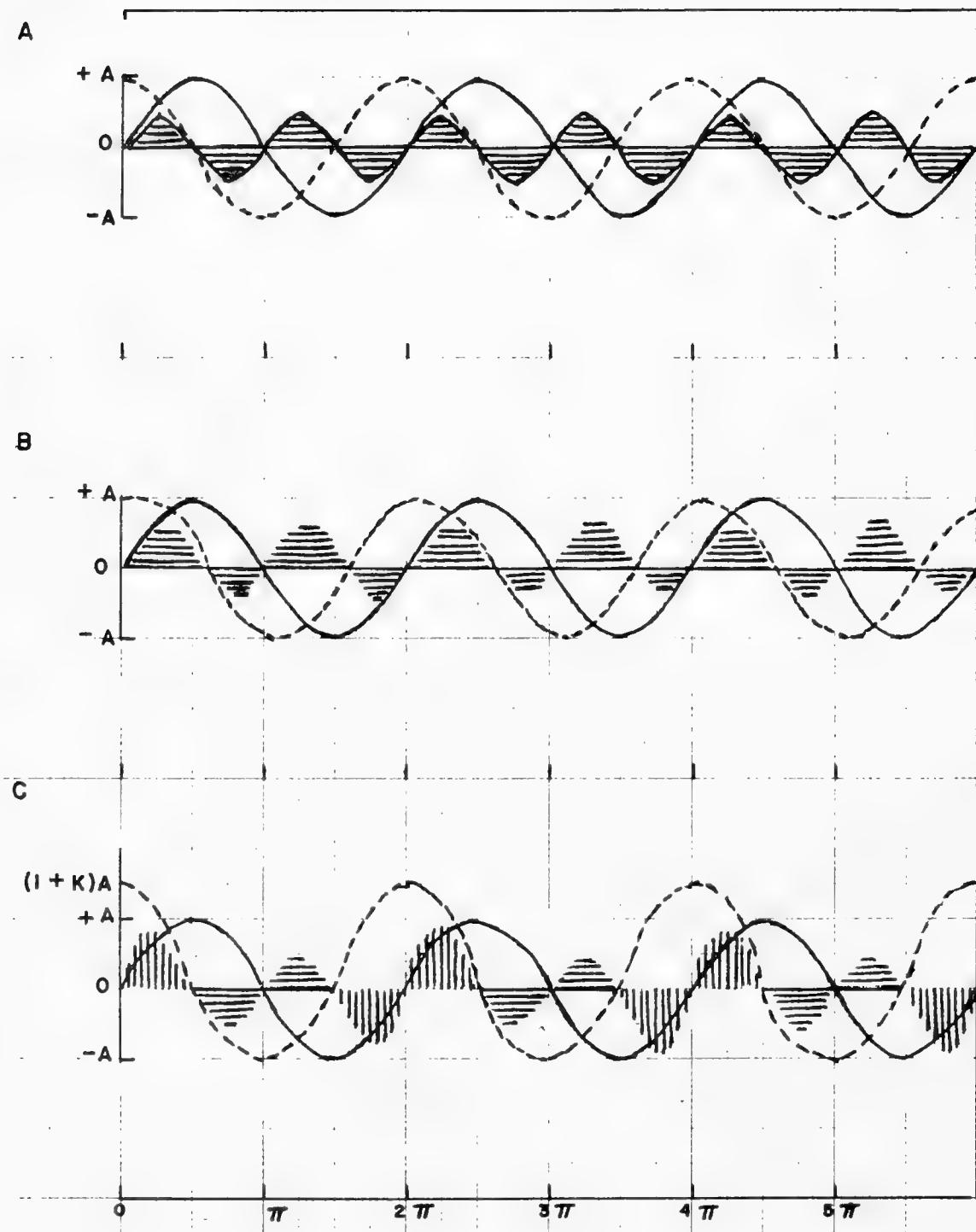
Illustration of Graphical Integrations.

Figure V-43

$$\text{or} \qquad \overline{u'w'} = \frac{A_u A_w}{2} \, \text{SIN} \Delta\phi. \qquad (V\text{-}43)$$

This integration is graphically shown in figure V-43B (middle curve) where the shaded areas above and below the abscissa sum to a non-zero value. For this phase-shifted model, the Reynolds stress term $-\rho\overline{u'w'}$, from equation (V-43), is proportional to the products of the amplitudes of the velocity functions and of the sine of the phase angle shift. The sign of the angle $\Delta\phi$ (i.e., the phase lead or lag) determines the sense of the stress.

It was assumed that $A_u = A_w$. Reynolds stresses were then calculated for various amplitudes of the orthogonal velocity functions and various values of $\Delta\phi$. In figure V-44 the stress $-\rho\overline{u'w'}$ (in dyne cm^{-2}) is plotted on the ordinate, and the phase angle $\Delta\phi$ on the abscissa. Some suggested wave parameters are given. The values of A from 20 to 60 cm sec^{-1} are representative of the amplitudes experimentally observed for the wide variety of wind and sea conditions. For example, the larger u or w variances (see figures V-26 and V-27) near the surface are of the order of 1200 cm^2 sec^{-2}. If the velocity functions were purely sinusoidal, as in equation (V-37), then the variances would be of the form:

$$\sigma_w^2 = \frac{1}{T} \int_{-T/2}^{T/2} A^2 \, \text{SIN}^2 \sigma t \, dt \, , \qquad (V\text{-}44)$$

$$\text{or} \qquad \sigma_w^2 = \frac{A^2}{2} .$$

For $\sigma_w^2 = 1200$ cm^2 sec^{-2}, A $\cong$ 49 cm sec^{-1}.

It is obvious from this that extremely large stresses can be associated with a relatively small phase shift between orthogonal velocity components.

The results of some of the LIMDUM I measurements have already been discussed, along with the vertical "spatial correlation" of similar velocity components. Covariance functions are also tabulated in appendix B for the LIMDUM I data for parallel u or w pairs. The covariances $\overline{u'_1 u'_2}$ or $\overline{w'_1 w'_2}$ are always very large and positive because the similar wave components at the two depths are almost in phase. The associated correlation coefficients are likewise large and positive; however, they show a reduction in magnitude with depth.

Since the LIMDUM I system registers the instantaneous velocities of u_1 and u_2 or w_1 and w_2, it is possible to examine the data pairs for a phase shift

REYNOLDS STRESS $-\rho \overline{u'w'}$

WHERE;

$u = A \sin \omega t$

$w = A \cos(\omega t + \Delta \phi)$

AND

$\omega = \frac{2\pi}{T}$

$T = 4.0$ SEC

$\rho = 1$ GM CM^{-3}

$A =$ AMPLITUDE CM SEC^{-1}

A= 60 CM SEC^{-1}

A = 50 CM SEC^{-1}

A = 40 CM SEC^{-1}

A = 30 CM SEC^{-1}

A = 20 CM SEC^{-1}

STRESS DYNE CM^{-2}

$\Delta \phi$ DEGREES
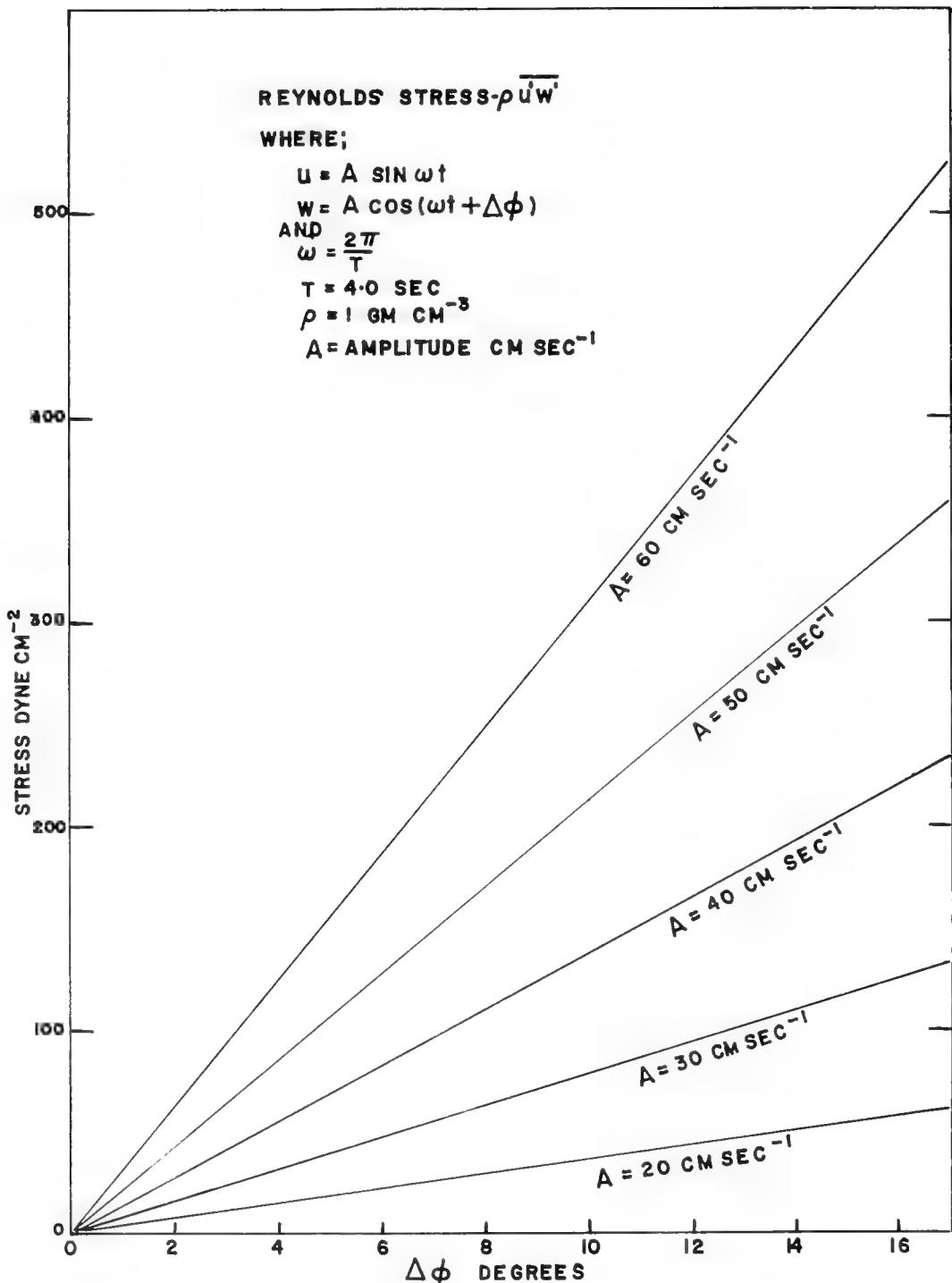
Reynolds Stress as a Function of Phase Angle.

Figure V-44

between the two velocity fluctuations. What, if any, is the significance of a phase lag or lead between two vertically separated velocity fluctuations within the wind wave regime? In a discussion by Starr (1948), it is suggested that poleward transfer of angular momentum is associated with horizontal velocity correlations. Velocity patterns which can perform this function are schematically shown in figure V-45A. These quasi-sinusoidal wave forms exhibit a northeast-southeast tilt of the trough lines of isobars (which approximate the wind stream-lines). Integration of the quasi-instantaneous u'v' around a latitude circle would give a spatially averaged value of $\overline{u'v'}$, interpreted as a net northward transfer of eastward momentum (i.e., $\rho\ \overline{u'(v)}$).

Starr (1961) also considers the possibility that such tilted troughs in the relative streamlines associated with wind waves may produce a downward momentum transfer. Figure V-45B shows a vertical section of an ocean wave (in the XZ plane) in which the wave is propagating in the +x direction. The instantaneous material surfaces or relative streamlines are shown as a function of depth. Since the waves travel at a constant speed without change in shape, a steady state picture may be obtained by the superposition of the phase speed (from left to right) on all water particles. This addition of a uniform velocity field does not interfere with the dynamic properties of the system (see further, Starr, 1945). The wavy lines represent the steady state streamlines relative to the moving wave. These can be interpreted in a manner analagous to the previous diagram and show a net downward transport of the downwind momentum. The significant feature is that a phase advance with depth is required to bring about this transport.

The spectral analyses of all LIMDUM I data provide phase angle data (PHI) as a function of frequency. These are tabulated in appendix B. If the order of tabulation is u_1 (or w_1) followed by u_2 (or w_2), then PHI gives the average phase angle lead of the latter over the former. (Note that in some cases, the order is reversed - u_2 followed by u_1. The PHI must then be multiplied by a minus sign.)

The values of PHI near the peak frequencies of either the auto-spectra or the coherence plots were examined for any indication of spatial phase lead by the dominant motions as a function of depth. Unfortunately, the PHI relation-ships show nearly an equal number of positive and negative values. In fact, the values appear disturbingly random in both sign and magnitude; hence, no con-clusions can be made regarding the phase evaluation.

The tilting phenomenon can also be considered with respect to the elliptical orbital motion depicted in figure V-45C. The top of the semi-major axis is tilted slightly backward. Since the wave is progressing, the Eulerian time variation is that of a vector forming an elliptical pattern, with a negative co-variance $\overline{u'w'}$ produced. To show this, simply integrate across a surface from A to B. The net value of $\overline{u'w'}$ is negative, indicating downward transport of ($\rho\ u'$). Note that such a tilted ellipse provides a variance of the w velocity component that is larger than the u variance. This is in accordance with what was found experimentally.
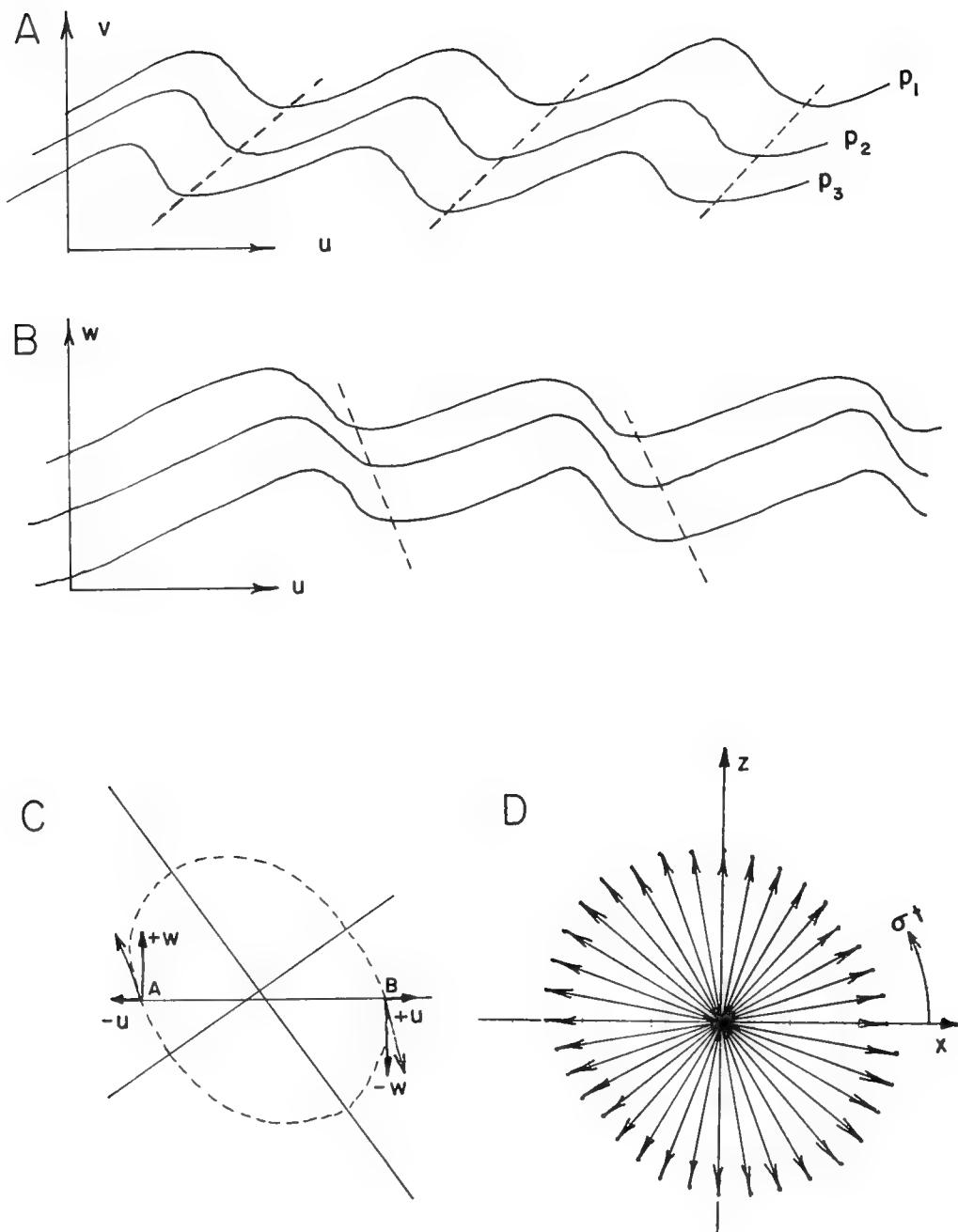
Schematic Wave Models.

Figure V-45

Using equations (V-39) and (V-40) to calculate the magnitude r of the vector having u' and w' components, given as

$$\left[u'^2 + w'^2\right]^{1/2} = f(\sigma t)$$

and plotting the vector magnitude r (σt) over one wave period, one obtains a quasi-ellipse. Figure V-45D is a hodograph depicting r as a function of σt . This is a quasi-ellipse (i.e., slightly pinched across the semi-minor axis) with the semi-major axis tilted back at about 45° from the vertical. Thus, a stress-generating Eulerian wave model has been produced which resembles the tilted ellipse and is proved by the phase-shift equations of motion (V-39) and (V-40).

The use of sinusoidal models to represent waves is very idealistic. The simple functions do, however, point up one important aspect which is true for any function employed to represent waves; namely, that small systematic phase discrepancies, by virtue of the correlation phenomena, can give rise to gross effects upon the measured momentum and energy transfer properties of the fluid.

Let us examine some wave models which provide statistical properties somewhat comparable to those obtained from actual wave meter measurements. Hypothetical wave data were generated which portray three different two-dimensional heuristic wave models.

1. Random-Biased Model (RBM). This wave system has orthogonal velocity components, u and w, which are quasi-random, having no preferred frequency peak in the auto-spectra. About 5 percent of the data are slightly adjusted to provide a small, negative covariance. A segment of the u and w traces is shown in figure V-46A (upper traces). This first hypothetical model can be envisaged as a surface wave field where the motion is quasi-random, such as might be produced by many oscillatory progressives moving in many directions. The value of the covariance is about -3.7 cm^{2}sec^{-2}. It is therefore necessary to simulate a value of the stress near the water surface of 3.7 dynes cm^{-2}. This is considered, ordinarily, to be the order of magnitude of wind stress upon the ocean surface (see Stommel, 1958).

2. Sinusoidal-Unbiased Model (SUM). This model is represented, approximately, by simple sine-cosine functions of u and w given by equations (V-36) and (V-37). The velocities were simulated by picking u and w from hand-drawn (hence, imperfect) sinusoidal curves. A segment of the simulated record is shown in figure V-46B (middle traces).

3. Sinusoidal-Biased Model (SBM). This model, shown in figure V-46C (bottom traces), is identical to the SUM except that the u function has been slightly increased at its positive maximum point. This intentional biasing was done for two reasons: (1) to synthesize a desired negative value of $\overline{u'w'}$; and (2) to bias the SUM model by a simple mechanism, perhaps not unlike that existing in some natural ocean waves. To appreciate this, examine a simple mechanism
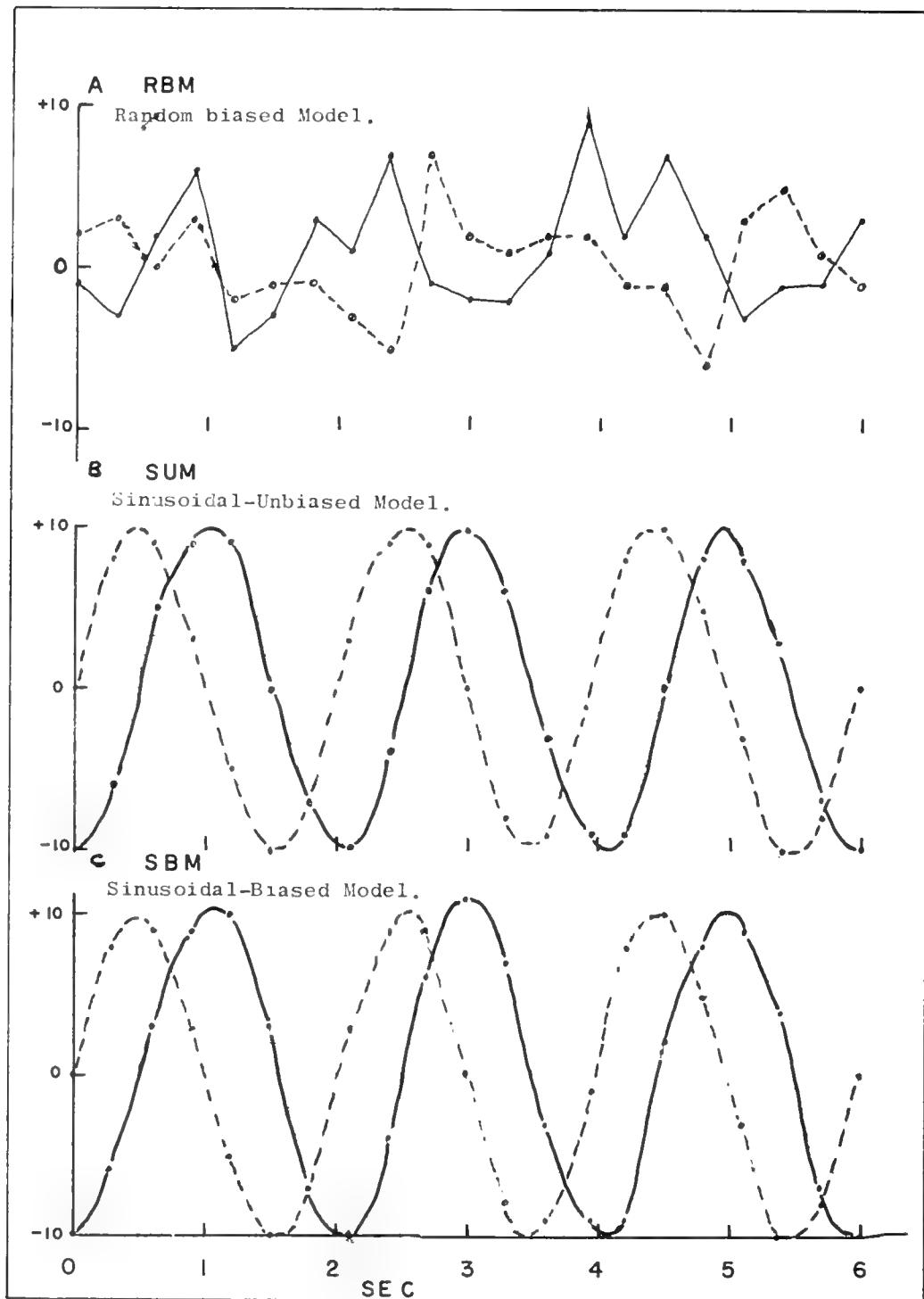
Segments of u and w Velocity Traces for Wave Models.

Figure V-46

whereby momentum may be transferred from the wind through the surface waves. Any energy and momentum within the wave must have been transmitted through the wave surface by an actual frictional drag and/or a pressure effect. Assume that the wind momentum is transferred by an eddy process in which the eddies are the waves themselves. As the wind blows horizontally across the waves, it produces a tractive stress on the tops of the waves and, perhaps also, a pressure force upon the upwind side of the waves. Both of these mechanisms could sensibly accelerate the particles when they are moving at the top of their orbits; i.e., when the u component is positive and maximum. Thus, a bias is placed within the horizontally oscillatory component of the SBM, a bias which is of the frequency of the waves themselves. At a fixed point in the water column, momentum transfer of this sort would appear as a direct coupling effect, occurring at the dominant wave frequency.

The three sets of data were analyzed, using the Tukey spectral estimate program, on the M.I.T. IBM 7090 computer. The results are listed in appendix C. The processing techniques used were identical to those used for the wave data (discussed in chapter III). Table V-4 gives a short summary of the pertinent statistics.

The variances $\overline{\sigma_u}^2$, $\overline{\sigma_w}^2$ of the RBM are about 15 cm^2 sec^{-2}, whereas the unbiased and biased sinusoidal models have variances of the order of 50 cm^2 sec^{-2}. The mean values are not listed; however, $\bar{u}$ and $\bar{w}$ did not exceed 0.5 cm sec^{-1} for any of the models. The covariances $\phi_{uw}(0)$ for the RBM and SBM are -3.70 and -2.6 cm^2 sec^{-2}, respectively; the SUM displays an expected vanishing covariance. The correlation coefficient r for the RBM (-0.24) is relatively large compared to that for the SBM (-0.03).

The spectral analysis of the hypothetical wave data serves a twofold purpose. It permits specific examination of the covariance properties of the biased data. More important, however, one can examine the cross properties of the statistical quantities derived from the "controlled data". One of the difficulties in interpretation of statistics such as auto-spectra and cross-spectra is that much of the actual data processing is hidden amidst the long series approximation formulas (see chapter III). It is therefore instructive to examine the relative magnitudes of the effects which different types of data have upon the derived statistics.

The spectral data for the three wave models are listed in appendix C. The auto-covariance functions $\phi_u(\tau)$ and $\phi_w(\tau)$ are plotted in figure V-47 for all three models. The RBM (upper traces) displays no obvious periodicity, oscillating rather chaotically about the abscissa. The SUM and SBM auto-covariances give almost identical oscillating curves with a period of about 2.1 seconds. The pattern of $\phi_u(\tau)$ and $\phi_w(\tau)$ is similar to a cosine curve (an even function), having a maximum value at $\tau = 0$. At this point, the auto-covariance defines the variances of u and w.
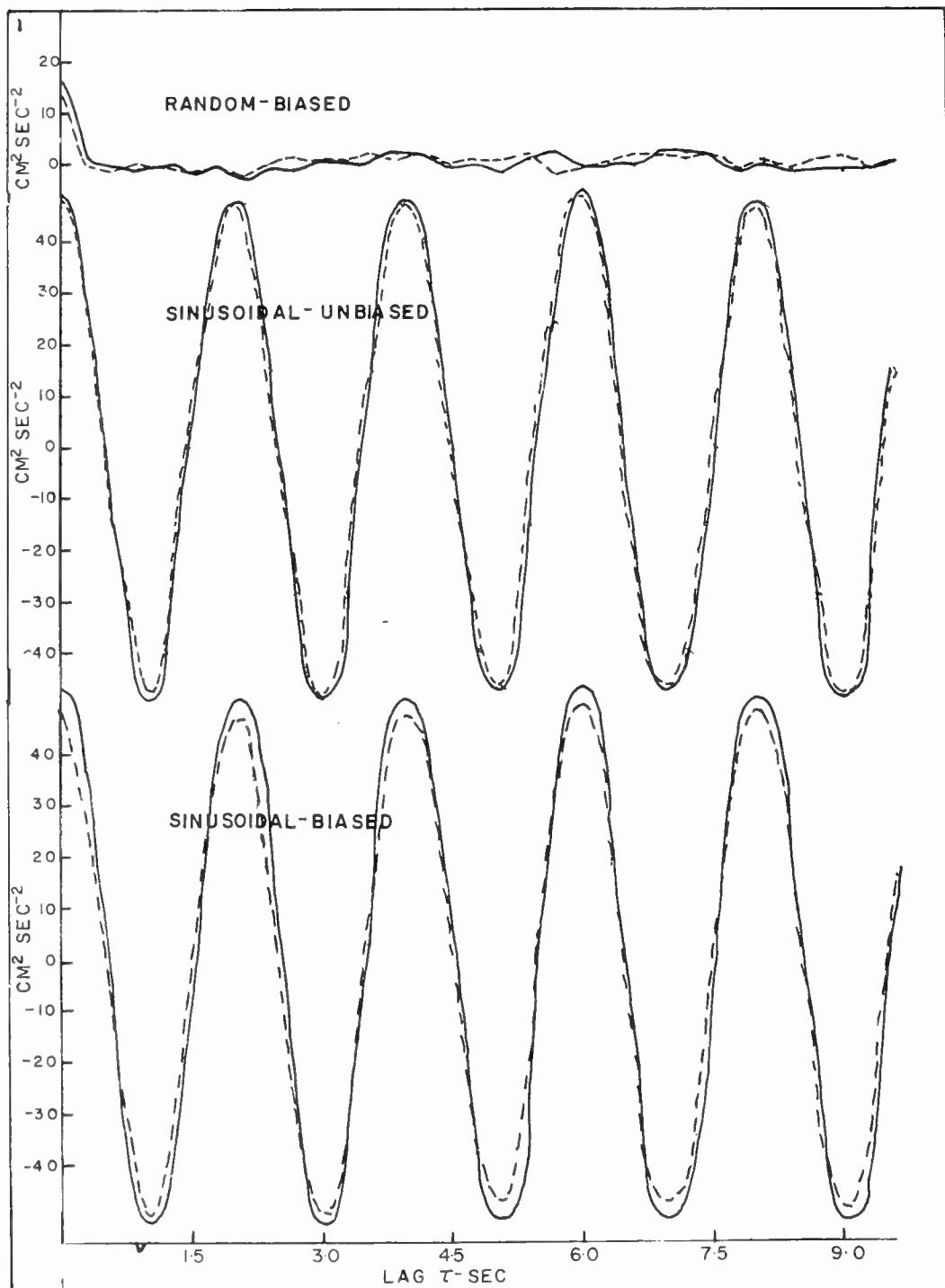
Auto-Covariance Functions for the Wave Models.

Figure V-47

Table V-4. Summary of Statistics of Wave Models

	Random Biased Model (RBM)	Sinusoidal Unbiased Model (SUM)	Sinusoidal Biased Model (SBM)
ΔT (sec)	0.3	0.3	0.3
N	600	600	600
M	32	32	32
DF	38	38	38
σ_u^2, σ_w^2 (cm^{2}sec^{-2})	$\sim$14.9	$\sim$49.9	$\sim$49.9
$\phi_{uw}(0)$ (cm^{2}sec^{-2})	-3.70	-0.05	-2.6
r	-0.24	0.00	-0.03

NOTE: For definition of symbols see appendix B (Plots of Auto-Spectra of Wave Meter Data).

Auto-Spectra for the Wave Models.

Figure V-48

The auto-spectra Φ_u and Φ_w of each model are shown in figure V-48. Again, the random model (RBM) shows no dominant peaks, whereas the sine-like systems display relatively strong, well-defined pedestals at a frequency of about 0.5 cps or a period of 2.0 seconds. Note that this is the period of the auto-covariance oscillation for the sine functions (SUM and SBM). Figure V-49 shows the co-spectra C_{uw} and the qua-spectra Q_{uw} for the three models. The co-spectrum scale is 1/20 the qua-spectrum scale.

The qua-spectrum Q_{uw} for the RBM shows no significant energy peaks, whereas strong peaks occur for both the SUM and SBM at the wave frequency of 0.5 cps. These strong qua-spectral peaks are to be expected (see equations (V-39) and (V-40)), since the fundamental sine and cosine functions are exactly out-of-phase (i.e., by $\pi/2$).

Examination of the co-spectral functions shows that the areas between the C_{uw} curves and the zero axes are equivalent to the value of the covariance $\overline{u'w'}$ (which for all three cases is negative). The co-spectra of the three models are the most interesting, since they are indicative of the sensitivity of the correlation phenomena. The C_{uw} for the RBM is highly random and (noting the difference in scaling of the C_{uw} and Q_{uw} axes) is similar over the whole frequency range to Q_{uw}.

The co-spectrum of the SUM is relatively flat with a slight disturbance indicated at about 0.5 cps. On the other hand, the co-spectrum for the SBM shows a very pronounced negative peak precisely at the wave frequencies. This indicates that, by altering the magnitude of the values of the u component by about 5 percent over small intervals near the wave peaks, the covariance obtained shows a strong negative peak at a frequency associated with the waves themselves.

A very real problem in measurement exists, since the instrumentation measuring the actual wave motions could provide an artificial correlation in the recorded data, in addition to the real correlation provided by the true motions themselves. It is therefore pertinent to ask to what extent the wave meter systems can bias the records.

Instrument Problems

In this study a new and relatively crude instrument was developed to examine wave motions. In spite of some obvious drawbacks in the wave meter, associated with limited calibration techniques and imperfect mounting methods, a good deal of plausible and probably valuable information was obtained about the gross properties of surface wind-wave motions. These results have been discussed in the preceding sections of this chapter. This section, which treats the observed time correlative properties of the wave motions, deals with more speculative interpretations of the observed data. It can be argued that much of the covariance information provided by the instrument is spurious. This possibility is acknowledged and examined in the light of the mechanism of such correlation discussed in the previous section. There are also four (not necessarily independent) effects which can be attributed to the OMDUM system,
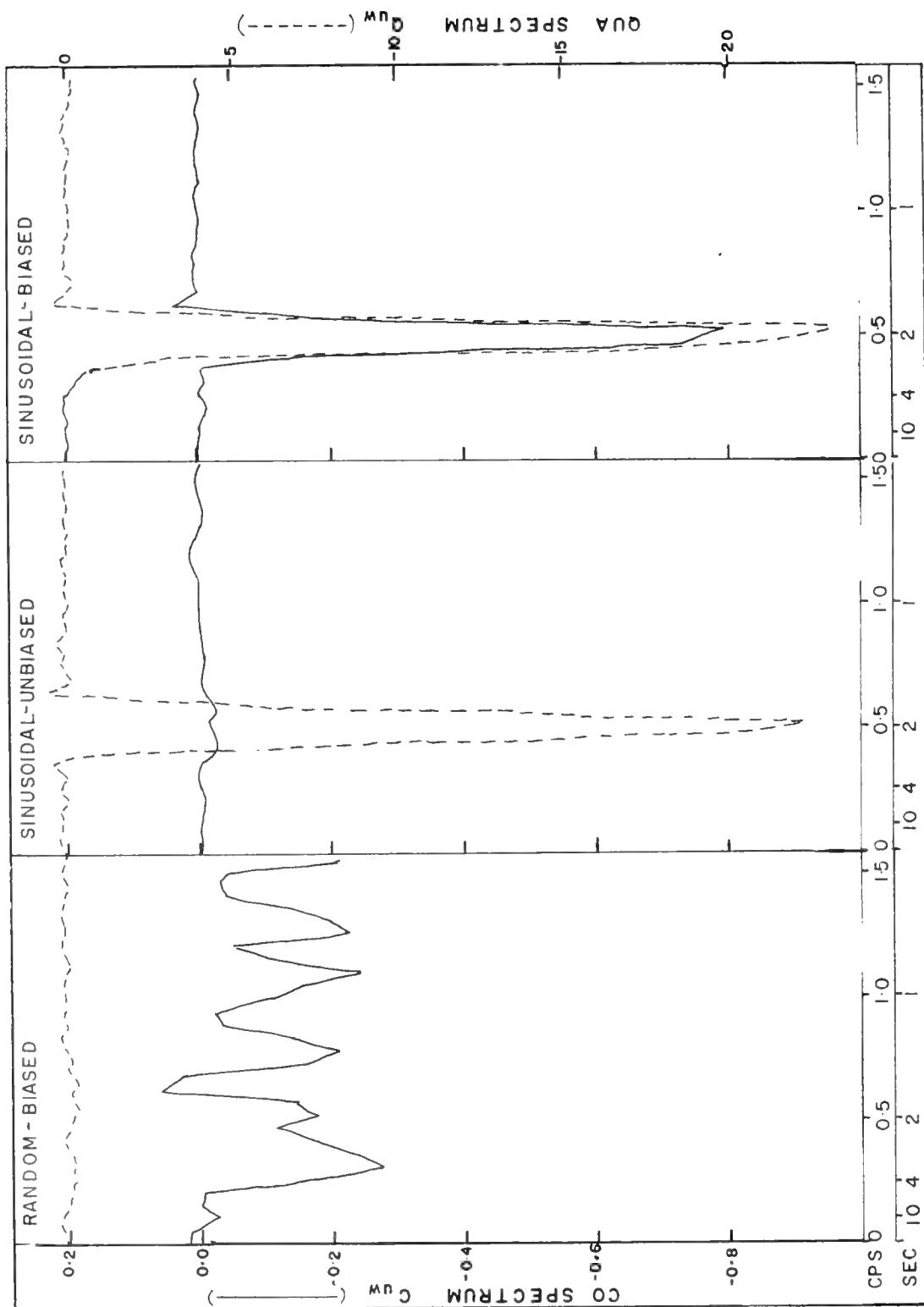
Cross-Spectra for the Wave Models.

Figure V-49

enabling it to produce artificial correlations in the wave motion data. In this discussion, it is again necessary to resort to the simple sinusoidal models with reference to the wave perturbations.

The simple expression for a covariance associated with the vertical and horizontal velocity components of a two-dimensional progressive wave having a small phase shift $\Delta\phi$ between the oscillations is given in equations (V-39) and (V-40) as:

$$u' = A_u \cos \sigma t . \tag{V-45}$$

$$w' = A_w \sin (\sigma t + \Delta\phi) .$$

A_u and A_W are the amplitudes, $\sigma = 2\pi T^{-1}$, and $\Delta\phi$ is the phase angle shift. (The plot of the vector having u' and w' orthogonal components as a function of σt appears in figure V-43D.) It has been shown that for $\Delta\phi = 0$, $\overline{u'w} \equiv 0$; and for $\Delta\phi \neq 0$,

$$\overline{u'w} = \frac{A_u A_w}{2} \sin\Delta\phi . \tag{V-46}$$

For small angles of $\Delta\phi$ (less than 10°) the following approximation may be written:

$$\overline{u'w} \cong \frac{A_u A_w}{2} \Delta\phi . \tag{V-47}$$

The covariance in equation (V-47) is only an artifice to help visualize the parameters controlling correlation properties. This formulation may be associated with either the original source motions or the output functions of the measuring instrument. A knowledge of these motions and of the instrument mechanism is therefore necessary in order to define the causes of the covariance; i.e., whether they are spurious or "real". These causes, if due to the instrument, can be ascertained by examining the sources of possible instrument distortion and their effect on the parameters A_u, A_W and $\Delta\phi$.

Direction Calibration Differences - Instrument bias or undesirable contributions to the covariance may be produced by a difference of forward and backward flow calibration in one or both of the impeller systems. Suppose that the slope of the calibration curve (see figure II-21) for a single impeller is different for each flow direction. If this impeller were coupled orthogonally with an impeller having no calibration anomaly, and then placed in a regime having pure sine and cosine motional components, the response would be given by:

$$u' = A_u \left(1 + \delta k \right) \sin \sigma t. \tag{V-48}$$

$$w' = A_w \cos \sigma t. \tag{V-49}$$

Here w' is of the same form as in equation (V-37). The δ is defined as:

$$\delta = \begin{cases} 1 & \text{FOR } 0 \leq \sigma t < \pi \\ 0 & \text{FOR } \pi \leq \sigma t < 2\pi \end{cases}; \tag{V-50}$$

and the value of K is small compared with unity. The functions u' and w' in equations (V-48) and (V-49) are simply sine and cosine forms, but with the u' term possessing a slightly larger positive amplitude. The traces are shown in figure V-44C (bottom curves), with the u' function depicted as a broken-line curve.

Evaluating the covariance $\overline{u'w'}$:

$$\overline{u'w'} = \frac{1}{T} \int_{-T/2}^{T/2} \left(1 + \delta k \right) \sin \sigma t \cos \sigma t \, dt. \tag{V-51}$$

The term $\left(1 + \delta k \right)$ is left inside the integral because, in a sense, it is a function of time. Splitting the integration for positive and negative summation gives:

$$\overline{u'w'} = \frac{A_u A_w}{2T\sigma} \left[\left(\sin^2 \sigma t \right)\left(1 + k \right) \right] \Big|_0^{T/2} - \sin^2 \sigma t \Big|_{-T/2}^0. \tag{V-52}$$

It is easily seen that $\overline{u'w'} = 0$. This integration is seen graphically in figure V-44C. The sum of the shaded areas, in spite of the damped positive amplitude, is equal to zero - just as with equation (V-38).

If both meters are biased toward higher positive or negative values, then contribution to the covariance does occur. This is easily seen, since the integration would be made in intervals of quarter periods (in lieu of half periods) for equation (V-52). These integrals do not vanish (vis. $\sin \pi/2 = 1$).

It should be noted in passing that if both ducted meters have calibrations which are linear (as was experimentally shown in chapter II), but which differ slightly, this alone produces no effect on the covariance except that, if it is non-zero, its magnitude (but not sign) is altered slightly.

It was noted in chapter II that for both the OMDUM II and OMDUM III systems, the forward and backward calibrations of the respective instruments proved identical within the limits of the accuracy of the determinations.

Instrumentation Time Lag - Time lag may be mechanically or electronically induced in the record pairs, u(t) and w(t), by either the sensors or the recording system.

Suppose the instrument has an inherent difference in frequency or time response between its two sensors so that the recording at the instant of time t is actually of the variables u'(t), w'($t + \Delta t$), or correspondingly, from equation (V-45),

$$A_u \sin \sigma t, \quad A_w \cos\left(\sigma t + \frac{\Delta T}{T} 2\pi\right) . \qquad \text{(V-53)}$$

The time lag $\frac{\Delta T}{T} 2\pi = \Delta\phi$ is the instrumental phase lag of the u' sensor over the w' sensor. For example, for a wave period of 4.0 seconds, an angular phase lag of 2° is equivalent to:

$$\Delta t = \frac{2}{360} \times 4 \, SEC \qquad = 22 \text{ milliseconds.}$$

Figure V-45 shows that a relatively small time shift (or phase shift) can produce relatively large covariances.

Let us examine possible phase lag induced by the recording or sensor systems. The recording systems described in chapter II were two-channel, general purpose recorders (model 320 and 322, manufactured by the Sanborn Co., Waltham, Mass.). The response time (reported in the Sanborn Co. catalogue S-15m-4-64) is 5 milliseconds for a 0-90 percent rise for a step input in voltage. By the definition given in appendix A, this is an equivalent response time T_r of about 2.5 milliseconds. This value is at least an order of magnitude less than the response time of the impellers (as discussed in chapter II). Therefore, the amplifier and recording system can produce no sensible time lags, and hence can cause no

bias in the covariances. Moreover, for an effective artificial stress to be observed, the phase lag or response time of the u and w channels must be different. If, in equation (V-45), an identical $\Delta\phi$ occurred in both the u' and w' functions, the resulting covariances would be identically zero.

What is the possibility of there being consistent differences in the response of the u and w sensors? Table II-4 lists estimated response times for each of the u and w impellers of the OMDUM III system (in both flow directions). The average response time T_r is 66.5 milliseconds with a standard deviation of $\sigma_{T_r} = 8.9$ milliseconds.

Again, assuming a sinusoidal wave with a 4-second period as the dominant motional contribution to the covariance, the resultant maximum phase shift of one meter (with respect to the other) would be:

$$\pm \sigma_{\Delta\phi} \cong \pm \frac{8.9 \times 10^{-3}}{4.0} \times 2\pi \cong \pm 0.8°.$$

The corresponding virtual stresses (from figure V-45) are ±2, ±5, ±8, ±14 dynes cm^{-2} for particle velocity amplitudes of 20, 30, 40 and 50 cm sec^{-1}, respectively. These estimates in table II-4 are only approximate, since only five observations of T_r were made; and the T_r values appear to have relatively wide random scatter. Specifically, the two values obtained for +u are as different from each other as they are from other channels. The scatter may therefore be caused by the errors of the experiment, and the actual response times of the two impellers (in either direction) could be closely identical. There is also a possibility that the covariance model in equation (V-47) may be over-simplified.

A phase shift could possibly result from an inadvertent shifting of the time axis of one of the velocity pairs (u,w), with respect to the other, during the data processing (particularly during the reading of the data strip charts, as discussed in chapter III). Note that the direction of the accidental time axis shift would control the sign of the covariance (see equation (V-47)). A rigorous attempt was made to preserve the simultaneity of the time scales of u and w. However, the checking was not fail-safe; and it is possible that the few excessively large (and seemingly spurious) covariances appearing in table V-4 could have been caused by such accidental time axis shifting in the data abstraction procedure.

Effect of Wave Meter Motion - Another possible effect of instrument bias is associated with the dynamic reaction of the suspended wave meter to the oscillatory wave forces. The pyramidal guy wire suspension (discussed in chapter IV) appeared from visual observations to hold the OMDUM III system virtually rigid at all depths, except when it was at the immediate trough level. With the passage of large waves, the maximum horizontal deflection of the wave meter was about 10 cm. The vertical damping appeared to be complete, as was expected because of the heavy counterweights (see figure V-15).

The suspended wave meter may be considered as a simple pendulum having a period represented by:

$$T_l = 2\pi \sqrt{\frac{L}{g}} \; ;$$

(V-54)

where T_l is the period of swing, L is the length from the point of pivot, and g is the acceleration of gravity. For the system mounted on BBELS, the value of L ranges from 19 meters, when the instrument is just beneath the water surface, to 24 meters when the instrument is 5 meters down. This gives $T_{19} = 8.75$ seconds, and $T_{24} = 9.83$ seconds. These periods are about twice the period of the wind waves usually observed at BBELS. Theoretically, this would tend to dampen the reaction of the suspended meter to the 4-5 second wave motions. These periods are, of course, for a simple pendulum suspended at one point. For the OMDUM observations the wave meter was suspended by no less than four guys. For the later observations (BBELS-14, 15, and 16) a vertical anchored guy was also used (see table V-1). The use of multiple guys should provide strong, if not critical, damping to the system. It should also tend to increase the natural period of swing of the system.

The manner by which the OMDUM or LIMDUM systems are suspended should, ideally, provide $\bar{w} = 0$. The records (see table IV-3) show that $\bar{w}$ generally lies within ± 2-3 cm sec^{-1}, but occasional values occur as high as ± 5-8 cm sec^{-1}. The most obvious explanation for a non-zero mean (of w) is that the axis of the vertical sensor may not be vertical due to deflection of the meters and suspension by the drag force of the current. If this is the case, then strong horizontal currents should correlate with a large negative value of $\bar{w}$. This is because z is positive upward, and the meter tilting away from the current would produce $\bar{w} < 0$ (mean flow downward). For the BBELS-11 observations, the LIMDUM I system was used to detect w. The instrument was suspended from the single main guy. Under these conditions, the tidal current should have tended to tilt LIMDUM away from the horizontal mean flow, and thus provide a mean value $\bar{w}$ less than zero. Of the thirty-six values of $\bar{w}$ from BBELS-11, 25 show $\bar{w} < 0$ and 11 show $\bar{w} > 0$, indicating that some mean tilt occurred in response to the current.

The OMDUM III system was, of course, supported by an array of cable guys, giving a certain amount of horizontal stability. It was of interest to see if large absolute values of $\bar{u}$ caused tilting of the system sufficient to produce a detectable increase in values of $\bar{w}$. A correlogram was plotted of the values of $\bar{u}$ versus $\bar{w}$ obtained from the tables in appendix B, but there was no significant relationship. Both large and small values of $\bar{w}$ corresponded to large values of $\bar{u}$. Also, out of 36 records examined, in 17 cases $\bar{w} < 0$, and in 19 cases $\bar{w} > 0$. This indicates no significant trend toward preferential tilting by the mean current component $\bar{u}$. Further, it indicates that the pyramidal guy system, when carefully adjusted, stabilized OMDUM from mean horizontal drag forces. One may therefore conclude that, in general, the values of $\bar{w}$ obtained were only slightly associated with the guy system maintaining the meter at a slight tilt.

153

Time-variable wave perturbations upon the suspended OMDUM system may also have biased the velocity data. (Examine the heuristic covariance model of equation (V-46) or (V-47).) What effect would instrument motion have upon the ability of the instrument to measure the amplitude of the u and w components? Assuming the ideal orbital motions associated with deep water waves (see equations (II-5) and (II-6)), the amplitudes A_u and A_w in equation (V-45) would be identical for intermediate or shallow water waves.

For simplicity, assume that the roots of the variances (σ_u and σ_w) are indicative of the approximate response of OMDUM III to a single wave system whose frequency is indicated by the Φ_u and Φ_w spectral peaks. Then the measurements obtained with the OMDUM system show that A_w generally ranged from 1.1 A_u to above 3 A_u (see table V-1). This effect seems to indicate a damping of the horizontal motion response, rather than an amplification of the vertical response. This is because the vertical stability of the suspended meter and counterweights far exceeded the horizontal stability (see chapter IV). Damping of the amplitude A_u in expression (V-47) would, if anything, bias the covariance u'w' toward lower values. This disproportion of the u and w amplitudes is something of an enigma. It has already been suggested that part of this inequality of amplitudes was caused by the presence of multi-directional wave trains. However, this does not explain the disproportion between A_u and A_w in the OMDUM I measurements in Narragansett Bay (see spectra in figure IV-2). Here, there was no swell present, and the OMDUM I system was held rigidly from a large vertical pipe. Hence, over and above the effects of other wave trains and of meter motion due to a non-rigid suspension, either the ducted meter configuration inherently distorts the oscillatory wave motions, or a true disproportion does indeed exist in the waves (which was suggested in the last section).

A simple estimate of the wave perturbation on the meter should help to assess the biasing in the horizontal amplitude A_u. Assume that the wave period T is 4 seconds, and that the height H is about 1 meter for the ambient wind wave. The horizontal excursion of a wave particle at the sea surface can be computed from equation (II-9), with the amplitude of the surface wave given as H = 1 meter. The wave particle travels this distance in 2 seconds, giving an average velocity of 50 cm sec^{-1}. (Actually, of course, the velocity is of a sinusoidal nature.)

From observations of the OMDUM instrument, the largest visual estimate of its horizontal excursion in response to wave faces (which are maximum at a wave crest and act in the +u direction) was about 10 cm, or an average of about 5 cm sec^{-1}. This indicates that the amplitude could be reduced by about 10 percent. This effect would show up (in relation (V-47) for the covariance) in both the variance σ_u^2 and in A_u and A_w.

It should be remembered that the particle displacement and the velocity components decrease exponentially with depth. If the drag of the u velocity is roughly proportional to u^2 (see Prandtl, 1952), then the force attenuates as the square of the exponential function (shown in equation (II-5)). This increase in the stability of the instrument with depth was noticed. At 0.5 to 1.0 meter beneath the trough, the suspension appeared completely stable with no observable swing.

Directional Response of the Wave Meter - The final effect of instrument bias to be considered is the deviation of the orthogonal sensors from the ideal cosine law. This is, indeed, a most complicated matter. Referring to the discussion of instrument response in chapter II for any factual evidence of response characteristics, let us again consider the possible effects of biasing of the amplitudes and of the phase relation.

The magnitude of the vector component was shown to be a function of the angle of attack Θ between the current vector and the cylinder axis. This function was approximately sinusoidal except at very large angles (Θ approaching 90°).

The magnitude of flow velocity calculated from the response of two orthogonally mounted meters was about 10-15 percent larger than the true velocity in the tow tests. A like positive error in the amplitude of both velocity components would produce a covariance 25 percent too large. Corrections were thus used on the orthogonal velocity data (see chapter II). The main weakness in this method is that true ocean waves were not used in the calibration. Because of the nature of the turbulent medium of ocean waves, the errors in the individual components may well be greater than 10-15 percent; however, it seems unlikely that they should be larger by more than a factor of two. In other words, the biasing of the covariance function caused by magnitude distortion should be much less than a factor of four.

The possibility of introducing an artificial phase lag through distortion of the wave flow caused by the geometry of the ducted meters is a most complicated question. One effect that can be readily examined is the biasing associated with the physical separation of the orthogonally mounted impellers. The axes of the coupled impellers (mounted as shown in figure II-16) have a separation of 11 cm. When the OMDUM system is aligned properly to detect wind waves, the line of axes separation l is parallel to the wave crests (see figure V-50). If the u meter axis subtends an angle Θ with respect to the mean direction of wave propagation, l makes an equivalent angle Θ with the y axis. In this position, the projection of l upon the x axis is defined as:

$$\Delta l = l \, TAN \, \Theta .$$
(V-55)

Since the two orthogonal sensors are mutually displaced with respect to the direction of wave propagation (defined as the +x axis), a constant phase difference occurs between the two sensors. This is given by:

$$\Delta \phi = \frac{2\pi \, l \, TAN \, \Theta}{L} ;$$
(V-56)

where L is the wavelength. The phase angle $\Delta \phi$ may be considered identical to that appearing in equations (V-45).
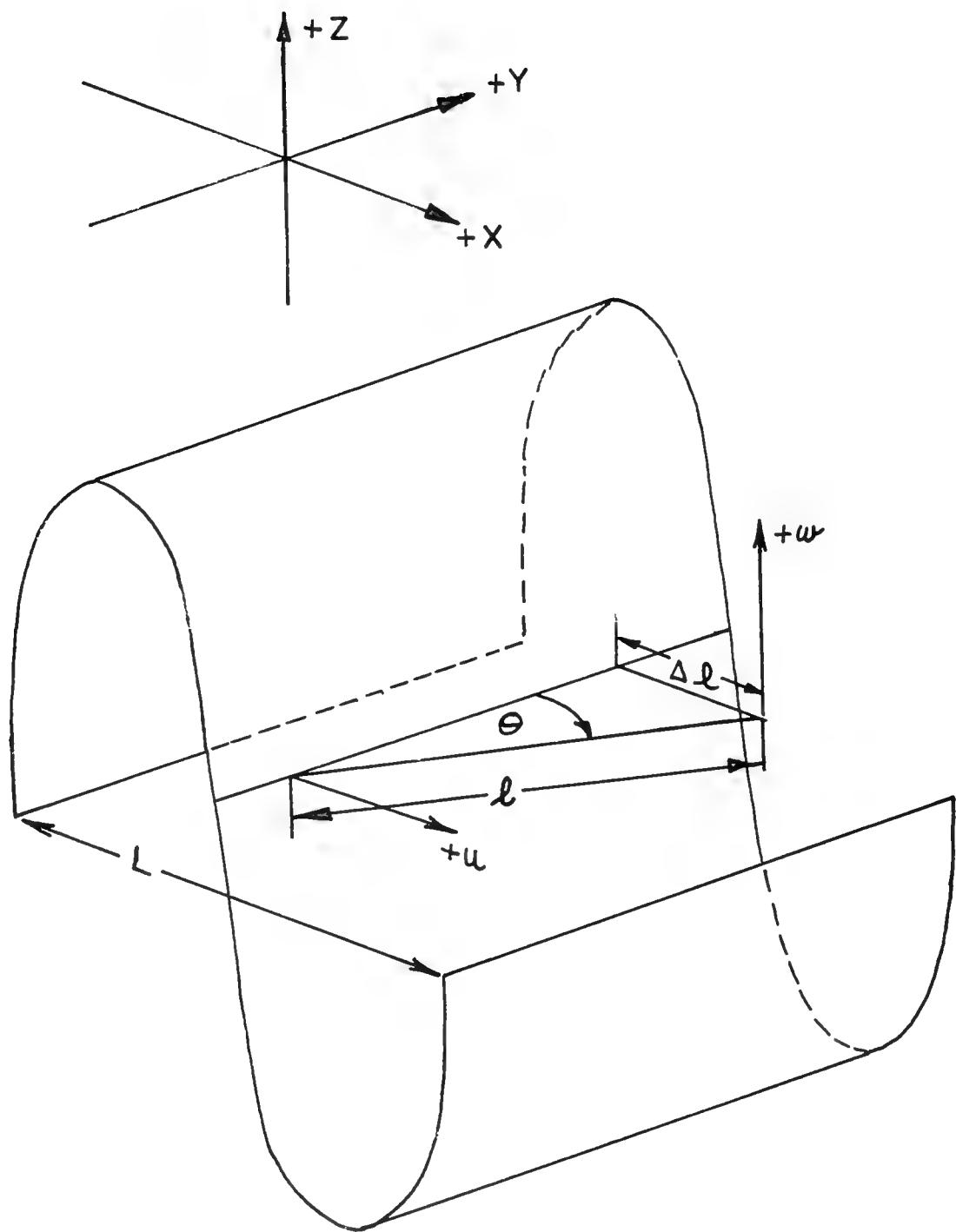
Parameters Used to Estimate Phase Shift Caused by Off-Angle Orientation.

Figure V-50

A typical value for Θ may be 5°; ℓ (for OMDUM III) is 11 cm; and, assuming short waves having L = 12 m, the resulting $\Delta\phi$ = 0.29°. Assuming velocity amplitudes for u' and w' of 20 cm sec^{-1}, the estimated stress $\tau \approxeq$ 1 dyne cm^{-2} (see equation (V-46)). Therefore, a non-zero average value of Θ could contribute to the covariance and associated stress.

Substituting equation (V-56) into (V-46) yields (for small $\Delta\phi$):

$$\overline{u'w'} = \frac{A^2 \pi \ell \; TAN \; \Theta}{L} \; . \qquad (V-57)$$

For small waves, L and A are small; but for large waves, A^2 dominates in equation (V-57) over L^{-1}. Thus, for a given angle Θ, an induced contribution to $\overline{u'w'}$ is more important for the smaller waves. Also, the amplitude A exponentially decreases with depth, whereas L is independent of depth. Statistically, L virtually increases with depth, since the higher frequency waves (i.e., those of shorter wave length) are rapidly filtered out with depth.

For serial 120-123, where the angle Θ varied from 0°, 20°, 50° and 80°; the covariances were -7.6, -10.3, -11.2 and -15.1 cm^2 sec^{-2}, respectively. The wind was increasing in speed and varying in direction, and swell direction was variable but roughly normal to the wind waves; but, aside from these factors, it appears that the directionality Θ may have provided a phase shift effect.

It is evident from this cursory perusal of the instrument-biasing effects, that the covariances $\overline{u'w'}$ obtained with the wave meters must be open to some question. Further work is required to verify or disprove their validity.

Dissipation of Kinetic Energy

It is instructive to consider the energy dissipation associated with the wave motions. By recalling term C of equation (V-35) and using actual data, one can estimate some values of the term:

$$\epsilon_w = -\rho \, \overline{u'w'} \, \frac{\partial \bar{u}}{\partial z} \; . \qquad (V-58)$$

This dissipation term is derived in appendix A.

During BBELS-15, using LIMDUM I, eight observations of the u wind wave component were made simultaneously at two depths 2.5 meters apart. The mean values $\bar{u}$ and the mean vertical gradients of $\bar{u}$ (i.e., $\partial\bar{u}/\partial z$) are given in table V-5. The last three columns list the values of equation (V-58) in

Table V-5. Estimates of Vertical Shear of the Horizontal Current, and Energy Conversion from Mean Flow

Serial	Depths m	$\bar{u}_1$ cm sec^{-1}	$\bar{u}_2$ cm sec^{-1}	$\dfrac{\partial \bar{u}}{\partial z}$ sec^{-1}	$\epsilon_w = -\rho\overline{u'w'}\dfrac{\partial \bar{u}}{\partial z}$		
					$\tau=5$	$\tau=20$	$\tau=80$
					erg cm^{-3} sec^{-1}		
111	0-2.5	+6.1	+3.1	+.012	+0.06	+0.24	+0.76
112	0-2.5	+3.2	+1.7	+.006	+0.04	+0.24	+0.54
113	0-2.5	+3.5	+6.9	-.014	-0.07	-0.28	-1.12
114	0-2.5	+26.4	+24.2	+.009	+0.05	+0.18	+0.72
115A	0-2.5	-12.7	-9.1	-.014	-0.07	-0.28	-1.12
116	1-3.5	-28.3	-28.4	+.0004	+0.002	+0.008	+0.32
117	3-5.5	-27.0	-26.5	-.002	-0.01	-0.04	-0.16
118	2-4.5	-28.1	-28.2	+.0004	+0.002	+0.008	+0.032

NOTE: Wind waves propagating in the +(positive) u direction.

erg cm^{-3} sec^{-1} for Reynolds stresses of 5, 20, and 80 dyne cm^{-2}. These values are representative of the magnitudes of $-\rho \overline{u'w'}$ obtained with the OMDUM III system at depth ranges from 0 to 4 meters (see table IV-2).

Positive values of $\bar{u}$ indicate a mean current flowing in the +x direction, defined as the direction of the wind wave propagation. Values of $\partial \bar{u}/\partial z > 0$ indicate a shear in which the upper velocity u_1 has a larger positive value than the lower velocity u_2. Note that in table V-5 all but three shears are positive, giving positive values for the energy dissipation ϵ_w. This is interpreted as the rate of energy transformed from the mean motion into the wave motions.

Quantities such as ϵ_w have little meaning unless they can be compared with other data. As mentioned in chapter I, Stewart and Grant (1962) presented some estimates of relatively high frequency (or high wave number) turbulent energy dissipation beneath the sea surface in the presence of deep water waves. In brief, they estimated the high wave number spectral contribution to the variance of a one-dimensional velocity record u(t), which was made using a "hot film" flow detector rigidly attached to the bow or suspended from the stern of a vessel underway. Auto-spectra Φ_u were derived from the time series records, using Taylor's hypothesis (see Hinze, 1959). These were transformed to wave number spectra Φ_u (k), where $K = 2\pi L^{-1}$.

In theoretical discussions of turbulence, a fundamental parameter associated with the energy of a particular wave number range is defined by Batchelor (1953) as E(k), where:

$$\int_0^\infty E(K)dK = \frac{1}{2}\left(\overline{u'^2} + \overline{v'^2} + \overline{w'^2}\right). \tag{V-59}$$

Here u', v' and w' are, as usual, the fluctuating velocities. The experimental measurements of the one-dimensional spectrum Φ_u (k) can be applied to the relation:

$$\int_0^\infty \Phi_u(K)dK = \overline{u'^2} . \tag{V-60}$$

When the concern is with small scale motions, the dissipation ϵ can be written (see Hinze, 1959) as:

$$\epsilon = 2\,\mu \int_0^{\infty} K^2 E(k)\, dK = 15\,\mu \int_0^{\infty} K^2 \Phi_u(K)\, dK ; \qquad \text{(V-61)}$$

where μ is the kinematic viscosity.

The functions $K^2 E(k)$ and $K^2 \Phi_u(k)$ are termed dissipation spectra, and describe the distribution (as a function of wave number) of the rate of decay of the turbulent energy to heat.

The validity of equation (V-61) is predicated on the Kolmogoroff hypothesis (Kolmogoroff, 1941): at sufficiently high wave numbers, the only parameters affecting the energy density $E(k)$ at wave number K are the rate of energy-dissipation ϵ and the kinematic viscosity μ. Also, since it is assumed for large wave numbers that the turbulence tends to be isotropic, measurement of a single velocity component suffices to describe the total energy of the system.

Estimates of ϵ obtained by Stewart and Grant (1962) at various depths and for various wind wave heights are listed in table V-6. Some of the tabulated data were reported earlier (see Grant, Stewart and Molliet, 1962). The values of ϵ are generally smaller than ϵ_w, even when a 5 dyne cm^{-2} stress is used to estimate ϵ_w (see table V-5). A relatively small variation of ϵ occurs with depth, and bears no resemblance to the distribution of kinetic energy with depth described earlier in this chapter. Stewart and Grant (1962) suggest that the observed turbulent velocity they measured is more associated with the "wind driven drift current" than with the waves.

This would tend to explain the large differences between ϵ and ϵ_w. Thus, ϵ is associated with the high frequency or dissipative turbulent range (as shown in figure V-38), whereas ϵ_w is associated with the inertial subrange or region of wind wave frequencies.

Since the kinetic energy is centered about the ambient wave frequencies, it is plausible that a relatively large amount of energy transfer occurs from the mean motion to the dominant wave frequencies.(see table V-5). Much of this wave energy is transported over great distances to the coastal beaches. A relatively small amount of wave energy would be dissipated directly to high frequency turbulence in the area of wave generation, as indicated by the magnitudes of ϵ.

The dissipation relation ϵ_w demonstrates how the large scale wave energy is dependent upon the mean current environment. The $\partial \bar{u}/\partial z$ term can be governed by several factors which control shear, such as tide, wind driven surface current interacting with the bottom, or wind stresses. Thus, the numerous factors which control the shear can have marked effects on the actual waves produced.

In the LIMDUM I results in table V-6, the mean vertical shear of the
horizontal current may actually be caused by wind stress accelerating the
surface water. This shear does not appear to be produced by instrument bias.
The positive shear is predominant in both positive and negative current direc-
tions with respect to the wind wave direction. However, more measurements are
needed to substantiate the existence of such shear phenomena.

Table V-6. Energy Dissipation as a Function of Wave Height and
Depth Below the Surface (from Stewart and Grant, 1962)

ENERGY DISSIPATION ϵ (in erg cm^{-3} sec^{-1})						
Depth (m)	Wave Height					
	10 cm	20 cm	30 cm	40 cm	50 cm	90 cm
1	-	-	-	-	0.042	-
1.5	-	0.015	-	0.023	-	-
2	0.0052		0.029	-	0.022	0.045
12	-	-	-	-	0.00025	-
15	0.0011	-	-	-	-	-

.

CHAPTER VI

CONCLUSIONS AND SUGGESTIONS FOR FURTHER STUDY

The aims of this study were of a twofold nature: (1) to design and fabricate an instrument system to measure wind wave particle motions in situ; and (2) to make subsequent exploratory measurements with emphasis on describing momentum and energy transfer processes within the waves.

The scope and the number of problems examined using the wave meter data make it difficult to integrate completely all the results discussed in chapter V. Hence, only highlights and conclusions are presented in this summary. The extent to which the goals were accomplished is left for the reader to determine. Some of the recommended future studies are actively being pursued.

Instrumentation

The apparent attributes and shortcomings of both the orthogonally mounted wave meter (OMDUM III) and the linearly mounted wave meter (LIMDUM I) are briefly stated, along with certain recommended improvements in the hardware, recording systems, calibration and measurement techniques.

Attributes of Instrumentation Used -- The ducted cylinder detectors are simple in construction, inexpensive, and easy to fabricate. The impellers and carborundum steel and quartz bearings are simple to replace.

The wave meter electronics, consisting of inexpensive miniature induction coils (potted in epoxy resin) that interact with tiny magnets mounted at the tips of the impeller blades, were found to be satisfactory. The coils are isolated from the sea water and require no power input or amplifier on the output. The voltage signals are fed directly to a strip chart recorder through a watertight cable. No electrical short or electrical signal interference occurred during two years of measurements at BBELS.

The individual ducted impellers are simple to calibrate for end-on or off-angle, steady or accelerative, rectilinear flow. The angular velocity of the impeller is directly proportional to the fluid flow through the impeller (whether it be water or air). Hence, only a minimum number of points are needed to establish the calibration curve. Calibration can be made in a wind tunnel or a towing tank or basin. Further, the ducted meters were easily fabricated to have virtually identical calibrations, including forward and backward flow through the cylinders.

The data obtained with the four different meters (OMDUM I, II, III and LIMDUM I) displayed consistently similar particle velocity characteristics and produced similar auto-spectra of the motions. This fact indicates that most of the meter response is caused by true motions, and that the signature of the individual wave meters upon the data is minimized. Also, similar results were obtained in spite of the use of different mounting or suspension methods, some of which were less stable than others.

Off-angle calibrations demonstrated a functional variation of instrument response with angle of attack of steady flow. In the orthogonal meters, a method was worked out (using the relative responses of the two meters) to correct for off-angle response aberrations in the measurement of the true flow vector lying in the plane formed by the two orthogonal meter axes.

The response time of the ducted meter (used in OMDUM III and LIMDUM I) was found experimentally to be about 60-70 milliseconds. Further tests showed that the OMDUM II system (slightly larger impeller) clearly resolved a simple harmonic vertical oscillation having a 0.7-second period. Hence, the system can faithfully respond to frequencies well above the 0.5 to 0.2 cps associated with wind waves. Moreover, the spectra of motions were analyzed from d.c. to 2.5 cps. Aside from the low moment of inertia of the impellers, the fast response is due to the geometric character of the enshrouded impeller. The flow which cannot diverge around the impeller, imparts dynamic pressure on the blades very efficiently and quasi-instantaneously.

The ducted meters were used in two ways: (1) mounted side-by-side and orthogonally to measure both the horizontal and the vertical velocity component simultaneously, as with OMDUM III; and (2) mounted rigidly and linearly on a vertical rod to measure either the horizontal or the vertical velocity component simultaneously at two different depths up to three meters apart, as with LIMDUM I. The couplings were simple, and the change could be made from one mode to another in several minutes.

The OMDUM I system was mounted on a rigid vertical pipe in Narragansett Bay. Both OMDUM III and LIMDUM I were suspended by a pyramidal and counterweighted system of guys from the BBELS. This guy system provided minimum horizontal swing and complete vertical damping. The guy device could be quickly lowered or raised, permitting rapid observations at different depths.

For gross measurements of velocity and auto-spectra, the method of suspension did not seem critical. However, the measurement of the co-variance properties of the motion is dependent heavily upon stable mounting of sensors.

Shortcomings of Instrumentation -- The raw wave meter data produced on two-channel strip charts required laborious editing and hand-reading for conversion to the computer format on punched cards. The preliminary processing was expensive, time consuming, and liable to human error. More advanced procedures are desirable.

The threshold velocity of the impellers (used in OMDUM III and LIMDUM I) was found to be about 7 cm sec^{-1}. Thus, oscillatory wave motion is not detected between $\pm 7 \text{ cm sec}^{-1}$. This presents, by virtue of the interpolation procedures, some bias in the record and its associated statistics, particularly when the wave motions are of small amplitude.

The wave meters, as with all current meters, have inherent imperfections in their ability to measure fluid flow. They impress their own signature into the wave data. Calibration normally allows one to assess the instrument bias in order to eliminate it from the instrument record. Unfortunately, all calibrations were

made under virtually ideal conditions of rectilinear flow; whereas the field measurements were made in actual turbulent ocean waves. The problem of proper or realistic calibration of the wave meters is difficult. It is a manifest impossibility to simulate true ocean wind waves in a laboratory tank. Further, there is no "standard wave", and no one knows how to generate a progressive wave of previously known form (see Kinsman, 1965). This same problem is well-known by workers making free surface elevation measurements with wave staff devices -- experimentally, a much simpler exercise than particle velocity determination.

The alternative to these laboratory calibrations is, of course, a field test where the response of the wave meters could be directly compared with some other instrument able to measure the same wave motions, preferably by an independent method. But this is not possible, since one is dealing with a unique measurement at the outset, and has to proceed with the handicap than no comparable measurements are readily available for comparison. Because of this unfortunate situation, one is forced to use his intuition as the main guide in interpreting instrument bias.

The most notable apparent biasing of the OMDUM III system was the damping effect of the horizontal velocity amplitude response. An explanation is presented in chapter V for the ways in which this effect was caused. These explanations, however, are less than completely satisfactory until a more suitable calibration is performed.

A rough comparison was obtained of the auto-spectra of particle velocity motions and free surface fluctuations, and the spectra displayed strong similarities. But again it is difficult to anticipate intuitively the physical interrelationships of the two functions, other than those indicated by simple small-amplitude wave theory.

Suggested Instrumental Improvements -- More precise calibration is required for a better understanding of the effects of the orthogonal meter arrangement upon oscillatory flow. The U. S. Corps of Engineers has a large wave tank at the Coastal Engineering Research Center in Washington, D. C. which can generate waves 1-2 meters high in a basin about 4 meters deep. The OMDUM III and improved systems should be tested with various size waves and at various depths in this tank. This would provide a better understanding of wave meter response to oscillatory motions, even though real wind waves would not be simulated.

Workers at the Chesapeake Bay Institute of Johns Hopkins University (Pritchard, 1964) are developing an acoustic current meter, mentioned in chapter I, which should be capable of measuring wave motions within a small volume. At the first opportunity, a direct comparison should be made of the two instrument records in real wave conditions.

A more refined impeller system has been fabricated by the Braincon Corp., Marion, Mass. The new system is similar in dimensions to OMDUM III, but with a lighter six-bladed impeller mounted on all-jewel bearings, and much smaller and lighter magnets and coils. The threshold velocity was found in recent tow tests to be less than 2 cm sec^{-1}. This would greatly improve the data record and allow more resolution of smaller scale wave motions.

A simple amplifier-converter system is being designed to accept raw voltage pulse signals from the wave meters and to convert this data directly into a series of ΔT values, recording them on binary digital tape. This will eliminate tape reading and many sources of error. The digital tape can be fed directly into a computer for analysis.

Note: A project to study wind and wave turbulence is being conducted jointly by the NUWS Oceanographic Branch and the M.I.T. Department of Meteorology. Field measurements are being made using vertical arrays of lightweight fast-response anemometers aboard the BBELS. Since the output of the ducted meters is similar to that of common cup anemometers, this magnetic tape conversion system will, hopefully, be adaptable to the anemometer system output for stationary time series studies.

Conclusions from Actual Wave Observations

The majority of the wave observations were made aboard the Buzzards Bay Entrance Light Station (BBELS). This facility proved highly successful as a platform from which to make the wind and wave observations.

Gross environmental measurements were made and reported of water temperature, winds, tidal height, and tidal currents to insure a basic understanding of the background from which to study the wind waves. This background information should also prove helpful to others who may wish to use the BBELS for similar or related studies. The following is a brief summary and interpretation of the results obtained with the wave meters.

1. The OMDUM III system produced realistic wave velocity patterns. However, the amplitude of the horizontal oscillatory velocity appeared damped, possibly caused by non-rigid instrument mounting. The LIMDUM I system depicted wave velocities showing quasi-exponential damped motion as a function of depth.

2. Histogram sorts of the equi-time spaced vertical particle velocities for several records showed an approximate Gaussian pattern, but with a bi-modal tendency. This effect was attributed to the detectable threshold velocity of the wave meter.

3. The variances $\overline{\sigma_u}^2$ and σ_w^2 showed consistent exponential attenuation with depth, but not as rapidly as the exponential decrease of an ideal trochoidal wave system.

4. Integration of $\frac{1}{2}\rho\overline{u'^2}$ and $\frac{1}{2}\rho\overline{w'^2}$ with depth gives a theoretical representation of the oscillatory kinetic energy of the wave motions. These values were found to be comparable to the estimated potential energy of the observed waves derived from wave height estimates.

5. The auto-spectra of wave motions display spectral peaks at the observed frequencies of the waves. The depth attenuation of wave motions is vividly portrayed in the auto-spectra as a gross decrease in energy and as a peak shift to lower frequencies, the latter associated with a hydrostatic filtering of

higher frequencies with depth. Auto-spectra of wave motions proved to have similar spectral peaks to the auto-spectra of free surface elevation data observed with an electronic wave staff.

6. Slopes of the auto-spectra of the particle velocity motions at the frequencies above the spectral peaks indicate that the spectral energy decreased as the minus-fifth power of the frequency. This law, predicted by Phillips (1958), has been observed for free surface auto-spectra (Burling, 1959), and is supposed to indicate the presence of an equilibrium range of frequencies where there exists a saturation of energy.

7. Continuous observations of wave motions under time-varying wind conditions show spectral changes associated with wave buildup, including the down-frequency shifting of the spectral density peak. A 24-hour study of the vertical motion auto-spectra, made during extreme condition of wind variations, delineated unique spectra associated with different parameters such as wind speed, fetch, and duration.

8. LIMDUM I data indicated a linear decrease in the spatial correlation coefficient of similar velocity components with depth.

9. The covariance function $\overline{u'w'}$ indicated predominantly negative and, in many cases, relatively large values. The inferred Reynolds stresses ($-\rho\overline{u'w'}$) were thus generally positive, with a large range of values averaging about 15-20 dyne cm^{-2}. This indicated a downward transport of wind-imparted horizontal momentum. The stresses tended to attenuate with depth in a manner similar to the variances of the motions.

10. Qua-spectra were much larger than co-spectra for the OMDUM III measurements. Contributions to both qua-spectra and co-spectra were predominantly from the ambient wave frequencies, as indicated by the auto-spectral and coherence function peaks.

11. Estimates of mean shear of horizontal motion allowed approximate evaluation of the dissipation function $-\rho\overline{u'w'}\frac{\partial\bar{u}}{\partial z}$. The positive values obtained indicate predominant kinetic energy flow from mean motion to the wave motions.

12. For completeness, some hypothetical two-dimensional wave models were constructed which contained perturbations realizable from physical interaction of wind stress at the wave surface. These models displayed variances, covariances, auto-spectra and cross-spectra similar to those obtained from the real data. These models also served to demonstrate how physical properties can be ascertained from the rather esoteric statistics of cross-spectra and coherence.

Small mean phase shifts (possibly caused by surface wind forces) can produce covariances of the order of magnitude observed within the wave motions; however, artificial phase shifts in the instrumentation can also contribute to the covariance.

The small phase shifts of one orthogonal velocity component with respect to the other are associated with orbits corresponding to a sloped ellipse (with the semi-major axis in the vertical, tipped backwards). This configuration was shown by Starr to suggest a mechanism for the downward transfer of horizontal wind imparted momentum.

A few additional words should be said regarding the apparently exceedingly large Reynolds stresses observed within the waves. Values of wind stress on the water (usually an order of magnitude smaller than the ones reported here) have been inferred by many authors, even though no direct measurements have thus far been made. In general, one chooses some value of mean stress appropriate for the particular ocean circulation model under examination. A stress value of one dyne cm^{-2} is often used (e.g., Stommel, 1958, page 90). If this is the value estimated for a large ocean area, it seems plausible that, since sea surface stress is a vector quantity having both magnitude and direction (which is that of the local wind), spatially and vectorially averaged values must be quite dependent on the direction of the stress vector at each point. Thus, the averaged vector magnitude may not be indicative of local magnitude. Furthermore, stress is generally associated with the approximate square of the wind speed. In local regions of high winds, there may be a disproportionately large contribution of stress (from these relatively small areas of ocean) to the mean wind stress over the whole ocean.

With regard to theories of wind-driven ocean circulation models, the wind stress is that which drives the ocean currents. It is possible that a considerable fraction of the wind-induced stress applied at the sea surface is utilized in wave generation and turbulent diffusion.

Although the reported stresses in the waves seem large, the vagaries inherent in this subject preclude sound justification for doubting these values at this time.

Future Studies

The following suggested future studies should prove of significant value to the investigations of turbulent processes in the ocean.

1. As previously mentioned, improved calibration procedures must be utilized, which will remove many of the uncertainties pertaining to the potential biasing of the wave meters. A new (OMDUM IV) system having a threshold velocity of less than 2 cm sec^{-1} would allow more precise examination of wave motions associated with higher frequencies and smaller velocity amplitudes.

The use of arrays of ducted meters could provide a much clearer picture of the instantaneous field of motion within the waves. With improved instrument suspension, more extreme wave conditions could be examined with regard to variance and auto-spectra distribution with depth, and estimates could be made of total wave kinetic energy.

The vertically mounted ducted impeller provided the most accurate data because of stability in the suspension from the BBELS. By attaching a fast-response thermal sensor to the w impeller, one can measure the quantity $-\rho C_\rho \overline{T'w'}$, where C_ρ is the thermal heat capacity of sea water, and T' is the temperature fluctuation about the mean. This quantity, which has units of cal cm^{-2} sec^{-1}, is a measure of net heat flux through a unit area brought about by the covariance $-\overline{T'w'}$. The BBELS, being located in an area having a shallow seasonal thermocline to provide maximum temperature gradients, provides a suitable platform from which to make such heat flux measurements. A small fast-response (0.1-0.2 sec) thermal sensor is under construction, and plans are being made to use it in conjunction with the new low-velocity-threshold ducted impeller.

2. There is little concrete evidence of the direct generation of a surface current by wind stress. Recent results of open ocean current measurements (Day and Webster, 1966) indicate fluctuations in near-surface currents which correlate with wind fluctuations. However, obvious difficulties, both in precise current measurements and in monitoring wind conditions, make the correlations somewhat tenuous. What is needed is a precise monitoring of both wind and surface current during a period of time when extreme wind variations occur, as with the passing of a line squall. Such measurements of surface current and vertical gradient of surface current, along with precise wind velocity monitoring, could be made from the BBELS. This fixed platform would allow positioning of a number of vertically spaced LIMDUM-type devices in the water column. By subtracting the effects of tide current from the records, one might be able to determine the correlation between wind intensity and wind-produced surface current.

3. Plans are underway to mount rigidly a three-component (x, y, z) ducted current meter (OMDUM IV) from the sea bottom to measure variances and covariances associated with mean flow interaction with bottom roughness elements. This system will contain a miniature battery-powered tape recorder to store the raw output of the u, v, and w velocity channels. It is hoped that a deep research vehicle can be used to plant this system and to observe its response.

4. The ducted meters, having both rapid response and directional characteristics, could be used to assess the dynamics of strings of Richardson current meter arrays placed in the deep ocean. These systems consist of several self-contained Savonius rotor meters tethered in series between the sea surface and the bottom, which may be deeper than 5000 meters. The dynamic motions, which may be highly oscillatory and occur at different depths, can cause complex perturbations of the suspended current meters, thus biasing the data.

This dynamic system of moored current meters is so complex that an attempt to analyze the three-dimensional motions of each tethered instrument from its own data is prohibitive, since the driving forces are not known with any degree of precision. It is, of course, these driving forces which we wish to determine in the first place.

By mounting orthogonal sets of ducted meters on the current meter system, one could monitor the various translational and rotational motions occurring at various points of the mooring system. In particular, the vertical surging motions could be

measured precisely. These perturbations recorded on the array would permit a better judgment of the records of the Savonius rotor systems.

5. The study of the mechanism of the production of ambient acoustic noise produced at the sea surface is still in its infancy. It is known, however, that noise is associated with wind and wave turbulence in the region of the air-sea interface. Further, it is evident that the intensity of wave turbulence over a wide frequency (or wave number) range is directly related to the gross kinetic energy associated with the wave motions.

The wave meters can be used to estimate both the total wave kinetic energy and its distribution with frequency from 0 to 2.5 cps. (Note that the variances written as $\rho \overline{u'^2}$ and $\rho \overline{w'^2}$ are dynamic pressure quantities, quite analagous to those which are sensed by a hydrophone, except at acoustic frequencies.) It would be of interest to attempt to correlate both the total energy and the spectral character of wind waves with similar properties of acoustic noise measured simultaneously in the waves.

If a sensible correlation of energy content were found in the two frequency ranges, then conversely, one might consider using the statistical properties of the wave-produced ambient noise to delineate sea state and, possibly, to study the waves themselves.

Analysis of the data obtained from the described BBELS wave measurements is continuing under projects sponsored by NUWS and M.I.T. Additional field and laboratory work is to follow.

It is anticipated (and, indeed, hoped) that other workers will join in this effort to directly measure wave motions, and that this report will serve as an impetus and guide for future studies. The technology is available to overcome the greatest difficulty -- that of developing instrumentation to accurately probe ocean turbulence. We need only apply it with experience and boldness to attain our goal.

REFERENCES

Barber, N. F. 1961. Experimental Correlograms and Fourier Transforms. Pergamon Press, New York; 136pp.

Batchelor, G. K. 1953. The Theory of Homogeneous Turbulence. Cambridge Univ. Press, London; 285pp.

Blackman, R. B., and J. W. Tukey. 1958. The Measurement of Power Spectra. Dover Pub. Inc., New York; 190pp.

Bowden, K. F. 1962-A. Turbulence. Sect. VI, The Sea. (M. N. Hill, Ed.) John Wiley and Sons, New York; pp 802-817.

Bowden, K. F. 1962-B. Measurements of Turbulence Near the Sea Bed in a Tidal Current. J. Geophys. Res. 67. No. 8; pp 3177-3180.

Bowden, K. F., and J. Proudman. 1949. Observations of the Turbulent Fluctuations of a Tidal Current. Proc. Roy. Soc., London. A 199; pp 311-327.

Bowden, K. F., and L. A. Fairbairn. 1952. Further Observations of the Turbulent Fluctuations in a Tidal Current. Phil. Trans. Roy. Soc., London. A 244; pp 335-356.

Bowden, K. F., and L. A. Fairbairn. 1956. Measurements of Turbulent Fluctuations and Reynolds Stresses in a Tidal Current. Proc. Roy. Soc., London. A 1210, Vol. 237.

Bridgman, P. W. 1956. Dimensional Analysis. Yale University Press., New Haven, Conn.; 113pp.

Bruch, H. 1940. Die Vertical Verteilung von Windgeschwindigkeit und Temperatur in den Untersten Metern Uber der Wasser Oberflache. Verof. Inst. f. Meerskunde. NFA Heft 38.

Burling, R. W. 1959. The Spectrum of Waves at Short Fetches. Deutschen Hydrogr. Zeitschrift. 12 (2) 45; 117pp.

Caldwell, J. M., and L. C. Williams. 1963. The Beach Erosion Boards Wave Analyzer and Its Purpose in Ocean Wave Spectra. Prentice-Hall, Inc., Englewood Cliffs, N. J.; 357pp.

Challupnik, J. D., and P. S. Green. 1962. A Doppler Shift Ocean Current Meter, Marine Sciences Instrumentation. Vol. 1, (R. Gaul, Ed.) Plenum Press, New York.

Chase, J., L.J. Cote, W. Marks, E. Mehr, W. J. Pierson, Jr., F. G. Ronne, G. Stephenson, R. C. Vetter, and R. G. Walden. 1957. The Directional Spectrum of a Wind Generated Sea as Determined from Data Obtained by the Stereo Wave Observation Project. N Y U. Coll. of Eng., Dept of Meteor. and Oceano. and Engineering Statistics Group. Tech. Rep. for ONR; 247 pp (unpublished manuscript).

Clark, J. (chairman). 1964. Techniques for Infrared Survey of Sea Temperature Report of a Workshop held at U.S. Dept. of Interior, 27-28 April 1964. Bu. Circ. 202, Sandy Hook Marine Laboratory (unpublished manuscript).

Coulson, C. A. 1958. Waves – A Mathematical Account of the Common Type of Wave Motion. Oliver and Boyd London; 159pp.

Cramer H. E. 1959. Measurements of Turbulent Structure Near the Ground within the Frequency Range from 0.5 to 0.01 cps. Adv. in Geophysics. (H Landsburg, Ed.) Academic Press, New York.

Cramer, H. E., F. A. Record, and J. E. Tillman. 1962. Studies of the Spectra of Vertical Fluxes of Momentum, Heat, and Moisture in the Atmospheric Boundary Layer, Final Report. DSR-MIT, Dept. of Meteorology, Round Hill Field Station, South Dartmouth, Mass. (unpublished manuscript).

Day, C. G., and F. Webster. 1965. Some Current Measurements in the Sargasso Sea. Deep Sea Res., Vol. 12; pp 805-814.

Deacon, E. L. 1955. The Turbulent Transfer of Momentum in the Lowest Layers of the Atmosphere. Tech. Paper No. 4, Melbourne C.S.I.R.O. Div. Meteor. Physics.

Defant, A. 1958. Ebb and Flow. University of Michigan Press Ann Arbor, Michigan; 121pp.

Doe, L. A. F. 1963. A Three Component Thrust Anemometer for Studies of Vertical Transports above the Sea Surface. Report 63-1. Bedford Inst. of Ocean., Dartmouth, N. S. (unpublished manuscript).

Doodson, A. T. 1940. A Current Meter for Measuring Turbulence. Hydrog. Rev. 17, pp79-100.

Eagleson, P. S., and W. P. M. Van de Watering. 1963. A Thermistor Probe for Measuring Particle Orbital Speed in Water Waves. Rep. No. 61. Hydrodynamics Laboratory, Dept. of Civ. Eng., Mass. Institute of Technology; 50pp (unpublished manuscript).

Eckart,C. 1955. Statistical Hydrodynamics. J. Mar. Res. 14; pp295-301.

Ekman, V. W. 1926. An Ocean Current Meter. Publ. Circ. Cons. Explor. Mer. 91; 27pp.

Ekman, V. W. 1953. Studies on Ocean Currents. Results of a **Cruise** on Board the "ARMOUR HANSEN" in 1930 under the leadership of Bjorn Helland-Hansen. Geophys. publ. 19 (1); pts I and II.

Ellis, G. E. and J. L. Collins. 1964. Practical Aspects of Bottom Studies. DRL-A-222. Def. Res. Lab. Univ. of Texas, Austin, Texas; 104pp (unpublished manuscript).

Flow Corp. 1965. Operation Manual for Oceanographic Sphere Current Meter. Cambridge, Mass. (unpublished manuscript).

Francis, J. R. B., H. Stommel, H. G. Farmer, and D. Parson, Jr. 1953. Observations of Turbulent Mixing Processes in a Tidal Estuary. Reference 53-22. W.H.O.I., Woods Hole, Mass. (unpublished manuscript).

Frenkiel, F. N. (Ed.) 1962. Symposium, Fundamental Problems in Turbulence and their Relation to Geophysics. (Held in Marseilles, France) J. Am. Geophys. U. 67; No. 8.

Grant, H. L., R. W. Stewart, and A. Moillet. 1962. Turbulent Spectra from a Tidal Channel. J. Fluid Mech. 12. Part 2.

Guelke, R. W., and C. A. Schoute-Vanneck. 1947. The Measurement of Sea Water Velocities by Electromagnetic Induction. Jour. Inst. Elect. Engineers (London) 94 II. No. 37; pp71-74.

Hamon, B. V., and E. J. Hannan. 1963. Estimating Relations between Time Series. J. Geophys. Res. 68, No. 21; p6033.

Hellstrom, B. 1953. Wind Effects on Ringkobing Fjord. Trans. American Geophys. U. 34, No. 2.

Hinze, J. O. 1959. Turbulence. McGraw Hill, New York; 586 pp.

Hunt, L. M. 1961. Wave Generated Oscillatory Currents along the Bottom in the Eulittoral and Sublittoral Zones. Rep. Nat. Acad. Sci. and Nat. Res. Council (unpublished manuscript).

Jacobson, J. P. 1918. Hydrographische Untersuchungen in Randersfjord (Jylland). Medd. Komm. Havundersgelser. Ser. Hydrogr. Bd. II. No. 7; pp1-46.

James, G., and R. C. James (Editors). 1949. Mathematics Dictionary. D. Van Nostrand Co., Inc., Princeton, N. J.; 432pp.

Keulegan, G. 1951. Wind Tides in Small Closed Channels. J. of Res. Nat. Bu. Standards. 46, No. 5 (unpublished manuscript).

Kinsman, B. 1960. Surface Waves at Short Fetches and Low Wind Speeds - A Field Study. (3 volumes) Tech. Report XIX, Chesapeake Bay Institute, Baltimore, Maryland (unpublished manuscript).

Kinsman, B. 1965. Wind Waves - Their Generation and Propagation on the Ocean Surface. Prentice-Hall, Inc., Englewood Cliffs, New Jersey; 676pp.

Kishi, T. 1954. Experimental Study of the Orbital Motion on the Surface Wave in Shallow Water. Jour. of Res., Public Works Res. Inst., Japan. 1. Res. Paper 10.

Kolmogoroff, A. N. 1941. On Degeneration of Isotropic Turbulence in an Incompressible Viscous Liquid. Comptes Rendus (Doklady) de l'Academie des Science de l'U.S.S.R. Vol. 31.

Lamb, H. 1945. Hydrodynamics. Dover Pub., New York; 738 pp.

Larsen, H. D. 1956. Rinehart Mathematical Tables, Formulas, and Curves. Rinehart and Co., Inc. New York; 280pp.

Lee, Y. W. 1960. Statistical Theory of Communication. John Wiley and Sons, Inc., New York; 509pp.

Lester, R. A. 1961. High Accuracy, Self Calibrating Acoustic Flow Meters. Marine Sciences Instrumentation. 1 (R. Gaul, Ed.) Plenum Press, New York.

Marks, W. 1964. Sea State Chart, Geo-Marine Technology. 1, No. 1 (Metric Units Conversion, F. G. Wyatt, Jr., N.U.O.S., Newport, R.I. 1965.)(unpublished manuscript).

Marlow, T. A. 1957. An Experimental Determination of Particle Velocities in the Oscillatory Water Wave. S. M. Thesis., M.I.T., Dept. of Civ. Eng. (unpublished manuscript).

Mee, T. R., Jr. 1963. Project Sea Surface _An Investigation of the Dynamics of Water Waves. Cal. Report No. RG-1623-P-1, Cornell Aeronautical Laboratory, Inc., Buffalo, New York; 35pp (unpublished manuscript).

Miller, R. L., and J. S. Kahn. 1962. Statistical Analysis in the Geological Sciences. John Wiley and Sons, Inc., New York; 483pp.

Mobarek, I. E. 1965. Comparison of Spectra Obtained by CERC Spectrum Analyzer and Digital Processes. Coastal Engineering Research Center, Washington, D. C. (unpublished manuscript).

Montgomery, R. B. 1936. On the Momentum Transfer at the Sea Surface; 11 Measurements of Vertical Gradient of the Wind over Water. Pap. Phys. Ocean. and Meteor. 4. No. 3.

Mossby, H. 1947. Experiments on Turbulence and Friction Near the Bottom of the Sea. Bergens Mus. Aarb., (3).

Mossby, H. 1949. Experiments on Bottom Friction. Bergens Mus. Aarb., (10).

Mossby, H. 1951. Bottom Current Fluctuations in the Open Sea. Assoc. Phys. Proc. Verb., 5; 195pp.

Munk, W. H. 1947. A Critical Wind Speed for Air-Sea Boundary Processes. J. Mar. Res., VI. 3; pp203-218.

Munk, W. H., and G. J. F. MacDonald. 1960. The Rotation of the Earth: A Geophysical Discussion. Cambridge University Press, London; 320pp.

Neumann, G. 1956. Wind Stress on Water Surfaces. Bul. Am. Meteor. Soc. 37, No. 5; pp 211-217.

Ocean Wave Spectra. 1963. Proceedings of a Conference sponsored by the National Academy of Sciences. Prentice-Hall, Inc., Englewood Cliffs, New Jersey; 258pp.

Palmen, E. 1932. Versuch zue Bestimmung des Tangentialdruckes des Windes auf die Meeresoberflache Mittels Wasserstands Schwankungen. Ann. d. Hydro und Marit. Meteorologie.

Phillips, O. M. 1957. On the Generation of Waves by Turbulent Wind. Jour. Fluid Mech., 2 (5); pp 417-445.

Phillips, O. M. 1958. The Equillibrium Range in the Spectrum of Wind Generated Waves. Jour. Fluid Mech., 4; pp 426-434.

Phillips, O. M. 1963. The Upper Ocean Layers. Technical Report 231-1, Hydronautics, Inc., Laurel, Maryland (unpublished manuscript).

Pierson, W. J., Jr. 1952. A Unified Mathematical Theory for the Analysis, Propagation and Refraction of Storm Generated Ocean Surface Waves, I and II. N.Y.U. Coll. of Eng., Res. Div. Dept. Meteorology and Oceanography. Prepared for the Beach Erosion Bd., Dept. of Army and ONR (unpublished manuscript).

Pierson, W. J., Jr. 1955. Wind-Generated Gravity Waves. Advances in Geophysics. Vol. 2 (H. Landsberg, Ed.) Academic Press, Inc., New York; pp 93-178.

Pierson, W. J., Jr. 1959. A Note on the Growth and Spectrum of Wind Generated Gravity Waves as Determined by Non Linear Considerations. Jour. Geophys. Res. 64; pp 1007-1011.

Pierson, W. J., Jr., G. Neumann, and R. W. James. 1955. Observing and Forecasting Ocean Waves by Means of Wave Spectra and Statistics. Hydro. Ofc., Washington, D. C.; 284pp.

Platzman, G. W., and D. B. Rao. 1964. Spectra of Lake Erie Water Levels. Jour. Geophys. Res. 69. No. 12; 2525pp.

Prandtl, L. 1952. Essentials of Fluid Dynamics. Hafner Pub. Co., New York; 452pp.

Priestly, C. H. B. 1959. Turbulent Transfer in the Lower Atmosphere. Univ. of Chicago Press, Chicago, Ill.; 130 pp.

Pritchard, D. W. 1952. Estuarine Hydrography. Advances in Geophysics, Vol. 1 (H. Landsberg, Ed.) Academic Press, Inc., New York' pp 243-280.

Pritchard, D. W. 1964. (personal communication) Chesapeake Bay Institute, Johns Hopkins University, Baltimore, Md.

Proudman, J. 1953. Dynamical Oceanography. Methuen Co., Ltd. London; 409pp.

Rice, S. O. 1944. Mathematical Analysis of Random Noise. Bell Syst. Tech.J. 23; pp 282-332.

Rice, S. O. 1954. Mathematical Analysis of Random Noise. In Noise and Stochastic Processes (N. Wax, Ed.) Dover Pub. Inc.; pp 133-294.

Roll, U. 1952. Gibt es Eine Kritische Windgeschwindigkeit fur Prozesse an der Grenzflache Wasser - 1 ft? Riv. Geofisica Pura e Applicata, Vol. 21.

Sheppard, P. A., and M. H. Omar. 1952. The Wind Stress over the Ocean from Observations in the Trades. Quart. J. Roy. Met. Soc., London, 28.

Shonting, D. H. 1964. A Preliminary Investigation of Momentum Flux in Ocean Waves. Pure and Appl. Geophys., Vol 57/1; pp 149-152.

Shonting, D. H. 1965. Preliminary Studies of Momentum Flux in Ocean Waves. Paper presented at Symposium on Diffusion in Oceans and Fresh Waters. Aug. 31-Sept. 2, Lamont Geological Observatory, Pallisades, New York.

Shonting, D. H., and G. S. Cook. 1964. Drogue Current Observations in the Thresher Search Area (29 May to 3 June 1963). Technical Mem. No. 307. U. S. Naval Underwater Ordnance Station (unpublished manuscript).

Shonting, D. H., and G. S. Cook. 1966. A Seasonal Study of the Distribution of Temperature and Salinity in Rhode Island Sound. Limnol. and Ocean. 11 (in preparation).

Shonting, D. H., G. S. Cook, and F. G. Wyatt, Jr. 1966 Oceanographic Observations in Rhode Island Sound 1963-64; A Data Report. Consecutive Report No. 423. U.S. Naval Underwater Ordnance Station (unpublished manuscript).

Shuleykin, V. V. 1959. Kratki Kurse Physiki Moria (A Short Course in the Physics of the Ocean). The Hydrometeorological Institute, Leningrad, U.S.S.R.; 478pp.

Snodgrass, F.,W. Munk, and M. J. Tucker. 1958. Off-Shore Recording of Low-Frequency Ocean Waves. Trans. Am. Geophys. Union, XXXXIX; pp 114-120.

Starr, V. P. 1945. Water Transport of Surface Waves. J.Meteor.Vol. 2, No. 2; pp 129-131.

Starr. V. P. 1946. A Quasi-Lagrangian System of Hydrodynamic Equations. J.Meteor.Vol. 2, No. 4; pp 227-237.

Starr, V. P. 1948. An Essay on the General Circulation of the Earth's Atmosphere. J.Meteor.Vol. 5, No. 2; pp 39-43.

Starr, V. P. 1956. Modern Development in the Study of the General Circulation of the Atmosphere. J. Geophys. Res. 61 .

Starr, V. P. 1961. Hydrodynamical Red-Shift Phenomena in Geophysics. Pure and Appl. Geophys. (formerly Geofiscia Pura e Applicata) Vol. 48 (1); pp 109-123.

Stewart, R. W. 1961. The Wave Drag of Wind over Water. J. Fluid Mech. Vol. 10; pp 189-194.

Stewart, R. W., and H. L. Grant. 1962. Determination of the Rate of Dissipation of Turbulence Near the Sea Surface in the Presence of Waves. J. Geophys. Res. 67, No. 8.

Stommel, H. 1958. The Gulf Stream. Univ. of Calif. Press. Berkeley, Calif.; 201pp .

Sutton, O. G. 1953. Micrometeorology. McGraw-Hill, New York.

Sverdrup, H. U., M. W. Johnson, and R. H. Fleming. 1942. The Oceans; Their Physics, Chemistry and General Biology. Prentice-Hall, Inc., Englewood Cliffs, New Jersey;1060pp.

Thompson, Sir William. 1871. Hydrokinetic Solutions and Observations. Phil. Mag. (4) 42; pp 362-377.

Thorade, H. 1934. Uber Stromunruhe Nach Beobachtungen im Kattegat, August 1931. Ann. Hydrog. Mar. 62; pp 365-377.

Thornthwaite, C. W., and M. Halstead. 1942. Notes on the Variation of Wind with Height in the Layer Near the Ground. Trans. Amer. Geophys. Union; p 249.

Tucker, M. J. 1956. A Shipborne Wave Recorder. Trans. Roy. Inst. Nav. Arch., Vol. 98; pp 236-250.

Tukey, J. W. 1949. The Sampling Theory of Power Spectrum Estimates. In Symposium on Applications of Autocorrelation Analysis to Physical Problems, Woods Hole, Mass., June 13-14, 1949. NAVEXOS - P - 735, Office of Naval Research, Washington, D. C.; pp 45-67 (unpublished manuscript).

Tukey, J. W., and R. W. Hamming. 1949. Measuring Noise Color. 1. Bell Telephone Labs., Inc., Murray-Hill, New Jersey Mem. for Five, MM-49-110-119; 120pp.

Von Arx, W. S. 1950. Some Current Meters Designed for Suspension from an Anchored Ship. J. Mar. Res., 9 (2); pp 93-99.

Von Arx, W. S. 1962. An Introduction to Physical Oceanography. Addison-Wesley Pub. Co., Reading, Mass.; 422pp.

Webster, F. 1961. The Effect of Meanders on the Kinetic Energy Balance of the Gulf Stream. Tellus. XIII. 3; pp 392-401.

Welander, P. 1961. Coupling Between the Sea and Air, Oceanography (M. Sears, Ed.) Am. Assoc. Adv. Sci., Washington, D. C. Pub. 67.

Wiegal, R. L. 1964. Oceanographical Engineering. Prentice-Hall, Inc., Englewood Cliffs, New Jersey; 532pp.

Wiener, N. 1933. The Fourier Integral and Certain of Its Applications. Dover Pub., New York.

Williams, L. C. 1964. (personal communication) Coastal Engineering Research Center of the U. S. Army Corps of Engineers, Washington, D. C.

Wust, G. 1937. Temperatur und Dampfdruck Gefalle in den Unterstnen Metern Uber der Meersoberflache. Met. Zeitschr. 54 .

Zeigler, J. M. 1963. (personal communication) Woods Hole Oceanographic Institution, Woods Hole, Mass.